Stony Brook University

Understanding the dielectric properties of water

A Dissertation Presented

by

Daniel Christopher Elton

to

The Graduate School

in Partial Fulfillment of the Requirements

for the Degree of

Doctor of Philosophy

in

Physics

Stony Brook University

December 2016

Stony Brook University

The Graduate School

Daniel Christopher Elton

We, the dissertation committee for the above candidate for the
Doctor of Philosophy degree, hereby recommend
acceptance of this dissertation

Marivi Fernández-Serra - Dissertation Advisor
Professor, Department of Physics and Astronomy

Phillip B. Allen - Chairperson of Defense
Professor, Department of Physics and Astronomy

Matthew Dawber
Associate Professor, Department of Physics and Astronomy

Alan Calder
Professor, Department of Physics and Astronomy

Matthew Reuter
Assistant Professor, Department of Applied Mathematics and Statistics

This dissertation is accepted by the Graduate School

Charles Taber
Dean of the Graduate School

Abstract of the Dissertation

Understanding the dielectric properties of water

by

Daniel Christopher Elton

Doctor of Philosophy

in

Physics

Stony Brook University

2016

Liquid water is a complex material with many anomalous properties. Three of these anomalies are an abnormally high dielectric constant, an abnormally high boiling point, and a solid phase which is less dense than the liquid phase. Each of these anomalies is known to have been critically important in the development of life on Earth. All of water's special properties can be linked to water's unique ability to form hydrogen bonds. Water's hydrogen bonds form a transient network. Understanding the average structure of this network and how it changes through the phase diagram remains the focus of intense research.

In this thesis we focus on understanding dielectric and infrared measurements, which measure the absorption and refraction of electromagnetic waves at different frequencies. Computer simulation is a necessary tool for correctly interpreting these measurements in terms of the microscopic dynamics of molecules.

In the first part of this thesis we compare three classes of water molecule model that are used in molecular dynamics simulation

rigid, flexible, and polarizable. We show how the inclusion of polarization is necessary to capture how water's properties change with pressure and temperature. This finding is relevant to biophysical simulation. In the next part, we conduct a detailed study of water's dielectric properties to discover vibrational modes that propagate through the hydrogen bond network. Parts of the absorption spectrum of water are due to electromagnetic waves coupling to these modes. Previously, vibrational motions in water were thought to be confined to small clusters of perhaps five molecules. Our work upends this view by arguing that dynamics occur on the hydrogen bond network, resulting in modes that can propagate surprisingly long distances of up to two nanometers. These modes bear many similarities to optical phonon modes in ice. We show how the LO-TO splitting of these modes provides a new window into the structure of the hydrogen bond network.

In the final part of this thesis we turn to the problems one encounters when trying to simulate water from "first principles", ie. from the laws of quantum mechanics. The primary technique that physicists use to approximate the quantum mechanics of electrons, density functional theory, does not work well for water, and much work is being done to understand how to fix this problem. A usual assumption in first principles simulation is that only electrons need to be treated quantum mechanically. We argue that both electrons and nuclei need to be treated quantum mechanically and we present a new code to do this. The custom code presented in this thesis implements a novel algorithm which greatly speeds up the calculation of nuclear quantum effects with only minor losses in accuracy. We hope that others will start using our technique to advance first principles simulation. Accurate first principles simulation of water is important for understanding and developing solar water splitting catalysts and batteries. First principles simulations are also being increasingly used to understand proteins and drug molecules, and this trend will continue with Moore's law.

To my parents

Contents

List of Figures

List of Tables

Acknowledgements

First and foremost I would like to thank my adviser, Prof. Marivi Fernández-Serra. Marivi cares a lot about every one of her PhD students and always makes sure they are working on worthwhile projects. Marivi held me to very high scientific standards and really pushed me to try to understand the results I got from simulations. When I first started working with her, Marivi entrusted me with a very exciting project rather than something simple or mundane. I am very thankful that she gave me leeway to explore things on my own and allowed me work on things that I found the most interesting. I am especially grateful for her patience and help as I faltered with my project in the final year of my PhD.

Many thanks go to Prof. Phil Allen for valuable feedback during group meetings and for stimulating discussions. I was humbled by the large number of typographical and mathematical errors he discovered during his thorough proofreading of this thesis. I would also like to thank the other professors who served on my annual review committee through the course of my PhD, Matt Dawber and Ken Dill. They each inspired me in their own way.

The two people who I am most grateful to overall are my parents, Richard Elton and Cheryl Elton. I am very thankful to my parents for providing me with a very happy and vibrant childhood. Both my parents read to me at a young age and provided me with a rich learning environment that led to me becoming interested in science and technology at a young age. My father, a chemical engineer, did chemistry experiments with me in the backyard, brought home appliances and computer equipment for me to take apart, and allowed me to have my own electronics and chemistry labs in the basement. I would especially like to thank my mom for her unwavering love and dedication over the years and for helping me through difficult times during the PhD. My mother recently fulfilled one of her life goals by writing a book, *Pathway of Peace*. Both my parents have been great role models in my life, each in their own way. I also acknowledge my uncle, Prof. David J. Elton (P.E., S.M., M.ASCE) as another role model who has influenced me.

All of the professors that I took courses with at Stony Brook were excellent,

but I would like to highlight two professors who challenged me during the first year of my PhD: Prof. Likharev and Prof. Koch. Prof. Likharev's lectures and homework were taught with a level of rigor I have not experienced before or since and have left quite an impression on me. TAing with Prof. Koch for three semesters was very stressful and challenging but I became a much better TA and grew as a person as a result.

I would also like to thank the labmates who I've worked with the past four years - Adrian Soto, Betül Pamuk, Simon Divlov, Luana Pedroza, Michelle Fritz, and Sriram Ganeshan. Each of them has provided important help with the research contained in this thesis. I'd also like to thank my close friends Eliza Guseva, Matthew von Hippel, Elena Hambardjieva, Kevin Hauser, Vladislav Zakharov, Matt Wroten, Helen Jolly, and Natalie Stenzoski for all of their help and support.

Chapter 1

Introduction

"There must be no barriers to freedom of inquiry... There is no place for dogma in science... And we know that as long as men are free to ask what they must, free to say what they think, free to think what they will, freedom can never be lost, and science can never regress." - J. Robert Oppenheimer

The dielectric properties of water are important for understanding its properties as a solvent and absorber of electromagnetic radiation. Precise knowledge of these properties is important in diverse areas such as biophysics, climate science, remote sensing and microwave engineering. For this reason, water's dielectric properties have been measured to high accuracy at a large gamut of state points.[6, 17] However the molecular origin of water's dielectric constant, and the inability for many forcefield molecular dynamics models to reproduce it, is not fully understood. Additionally the molecular origins of many features of water's dielectric spectra are poorly understood, especially in the THz and far infrared regions.

The abnormally high dielectric constant of water is often explained as being due to a large liquid phase dipole moment ($\approx$ 2.95 D[18]). This explanation misses the critical role of dipole correlation which is mediated by H-bonds.

Kirkwood showed in 1939 that the dielectric constant depends not just on the size of dipoles but also on the degree of correlation between neighboring dipoles.[19] Kirkwood's 1939 work showed that the tetrahedral coordination of hydrogen bonds increases dipolar correlation, which in turn increases the dielectric constant (see section 3.3 for a detailed discussion of Kirkwood's theory). Figure 1 shows the geometry of perfect tetrahedral coordination and the resulting dipole moments of the molecules.

Assuming a dipole moment of 2.95 D, Kirkwood's equation (ref. 3.28), which is an exact result, indicates that the large dipole moment of water only

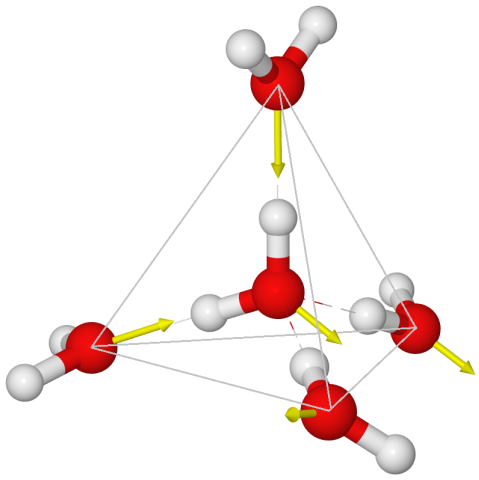

Figure 1.1: Schematic of the tetrahedral coordination of water molecules. The yellow arrows show dipole moments Overall, the 5 molecule tetrahedron has a larger dipole than that of a single molecule.

accounts for 40 % of the magnitude of the dielectric constant and that the rest is due to dipole-dipole correlation. The large dipole moment of water itself is largely caused by H-bond interactions – the dipole moment of the water molecule increases from the gas phase value of $\mu_g = 1.85$ D as a result of local interactions, in particular the hydrogen bond interaction. The most widely used method for quantum mechanical simulation, density functional theory (DFT) shows that a water molecule's dipole moment increases in proportion to the number of hydrogen bonds it has.[20] The dipole moment of H_20 in liquid water is not known exactly. An x-ray study by Badyal, et. al. yielded $\mu = 2.95 \pm .6$ D,[21] and a detailed study of index of refraction data by Gubskaya & Kusalik data yielded a value of $\mu = 2.95 \pm .2$ D.[18] The dipole moment of Ice Ih is well established to be $3.0-3.1$ D, which effectively sets an upper bound on the dipole moment for the liquid phase.[18, 22] The importance of the H-bond network is confirmed in computer simulations which show a strong correlation between the density of hydrogen bonds and dielectric constant.[23, 24] The importance of the extended H-bond network can also be inferred from the observation that dissolved solutes decrease $\varepsilon(0)$. Remarkably, the decrease in $\varepsilon(0)$ with solute concentration is largely independent of the type of solute,[25] suggesting that the depression in $\varepsilon(0)$ is not due to local interaction of water with the solute but rather a longer scale disruption of the H-bond network.

1.1 Some open questions about water

Liquid water has a lot of anomalous properties which cannot be found in other liquids. On his website, Martin Chaplin identifies 69 different anomalous properties.[2] Chief among these are water's anomalously high melting and boiling points relative to water's small molecular weight, water's expansion of volume upon freezing, and the lowering of the freezing point with pressure. Closely related to these is a class of response function anomalies:

- The isothermal compressibility K_T has a minimum at 46 C and then increases at lower temperatures. (Usually K_T decreases monotonically with T.)
- The specific heat C_P has a minimum at 36 C and increases at lower temperatures. (Usually C_P decreases monotonically with T.)
- The thermal conductivity κ of water is unusually high and increases with temperature until reaching a maximum at 130 C. (Usually κ decreases monotonically with temperature)

1.2 The liquid-liquid phase transition hypothesis

Currently, much work is being done to provide a unified framework for understanding water's anomalies. One such framework is the liquid-liquid phase transition idea, which says liquid water is best understood as a mixture of two types of liquid - high density liquid (HDL) and low density liquid (LDL). This according to this idea, liquid water lies above a second order critical point which lies hidden in the deeply supercooled region of the phase diagram.[26] Many thermodynamic properties of water (in particular isothermal compressibility) show an unexpected rapid increase as the temperature of supercooled water is lowered, suggesting a thermodynamic singularity is being approached.[27] Above a 2nd order critical point, one can define a Widom line that extends the phase transition line. One way to define it is as the line where the thermal compressibility reaches its maximum. Molecular dynamics simulations performed by Abascal & Vega have charted the Widom line from room temperature water into the deeply cooled region.[28] In one simulation at 191 K, 1450 bar they observed a transition between HDL and LDL.[28]

Water can be easily supercooled down to -20 C, and this is an important fact in determining when ice crystals will form in the upper atmosphere. However between -40 to -45 C one runs into a limit where internal density

fluctuations cause auto-nucleation, which is called the homogeneous nucleation limit.[26] The hypothetical supercooled region below -40 C is called the "no-mans land", and it is in this region that the liquid-liquid phase transition line and critical point is believed to exist. The no-mans land may also contain a spinoidal line,[26] which represents points where the liquid becomes thermodynamically unstable. A spinoidal line would be a true hard limit to supercooling. The existence of a spinoidal line in the no-mans land and whether it would connect to the liquid-gas spinoidal by passing through the region of negative pressure in the phase diagram is also debated.[29]

One can also approach the "no-mans" land region of the phase diagram from below by studying amorphous ice. One way to make amorphous ice by either cooling water at an extremely rapid rate or by putting normal ice under high pressure. Water molecules in amorphous ice are trapped in a a glass state which is technically a supercooled liquid state, but so cold that it behaves like a solid. Interestingly, at different pressures amorphous ice exists in two forms, low density amorphous (LDA) and high density amorphous (HDA). If pressure is removed from HDA, it quickly transforms into LDA. One might think that one can make water in the "no mans land" by heating up amorphous ice, but when heated amorphous ice transforms into normal ice, since molecules then have enough thermal energy to jump energy barriers into their preferred configuration.

Another way to probe the no-mans land is to use supercooled droplets,[30] since the probability of auto-nucleation is significantly decreased. Unfortunately, the thermodynamics of droplets is different than bulk water, largely due to surface tension effects which creates pressure on the liquid (Laplace pressure), but also from subtle confinement effects which change the structure of the H-bond network. Still, it may be possible to test the liquid-liquid phase transition in the case of droplets, lending credence to the idea.

The liquid-liquid phase transition hypothesis may sound pointless to debate, since bulk water cannot exist in the no-mans land, but is currently of great interest because it provides a framework for understanding many of water's anomalies.

1.2.1 Issues regarding water structure

Discussion of water structure goes back to 1892, when W.K. Röntgen proposed that water contains a mixture of two structural motifs "ice like" and "liquid like".[31] Today, the local structure of water as a function of temperature remains a source of research and lively debate.[32, 33, 34, 35, 36, 37]

The nature of the water structure debate has changed as more has been learned about the hydrogen bond network of water. In the 80s and 90s there

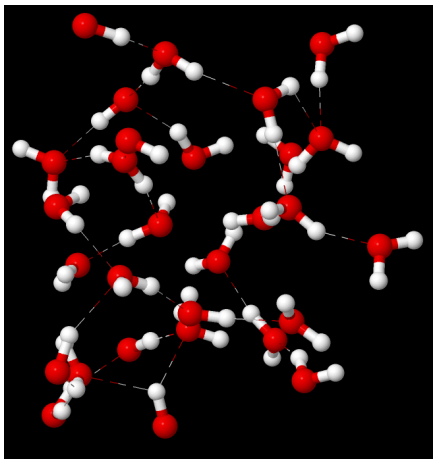

Figure 1.2: Schematic cross section of water, showing the H-bond network.

was also intense debate between experimentalists about how many H-bonds water molecules have on average. By the early 2000s, most scientists had reached a consensus that the average number in room temperature water was around 3.5. With many water molecules having 3 or 4 bonds, and almost no molecules having zero bonds, this implies that the hydrogen bond network is "fully connected" and extends through all of space (see fig. 1.2.1) for a schematic picture). Figure 1.2.1 shows the distributions of how many H-bonds molecules have at different temperatures, as obtained from classical MD simulations with the TIP4P/2005 model. Computer simulations using both classical molecular dynamics and *ab-initio* simulation have overall been very consistent in confirming this picture.

In 2004 x-ray scattering experimentalists published a provocative paper claiming that many molecules in water have only two hydrogen bonds, and that these molecules are connected in long chains. This possibility was debated for some time and is now largely believed to be incorrect.[38]

The present debate about the structure of water originates in large part from the publication of "The inhomogeneous structure of water at ambient conditions" by Huang, Nilsson, et al. in 2009.[35] Their argument largely rests on their interpretation of small angle X-ray scattering (SAXS) below 0.4Å^{-1}, where a minimum is observed at small q and enhancement is observed as $q \to 0$. The paper failed to find the enhancement when using a popular three-site forcefield model for water, SPC/E, and therefore implied that MD simulation could not be trusted to correctly reproduce the structure of water.

However, the region of small q is tricky to calculate from MD simulation, especially when calculating it by Fourier transforming the structure factor as

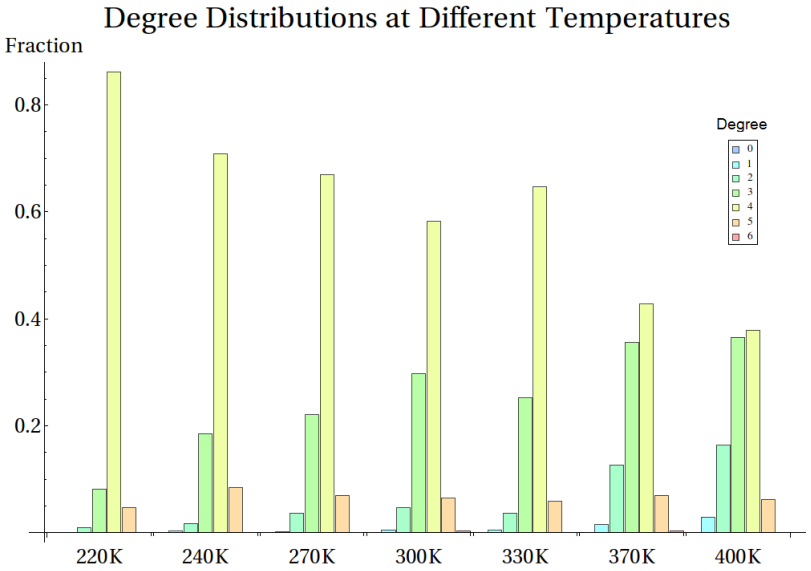

Figure 1.3: Distributions of the number of hydrogen bonds molecules have (the "degree") at different temperatures, as obtained from classical MD simulations with the TIP4P/2005 model. These distributions are well fit by a binomial distribution.

they did. Later MD simulation by Sedlmeier, Horinek, and Netz that used a better calculation method and larger simulation cell did recover a slight enhancement with SPC/E, and an even more pronounced enhancement is observed with the more accurate TIP5P and TIP4P/2005 models.[39]

Huang et al. claim the enhancement at small q is due to significant density fluctuations between regions of high density and low density liquid. However, in their own analysis Clark, Hura, Teixeira, Soper, and Teresa Head-Gordon conclude:

> "The increase in $S(q)$ at small angle is due to the normal density fluctuations which arise from stochastic processes in a single component fluid. The tetrahedral network forming TIP4P-Ew model of water qualitatively reproduces the trend in $S(q)$ at ambient conditions and yields the same correlation lengths arrived at by experiment."[40]

While molecular dynamics simulations of well-validated force-field models do show co-existence of HDL-like and LDL-like domains at very low temperature, they do not show such heterogeneity in room temperature water. The structure of the hydrogen bond network of water can be quantified using various "structure factors" or order parameters. The most popular of these is the

tetrahedral order parameter:[33]

$$q_4 = 1 - \frac{3}{8}\sum_{j=1}^{3}\sum_{k=j+1}^{4}\left(\cos(\Psi_{jk}) + \frac{1}{3}\right)^2 \tag{1.1}$$

Here $\Psi_{ij} = \arccos(\hat{\boldsymbol{r}}_{ij} \cdot \hat{\boldsymbol{r}}_{ik})$ is the angle between the selected oxygen atom i and the vectors pointing from that oxygen's position to the positions of two of its four nearest neighbours, $\boldsymbol{r}_j$ and $\boldsymbol{r}_k$. Other order parameters are Q_4, Q_6, S_k and the local structure index (LSI).[39]

The distributions of various local structure parameters as a function of temperature show a decrease in LDL-like molecules and increase in HDL-like molecules as the temperature is lowered. Very little bimodality in the distributions of order parameters is seen at room temperature, but bimodality increases as the temperature is lowered. When energy minimization is run on snapshots from MD simulation, one obtains so-called "inherent" structures. Inherent structures calculated from room temperature simulations of water exhibit a clearly bimodal distribution of Q_4.[41] However, Seldemeir et al. show that $Q_4 - Q_4$ correlations do not extend beyond 6 Angstroms, or the 2nd H-bonding shell. Furthermore, they note that the correlation between Q_4 and local density is rather small.[39]

The extent and nature of inhomogeneities in room temperature water remains controversial. A Dec. 2015 review by Nilsson & Pettersson does a good job defending the validity of the two-liquid model through several lines of experimental evidence, but goes too far by invoking a picture of HDL/LDL domains at room temperature.[42] Additionally, the isosbestic points[1] found in Raman and IR spectra are cited by Nilsson as evidence for HDL/LDL domains in liquid water, but this interpretation has been called into question.[43, 44]

1.3 Some questions that are explored in this thesis

- What can mean field theories tell us about the origin of the high dielectric constant of water? (chapter 3)
- What is the most efficient way to calculate the dielectric constant in a simulation? (chapter 4)

[1] In this context, an isosbestic point refers to a point in the spectrum where the absorption is independent of temperature.

- What are the relative contributions of dipolar reorientation, molecular flexibility, and electronic polarization to the dielectric constant? (Chapter 5)
- What role does hydrogen bonding play in determining the dielectric properties? What is the structure and spatial extent of dipolar correlations in liquid water? (chapter 6)
- What is the origin of the Debye relaxation of water? Why is it a simple exponential, while molecular orientation relaxation is a stretched exponential? (chapter 7)
- Does water contain polarizable nanodomains which contribute to its dielectric properties in a way which is equivalent to what happens in a relaxor ferroelectric? (chapter 8)
- What is the origin of the dispersive modes observed in k-dependent (nonlocal) dielectric spectra? (chapter 10)
- What can the dielectric properties and LO-TO splitting tell us about liquid structure? (chapter 10)
- What are the effects of nuclear quantum effects on liquid structure and dielectric properties? (Chapters 11)
- Is there a more computationally efficient way to perform PIMD simulations with minimal losses in accuracy? (chapter 12)

Chapter 2

Introduction to dielectric properties

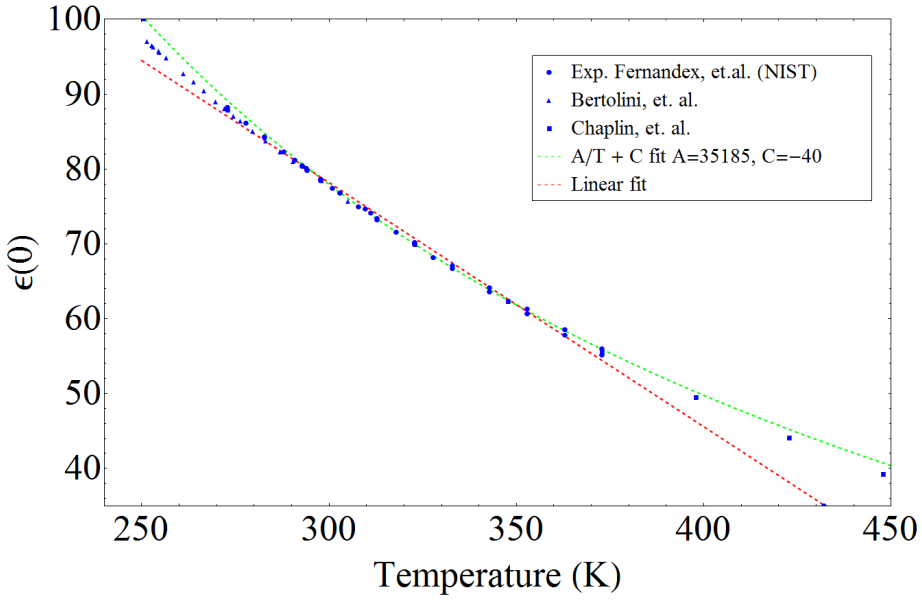

Figure 2.1: Experimental data on $\varepsilon(0)$ taken from Fernandez et al.,[**?**] Bertolini, et al.,[1] and Chaplin et al.[2] Although a $\varepsilon(0)(T)$ is roughly linear in the range 273 - 373 K, the overall behaviour is better described by $A/T + C$. The data above 373 K is taken along the liquid-vapor coexisitence curve with increased pressure.

In this chapter we review fundamentals of the dielectric constant and frequency dependent dielectric function. The material in this section lays down

the conventions used in the rest of the thesis. We explain how the dielectric constant is calculated in MD simulation and explain the importance of boundary conditions when calculating the dielectric constant. The concept of a "reaction field" is shown to be central to understanding how boundary conditions effect the calculation of the dielectric constant.

2.1 Key equations and conventions

The dielectric constant is best defined in terms of how it is traditionally measured. Consider a hollow core capacitor with capacitance $C_0 = Q/V$. The insertion of a dielectric will, as simple physical arguments show, allow for more charge to accumulate, because surface charges will be present on the surface of the dielectric to compensate the extra accumulated charge. As a result the capacitor will be able hold a charge of $Q + Q_p$, increasing the capacitance to $C = (Q + Q_p)/V$. The static dielectric constant is defined as:

$$\varepsilon \equiv \frac{C}{C_0} = \frac{Q + Q_p}{Q} \tag{2.1}$$

The polarization of a medium is described by the polarization vector $\mathbf{P}(r)$ which gives the polarization per unit volume at point r. It can be shown (cf. any book on electromagnetic theory) that the presence of a gradient in the polarization vector is equivalent to a fictitious charge density, so that Gauss's law holds:

$$\nabla \mathbf{P} = -\rho_b \tag{2.2}$$

We distinguish here between bound charge density ρ_b and the free charge density ρ_f. Gauss's law then reads:

$$\nabla \mathbf{E} = \frac{\mathbf{1}}{\epsilon_\mathbf{0}}(\rho_\mathbf{f} + \rho_\mathbf{b}) = \frac{\mathbf{1}}{\epsilon_\mathbf{0}}(\rho_\mathbf{f} - \nabla \mathbf{P}) \tag{2.3}$$

This motivates the definition of a new field called the electric displacement $\boldsymbol{D}$:

$$\begin{aligned} \boldsymbol{D} &= \epsilon_0 \boldsymbol{E} + \boldsymbol{P} \quad \text{(SI units)} \\ \boldsymbol{D} &= \boldsymbol{E} + 4\pi \boldsymbol{P} \quad \text{(Gaussian-cgs units)} \end{aligned} \tag{2.4}$$

In this chapter of the thesis we will use SI units, since they are the ones most relevant when comparing to experimental values. Later, we will switch to cgs units, which are more standard in theoretical physics. Regardless of what unit system one uses, introducing $\mathbf{D}$ allows for a simple equation to be written in

terms of just the free charge density ρ_f:

$$\nabla \boldsymbol{D} = \rho_f \tag{2.5}$$

How does P depend on E? For a local, linear, isotropic media :

$$\mathbf{P} = \chi \epsilon_\mathbf{0} \mathbf{E} \tag{2.6}$$

χ is called the electric susceptibility. Of course, in any real material, $\mathbf{P}$ cannot linearly increase without bound, and there is saturation. If we assume the material has dipoles of magnitude 1 D, the E-field at a distance of 5Å is on the order of 10^6 volt/cm. As a rough rule, for field strengths less than this the linear relation works fairly well. Returning to equation 2.6, we see:

$$\boldsymbol{D} = \epsilon_0(1 + \chi)\boldsymbol{E} \tag{2.7}$$

We now define the static dielectric constant, (also called the static relative permittivity) as

$$\varepsilon \equiv 1 + \chi \tag{2.8}$$

$$\mathbf{D} = \epsilon_\mathbf{0} \varepsilon \mathbf{E} \tag{2.9}$$

The absolute permittivity, (which is sometimes also called the dielectric constant) is defined as:

$$\varepsilon_a \equiv \epsilon_0 \varepsilon \tag{2.10}$$

In his popular book, J.D. Jackson chooses to work in terms of the absolute dielectric constant, which he denotes ε.[45] The reason for this is that in the type of electrodynamics covered by Jackson, one is mainly interested in utilizing eqn. 2.10 between $\boldsymbol{D}$ and $\boldsymbol{E}$, while in materials science one is more interested in relation 2.11 between $\boldsymbol{P}$ and $\boldsymbol{E}$. Physicists can be forgiven a bit for this inconsistent use of the term "dielectric constant" since in the popular Gaussian-cgs system (and Heaviside-Lorentz units) $\epsilon_0 \equiv 1$ so the absolute and relative dielectric constants are equal.[1]

With this new definition, eqn. 2.6 becomes

$$\boldsymbol{P} = \epsilon_0(\varepsilon - 1)\boldsymbol{E} \tag{2.11}$$

[1]Note, in at least one textbook,[46] ϵ_0 is used to refer to the absolute permittivity while ε is reserved for the permeability of free space. The symbol used for the dielectric constant varies, with physicists using a symbol from the set $\{\varepsilon, \epsilon, \varepsilon(0), \epsilon_r, \epsilon(0), \varepsilon_0, \epsilon_0\}$ and engineers frequently using either κ, k, or K. Because of these unfortunate vagaries in convention, it is always important to check the context of how a symbol is being used.

Alternatively, some authors prefer to work in terms of $\boldsymbol{D}$:

$$\boldsymbol{P} = \left(1 - \frac{1}{\varepsilon}\right) \boldsymbol{D} \tag{2.12}$$

and then define a different susceptibility χ':

$$\chi' = 1 - \frac{1}{\varepsilon} \tag{2.13}$$

In the chapter on nonlocal dielectric response we will see that χ' is the longitudinal susceptibility while the more conventional χ is the transverse susceptibility.

2.1.1 The polarizability

Several terms are in use to describe different components of the polarizability. We will consider the polarizability of a molecule to consist of three parts:

$$\alpha = \alpha_e + \alpha_m + \alpha_d \tag{2.14}$$

Where:
α_e is electronic polarizability due to the shifting of the electron clouds
α_m is the molecular polarizability due to the stretching of the molecules (also called the "vibrational polarization" or, in older literature, the "atomic polarizability".[47])
α_d is the dipolar polarizability due to the reorientation of the intrinsic molecular dipoles

2.2 The dipole-dipole interaction

Consider a system of two opposite charges, one at the origin and one at $\boldsymbol{r}'$. Then the potential at a point $\boldsymbol{r}$ is:

$$\phi(\boldsymbol{r}) = q\left(\frac{1}{|\boldsymbol{r} - \boldsymbol{r}'|} - \frac{1}{|\boldsymbol{r}|}\right) \tag{2.15}$$

The multipole expansion (described in many physics textbooks), which is essentially a type of Taylor expansion, yields the following expression for the

potential:

$$\phi(\boldsymbol{r}) = q\left[\frac{\boldsymbol{r}\cdot\boldsymbol{r'}}{r^2} + \frac{3(\boldsymbol{r}\cdot\boldsymbol{r'})^2 - r'^2r^2}{2r^4} + \frac{5(\boldsymbol{r}\cdot\boldsymbol{r'})^3 - 3(\boldsymbol{r}\cdot\boldsymbol{r'})r'^2r^2}{2r^6} + \cdots\right] \tag{2.16}$$

When $\boldsymbol{r'}$ becomes small, only the first term dominates. A idealized object can be introduced now, the point dipole, which corresponds to potential of two equal and opposite charges that are brought infinitely close, while making the charges infinitely large at the same time:

$$\phi_{\text{dip}}(\boldsymbol{r}) = \frac{\boldsymbol{\mu}\cdot\boldsymbol{r}}{r^3} \tag{2.17}$$

Here we introduced the dipole moment as $\boldsymbol{\mu} \equiv q\boldsymbol{r'}$. Since $\boldsymbol{r'} \to 0$, $q \to \infty$ to yield a finite dipole moment for the point dipole. The electric field produced by a point dipole is $\boldsymbol{E} = -\nabla\phi_{\text{dip}}$. It is most easily expressed using the dipole tensor. Using Einstein summation notation we have:

$$\begin{aligned} E_i &= -\frac{\partial}{\partial r_i}\frac{\boldsymbol{\mu}\cdot\boldsymbol{r}}{r^3} \\ E_i &= -\mu_i\left[\frac{1}{r^3}\frac{\partial r_i}{\partial r_j} + r_j\frac{\partial}{\partial r_i}\frac{1}{r^3}\right] \end{aligned} \tag{2.18}$$

After a bit of algebra , one gets

$$E_i = T_{ij}\mu_j \tag{2.19}$$

Where the dipole-dipole interaction tensor is:

$$\begin{aligned} T_{ij} &= \frac{1}{r^3}\left[\frac{3r_ir_j}{r^2} - \delta_{ij}\right] \qquad \text{if} \quad r > 0 \\ T_{ij} &= \frac{4\pi}{3}\delta(r)\delta_{ij} \qquad\qquad \text{if} \quad r = 0 \end{aligned} \tag{2.20}$$

A dipole-dipole tensor can also be written for continuous charge distributions described by a polarization density $\boldsymbol{P}(\boldsymbol{r})$:

$$\boldsymbol{T}_{ab}(\boldsymbol{r}_a - \boldsymbol{r}_b) = \frac{1}{r}\nabla_a\nabla_b \tag{2.21}$$

Here we purposefully used the subscripts a and b to indicate gradients at the locations $\boldsymbol{r}_a$ and $\boldsymbol{r}_b$, rather than i and j, to avoid confusion with the Cartesian

indices. In the continuous case it can also be written as:[48]

$$\boldsymbol{T}(\boldsymbol{r}_a - \boldsymbol{r}_b) = \frac{3(\boldsymbol{r}_a - \boldsymbol{r}_b)(\boldsymbol{r}_a - \boldsymbol{r}_b)}{r^5} - \frac{\boldsymbol{I}}{r^3} \tag{2.22}$$

Now let us consider the dipole-dipole interaction in angular notation. Consider two bodies A and B separated by a vector $\mathbf{R}$. After a multipole expansion the interaction potential is:

$$\begin{aligned} V_{AB}(\mathbf{R}) =& \frac{1}{4\pi\epsilon_0}\Big(\frac{q_A q_B}{R} + \frac{q_A \boldsymbol{\mu}_A \cdot \hat{\mathbf{R}}}{R^2} - \frac{q_B \boldsymbol{\mu}_A \cdot \hat{\mathbf{R}}}{R^2} \\ &+ \frac{\boldsymbol{\mu}_A \cdot \boldsymbol{\mu}_B - 3(\boldsymbol{\mu}_A \cdot \hat{\mathbf{R}})(\boldsymbol{\mu}_B \cdot \hat{\mathbf{R}})}{R^3} + \cdots\Big) \end{aligned} \tag{2.23}$$

The first term is the charge-charge interaction and the second and third terms are charge-dipole interactions. The first three terms will be zero if A and B both carry no net charge. In that case the fourth term is the leading term, which is the dipole-dipole interaction. Now we define three angles, θ_A and θ_B which are the angles between $\boldsymbol{\mu}_A$ and $\boldsymbol{\mu}_B$ and $\mathbf{R}$, and θ_{AB}, which is the angle between $\boldsymbol{\mu}_A$ and $\boldsymbol{\mu}_B$.

$$U_{AB} = \frac{1}{4\pi\epsilon_0}\frac{\mu_A\mu_B\left[\cos\theta_{AB} - 3\cos\theta_B\cos\theta_A\right]}{R^3} \tag{2.24}$$

Using geometry, one can show that $\cos\theta_{AB} = \sin\theta_A\sin\theta_B\cos\phi_B + \cos\theta_A\cos\theta_B$, where ϕ_B is the azimuthal angle. Then we can rewrite 2.24 as :

$$U_{AB} = \frac{1}{4\pi\epsilon_0}\frac{\mu_A\mu_B\left[\sin\theta_A\sin\theta_B\cos\phi_B - 2\cos\theta_B\cos\theta_A\right]}{R^3} \tag{2.25}$$

Now we can make some elementary observations about the angular dependence of interaction. Let us assume $\phi_B = 0$. The combinations and their relative potential energies are are as follows:

				E
←	←	→	→	-2
↓	↑	↑	↓	-1
↓	↓	↑	↑	1
←	→	→	←	2

(2.26)

The most favored is to have to two dipoles aligned tip to tail, with the next most favorable being anti-aligned. Now let's consider 4 dipoles (neglecting

diagonal interactions for simplicity):

$$\begin{array}{cc} & \text{E} \\ \rightarrow \ \rightarrow & \\ & \text{-6} \\ \rightarrow \ \rightarrow & \\ \uparrow \ \downarrow & \\ & \text{-8} \\ \uparrow \ \downarrow & \end{array} \tag{2.27}$$

This illustrates why for dipolar crystals with cubic symmetry, the antiferroelectric state is preferred.

Thermodynamically averaged dipole-dipole interaction

In a liquid, random thermal motion prevents dipoles from assuming an ordered state. An effective interaction can be calculated by doing a thermodynamic average over the angular degrees of freedom. This angle-averaged interaction is called the Keesom interaction, which was first described in 1921 by Willem Hendrik Keesom, a doctoral student of van der Waals. The derivation is fairly straightforward. We wish to find the average interaction energy, which is:

$$\langle U_{AB} \rangle = \frac{\int\int\int \sin\theta_A d\theta_A \sin\theta_B d\theta_B d\phi_B U_{AB} \exp\left(\frac{-U_{AB}}{k_B T}\right)}{\int\int\int \sin\theta_A d\theta_A \sin\theta_B d\theta_B d\phi_B \exp\left(\frac{-U_{AB}}{k_B T}\right)} \tag{2.28}$$

In the case where the energy between the dipoles $U_{AB} << k_B T$ then we can expand the exponential to leading order in the denominator:

$$\begin{aligned} U_{AB} &= \frac{\mu_A \mu_B f(\theta_A, \theta_B)}{4\pi\epsilon_0 r^3} \\ \langle \exp\left(\frac{-U_{AB}}{k_B T}\right) \rangle &= \langle 1 \rangle - \frac{\mu_A \mu_B}{4\pi\epsilon_0 r^3 k T} \langle f \rangle + \left(\frac{\mu_A \mu_B}{4\pi\epsilon_0 r^3 k T}\right)^2 \langle f^2 \rangle + \cdots \end{aligned} \tag{2.29}$$

The first angular average $\langle f \rangle$ is zero because $\sin(\theta)$ averages to zero over 0 to π. The angular average $\langle f^2 \rangle$ is not zero however, and turns out to be 2/3. A similar computation is done for the numerator. We obtain the Keesom interaction:[2]

$$\langle U_{AB}(r) \rangle = -\frac{2\mu_A^2 \mu_B^2}{3(4\pi\epsilon_0)^2 k_B T r^6} \tag{2.30}$$

[2]One can also calculate the free energy $A \equiv U - TS = -k_B T \ln(Z)$, where Z is the partition function. It turns out the free energy of interaction is exactly 1/2 the energy given by eqn. 2.30.

Because of the $1/r^6$ nature of this interaction, it is often considered a type of "van der Waal" interaction in the chemistry community. One might wonder under what circumstances the condition $U_{AB} << k_BT$ holds in water. The most likely configuration of two water molecules is to be tetrahedrally coordinated. Taking the tetrahedrally-coordinated geometry and assuming dipole moments of 3D and an O-O distance of 3Å, the dipole-dipole interaction energy is -.241 eV. By comparison the "thermal energy" at 300K is $k_BT =$ .026eV. Using equation 2.30 and a dipole moment of 3 D we find that $U_{AB} = k_BT$ at $r = 4.7$Å.

2.3 A unified treatment of fluctuation formulas for the dielectric constant

With the advent of atomistic dynamics simulation in 1959,[49] the question of whether it was possible to compute a macroscopic dielectric constant from such simulations quickly rose to the fore. Because dipole-dipole forces are long range it was realized that different boundary conditions and simulation techniques led to different equations for the dielectric constant of the simulated system, which is only microscopic in extent. The situation was complicated because authors were using a variety of techniques to calculate the long range Coulomb interactions:

1. **spherical cutoff** - a simple truncation or shifted truncation of the Coulomb interactions at a radius r_c, normally taken to be half the box length.

2. **cubic cutoff** a truncation of the Coulomb interactions within a cube, usually equal to the size of the box.

3. **reaction field** - placement of each particle in the system in a hollow cavity in an infinite uniform dielectric media, resulting in a polarization of the media and a reaction field.

4. **lattice summation** - a real-space sum over the infinite periodic lattice of systems, carried out over a finite portion of the lattice. Can be combined with reaction field.

5. **Ewald summation** - a real-space and reciprocal space sum carried over the entire infinite periodic lattice of systems.

All simulations attempting to reproduce bulk properties use either toroidal boundary conditions or periodic boundary conditions. In the older literature

"periodic boundary conditions" (PBCs) refers to an infinite lattice of simulation cells (as occurs in Ewald summation) while "toroidal boundary conditions" (TBCs) refers to a single simulation cell surrounded by six "image" cells. Today the term "periodic boundary conditions" is used to refer to both cases. It is clear that either case is substantially different than the true infinite system when considering non-periodic systems like water.

Initially it was not clear how to relate a dielectric constant calculated from a given simulation to the dielectric constant of a real media of infinite extent. It was also sometimes not clear how to consistently relate the dielectric constants computed for the same system using different simulation techniques. The situation was not conclusively resolved until a series of landmark papers by Neumann and Steinhauser published in the 1980s.[50, 51, 52, 53, 54, 55, 56, 57] Here we summarize these papers for the first time and see how the results relate to each other.

2.3.1 The relation between P and E from electrostatics

This section is based on (Neumann,1983).[50] The presence of an externally-applied field $\boldsymbol{E}_0$ will induce a polarization in a material. The total field at point $\boldsymbol{r}$ will be:

$$\boldsymbol{E}(\boldsymbol{r}) = \boldsymbol{E}_0(\boldsymbol{r}) + \int d^3r' \boldsymbol{T}(\boldsymbol{r} - \boldsymbol{r'}) \cdot \boldsymbol{P}(\boldsymbol{r}') \tag{2.31}$$

The total field $\boldsymbol{E}$ is sometimes called the Maxwell field to distinguish it from the applied field $\boldsymbol{E}_0$. Here $\boldsymbol{T}(\boldsymbol{r}-\boldsymbol{r'})$ is the dipole-dipole interaction tensor given in eqn. 2.21

With the relation $\boldsymbol{P}(\boldsymbol{r}) = \chi \boldsymbol{E}(\boldsymbol{r})$ (setting $\epsilon_0 = 1$ here temporarily for simplicity), $\boldsymbol{E}$ may be eliminated from 2.31 yielding an integral equation for $\boldsymbol{P}$:

$$\boldsymbol{P}(\boldsymbol{r}) = \chi \left(\boldsymbol{E}_0 + \int d^3r' \boldsymbol{T}(\boldsymbol{r} - \boldsymbol{r}') \cdot \boldsymbol{P}(\boldsymbol{r}) \right) \tag{2.32}$$

Since $\boldsymbol{T}$ is singular at $r = 0$ it is convenient to split the integral over $\boldsymbol{T}$ into two parts – $|\boldsymbol{r} - \boldsymbol{r}'| < R$ and $|\boldsymbol{r} - \boldsymbol{r}'| > R$. For the part containing the singularity, one can rewrite the divergence of $\boldsymbol{P}$ as a surface integral, following an oft-repeated procedure in electrostatics, to obtain:

$$\lim_{R \to 0} \int\limits_{|\boldsymbol{r}-\boldsymbol{r}'|<R} d^3r' \boldsymbol{T}(\boldsymbol{r} - \boldsymbol{r}') \cdot \boldsymbol{P}(\boldsymbol{r}') = -\frac{4\pi}{3} \boldsymbol{P}(\boldsymbol{r}') \tag{2.33}$$

Doing a bit of algebra, we find that the equation for $\boldsymbol{P}$ becomes:

$$\boldsymbol{P}(\boldsymbol{r}) = \frac{1}{3\epsilon_0}\frac{\varepsilon-1}{\varepsilon+2}\left(\boldsymbol{E}_0(\boldsymbol{r}) + \lim_{R\to 0}\int\limits_{|\boldsymbol{r}-\boldsymbol{r}'|<R} d^3r'\boldsymbol{T}(\boldsymbol{r}-\boldsymbol{r}')\cdot\boldsymbol{P}(\boldsymbol{r}')\right) \tag{2.34}$$

Equation 2.34 involves a convolution, suggesting that it will be easier to recast this equation into Fourier space. Neumann proves that the convolution theorem still holds when toroidal boundary conditions are used, allowing eqn. 2.34 to be written in Fourier space as

$$\tilde{\boldsymbol{P}}(\boldsymbol{k}) = 3\varepsilon_0\frac{\varepsilon-1}{\varepsilon+2}\left(\tilde{\boldsymbol{E}}_0(\boldsymbol{k}) + \tilde{\boldsymbol{T}}(\boldsymbol{k})\cdot\tilde{\boldsymbol{P}}(\boldsymbol{k})\right) \tag{2.35}$$

The solution for $\boldsymbol{P}$ is:

$$\tilde{\boldsymbol{P}}(\boldsymbol{k}) = 3\varepsilon_0\frac{\varepsilon-1}{\varepsilon+2}\left(\boldsymbol{I} - \frac{3}{4\pi}\frac{\varepsilon-1}{\varepsilon+2}\tilde{\boldsymbol{T}}(\boldsymbol{k})\right)^{-1}\tilde{\boldsymbol{E}}_0(\boldsymbol{k}) \tag{2.36}$$

The dielectric constant is calculated by setting $\boldsymbol{k}=0$. We assume a uniform electric field, which only has a $\boldsymbol{k}=0$ component. Additionally, $\tilde{\boldsymbol{P}}(0) = \int d^3r\boldsymbol{P}(r) = V\boldsymbol{P}$ and $\tilde{\boldsymbol{E}}_0(0) = V\boldsymbol{E}_0$. Therefore

$$\boldsymbol{P} = 3\varepsilon_0\frac{\varepsilon-1}{\varepsilon+2}\left(\boldsymbol{I} - \frac{3}{4\pi}\frac{\varepsilon-1}{\varepsilon+2}\tilde{\boldsymbol{T}}(0)\right)^{-1}\boldsymbol{E}_0 \tag{2.37}$$

This is the central result of this section.

2.3.2 The relation between P and E from statistical mechanics

One way to apply eqn. 2.37 in computer simulations is to apply a uniform field to the system and look at the polarization response of the system. However, linear response theory allows us to relate the polarization response in the presence of a field to fluctuations of the polarization in equilibrium. The following follows the notation found in Frankel and is an example of a linear-response theory calculation.[58]

In linear response theory one assumes that the perturbed system's Hamiltonian can be described by $\mathcal{H} = \mathcal{H}_0 + \lambda B$, where $\mathcal{H}_0$ is the unperturbed Hamiltonian and λB is the perturbation. In our case, the perturbation is the application of a uniform electric field, which contributes to the Hamiltonian as $-\mathbf{E_0}\cdot\mathbf{M}$ where $\mathbf{M}$ is the total dipole moment of the system. The expression

for the total dipole moment in equilibrium is easy to write down:

$$\langle \mathbf{M} \rangle + \langle \Delta \mathbf{M} \rangle = \frac{\int d\Gamma \exp[-\beta(\mathcal{H}_0 - \mathbf{E_0} \cdot \mathbf{M})]\mathbf{M}}{\int d\Gamma \exp[-\beta(\mathcal{H}_0 - \mathbf{E_0} \cdot \mathbf{M})]} \tag{2.38}$$

where $\int d\Gamma$ denotes an integral over the entire phase space of the system. We now simplify this expression by first setting the perturbation to zero in the demoninator and considering only the part which varies linearly with $\mathbf{E_0}$ in the numerator. Since $\mathbf{E_0}$ is a vector quantity, let us consider only the part which varies due to E_x first:

$$\langle \Delta M_x \rangle = \left. \frac{\partial \langle M \rangle}{\partial E_x} \right|_{E_x=0} E_x = \beta E_x \left(\langle M_x^2 \rangle - \langle M_x \rangle^2 \right) \tag{2.39}$$

Here the right hand side was obtained by straightforward differentiation of the numerator of eqn. 2.38. For our systems, we know that $\langle \mathbf{M} \rangle_0 = 0$ (In equilibrium the average polarization is zero). In computer simulations, such averages are only performed over a finite time, therefore it is useful to keep the $\langle \mathbf{M} \rangle_0 = 0$ term. We will drop this term here though for simplicity. Thus:

$$\langle \Delta \mathbf{M} \rangle = \beta \langle M_x^2 \rangle E_{0x} \tag{2.40}$$

We also know that in equilibrium the fluctuations will be isotropic, so that $\langle M_x^2 \rangle = \langle M_y^2 \rangle = \langle M_z^2 \rangle = \frac{1}{3}\langle M^2 \rangle$. Finally, we know the polarization $\boldsymbol{P} = \frac{\langle \Delta \mathbf{M} \rangle}{V}$. Combining these two facts into eqn. 2.40, we get:

$$\boldsymbol{P} = \frac{\langle \boldsymbol{M}^2 \rangle}{3 k_B T V} \boldsymbol{E}_0 \tag{2.41}$$

This the central result of this section.

2.3.3 The equation for the dielectric constant for different boundary conditions

Combining the two central results from the previous sections, we arrive at the following general equation:

$$3\frac{\varepsilon - 1}{\varepsilon + 2} \left(\boldsymbol{I} - 3\epsilon_0 \frac{\varepsilon - 1}{\varepsilon + 2} \tilde{\boldsymbol{T}}(0) \right)^{-1} = \frac{\langle \boldsymbol{M}^2 \rangle}{3\varepsilon_0 k_B T V} \tag{2.42}$$

where

$$\tilde{\boldsymbol{T}}(0) = \int d^3 r \boldsymbol{T}(r) \tag{2.43}$$

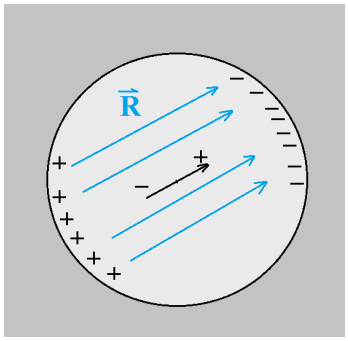

Figure 2.2: Illustration of the reaction field around a molecular dipole.

To analyze $\tilde{\boldsymbol{T}}(0)$ it is easier to work with the discrete form (eqn. 2.20):

$$T_{ij} = \frac{1}{4\pi\epsilon_0}\frac{1}{r^3}\left[\frac{3r_i r_j}{r^2} - \delta_{ij}\right] \tag{2.44}$$

Spherical cutoff

In the spherical cut off case, one can make the following hand-waving argument – since the off-diagonal terms of T_{ij} are antisymmetric, $\int d^3r T_{ij}(r) = 0$. Likewise it can be shown that the sum of the on diagonal terms $\int d^3r T_{ii}(r) = 0$. Therefore a Clausius-Mossotti-like equation holds for spherical cutoff:

$$3\frac{\varepsilon - 1}{\varepsilon + 2} = \frac{\langle \boldsymbol{M}^2 \rangle}{3\varepsilon_0 k_B T V} \tag{2.45}$$

Reaction field

The reaction field technique treats the Coulomb interactions in a similar fashion to spherical cutoff, but instead of assuming a vacuum $\varepsilon = 1$ beyond the cutoff radius, a homogeneous dielectric continuum with $\varepsilon = \varepsilon_{\mathrm{RF}}$ is assumed. In other words, each molecule in the system is modelled as being in a spherical cavity. A polarization charge is induced on the surface of the cavity, which creates a reaction field. The reaction field always points in the same direction as the polarization of molecule (see fig 2.3.3). While the reaction field method is much faster than Ewald summation and appears to yield sensible thermodynamic properties,[59] it leads to a large artifact in the dipolar correlations,[4] so its use is not recommended. In reaction field both the Coulomb interaction

and the dipole-dipole tensor are modified. We will not cover the analysis of $\tilde{\boldsymbol{T}}(0)$ here, but we will state the final result since it gives a lot of insight.[50]

$$3\frac{\varepsilon-1}{\varepsilon+2}\left(1-\frac{\varepsilon-1}{\varepsilon+2}\frac{\varepsilon_{\mathrm{RF}}-1}{\varepsilon_{\mathrm{RF}}+1}\right)^{-1}=\frac{\langle\boldsymbol{M}^2\rangle}{3\varepsilon_0 k_B TV} \tag{2.46}$$

As we will see in the conclusion of this section the concept of a reaction field plays a fundamental role in dielectric theory.

Ewald summation

The case of Ewald summation, or more specifically, the Ewald-Kornfield technique, was first analyzed by DeLeeuw, Perram & Smith.[60] However, as pointed out by Neumann showed that these authors actually made a slight mistake in analyzing $\tilde{\boldsymbol{T}}(0)$, and presents a more rigorous version:[54]

$$3\frac{\varepsilon-1}{\varepsilon+2}\left(1-\frac{\varepsilon-1}{\varepsilon+2}Q\right)^{-1}=\frac{\langle\boldsymbol{M}^2\rangle}{3\epsilon_0 k_B TV} \tag{2.47}$$

where

$$Q=\int_0^{r_c}4\pi r^2\left(\frac{\eta}{\pi^{1/2}}\right)^3\exp(-\eta^2 r^2) \tag{2.48}$$

Here $\eta=1/\beta$, where σ is the width of the smearing Gaussian used in Ewald summation. Setting $Q=1$ yields the standard formula for Ewald as used by most authors:

$$\varepsilon-1=\frac{\langle\boldsymbol{M}^2\rangle}{3\epsilon_0 k_B TV} \tag{2.49}$$

Indeed, in the limit $r_c\to\infty, Q\to 1$ since the integral in eqn. 2.48 is over a normalized Gaussian function. In practice Q is slightly smaller than 1. The width of the Gaussian function is chosen automatically by most MD codes by finding an optimum balance between accuracy and computational efficiency.[58] It is useful to combine eqn. 2.49 with eqn. 2.47 to create a correction formula to correct values of ε calculated with the approximate equation:

$$\varepsilon_{\mathrm{corrected}}=\frac{(Q+2)(\varepsilon_A-1)+3}{(Q-1)(\varepsilon_A-1)+3} \tag{2.50}$$

As an example, for a simulation of 512 water molecules in GROMACS using the TIP3P empirical potential, $r_c=1.5$ nm, $1/\eta=.34$ nm and $Q=.999$. The incurred error from using eqn. 2.49 instead of eqn. 2.47 was only -.3 %. In practice the error from using the approximate formula is usually very small.

One should also be wary of results published in older literature, though.. In his 1983 paper, Neumann found errors in previously reported values for ε ranging from -60 % for small systems (108 molecules) to -10 % for larger systems (500 molecules). Since the publication of the exact formula, it appears that very few authors have adopted its use.

2.3.4 The infinite system

Analyzing $\tilde{\boldsymbol{T}}(0)$ for the infinite system is tricky. The issue is that the value of $\tilde{\boldsymbol{T}}(0)$ varies depending on the direction with which $\boldsymbol{k} \to 0$.[57] Neumann presents a rigorous derivation of the infinite system formula which easily extends to finding the finite wavelength dielectric tensor $\boldsymbol{\varepsilon}(\boldsymbol{k})$ in different geometries. Here we present a more straightforward derivation, following the presentation of McDonald (1986).[48] To properly analyse the situation, we must consider $\varepsilon(\boldsymbol{k})$ as a tensor $\boldsymbol{\varepsilon}(\boldsymbol{k})$. An arbitrary $\tilde{\boldsymbol{E}}(\boldsymbol{k})$ can always be broken up into parallel and perpendicular components as $\tilde{\boldsymbol{E}}(\boldsymbol{k}) = \hat{\boldsymbol{k}}(\hat{\boldsymbol{k}}\cdot\tilde{\boldsymbol{E}}(\boldsymbol{k}))+(\boldsymbol{I}-\hat{\boldsymbol{k}}\hat{\boldsymbol{k}})\cdot\tilde{\boldsymbol{E}}(\boldsymbol{k})$. The dielectric tensor can also be broken up as

$$\boldsymbol{\varepsilon}(\boldsymbol{k}) = \varepsilon_T(k)\boldsymbol{I} + (\varepsilon_L(k) - \varepsilon_T(k))\hat{\boldsymbol{k}}\hat{\boldsymbol{k}} \tag{2.51}$$

where

$$\tilde{\boldsymbol{P}} = \begin{cases} \epsilon_0(\varepsilon_L(k)-1)\tilde{\boldsymbol{E}} & \text{if} \quad \tilde{\boldsymbol{E}}(\boldsymbol{k}) \parallel \boldsymbol{k} \\ \epsilon_0(\varepsilon_T(k)-1)\tilde{\boldsymbol{E}} & \text{if} \quad \tilde{\boldsymbol{E}}(\boldsymbol{k}) \perp \boldsymbol{k} \end{cases} \tag{2.52}$$

To start the derivation it is necessary to Fourier transform eqn. 2.31:

$$\boldsymbol{E}(\boldsymbol{k}) = \boldsymbol{E}_0(\boldsymbol{k}) - \frac{4\pi}{k^2}\boldsymbol{k}\boldsymbol{k}\cdot\boldsymbol{P}(\boldsymbol{k}) \tag{2.53}$$

We know that the *local* constitutive relation $\boldsymbol{P} = (\varepsilon - 1)\boldsymbol{E}$ holds and we know that the dielectric constant is independent of the direction of $\boldsymbol{k}$ and the shape of the sample. We desire that a constitutive relation holds for the infinite sample: $\boldsymbol{P}(\boldsymbol{k}) = \boldsymbol{\chi}^0(\boldsymbol{k})\boldsymbol{E}_0(\boldsymbol{k})$ in the infinite wavelength limit, except here $\boldsymbol{\chi}(\boldsymbol{k})^0$ is direction dependent. We insert this desired relation into eqn. 2.53

$$\boldsymbol{E}(\boldsymbol{k}) = \frac{\boldsymbol{P}(\boldsymbol{k})}{\boldsymbol{\chi}^0(\boldsymbol{k})} - \frac{4\pi}{k^2}\boldsymbol{k}\boldsymbol{k}\cdot\boldsymbol{P}(\boldsymbol{k}) \tag{2.54}$$

Rearranging this equation:

$$\boldsymbol{P}(\boldsymbol{k}) = \frac{\boldsymbol{\chi}^0(\boldsymbol{k})}{\boldsymbol{I} - \frac{4\pi}{k^2}\boldsymbol{k}\boldsymbol{k}\boldsymbol{\chi}^0(\boldsymbol{k})}\boldsymbol{E}(\boldsymbol{k}) \tag{2.55}$$

So clearly

$$\frac{\boldsymbol{\chi}^0(\boldsymbol{k})}{\boldsymbol{I} - \frac{4\pi}{k^2}\boldsymbol{k}\boldsymbol{k}\boldsymbol{\chi}^0(\boldsymbol{k})} = \boldsymbol{\chi} \tag{2.56}$$

Now for simplicity, let's assume that $\boldsymbol{k}$ is in the z direction. Using eqn. 2.56 we find that observe that

$$4\pi \lim_{\boldsymbol{k}\to 0} \chi^0_{xx}(\boldsymbol{k}) = \varepsilon - 1 \tag{2.57}$$

$$4\pi \lim_{\boldsymbol{k}\to 0} \chi^0_{zz}(\boldsymbol{k}) = \frac{\varepsilon - 1}{\varepsilon} \tag{2.58}$$

We end up with the following fluctuation formulas:

$$\begin{aligned} \varepsilon - 1 &= \frac{\langle M_x^2 \rangle}{\epsilon_0 k_B T V} \\ \varepsilon - 1 &= \frac{\langle M_y^2 \rangle}{\epsilon_0 k_B T V} \\ 1 - \frac{1}{\varepsilon} &= \frac{\langle M_z^2 \rangle}{\epsilon_0 k_B T V} \end{aligned} \tag{2.59}$$

Combining these equations we find that

$$2(\varepsilon - 1) + 1 - \frac{1}{\varepsilon} = \frac{\langle \boldsymbol{M}^2 \rangle}{3\varepsilon_0 k_B T V} \tag{2.60}$$

$$\frac{(2\varepsilon + 1)(\varepsilon - 1)}{3\varepsilon} = \frac{\langle \boldsymbol{M}^2 \rangle}{3\varepsilon_0 k_B T V} \tag{2.61}$$

Equation 2.61 is a version of the Kirkwood equation, which will be discussed later (see eqn. 3.27).

2.3.5 Summary of formulas

We now repeat all of the formulas for reference and comparison:

$$\frac{\langle \boldsymbol{M}^2 \rangle}{3\epsilon_0 k_B T V} = \begin{cases} 3\dfrac{\varepsilon-1}{\varepsilon+2}\left(1-\dfrac{\varepsilon-1}{\varepsilon+2}\dfrac{\varepsilon_{\mathrm{RF}}-1}{\varepsilon_{\mathrm{RF}}+1}\right)^{-1} & \text{reaction field} \\ 3\dfrac{\varepsilon-1}{\varepsilon+2} & \text{spherical cutoff, } \varepsilon_{\mathrm{RF}}=1 \\ \dfrac{(2\varepsilon+1)(\varepsilon-1)}{3\varepsilon} & \text{Infinite system, } \varepsilon_{\mathrm{RF}}=\varepsilon \\ \varepsilon-1 & \text{Ewald } (Q=1), \varepsilon_{\mathrm{RF}}=\infty \end{cases} \tag{2.62}$$

Each of the equations is a special case of the reaction field equation with different values of ε_{RF}. Thus we see that the concept of the reaction field plays a central role in differentiating the relation between $\boldsymbol{P}$ and $\boldsymbol{E}_0$ in the different geometries.

2.4 The Kirkwood g-factor

Kirkwood's g-factor can be defined as:

$$G_K \equiv \frac{1}{N\langle \mu^2 \rangle}\left(\langle M^2 \rangle - \langle M \rangle^2\right) \tag{2.63}$$

If there are no interactions between the dipoles then $\langle \mathbf{M}^2 \rangle = N\mu^2$ and $\langle \mathbf{M} \rangle^2 = 0$ and $g_K = 1$. We can rewrite eqn. 2.63 into Kirkwood's form. First we set $\langle \boldsymbol{M} \rangle = 0$:

$$\begin{aligned} G_K &= \frac{1}{N\langle \mu^2 \rangle}\left\langle \left(\sum_{i=1}^{N} \boldsymbol{\mu}_i\right) \cdot \left(\sum_{j=1}^{N} \boldsymbol{\mu}_j\right) \right\rangle \\ &= \frac{1}{N\langle \mu^2 \rangle}\left\langle \sum_{i=1}^{N} \boldsymbol{\mu}_i^2 + \sum_{i=1}^{N}\sum_{j\neq i}^{N} \boldsymbol{\mu}_i \cdot \boldsymbol{\mu}_j \right\rangle \\ &= 1 + \frac{N^2 - N}{N\langle \mu^2 \rangle}\langle \boldsymbol{\mu}_i \cdot \boldsymbol{\mu}_j \rangle \\ &= 1 + (N-1)\langle \cos\theta \rangle \end{aligned} \tag{2.64}$$

This is often written as

$$g_K = 1 + N\langle \cos\theta \rangle \tag{2.65}$$

Where N is now the number of molecules surrounding the central molecule.

As a simplification, Kirkwood proposed only considering the nearest neighbors to a given molecule, resulting in the following formula for water:

$$\begin{aligned} g_K &= 1 + z\langle\cos(\theta)\rangle \\ g_K &= 1 + z\langle\cos(\frac{\theta_{\mathrm{HOH}}}{2})\rangle \end{aligned} \tag{2.66}$$

where $z = 4$ is the number of nearest neighbors. Assuming an HOH bond angle of 100 deg, one obtains $g = 3.55$ which with a dipole moment of 2.18 yields $\varepsilon(0) = 67$. Assuming an angle of 109.5 one obtains $g = 2.91, \varepsilon(0) = 55$. Obviously these estimates are low in part because experiments show the actual dipole moment is between 2.5-3 D.

Incidentally, there are also "higher order" g-factors:

$$G_l = 1 + \langle\mathcal{P}_l(\theta)\rangle = 4\pi\rho\int\langle\mathcal{P}_l(\theta)\rangle(r)r^r dr \tag{2.67}$$

Where $\mathcal{P}_l$ is the lth Legendre polynomial ($\mathcal{P}_1 = x, \mathcal{P}_\in = 1/2(3x^2 - 1)$, etc.). G_2 is important in NMR experiments, and a combination of G_1 and G_2 are relevant to the optical Kerr effect.[61] In a simulation, one deals with only a finite system. The g-factor calculated from just the molecules in the finite simulation box is called the "finite system g-factor", denoted G_K. The relation between G_k and ε differs depending on boundary conditions of the system, in accordance with eqn. 2.62. The relation between G_K and g_K (the infinite system g-factor) is:[57, 62]

$$g_K = \frac{(2\varepsilon_{RF} + \varepsilon(0))(2\varepsilon(0) + 1)}{3\varepsilon(0)(2\varepsilon_{RF} + 1}G_K \tag{2.68}$$

In the case of Ewald summation one has:

$$g_K = \frac{2\varepsilon(0) + 1}{3\varepsilon(0)}G_K \tag{2.69}$$

2.5 Systems of polarizable point dipoles

The following derivations were, strictly speaking, only valid for rigid (fixed magnitude) dipoles. In this section we consider polarizable dipoles. Consider a set of N linearly polarizable point dipoles distributed throughout space along with an externally applied electric field $\boldsymbol{E}_0$. The dipoles will polarize themselves until an equilibrium situation is reached. In equilibrium, the dipole

moment of dipole p satisfies the following equation:

$$\boldsymbol{\mu}_p = \boldsymbol{\alpha}_p \left[\mathbf{E}_0 - \sum_{q \neq p}^{N} \mathbf{T}_{pq} \boldsymbol{\mu}_q \right] \tag{2.70}$$

Here $\boldsymbol{\alpha}$ is the polarizability tensor and $\mathbf{T}_{pq}$ is the dipole field tensor, (eq. 2.20) which gives the electric field experienced at the location of dipole p created by dipole q.

Equation 2.70 has the form of a matrix equation for the $\boldsymbol{\mu}_p$'s:

$$\begin{aligned} \boldsymbol{\mu} &= \boldsymbol{\alpha}\boldsymbol{E}_0 - \boldsymbol{\alpha}\boldsymbol{T}\boldsymbol{\mu} \\ (\boldsymbol{\alpha}\boldsymbol{I} + \boldsymbol{T})\boldsymbol{\mu} &= \boldsymbol{\alpha}\boldsymbol{E}_0 \\ \boldsymbol{A}\boldsymbol{\mu} &= \boldsymbol{E} \end{aligned} \tag{2.71}$$

Where $\boldsymbol{\mu} \equiv (\boldsymbol{\mu}_1, \boldsymbol{\mu}_2, \cdots, \boldsymbol{\mu}_N)$ is a vector of length $3N$, $\boldsymbol{E}$ is a vector of the the applied electric field $\boldsymbol{E} \equiv (\boldsymbol{E}_0, \boldsymbol{E}_0, \cdots$ and we have constructed a $3N \times 3N$ matrix A:

$$A \equiv \begin{bmatrix} \boldsymbol{\alpha}_1^{-1} & \boldsymbol{T}_{12} & \boldsymbol{T}_{13} & \cdots \\ \boldsymbol{T}_{21} & \boldsymbol{\alpha}_2^{-1} & \boldsymbol{T}_{23} & \cdots \\ \boldsymbol{T}_{31} & \boldsymbol{T}_{32} & \boldsymbol{\alpha}_3^{-1} & \cdots \\ \vdots & \vdots & \vdots & \ddots \end{bmatrix} \tag{2.72}$$

Inversion of A yields:

$$\boldsymbol{\mu} = \boldsymbol{A}^{-1}\boldsymbol{E} \tag{2.73}$$

Here we see that $\boldsymbol{A}^{-1}$ acts like a polarizability matrix for the entire system. In some literature, $A^{-1} \equiv B$ is called the "relay matrix".

Another way to formulate this is to create a tensor B_{pqij}, where p, q are block indices for different 3×3 blocks of B and $i, j \in \{x, y, z\}$. Then we can construct a polarizability tensor *for the entire system* as follows:

$$\begin{aligned} \alpha_{ij}^{\text{sys}} &\equiv \sum_{p}^{N} \sum_{q}^{N} B_{pqij} \\ \mu_i^{\text{system}} &= \alpha_{ij}^{e} E_j \end{aligned} \tag{2.74}$$

Several applications of 2.71 were studied in detail by P. B. Allen, who applied it to study the 1D dipole stack, interacting dipole stacks, dipolar simple cubic lattice, and to make conjectures about the stacking behaviour of nanoparticles.[63, 64]

2.5.1 Polarization catastrophe & smeared dipoles

We make a detour here which shows why smeared dipoles are used in the TTM series of water models. A property of eqn. 2.73 is that there may be singular solutions. An infinite polarizability corresponds to a polarization catastrophe where a small perturbation to the system causes run away polarization in the system. As a simple example of this, consider a system of just two isotropically polarizable point dipoles, A and B. Define $\alpha_{\parallel}$ to be the polarizability of the system in the direction pointing from A to B and $\alpha_{\perp}$ to be the polarization in directions orthogonal. One can show that:

$$\begin{aligned} \alpha_{\parallel} &= \frac{\alpha_A + \alpha_B + 4\alpha_A\alpha_B r^{-3}}{1 - 4\alpha_A\alpha_B r^{-6}} \\ \alpha_{\perp} &= \frac{\alpha_A + \alpha_B - 4\alpha_A\alpha_B r^{-3}}{1 - 4\alpha_A\alpha_B r^{-6}} \end{aligned} \tag{2.75}$$

There is a singularity in $\alpha_{\parallel}$ when $r = (4\alpha_A\alpha_B)^{1/6}$ and it becomes negative for smaller distances, which doesn't make much sense physically. Thole shows that while the negative polarizability solutions are valid solutions, they are energetically unstable. This makes sense - a negative polarizability corresponds to a dipole which is directly facing the field, which is analogous to a ball which is at the very top of a hill. Such solutions are unphysical. Thole notes that a necessary condition for a non-singular solution is for A to be positive definite – or in other words, for A to have no negative eigenvalues. This condition also removes the possibility of negative polarizabilities.

Thole introduced a tensor $\boldsymbol{t}$ which he calls the shape function:[65]

$$\boldsymbol{T} = (\alpha_A\alpha_B)^{-1/2}\boldsymbol{t}(\boldsymbol{u}) \tag{2.76}$$

Here $\boldsymbol{u} \equiv \boldsymbol{x}/(\alpha_A\alpha_B)^{1/6}$. (In everything that follows, we will continue to assume that the atomic polarizabilies are isotropic.) In electrodynamics one always finds that if we take a macroscopic dielectric system and scale all the distances by a factor L then the polarizability of the system scales as L^3. Eqn. 2.76 preserves this property, provided that the atoms have isotropic polarizabilities and that $\boldsymbol{t}(\boldsymbol{u})$ depends only on the distance between the molecules, as indicated. This is a simplifying assumption because atoms do have internal structure, but it makes things drastically simplier. A simple calculation shows that if we multiply $\boldsymbol{u}$ by a scaling factor λ and multiply α_A and α_B by λ^3 then the polarizability of the system does indeed scale as λ^3.

He then assumes that $\boldsymbol{t}$ is further constrained to the following form:

$$t_{ij} = -\frac{\partial^2 \phi(u)}{\partial u_i \partial u_j} \tag{2.77}$$

Where $u = (u_1^2 + u_2^2 + u_3^2)^{1/2}$. The motivation of this form is to still consider a dipole as two infinitely close opposite charges, but now the charge charge interaction $\phi(u)$ is arbitrary, and can correspond to the interaction of smeared charges instead of point charges.

Then using the chain rule and product rule for derivatives along with the fact that $\partial u_i / \partial u_j = \delta_{ij}$ one can show:

$$t_{ij} = \left(\frac{1}{u} \frac{\partial u}{\partial r} - \frac{\partial^2 u}{\partial r^2} \right) \frac{u_i u_j}{u^2} - \frac{1}{u} \frac{\partial u}{\partial r} \delta_{ij} \tag{2.78}$$

The case of $\phi = u^{-1}$ gives the point dipole tensor:

$$t_{ij} = \delta_{ij} u^{-3} - 3 u_i u_j u^{-5} \tag{2.79}$$

For the case of two dipoles (a diatomic molecule), a repetition of the calculation for the polarizability of the system yields:

$$\begin{aligned} \alpha_{\parallel} &= \frac{2}{1 - \phi''} \\ \alpha_{\perp} &= \frac{2}{1 - \phi'/u} \end{aligned} \tag{2.80}$$

Here the primes represent derivatives. Thole now assumes that as $u \to 0$, then $\alpha_{\parallel} = \alpha_{\perp}$. In other words, when the two atoms overlap, the polarizability of the system is isotropic. Thole then shows that with this constraint, the $\phi(u)$ potentials must correspond to charge densities which are non-zero at the origin, spherically symmetric, and go to zero at large r. Additionally, because of the way things are normalized, the integral of the charge density must be unity.

If we look at eqn. 2.80 it becomes clear that in order to avoid singularities and unphysical negative solutions, ϕ'' and ϕ'/u must remain less than one. In other words, there is a smoothness condition on ϕ and thus a smoothness condition on the charge density. In the case of more than two atoms, things will become more complicated and there will be more cooperativity, so the derivatives may need to be much less than one. However, Thole reports that in practice keeping ϕ'' and ϕ'/u less than .5 is adequate. (The dipole-dipole interaction drops off quickly, so really large cooperative effects are hard to

achieve.) Thole considered forty different smearing functions and tested them comparing the results with the experimental polarizabilities for sixteen simple molecules.[65]

2.5.2 Dielectric constant and $\varepsilon(\omega)$ for polarizable dipoles

The addition of linear, isotropic polarizability ($\boldsymbol{\mu} = \alpha \boldsymbol{E}$) to a system of dipoles (either point or smeared) adds an additional term to the Hamiltonian of the system. Let us consider out system to consist of particles with a fixed dipole $\boldsymbol{\mu}_0$ and a polarizable dipole $\boldsymbol{\mu}_p$. In addition to the usual energy term $\boldsymbol{\mu}_0 \cdot \boldsymbol{E}$ the polarizable dipoles also have "internal energy":

$$U_{\text{pol}} = \sum_{i=1}^{N} \frac{\mu_{pi}^2}{2\alpha_i} \tag{2.81}$$

This can be derived as follows:

$$\begin{aligned} U &= \boldsymbol{\mu}_p \cdot \boldsymbol{E} \\ dU &= d\boldsymbol{\mu}_p \cdot \boldsymbol{E} = d\boldsymbol{\mu}_p \cdot \boldsymbol{\mu}_p/\alpha \\ U &= \int_0^{\boldsymbol{\mu}_p} \frac{\boldsymbol{\mu}_p}{\alpha} d\boldsymbol{\mu}_p = \frac{\boldsymbol{\mu}_p \cdot \boldsymbol{\mu}_p}{2\alpha} \end{aligned} \tag{2.82}$$

Because of this "internal energy" term, the linear response calculations of section 2.3.2 need to be repeated. The perturbation to the Hamiltonian due to an applied field $\boldsymbol{E}_0$ is :[56]

$$\Delta H = -\boldsymbol{M} \cdot \boldsymbol{E}_0 - \frac{1}{2} \boldsymbol{E}_0 \boldsymbol{\alpha}^{\text{sys}} \boldsymbol{E}_0 \tag{2.83}$$

Here $\boldsymbol{M}$ is the total dipole moment of the system $\boldsymbol{M} = \sum_i^N \boldsymbol{\mu}_0^i + \boldsymbol{\mu}_p^i$ and $\boldsymbol{\alpha}^{\text{sys}}$ is the total polarizability of the system as defined by eqn. 2.74.

The resulting equations for Ewald summation (or $\varepsilon_{\text{RF}} = \infty$) are:

$$\frac{\varepsilon(\omega) - \varepsilon_\infty}{(\varepsilon - \varepsilon_\infty)} = \mathcal{L}[-\dot{\phi}] \tag{2.84}$$

$$\varepsilon - \varepsilon_\infty = \frac{\langle \boldsymbol{M}^2 \rangle}{3\epsilon_0 k_B T V} \tag{2.85}$$

$$\varepsilon_\infty - 1 = \frac{\langle \text{Tr}(\boldsymbol{\alpha}^{\text{sys}}) \rangle}{\epsilon_0 V} \tag{2.86}$$

Where $\mathcal{L}[-\dot{\phi}]$ is the one-sided Fourier transform of the dipole-dipole au-

tocorrelation function (see 2.108, etc). Here we discussed the case of linearly polarizable point dipoles, but a similar situation holds whenever there are internal degrees of freedom which couple to the dipole moment, for instance, with flexibility. For path integral simulation, equation 2.86 no longer holds and requires slight modification.[66] For ab-initio simulation (DFT) calculation of ε_∞ appears to be non-trivial and to our knowledge no analog to eqn 2.86 has been derived. One difference is that in the quantum case different terms in $\Delta\hat{H}$ will not commute when Taylor expanding $e^{-\beta(\hat{H}_0+\Delta\hat{H})}$, as was assumed here.

Because analysis of $\langle \mathrm{Tr}(\boldsymbol{\alpha}^{\mathrm{sys}})\rangle$ requires some work, most authors use the Clausius-Mosotti equation to estimate ε_∞, which is known to work very well for most substances:

$$\frac{\varepsilon_\infty - 1}{\varepsilon_\infty + 2} = \frac{N\alpha}{3V\epsilon_0} \tag{2.87}$$

Neumann shows that the validity of this equation for ε_∞ does not change with different boundary conditions.[56]

For completeness, we would like to present the analog of eqns. 2.84, 2.85 and 2.86 for the infinite case. Such an expression would be useful for deriving g_K in the true infinite system with polarization.[56] As mentioned, ε_∞ is small, but it is worth investigating how g_K changes with the introduction of ε_∞. As we will see later in the section on mean field theories, the Onsager expression relating $\varepsilon(0)$ and g_K is sensitive to ε_∞.

One set of equations for the infinite system (or $\varepsilon_{\mathrm{RF}} = \varepsilon(0)$) is:[56]

$$\frac{3\varepsilon(0)(\varepsilon(\omega) - \varepsilon_\infty)}{(\varepsilon(\omega) + 2\varepsilon(0))(\varepsilon(0) - \varepsilon_\infty)} = \mathcal{L}[-\dot{\phi}] \tag{2.88}$$

$$\frac{(\varepsilon - \varepsilon_\infty)(2\varepsilon + 1)^2}{3\varepsilon(2\varepsilon + \varepsilon_\infty)} = \frac{\langle \boldsymbol{M}^2\rangle}{3\epsilon_0 k_B T V} \tag{2.89}$$

$$\frac{(\varepsilon_\infty - 1)(2\varepsilon + 1)}{2\varepsilon + \varepsilon_\infty} = \frac{\langle \mathrm{Tr}(\boldsymbol{\alpha}^{\mathrm{sys}})\rangle}{\epsilon_0 V} \tag{2.90}$$

Equations 2.88 and 2.89 were given by Glarum (1960)[67] and equation 2.89 was given independently by Fröhlich (1958).[68] The validity of such expressions (especially eqn. 2.88) was the subject of an extended controversy.[69, 70, 71] Equations 2.88 and 2.89 describe the fluctuations of a spherical sample embedded in a medium with a *frequency independent* dielectric constant.[71] This is the case in a computer simulation, but is not the case in real materials. Additionally, as was shown by Felderhof, these equations only describe what he calls low-frequency fluctuations and do not properly account for high frequency fluctuations due to polarizability.[69, 70]

Expression	g_K
Kirkwood's equation (eqn. 2.61)	1.7714
Incorrect polarization equation (eqn. 2.89)	1.7449
Correct polarization equation (eqn. 2.93)	1.7940
Kirkwood-Fröhlich expression (eqn. 2.94)	1.0983

To describe the fluctuations of a spherical sample embedded in an infinite medium with the same frequency-dependent dielectric constant, an expression was derived by Fatuzzo & Mason:[71]

$$\frac{(\varepsilon(\omega)-1))(2\varepsilon(\omega)+1)\varepsilon(0)}{(\varepsilon(0)-1)(2\varepsilon(0)+1)\varepsilon(\omega)} = \mathcal{L}[-\dot{\phi}] \tag{2.91}$$

The weakness of this equation is that it does not include polarization, hence there is no ε_∞ in the equation. The correct analog for eqn. 2.88 was derived by Wertheim in 1978[72] and the correct analog for eqn. 2.91 was derived by Felderhof.[69, 70] The resulting formulas are:

$$\frac{(2\varepsilon(\omega)+1)(\varepsilon(\omega)-1)}{3\varepsilon(\omega)} + \frac{(2\varepsilon_\infty+1)(\varepsilon_\infty-1)}{3\varepsilon_\infty} = \mathcal{L}[-\dot{\phi}] \tag{2.92}$$

$$\frac{(2\varepsilon+1)(\varepsilon-1)}{3\varepsilon} + \frac{(2\varepsilon_\infty+1)(\varepsilon_\infty-1)}{3\varepsilon_\infty} = \frac{\langle \boldsymbol{M}^2\rangle}{3\varepsilon_0 k_B T V} \tag{2.93}$$

These are the exact results describing the fluctuations of a spherical sample embedded in an infinite medium with the same $\varepsilon(\omega)$.[56] A detailed discussion of these equations is given by Madden & Kivelson (1984).[73] I could not find an analogous expression for 2.90. While in retrospect the form of these equations may be intuitive, a rigorous derivation of these results is non-trivial and required the work of many people over several decades.

As a conclusion to this section, we note that it is not uncommon to come across an equation known as the "Kirkwood-Fröhlich" expression (Fröhlich, 1949)[68]:

$$\frac{3(\varepsilon-\varepsilon_\infty)(2\varepsilon+\varepsilon_\infty)^2}{3\varepsilon(\varepsilon_\infty+2)^2} = \frac{\langle \boldsymbol{M}^2\rangle}{\epsilon_0 k_B T V} \tag{2.94}$$

This is Onsager's equation (eqn. 3.20) with μ^2 replaced with $g_K\mu^2$. As pointed out by Wertheim, this expression is not rigorously valid, the correct expression being eqn. 2.93.

At this point one may wonder if any of these equations yield a significant difference in g_K. We will do a comparison for water with $\varepsilon(0) = 80$, $\varepsilon_\infty = 1.8$, $T = 293$ K, $N/V = .0333679\text{Å}^{-3}$ and $\mu = 2.95$. The results are reported

in table 2.5.2. The difference between the correct equation and Kirkwood's equation is small (1.3 %). For other materials where $\varepsilon \approx \varepsilon_\infty$ the difference can be very significant. The Kirkwood-Fröhlich equation fails here. This is partly because the Onsager equation, on which it is based, assumes μ to be the gas-phase dipole. If we use the gas-phase dipole of $g_K = 1.85$ then we obtain $g'_K = 2.7927$. The prime on g_K indicates that we are refering to a g_K factor measured relative to the gas phase dipole, in contrast to the standard convention where g_K relates to the liquid phase dipole. Attempting to correct for the artificial increase, which accounts for 60% of g'_K we obtain $g_K = 1.145$. These points seem to have been missed by at least one author, who used the Kirkwood-Fröhlich expression to find g_K and took $g_K = 2.79$ to be the true g_K for water.[74] As we have shown that the "Kirkwood-Fröhlich" expression is not rigorous and gives a result at odds with the correct equation, its use should be discontinued.

2.6 The frequency-dependent dielectric function

Consider a time dependent field $E(t)$ given by:

$$E = E_0 \cos(\omega t) \tag{2.95}$$

At low frequencies, the polarization of the material will be in sync with the electric field, but as the frequency is increased, it will start to lag behind. After waiting a sufficiently long time, the electric displacement D will have the same time dependence, but with a phase lag:

$$\begin{aligned} D = D_0 \cos(\omega t - \phi) &= (D_0 \cos\phi)\cos(\omega t) + (D_0 \sin\phi)\sin(\omega t) \\ &\equiv \varepsilon' E(t) + \varepsilon'' E(t + \pi/2) \end{aligned} \tag{2.96}$$

These relations are more easily written using complex notation:

$$\begin{aligned} E &= E_0 e^{\pm i\omega t} \\ \varepsilon(\omega) &\equiv \epsilon(\omega)' \pm i\varepsilon(\omega)'' \\ D &= \varepsilon(\omega) E \end{aligned} \tag{2.97}$$

Note that either a plus or minus sign can be chosen in the definition of ε which corresponds to whether one chooses $E_0 e^{i\omega t}$ or $E_0 e^{-i\omega t}$ to represent the electric

field.[3]

2.6.1 The dielectric response function

The polarization response of a material to an arbitrarily time-dependent electric field $E(t)$ can be described using a response function. To define the response function, one should first consider an electric field which suddenly turns on at time t_0:

$$E(t) = E_2 H(t - t_0) \tag{2.98}$$

Where $H(t)$ is the Heaviside step function defined as:

$$H(t) = \begin{cases} 0 & t < 0, \\ 1 & t \geq 0 \end{cases} \tag{2.99}$$

The polarization will respond as:

$$P(t) = \chi E_2[1 - \phi(t - t_0)] \quad t > t_0 \tag{2.100}$$

Here $\phi(t)$ can be called the "step-response function" or the "decay function" of the response.[4] In principle many different behaviors are possible for $\phi(t)$ but in all cases we require $\phi(0) = 1$ and $\phi(\infty) = 0$. Now we can consider a block function, which can be considered as the superposition of two step functions:

$$E(t) = E_2[H(t - t_0) - H(t - t_0 - \Delta t)] \tag{2.101}$$

Likewise, the polarization can be considered as the superposition of the responses to both step functions:

$$\begin{aligned} P(t) &= \chi \epsilon_0 E_2[1 - \phi(t - t_0) - 1 + \phi(t - (t_0 - \Delta t))] \\ &= \chi \epsilon_0 E_2[\phi(t - t_0) - \phi(t - t_0 + \Delta t)] \end{aligned} \tag{2.102}$$

An arbitrary function $E(t)$ can be broken up into a series of blocks, each with width Δt.

[3] I have read that physicists usually use the plus sign, whereas engineers use the minus sign, but I have also seen physicists use the minus sign, so apparently there is no agreement on which sign to use. I prefer the plus sign for simplicity, but admit that I am not 100% consistent in this thesis.

[4] Alternatively, one can consider the case where a constant field E_2 is suddenly turned off, in which case the response is simply $P(t) = \chi E_2 \phi(t - t_0)$.

In the limit of an infinite number of blocks ($\Delta t \to dt$) we get an integral :

$$\begin{aligned} P(t) &= \chi\epsilon_0 \int_{\infty}^{t} E(t') - \frac{\partial\phi(t-t')}{\partial t} dt' \\ P(t) &= \chi\epsilon_0 \int_{\infty}^{t} E(t')\Phi(t-t')dt' \end{aligned} \tag{2.103}$$

Equation 2.103 contains $\Phi(t-t') = \dot{\phi}(t-t')$ which is the Green function, also called the "pulse-response function". It is the response function for a delta-function perturbation. Equation 2.103 is often the starting point for such discussions, however, I choose to include both the step-response function $\phi(t)$ and the pulse (delta) response function $\Phi(t)$ in my discussion since both are important. We now take the "Fourier-Laplace transform" (a one-sided Fourier transform) of both sides and use the convolution theorem, yielding the equation

$$P(\omega) = \chi(\omega)\epsilon_0 E(\omega) \tag{2.104}$$

where

$$\chi(\omega) = \chi(0)\epsilon_0 \int_0^{\infty} \dot{\phi}(t) e^{-i\omega t} dt \tag{2.105}$$

$\chi(\omega)$ is called the complex susceptibility, with real and imaginary parts defined as $\chi(\omega) \equiv \chi'(\omega) - i\chi''(\omega)$.

It is possible to relate $\phi(t)$ found in eqn. 2.105 to fluctuations in the total dipole moment of the material in equilibrium.The relation is:

$$\phi(t) = \frac{\langle \mathbf{M}(0) \cdot \mathbf{M}(t) \rangle}{\langle M^2 \rangle} \tag{2.106}$$

Where $\mathbf{M} = \sum \boldsymbol{\mu}_i$ is the total dipole moment of the system.

The earliest derivation of this relation comes from Onsager's "regression hypothesis" (1931).[75, 76]

To get the equation for the dielectric function from we plug eqn. 2.106 into eqn. 2.105 and use the definition $\chi(\omega) \equiv \varepsilon(\omega) - 1$, yielding

$$\begin{aligned} \varepsilon(\omega) - 1 &= (\varepsilon(0) - 1)\mathcal{L}[\dot{\phi}] \\ &= (\varepsilon(0) - 1)(1 - i\omega)\mathcal{L}[\phi] \end{aligned} \tag{2.107}$$

$\mathcal{L}[]$ implies the "Fourier-Laplace" transform:

$$\mathcal{L}[f] = \int_0^{\infty} dt e^{-i\omega t} f(t) \tag{2.108}$$

Eqn. 2.107 can be seen as a consequence of Callen and Welton's famous fluctuation-dissipation theorem of 1951. It can also be derived from "Green-Kubo" theory, which was derived in 1954 by Melville S. Green and extended by Ryogo Kubo in 1957. Green-Kubo theory, also called dynamic linear response theory, will not be explained here as it can be found in many textbooks.

2.6.2 The "infinite frequency" dielectric constant

Typically it is hard to take into account the really fast polarization response. In computer simulations, for instance, the output data will have finite time resolution. Experimentally, measuring devices are also limited - they have a maximum frequency they are capable of probing. Typically, this fast response is represented as an instantaneous response Then:

$$\mathbf{D}(t) = \varepsilon_\infty \mathbf{E}(t) + \epsilon_0 \mathbf{P}_{electronic}(t) \tag{2.109}$$

This leads to:

$$\varepsilon(\omega) - \varepsilon_\infty = (\varepsilon(0) - \varepsilon_\infty)\mathcal{L}[-\dot{\Phi}] \tag{2.110}$$

Where we have introduced the "infinite frequency" or "high frequency" dielectric constant ε_∞. We have avoided the notation $\varepsilon(\infty)$, since ε_∞ does not literally mean the response at infinite frequency. In any physical system $\varepsilon(\infty) = 1$, since no system can respond infinitely fast to an infinitely high frequency. X-ray diffraction data and other high-energy data indicate that the correct limit $\varepsilon(\infty) = 1$ is approached in water.[77] ε_∞ quantifies the response arising from electronic resonances that arrises when measurements are made well below them. One often sees the relation $\varepsilon_\infty = n^2$, where n is the index of refraction. It is usually assumed that the index of refraction is measured in the visible range. In this case $\varepsilon_\infty \approx 1.8$ for water. This value represents the dielectric increment for electronic response. However, many different values for ε_∞ can be found in the literature. In dielectric experiments, one typically is limited to probing in the range of 1 GHz - 1 THz. At these low frequencies, the decrement in the dielectric function from libation, vibration, and electronic response are not measured, so values of $\varepsilon_\infty \approx 4.5$ are often found.[46] A popular way of "measuring" ε_∞ in dielectric experiments is to extrapolate one's data on a Cole-Cole plot (described below) assuming that it follows a perfect Debye semicircle, for water this yields values around 5.

2.6.3 Kramers-Kronig relation

No discussion of the dielectric function would be complete without a mention of the Kramer-Kronig (KK) relation, which allows one to deduce $\varepsilon(\omega)''$

from complete knowledge of $\varepsilon(\omega)'$ and vice-versa. The KK relation holds whenever the dielectric function is analytic in the upper half plane. Because of the causal nature of $\varepsilon(\omega)$, the KK relation always holds for local dielectrics (or non-local dielectrics when $\boldsymbol{k} = 0$).[78, 79]

The KK relation can be derived using Cauchy's theorem from complex analysis. We will not repeat the derivation here as it can be found in many books, such as Jackson, 3rd edition, pg. 333.[45] The KK relation is:

$$\begin{aligned} \varepsilon'(\omega) &= \varepsilon_\infty + \frac{1}{\pi}\mathrm{P}\int_{-\infty}^{\infty}\frac{\varepsilon''(x)}{x-\omega}dx \\ \varepsilon''(\omega) &= -\frac{1}{\pi}\mathrm{P}\int_{-\infty}^{\infty}\frac{\varepsilon'(x)-1}{x-\omega}dx \end{aligned} \tag{2.111}$$

From causality, it holds that $\varepsilon'(\omega)$ is even in ω while $\varepsilon''(\omega)$ is odd in ω.[45] Thus we can rewrite eqn. 2.111 using the following trick – we multiple the numerator and denominator of both equations by $x+\omega$. For instance, for $\varepsilon'(\omega)$ we get:

$$\varepsilon'(\omega) = \varepsilon_\infty + \frac{1}{\pi}\mathrm{P}\int_{-\infty}^{\infty}\frac{x\varepsilon''(x)}{x^2-\omega^2}dx + \frac{1}{\pi}\mathrm{P}\int_{-\infty}^{\infty}\frac{\omega\varepsilon''(x)}{x^2-\omega^2}dx \tag{2.112}$$

Because $\varepsilon''(\omega)$ is odd, the second term vanishes. We repeat this procedure for the second equation in 2.111, yielding:

$$\begin{aligned} \varepsilon'(\omega) &= \varepsilon_\infty + \frac{2}{\pi}\mathrm{P}\int_{0}^{\infty}\frac{x\varepsilon''(x)}{x^2-\omega^2}dx \\ \varepsilon''(\omega) &= -\frac{2}{\pi}\mathrm{P}\int_{0}^{\infty}\frac{\omega\varepsilon'(x)-1}{x^2-\omega^2}dx \end{aligned} \tag{2.113}$$

2.6.4 Theory of absorption / loss

There are several conventions of quantifying loss which are currently used. We know a plane wave moving in one dimension is given by the equation

$$u(x,t) = ae^{ik(x-vt)} \tag{2.114}$$

As was just mentioned we also know the relations between k, the phase velocity v and the dielectric constant ε:[45]

$$v = \frac{\omega}{k} = \frac{1}{\sqrt{\mu\varepsilon}} = \frac{c}{n} \tag{2.115}$$

Thus we can rewrite our plane wave as

$$u(x,t) = ae^{iknx - i\omega t} \tag{2.116}$$

In general, ε is complex, thus n can be complex as well:

$$k = \beta + i\frac{\alpha}{2} \tag{2.117}$$

Here α is the absorption coefficient.[5] By substituting If we solve this for α we get the well known relation:

$$\alpha = \frac{\varepsilon''(\omega)\omega}{cn(\omega)} \approx \frac{\varepsilon''(\omega)\omega}{c} \tag{2.118}$$

The approximate only holds if $n(\omega) \approx 1$. Ideally, we would like an expression completely in terms of the dielectric function, but doing this requires using the formula $n = \sqrt{\varepsilon(\omega)}$ and the cumbersome relation:

$$\begin{aligned} \sqrt{\varepsilon' + i\varepsilon''} &= \sqrt{\frac{|\varepsilon| + \varepsilon'}{2}} + i\ \mathrm{sgn}(\varepsilon'')\ \sqrt{\frac{|\varepsilon| - \varepsilon'}{2}} \\ |\varepsilon| &= \sqrt{\varepsilon'^2 + \varepsilon''^2} \end{aligned} \tag{2.119}$$

This yields:

$$\alpha = \frac{\sqrt{2}\varepsilon''\omega}{c\sqrt{\varepsilon' + \sqrt{\varepsilon''^2 + \varepsilon'^2}}} \tag{2.120}$$

Given the cumbersome nature of 2.120, several other conventions are used to quantify loss. Engineers like to work in terms of the "loss tangent", which is defined as :

$$\tan\delta \equiv \frac{\varepsilon''}{\varepsilon'} \tag{2.121}$$

The loss tangent is a useful quantity for several reasons. The first is that it equal to the the phase lag of the polarization with respect to the applied field.[6]

[5] This is the infrared absorption coefficient, and also the one appearing the Beer-Lambert law

[6] To see this, recall the basic relation $P = \varepsilon(0)\epsilon_0 E$, with our convention of a complex electric field and complex dielectric constant, $P = (\varepsilon' + i\varepsilon'')\epsilon_0 E_0(\cos(\omega t) + i\sin(\omega t))$. The real (physical) part is $P = \epsilon_0 E_0(\varepsilon'\cos(\omega t) - \varepsilon''\sin\omega t)$. Elementary trig shows this equivalent to $P = \epsilon_0 E_0\cos(\omega t - \delta)$

Secondly, we can substitute the loss tangent into the messy eqn. 2.120 yielding

$$\alpha = \frac{\sqrt{2}\varepsilon''\omega}{c\sqrt{\varepsilon'(1+\sqrt{\tan\delta^2+1})}} \tag{2.122}$$

Then, if $\tan\delta < 1$, ie. if the losses are small, then

$$1+\sqrt{\tan\delta^2+1} \approx \frac{\tan\delta^2}{2} \tag{2.123}$$

Substituting this into eqn. 2.122 yields:

$$\alpha \approx \frac{2\varepsilon''\omega}{c\sqrt{\epsilon'}\tan\delta} \tag{2.124}$$

This can be simplified further by assuming $\tan\delta \approx 1$, yielding

$$\alpha(\omega) \approx \frac{2\varepsilon''(\omega)\omega}{c\sqrt{\epsilon'(\omega)}} \tag{2.125}$$

2.7 Summary of important relations

Relation of the index of refraction $n(\omega)$ and extinction coefficient $k(\omega)$ to the dielectric function:

$$\begin{aligned}\varepsilon'(\omega) &= n^2(\omega) - k^2(\omega)\\ \varepsilon''(\omega) &= 2n(\omega)k(\omega)\end{aligned} \tag{2.126}$$

inverse relation:

$$\begin{aligned}n(\omega) &= \sqrt{\frac{\sqrt{\varepsilon'(\omega)^2+\varepsilon''(\omega)^2}+\varepsilon'(\omega)}{2}}\\ k(\omega) &= \sqrt{\frac{\sqrt{\varepsilon'(\omega)^2-\varepsilon''(\omega)^2}+\varepsilon'(\omega)}{2}}\end{aligned} \tag{2.127}$$

relation between $k(\omega)$ and the infrared absorption coefficient, $\alpha(\omega)$:

$$\alpha(\omega) = \frac{2\omega k(\omega)}{c} \tag{2.128}$$

Relation between the reflectance, R, of normally incident light at a vacuum interface and the index of refraction of the material:

$$R = \frac{(n-1)^2+k^2}{(n+1)^2+k^2} \tag{2.129}$$

Chapter 3

Simple mean field theories

In this chapter we will describe three simple mean-field theories and apply each theory to water. These theories are rather crude, but each mean field theory yields insights into how the hydrogen bonding of water effects the dielectric constant of water.

3.1 Debye's theory

The first theory of the dielectric constant, which is still often cited today, was published by Debye in 1929.[80] The derivation begins by considering the energy of a dipole in an electric field F:

$$U = -\mu F \cos\theta \tag{3.1}$$

where μ is the dipole moment and θ is the angle between the dipole and the field. According to Boltzmann's law, dipoles will have some probability distribution. In spherical coordinates, the differential solid angle is $d\Omega = \sin(\theta)d\theta d\phi$. From Boltzmann's law, the probability that a dipole will lie on a cone with an angle between θ and $\theta + d\theta$ from the field is given by:

$$P(\theta) = \frac{e^{\beta\mu F\cos\theta}\sin\theta d\theta}{\int e^{\beta\mu F\cos\theta}\sin\theta d\theta} \tag{3.2}$$

The average value of $\cos(\theta)$ is given by :

$$\begin{aligned}\langle\cos\theta\rangle &= \frac{\int_0^\pi \cos\theta e^{\beta\mu F\cos\theta}\sin\theta d\theta}{\int_0^\pi e^{\beta\mu F\cos\theta}\sin\theta d\theta} \\ &= \frac{\int_0^\pi x e^{\beta\mu F x}dx}{\int_0^\pi e^{\beta\mu F x}dx}\end{aligned} \tag{3.3}$$

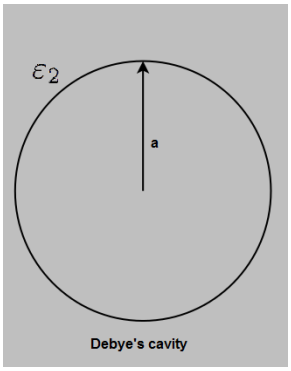

Figure 3.1: The Debye "cavity".

The numerator can be integrated by parts and the denominator is a trivial integral. The result is:

$$\langle \cos(\theta) \rangle = \coth(\beta\mu F) - \frac{1}{\beta\mu F} \equiv L(\beta\mu) \tag{3.4}$$

Where $L(x) = \coth(x) - 1/x$ is known as Langevin's function. In experimental conditions, it is usually the case that $\beta\mu F << 1$. In that case, we can safely expand Langevin's function using the expansion for $\coth(x)$ and ignore the $1/x$ term, so $L(x) \approx x/3$ Thus we get, for the average dipole polarization per molecule

$$P = \mu \langle \cos\theta \rangle = \frac{\beta\mu^2 F}{3} \tag{3.5}$$

$\beta\mu^3/3$ is the gas phase polarizability for rigid dipoles. If we add the electronic and distortion polarizations then we get

$$P = N(\alpha + \frac{\beta\mu^2}{3})F \tag{3.6}$$

To find the magnitude of the internal field, Debye drew on the work of Lorentz, for this reason, this type of internal field is refereed to a "Lorentz internal field". He then considered a spherical "cavity" around each molecule, with the same dielectric constant inside as outside. (The only difference between the inside and outside of the sphere are the ways they are considered.) The field experienced by a molecule in the center of this sphere will be due to three separable sources:

1. The "background field", which is the applied field due to the charges on the plates and the polarization charges on the outer surface of the material.

2. The field due to the polarization on the inner surface of the cavity.

3. The field due to other molecules in cavity

Crucially, Debye assumed that the contribution from (3) was zero, which is *not* a good assumption for a liquid.[1] The contribution from (2) can be easily calculated, however, using classical electrostatics. Consider the differential element of surface swept out by a cone between θ and $\theta + d\theta$. By symmetry one can see that F_y and F_z will be zero. F_x caused by this differential element will be :

$$dF_x = \frac{\text{area} \times \text{charge density} \times \cos\theta}{4\pi\epsilon_0 r^2} = \frac{2\pi r^2 \sin\theta P \cos\theta \cos\theta}{4\pi\epsilon_0 r^2} \tag{3.7}$$

Here we used the fact that the surface charge density is equal to the normal component of the polarization, $P\cos\theta$. To find F_x we integrate over all θ:

$$\begin{aligned} F_x &= \int_0^\pi \frac{2\pi}{4\pi\epsilon_0} P_{mol} \cos^2\theta \sin\theta d\theta \\ F_x &= \frac{P}{3\epsilon_0} \end{aligned} \tag{3.8}$$

This is the "Lorentz field" (in SI units). The total field is

$$F = E + \frac{P}{3\epsilon_0} \tag{3.9}$$

We now use $P = (\varepsilon - 1)\epsilon_0 E$ and rearrange the resulting expression to get:

$$F = \frac{(\varepsilon + 2)}{3} E \tag{3.10}$$

Substitution of this into equation 3.6 yields:

$$\frac{\varepsilon - 1}{\varepsilon + 2} = \frac{n(\alpha + \beta\mu^2/3)}{3\epsilon_0} \tag{3.11}$$

[1]However, for dipoles on a cubic lattice, this is a very good approximation. In fact, if one assumes a system of dipoles on a cubic lattice with uniform polarization, the contribution from (3) is exactly zero.[79]

This is Debye's equation. It is common to see this formula in terms of the molar mass M, Avogadro's number N_a and the density ρ through the relation $n = \frac{m_{tot}}{mV} = \frac{N_a \rho}{M}$. If we ignore the term from dipolar polarizability in eqn. 3.11 we recover the famous Clausius-Mossotti relation from 1879 (eqn. 2.87). If one substitutes the index of refraction squared in for $\varepsilon(0)$ in the Clausius-Mossottie relation one gets the Lorentz-Lorenz equation (1880), which is essentially the same equation but with a different name.

Now let us consider what happens when μ becomes very large or T becomes very small.[46] In that case we can disregard the "Clausius - Mossotti part" involving α, which will be very small in comparison. We get:

$$\begin{aligned} \frac{\varepsilon - 1}{\varepsilon + 2} &= \frac{n\mu^2}{9k_B T \epsilon_0} \equiv \frac{C}{T} \\ \varepsilon - 1 &= \frac{\frac{2C}{T}}{1 - \frac{C}{T}} \\ \varepsilon - 1 &= \frac{2C}{T - C} \end{aligned} \tag{3.12}$$

We see there is a singularity when $T = C$. The case of an infinite dielectric constant corresponds to a transition from paraelectric to ferroelectric behavior. In direct analogy with the magnetic case, C is called the electric Curie-Weiss temperature. Here $C \equiv \frac{n\mu^2}{9\epsilon_0 k_B}$, or $C = 330.8\mu^2$, where μ is in Debye. For water, Debye's theory predicts a ferroelectric Curie point of 1100 K, assuming the gas phase moment $\mu = 1.85$ D. If one uses the liquid phase moment of $\mu \approx 3$ one gets $T = 2970$ K. Furthermore, plugging into 3.11 with $\mu = 3$ D, $\alpha = 0$ at 300K yields $\varepsilon(0) = -1.22$. These calculations show the severe inadequacy of this theory to the liquid phase, due to the neglect of local interactions, which in water are mediated by hydrogen bonds.

3.2 Onsager's theory

Onsager developed a mean field theory very similar to Debye's in 1936, but with a real cavity with $\varepsilon = 1$ rather than the artificial "cavity" used by Debye.[46] Although Onsager's theory is a step up from Debye's and works very well for many dipolar fluids, it is still not a very good theory for water since does not take into account the local influence of hydrogen bonding. For this reason we will not discuss the details of Onsager's theory and will only report the key results. In Onsager's cavity the local field can be broken into two parts: the cavity field **G**, which would be produced in an empty cavity by the applied field **E**, and the "reaction field", **R** produced by the polarization

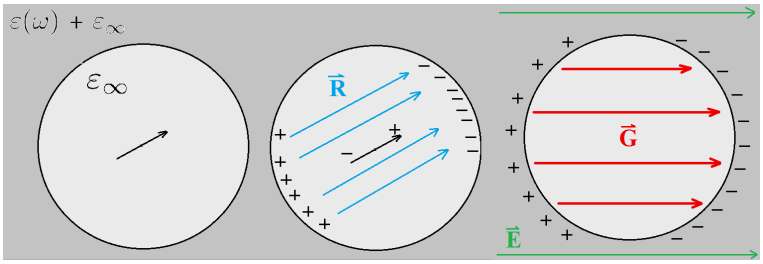

Figure 3.2: The Onsager cavity (left), the reaction field (middle), and the cavity field (right).

charge induced by the central dipole on the inner surface of the cavity.

The cavity field turns out to be:

$$\mathbf{G} = \frac{3\epsilon_2 \mathbf{E}}{2\varepsilon_2 + 2} \tag{3.13}$$

And the reaction field turns out to be:

$$\mathbf{R} = \frac{2(\varepsilon_2 - 1)\boldsymbol{\mu}}{\epsilon_0(2\varepsilon_2 + 1)a^3} \tag{3.14}$$

The radius of the cavity a is defined so that

$$\rho = \frac{m}{4/3\pi a^3} \tag{3.15}$$

Onsager defines an "internal refractive index" using the Lorentz-Lorenz equation (eqn. 2.87):

$$\frac{n^2 - 1}{n^2 + 2} = \frac{\alpha}{\epsilon_0 a^3} \tag{3.16}$$

In the case of water n should be the refractive index at infrared frequencies ($n = 1.33$).[81][46] The reason for taking n in the infrared range is that α needs to include the electronic and molecular polarizability, and the molecular polarizability is not active at higher frequencies. The total internal field is

$$\mathbf{F} = \frac{3\varepsilon_2 \mathbf{E}}{2\varepsilon_2 + 2} + \frac{2(\varepsilon_2 - 1)\boldsymbol{\mu}}{\epsilon_0(2\varepsilon_2 + 1)a^3} = A\boldsymbol{E} + \frac{B\boldsymbol{\mu}}{a^3} \tag{3.17}$$

μ	n^2	$\varepsilon(0)$
1.85	1	17.8
1.85	2	31.7
1.85	4	71.2
2.95	1	44
2.95	2	79
2.95	4	177

Table 3.1: Values obtained from eqn. 3.20 at 300K. Onsager's equation is supposed to take the gas phase dipole as input, and the effective ehancement of the dipole depends strongly on $n^2 = \varepsilon_\infty$. Onsager's equation can work remarkably well if the correct value for $n^2 = \varepsilon_\infty$ is chosen. However, one can see that something fishy is going on by using substituting the correct liquid phase dipole ≈ 2.95 and $\varepsilon_\infty = 1$.

The dipole moment will change due to the internal field:

$$\begin{aligned} \boldsymbol{\mu} &= \boldsymbol{\mu}_0 + \alpha A \mathbf{E} + \frac{\alpha B \boldsymbol{\mu}}{a^3} \\ &= \frac{\boldsymbol{\mu}_0 + aA\mathbf{E}}{1 - \frac{B\alpha}{a^3}} \end{aligned} \tag{3.18}$$

This equation can be used to relate the gas phase moment of a molecule to its liquid phase moment:

$$\begin{aligned} \mu &= \frac{\mu_g}{1 - \frac{B\alpha}{a^3}} \\ B &= \frac{2(\varepsilon_2 - 1)}{\epsilon_0(2\varepsilon_2 + 1)} \end{aligned} \tag{3.19}$$

To apply eqn. 3.19 to water, let's take $\varepsilon_2 = 80, \mu_g = 1.8$ and $\alpha = 1.596 \times 10^{-40}$. Then we find that $\mu = 2.4$D. Experiments show it to be closer to 2.95, but overall this formula works fairly well.

Onsager's equation turns out to be:

$$\frac{(\varepsilon - n^2)(2\varepsilon + n^2)}{\varepsilon(n^2 + 2)^2} = \frac{\rho_n \mu^2}{9 k_B T \epsilon_0} \tag{3.20}$$

Where ρ_n is the number density. Eqn. 3.20 can be used to estimate the gas phase dipole moments of molecules given only macroscopic observables and historically this was very useful. For water, if we use $n^2 = \varepsilon_\infty \approx 4.55$ and $\varepsilon = 80$ this yields $\mu_g = 1.77$.[46]

As was mentioned, the value of $\varepsilon(0)$ predicted by Onsager's model depends

on the value of $n^2 = \varepsilon(\infty)$, which should be taken in the infrared range. If we take $n^2 = 4$ and $\mu = 1.85$ we get $\varepsilon(0) = 71$, a rather reasonable value. Other values are shown in table 3.2. Unlike Deybe's model, Onsager's model does not predict a ferroelectric phase transition, although it does predict that $\varepsilon(0) \to \infty$ as $T \to 0$.

3.3 Kirkwood's theory

Kirkwood's theory expanded upon Onsager's by using a statistical treatment.[19, 46] He begins with a linear response type derivation which is nearly identical to the derivation covered in section 2.3.2, except instead of finding the average total dipole of the system, he wishes to the average component of the dipole of a given molecule i in the direction of the *local* field $\boldsymbol{E}$. He assumes the local field inside the dielectric is given by Debye's expression (eqn. 3.10):

$$\boldsymbol{E} = \frac{\varepsilon + 2}{3}\boldsymbol{E}_0. \tag{3.21}$$

The result Kirkwood obtains is:

$$\langle \boldsymbol{\mu}_i \cdot \hat{\boldsymbol{E}}_0 \rangle = \frac{\langle \boldsymbol{\mu}_i \cdot \boldsymbol{M} \rangle \beta \boldsymbol{E}_0}{3} = \frac{(\varepsilon + 2)\langle \boldsymbol{\mu}_i \cdot \boldsymbol{M} \rangle \beta \boldsymbol{E}_0}{9} \tag{3.22}$$

Where $\boldsymbol{M}$ is the total dipole moment of the sample. Next Kirkwood considers how the average $\langle \mu_i \cdot \mathbf{M}(X) \rangle$ can be computed. First one can average over all possible configurations with the molecule i fixed, obtaining an average $\bar{\mathbf{M}}$. Next one can average over all the configurations of molecule i. Since, as we have been assuming, our sample is uniform and isotropic, the result for

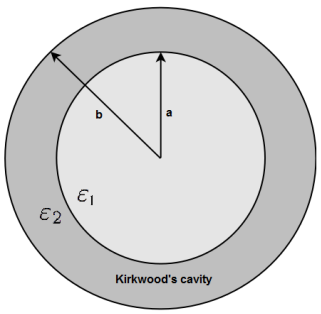

Figure 3.3: The Kirkwood cavity.

each molecule should be the same except for some molecules at the surface, which can be neglected if the sample is large enough. Thus we can assert that

$$\langle \boldsymbol{\mu}_i \cdot \boldsymbol{M} \rangle = \langle \boldsymbol{\mu}_i \cdot \bar{\boldsymbol{M}} \rangle \tag{3.23}$$

Next, Kirkwood attempts to take into account local interactions around the molecule which is considered fixed. Local interactions will effectively increase or decrease $\boldsymbol{\mu}_i$. He defines a radius r_0 within which the local ordering is confined. At distances larger than r_0 the medium is considered homogeneous. The size of the sample, R must be much larger than r_0, yet, to capture the local ordering, r_0 needs to be quite a bit larger than the molecular dimensions. To capture this, Kirkwood takes a peculiar double limit: $r_0 \to \infty$ and $R/r_0 \to \infty$.

Next, by solving a boundary value problem in electrostatics, (which is actually not completely trivial) he shows that:

$$\bar{\mathbf{M}} = \frac{9\varepsilon}{(\varepsilon+2)(2\varepsilon+1)}\bar{\boldsymbol{\mu}} \tag{3.24}$$

To relate $\bar{\boldsymbol{\mu}}$ to $\boldsymbol{\mu}$ he introduces a correlation parameter g_K:

$$\bar{\boldsymbol{\mu}} = g_K \boldsymbol{\mu} \tag{3.25}$$

This is the "Kirkwood g-factor" and is equivalent to the average total dipole moment in a spherical volume around a given (fixed) molecule in the absence of any applied field. Now we use eqn. 2.11 defining the dielectric constant along with eqn. 3.21:

$$\begin{aligned} \epsilon_0(\varepsilon - 1) &= \frac{\mathbf{P}}{\mathbf{E_0}} \\ &= \frac{N\langle \boldsymbol{\mu}_i \cdot \hat{\boldsymbol{E}}_0 \rangle}{V\mathbf{E_0}} \\ &= \frac{N(\varepsilon+2)\langle \boldsymbol{\mu}_i \cdot \bar{\boldsymbol{M}} \rangle \beta}{9V} \end{aligned} \tag{3.26}$$

Now using eqn. 3.24 and eqn. 3.25 we arrive at:

$$\frac{(\varepsilon-1)(2\varepsilon+1)}{3\varepsilon} = \frac{ng\mu^2}{3\epsilon_0 k_B T} \tag{3.27}$$

Note that this equation has the same form as eqn. 2.61. If one now includes

a contribution from an intrinsic distortional polarization α, one arrives at:

$$\frac{(\varepsilon-1)(2\varepsilon+1)}{3\varepsilon} = \frac{n}{3\epsilon_0}\left(\alpha + \frac{g_K\mu^2}{3k_BT}\right) \tag{3.28}$$

This is called Kirkwood's equation. In principle this equation is exact for an infinite system, but in practice it may not be possible to calculate g_K a priori. Kirkwood estimated g_K for water using a tetrahedral bonding model, and by doing this he was able to find an approximate value of ε.

3.3.1 Application of the Kirkwood equation

Suresh et al. assume a four-site tetrahedral bonding model similar to Kirkwood's, but where the bonds exist only with probability P.[74] In that case the contribution of the ith H-bonded shell to G_K is given by:

$$4P^i\cos^2(\theta_{\mathrm{HOH}}/2)\cos(\pi-\theta_{\mathrm{HOH}})^{i-1} \tag{3.29}$$

In this model the H-bond network is viewed as a "branching tree", and the presence of loops is completely ignored. Surprisingly, this model of H-bonding works well for both water and ice and the correction from loops is small. Assuming $\theta_{\mathrm{HOH}} = 109\,^\circ$ and $P = .875$ then this yields $G_K = 2.65$ with contributions of $G_K - 1 = 1.18 + .34 + .09 + .03 + \cdots$. This approach to understanding the dielectric constant of water, coupled with the mean field theory of Onsager, has been shown to reproduce the temperature dependence of $\varepsilon(0)$ (fig 2) using three input parameters - the HOH angle, ε_∞, and μ_{gas} along with two fitting parameters H and S.[74, 82] This type of theory also predicts the dielectric constant of ice almost perfectly with only the three input parameters (taken from experiment) and no additional fitting.

The success of this model is surprising given that the actual H-bond network in water contains distortions away from tetrahedrality and contains loops. There are also effects from cooperative H-bonding - molecules with four bonds have stronger bonds than those with two or three.

3.4 Conclusions

Each of the three mean field theories discussed in this chapter builds on the last. The failure of Debye's theory shows the importance of local interactions, and how they frustrate the natural tendancy of a dipolar system to order. Onsager's theory is a big step up, and can approximately describe the increase in the dipole moment going from the gas to the liquid. While Onsager's theory

can reproduce the dielectric constant, it depends sensitively on the choice of ε_∞. Kirkwood's theory is actually an exact theory, provided one knows the g-factor g_K, which depends on the details of dipolar ordering. Kirkwood's use of a tetrahedral bonding model yields an approximately correct value for the dielectric constant, and is the basis for our modern understanding of the dielectric constant of water and ice. All three of these theories have time-dependent extensions which can be used to describe $\varepsilon(\omega)$. Such extensions will be discussed in chapter 7.

Chapter 4

Computational methods

"It is generally agreed that the usefulness of measurement results... is to a large extent determined by the quality of the statements of uncertainty that accompany them. - Dr. John W. Lyons, Director of NIST, Technical Note 1297, 1994

In this chapter we discuss some of the methods of molecular dynamics simulation and analysis which were important for this work. We present a new comparison of different ways of computing the dielectric constant.

4.1 Integrating Newton's equations

4.1.1 Velocity-Verlet method

There are many possible algorithms one can use to integrate Newton's equations of motion. Arguably the two most important features we would like an algorithm to have are time reversibility and phase area-preservation (the "symplectic" property). Tuckerman et al. have given a method for systematically developing such algorithms for an arbitrary Hamiltonian.[83] It can be shown algorithms that are symplectic and reversible have long term energy conservation. More specifically, they conserve the energy of a "shadow Hamiltonian" or "pseudo-Hamiltonian". The difference between the shadow Hamiltonian and real Hamiltonian is small and is on the order of $(\Delta t)^{2n}$ where Δt is the timestep and n is the order of the integrator.

To start it is helpful to review the role of the Liouville operator in classical mechanics. The first step is to consider an arbitrary function that depends on the phase space variables. For instance, for a system of N interacting particles, this function will be denoted $f(\boldsymbol{p}, \boldsymbol{r})$, where we have employed a

shorthand notation where $\boldsymbol{p}$ denotes a vector containing all of the momentum variables and $\boldsymbol{r}$ contains all the position variables in the system.

The time derivative of f is

$$\begin{aligned} \dot{f} &= \dot{\boldsymbol{r}}\frac{\partial f}{\partial \boldsymbol{r}} + \dot{\boldsymbol{p}}\frac{\partial f}{\boldsymbol{p}} \\ &= iLf \end{aligned} \tag{4.1}$$

Where we have defined the Liouville operator:

$$iL \equiv \dot{\boldsymbol{r}}\frac{\partial}{\partial \boldsymbol{r}} + \dot{\boldsymbol{p}}\frac{\partial}{\partial \boldsymbol{p}} \tag{4.2}$$

The formal solution of 4.1 is:

$$f(\boldsymbol{p}(t), \boldsymbol{r}(t)) = \exp(iLt) f(\boldsymbol{p}(0), \boldsymbol{r}(0)) \tag{4.3}$$

While this equation is a formal solution for any function f so far we have not made the solution of the trajectory any simpler. It is possible however to evaluate the action of the two terms in the Liouville operator separately. The first term,

$$iL_r \equiv \dot{\boldsymbol{r}}\frac{\partial}{\partial \boldsymbol{r}} \tag{4.4}$$

shifts all the position variables so that

$$\exp(iL_r t) f(\boldsymbol{p}(0), \boldsymbol{r}(0)) = f(\boldsymbol{p}(0), \boldsymbol{r} + \dot{\boldsymbol{r}}(0)t) \tag{4.5}$$

Similarly, the operator

$$iL_p \equiv \dot{\boldsymbol{p}}\frac{\partial}{\partial \boldsymbol{p}} \tag{4.6}$$

shifts all of the momentum variables. The action of these two operators together however cannot be evaluated since they do not commute and for non-commuting operators,

$$\exp(A + B) \neq \exp(A)\exp(B) \tag{4.7}$$

We can use the Trotter formula, however:

$$\begin{aligned} e^{A+B} &= \lim_{P\to\infty} \left(e^{A/2P} e^{B/P} e^{A/2P}\right)^P \\ e^{(iL_r + iL_p)t} &= \lim_{P\to\infty} \left(e^{iL_p t/2P} e^{iL_r t/P} e^{iL_p t/2P}\right)^P \end{aligned} \tag{4.8}$$

We now define a timestep $\Delta t = t/P$, yielding

$$e^{(iL_r+iL_p)t} = \lim_{P\to\infty,\Delta t\to 0} \left(e^{iL_p\Delta t/2} e^{iL_r\Delta t} e^{iL_p\Delta t/2}\right)^P \tag{4.9}$$

Tuckerman, Berne, & Martyna showed that this equation can be used to derive time-reversible numerical algorithms by truncating the expansion to finite P and using a small enough timestep. For finite P we get the following approximation:[84]

$$e^{(iL_r+iL_p)t} \approx \left(e^{iL_p\Delta t/2} e^{iL_r\Delta t} e^{iL_p\Delta t/2}\right)^P + \mathcal{O}(P\Delta t^3) \tag{4.10}$$

Since $P = t/\Delta t$ the global error is actually proportional to $(\Delta t)^2$.

In this scheme each time step corresponds to applying the operator

$$e^{iL_p\Delta t/2} e^{iL_r\Delta t} e^{iL_p\Delta t/2} \tag{4.11}$$

Note that this operator is time symmetric in the sense that if we "move back a timestep" $-\Delta t$ we arrive back where we were:

$$e^{-iL_p\Delta t/2} e^{-iL_r\Delta t} e^{-iL_p\Delta t/2} e^{iL_p\Delta t/2} e^{iL_r\Delta t} e^{iL_p\Delta t/2} = 1 \tag{4.12}$$

We already know the action of $e^{iL_p\Delta t}$ (a shift in momentum by $\dot{\boldsymbol{p}}\Delta t$)) and likewise that the action of $e^{iL_r\Delta t}$ is a shift in position by $\dot{\boldsymbol{r}}\Delta t$). Therefore we can simply "directly translate" 4.11 into an algorithm:

- update the momentum by a half timestep using the forces
- update the positions a full timestep using the momentum
- positions have changed, so recalculate forces
- update the momentum by a half timestep using the forces

4.1.2 Multiple timestep (RESPA) method

A benefit of the propagator approach to deriving time-reversible integrators is that it gives rigorous way of introducing multiple timestep integration. For historical reason the method goes by the name "reversible reference system propagator algorithmn" (RESPA). Multiple timestep integration is possible when the force on each atom can be broken into "fast varying" and "slow varying" components. Long range forces are usually slower varying than short range forces. Thus we will denote the fast varying forces F_s (s is for short range) and the slow varying forces F_l (l is for long range).

We split the propagator as:

$$\begin{aligned} iL &= L_r + L_p \\ &= \dot{\boldsymbol{r}}\frac{\partial}{\partial \boldsymbol{r}} + F_s(\boldsymbol{r})\frac{\partial}{\partial \boldsymbol{p}} + F_l(x)\frac{\partial}{\partial \boldsymbol{p}} iL \quad = (L_r + L_s) + L_l \end{aligned} \tag{4.13}$$

We first perform a Trotter splitting between $(L_r + L_s)$ and L_l as we did in eqn. 4.14:

$$e^{iLt} \approx \left(e^{iL_l\Delta t/2} e^{i(L_r+L_s)\Delta t} e^{iL_l\Delta t/2}\right)^P \tag{4.14}$$

We now perform another Trotter splitting between L_r and L_s:

$$e^{iLt} \approx \left(e^{iL_l\Delta t/2}\left[e^{iL_s\delta t/2} e^{iL_r\delta t} e^{iL_s\delta t/2}\right]^n e^{iL_l\Delta t/2}\right)^P \tag{4.15}$$

where we have defined an inner (fast) timestep $\delta t = \Delta t/n$.

4.2 The TTM series of models

We use the polarizable model TTM3-F extensively in this thesis. TTM stands for "Thole type model", referring to the fact that the dipole moment is smeared (the need for smearing was discussed in section 2.5.1). Each TTM3-F molecule has one polarization dipole. In addition all charges are also smeared. The charges are smeared using the smearing function:

$$\rho(r) = \frac{1}{\alpha}\frac{3a}{4\pi}\exp\left[-\frac{ar^3}{\alpha}\right] \tag{4.16}$$

where α represents the atomic polarizability. The result of the smearing is shown in figure 4.2, where the smearing functions and equilibrium geometry of TTM3F have been plotted in Mathematica. Of course, the smearing is not directly implemented, but rather the charge-charge, charge-dipole, and dipole-dipole interactions are appropriately modified with smearing functions.

The first TTM model was a rigid model (TTM1-R) used to simulate $n = 1 - 21$ water clusters and ice, published in 1998 by Burnham, Li, Xantheas & Leslie.[85] In 2002 TTM1-R was extended first to TTM-2R[86] and then later to TTM2F by Burnham & Xantheas.[87] TTM2F was subsequently revised slightly to correct a problem with how the charge is redistributed onto the m-site, resulting in TTM2.1F.[88] TTM3-F was published in 2008 by Fanourgakis & Xantheas.[15] The biggest difference between TTM2F and TTM3F is that TTM2F contains a polarization dipole on each atom while TTM3F only contains a polarization dipole on the m-site. More recently Burnham, Anick,

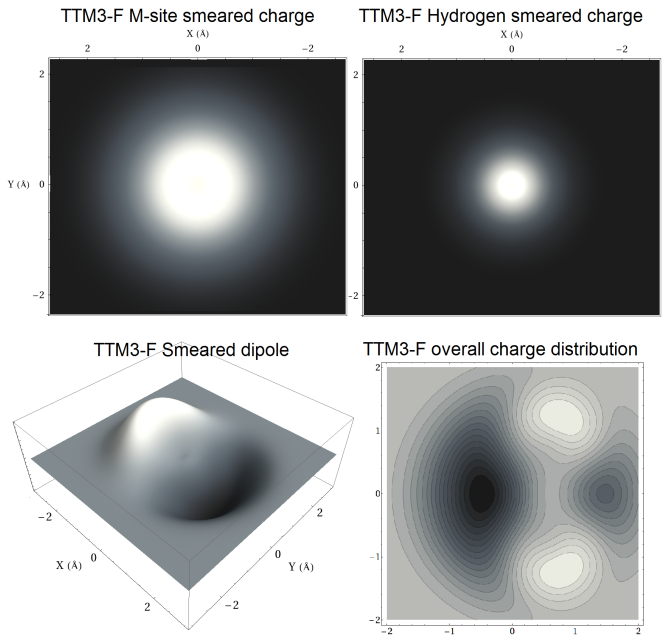

Figure 4.1: Smeared charges, smeared dipole and the total equilibrium charge distribution, plotted by the author in *Mathematica*.

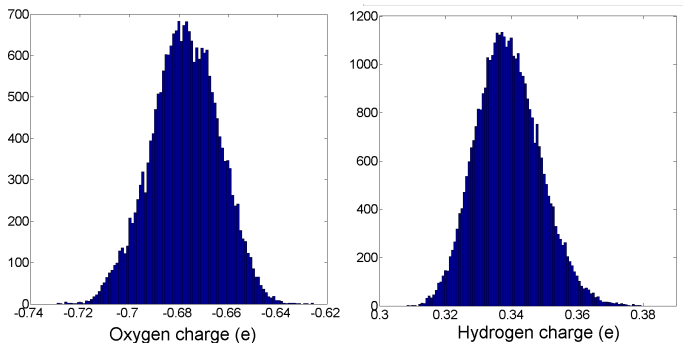

Figure 4.2: Distribution of the fluctuating charges in TTM3F.

Mankoo & Reiter developed TTM4F, which has a different smearing function and several other significant changes.[66] Imoto et. al (2013) study the IR spectra and HOH bond geometry of TTM3F water & ice.[89] In the view of its creators, one of the standout achievements of the TTM3F model is that it is the only empirical (non ab-initio) model which correctly predicts the decrease in the HOH bond angle in water & ice as compared to the angle found in an isolated water molecule.[89][15]

In place of the 6-10-12 potential used in TTM2F, TTM3F uses the "Buckingham exponential-six" potential:

$$U_{pair} = \frac{\varepsilon}{1 - 6/\lambda} \left[\frac{6}{\lambda} e^{\lambda(1-\frac{r}{\sigma})} - \left(\frac{\sigma}{r}\right)^6 \right] \tag{4.17}$$

The total energy of TTM3F can be decomposed as:

$$\begin{aligned} U_{\text{tot}} &= U_{\text{LJ}} + U_{\text{elec}} + U_{\text{pol}} \\ U_{\text{elec}} &= U_{\text{CC}} + U_{\text{CD}} + U_{\text{DD}} \end{aligned} \tag{4.18}$$

Here, the polarization energy is

$$U_{\text{pol}} = \sum_{i=1}^{N} \frac{\mu_i^2}{2\alpha_i} \tag{4.19}$$

Both TTM2-F and TTM3-F use the potential energy surface (PES) and nonlinear dipole moment surface (DMS) developed by Partridge & Schwenke (PS), which is fitted to high precision ab initio and experimental results.[90] The PS model takes the coordinates of a molecule in and returns the potential energies and and effective charges, which are denoted $\{q^{\text{H1}}, q^{\text{O}}, q^{\text{H2}}\}$. However, because the PS PES & DMS were designed for the water monomer, they do not accurately reproduce the liquid PES & DMS, predicting a homolytic (non-charged) dissociation, rather than the charged (ionic) dissociation known to occur in the liquid.[15] In the face of this worrisome feature threatening to derail its use in the liquid, Fanourgakis & Xantheas proceeded to correct it by introducing two linear fitting parameters , d_r and d_θ to be added to the output:

$$\begin{aligned} \tilde{q}^{\text{H1}} &= q^{\text{H1}} + d_r(r_{\text{OH1}} - r_{\text{eq}}) + d_\theta(\theta - \theta_{\text{eq}}) \\ \tilde{q}^{\text{H2}} &= q^{\text{H2}} + d_r(r_{\text{OH2}} - r_{\text{eq}}) + d_\theta(\theta - \theta_{\text{eq}}) \\ \tilde{q}^{\text{O}} &= -\tilde{q}^{\text{H1}} - \tilde{q}^{\text{H2}} \end{aligned} \tag{4.20}$$

These effective charges now need to be re-distributed from { O, H1, H2 } to {

M, H1, H2 }. This is done via:[15]

$$\begin{aligned}\tilde{q}_{\mathrm{H1}} =& \tilde{q}^{\mathrm{H1}} - \frac{\gamma}{2(1-\gamma)}\tilde{q}^{\mathrm{M}} \\ \tilde{q}_{\mathrm{H2}} =& \tilde{q}^{\mathrm{H2}} - \frac{\gamma}{2(1-\gamma)}\tilde{q}^{\mathrm{M}} \\ \tilde{q}_{\mathrm{O}} =& -\tilde{q}_{\mathrm{H1}} - \tilde{q}_{\mathrm{H2}}\end{aligned} \tag{4.21}$$

This effective charge redistribution scheme is repeated each timestep. The use of the DMS means the charges fluctuate, which can be considered an additional source of polarization in the model, in addition to the polarization dipole. However we measured the charge fluctuations to be small (only $\pm 2\%$ at 300 K). We determined that the contribution to the dipole fluctuation from charge fluctuation is about 4 times smaller than the contribution from the polarization dipole at 300 K.

During each timestep the intramolecular forces on the each atom are also calculated from the PS PES & DMS. In the code this is done in the routine "nasa.f90" (the work was done at the NASA Ames Research Center). The calculation of the forces on each atom from the PES is cumbersome but straightforward - details can be found in the appendix of ref. [87].

1. Call PS potential energy and dipole moment surface, get charges and intramolecular energies & forces
2. Calculate intermolecular VdW and electrostatic interactions
3. Calculate charge-charge long range Ewald contribution to energies & forces
4. Solve the matrix equation for the induced dipoles (eq. 2.70) using an iterative technique
5. Calculate dipole-dipole interaction and charge-dipole energies & forces
6. Calculate dipole-dipole and charge-dipole self energies & forces
7. Calculate dipole-dipole long range Ewald contribution to energies & forces
8. Add on a long range VdW correction factor to the total energy
9. Return total energy and forces and dipole moment for each molecule

Thermostat	τ (ps)	Length (ns)	P (bar)	$\varepsilon(0)$
Nosé -Hoover	.01	9	1264	52.5±.5
Nosé -Hoover	1	10	1260	53.1±.5
Nosé -Hoover	100	9	1265	53.6±.5
Berendsen	.01	9	1261	54.0±.6
Berendsen	1	9	1265	53.8±.6
Berendsen	100	10	1367	53.6±.4
F				

Table 4.1: Test thermostating runs at 300 K performed with 512 TIP4P.

4.3 Test for artifacts from thermostating

Gerben et al. claim that changing from a Berendsen to a Nosé-Hoover thermostat results in an increase in $\varepsilon(0)$ of 5%.[91] To see if thermostating has any effect on $\varepsilon(0)$ and $\varepsilon(\omega)$ a series of simulations were run at 300 K with 512 TIP4P molecules using Berendson and Nosé-Hoover thermostats with time constants of $\tau = .01$, 1, and 100 ps. It was observed that all of the simulations maintained their temperatures properly and yielded $\varepsilon(0)$ which were equivalent within their errors (table 4.1). No systematic dependence of $\varepsilon(0)$ on τ was discernible, nor was there any discernible difference between the Berendson & Nosé-Hoover techniques. The previously reported discrepancy of 5 % is likely attributable to improper convergence as their simulations were only 8 ns.[91] When comparing $\varepsilon(\omega)$ for these simulations no noticeable differences were observed even with $\tau = .01$ ps.

Even though thermostating had no effect on $\varepsilon(0)$ or $\varepsilon(\omega)$ it was noticed that the presence of a thermostat did increase the time required for proper convergence compared to an NVE simulation. This is not surprising, especially for the Berendson thermostat which periodically rescales the velocities of molecules, interrupting cooperative fluctuations in $\mathbf{M}$.

4.4 Box size dependence

Whenever one does a computer simulation one should always consider the possibility of finite size effects, especially when using periodic boundary conditions to simulate a non-periodic system. For a system of dipoles on a cubic lattice with PBC and Ewald summation it has been shown that $\varepsilon(0)$ approaches the proper thermodynamic limit from below as $N^{-2/3}$.[92] To see if this is the case in water we ran a series of 20 ns TIP4P simulations at 300 K with 16, 64, 256, 512 and 1000 molecules (fig. 4.3). There was no difference in $\varepsilon(0)$

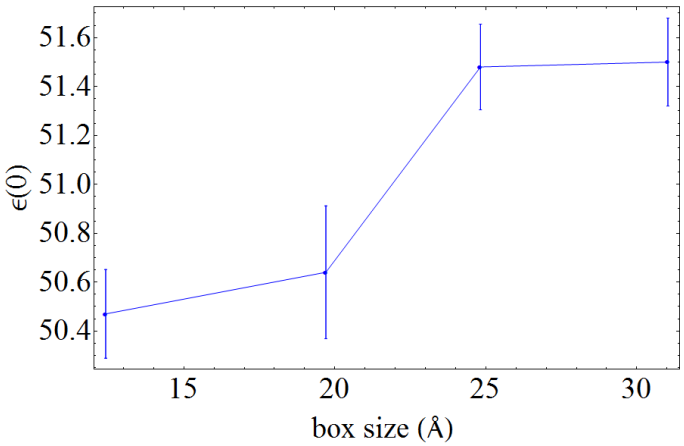

Figure 4.3: $\varepsilon(0)$ vs. box size for TIP4P at 300 K for boxes with 64, 256, 512 and 1000 molecules. Similar results were found when comparing TIP4P/2005 boxes with 64, 512 and 1000 (not shown).

between 512 and 1000 molecules, suggesting 512 is adequate. The convergence does not follow the $N^{-2/3}$ law, but the system appeared to be approaching the thermodynamic limit from below as expected.

4.5 Comparison of three methods for calculating $\varepsilon(0)$

Calculating the dielectric constant of water requires a lot of simulation time, making it difficult to compute with DFT simulation. Even in the case of classical MD, many studies in the literature (especially prior to 2000) do not allow enough time for adequate convergence (ie. to within 10%).[62]) The long convergence times required for water are in contrast to non-hydrogen bonding liquids, such as acetonitrile, where $\varepsilon(0)$ converges in less than 1 ns using the linear response equation.[93] The presence of hydrogen bonding slows down dipolar fluctuations and leads to longer convergence times. On the other hand, as shown in section 4.4, the box size dependence of the dielectric constant is rather small, which is advantageous for DFT. Previous DFT studies that looked at the dielectric constant used either 64 or 32 molecules. Here we compare several methods of computing $\varepsilon(0)$ and quantify the error for 64 molecules by running many simulations with TIP4P/2005. Using 64 water molecules results in an $\varepsilon(0)$ which is artificially , but only by ≈ 5 percent.

Using the traditional linear response equation, the time required for con-

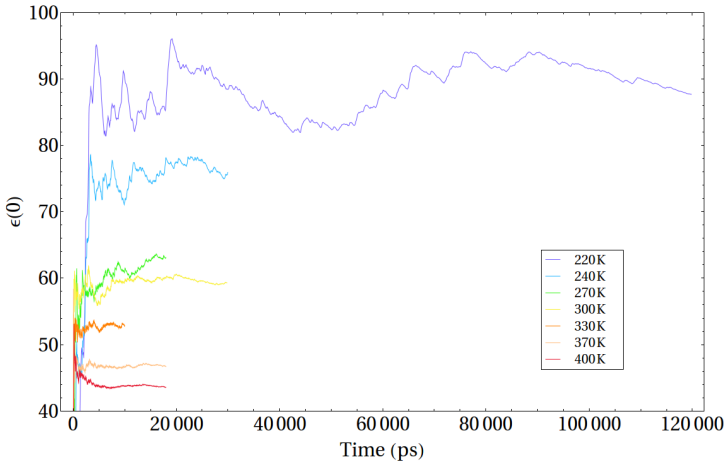

Figure 4.4: Convergence of $\varepsilon(0)$ for 512 TIP4P/2005.

vergence varies dramatically with temperature from 1 - 2 ns at 400 K to 100+ ns at 220 K, as shown in fig. 4.5. Thus, using higher temperatures (ie 350 - 450 K or even higher) can greatly reduce the computational time required to test the accuracy of various functionals.

4.5.1 Method I: linear response equation

Recall the linear response equation for Ewald summation (eqn. 2.62):

$$\begin{aligned} \varepsilon(0) - \varepsilon_\infty &= \frac{1}{3k_B\epsilon_0 TV}\left(\langle \mathbf{M}^2\rangle - \langle \mathbf{M}\rangle^2\right) \\ \boldsymbol{M} &= \sum_i^N \mu_i \end{aligned} \tag{4.22}$$

It is well known that $\varepsilon(0)$ calculated using eqn. 4.22 converges rather slowly. At 300K at least 10 ns are required to yield a value of $\varepsilon(0)$ that is within % 5.[94] The errorbar is best quantified by doing multiple runs and looking at the variance as a function of time, rather than by looking at the running average of a single run. We average 10 simulations of TIP4P/2005 and show the error as a function of time for a 100 ps runs and 50 ns runs are shown in figures. 4.5 and 4.6.

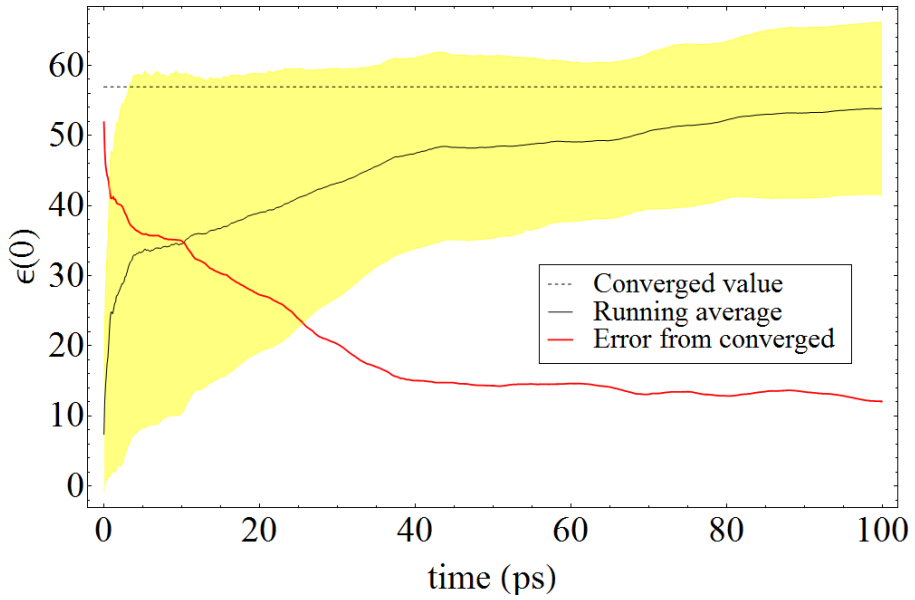

Figure 4.5: Running average for $\varepsilon(0)$ using eqn. 4.22 for 64 TIP4P/2005 at 298 K. Ten simulations were run and the combined running average and standard deviation (yellow) of the runs is shown.

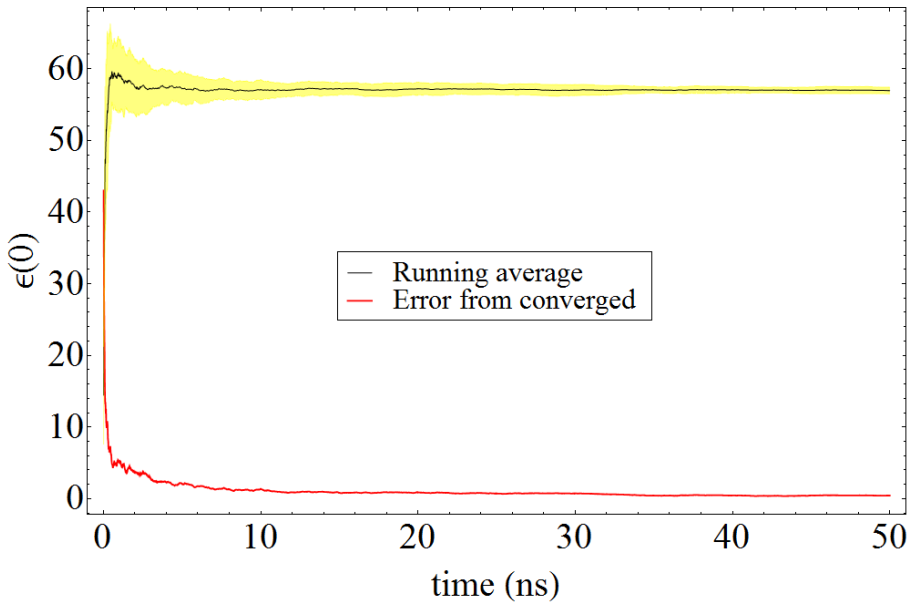

Figure 4.6: Same as figure 4.5 but showing 50 ns. Well converged values can be obtained in 10 ns.

4.5.2 Method II: Kirkwood g-factor

To see the dependence of $\varepsilon(0)$ on dipolar correlation it is useful to recast equation 4.22 as:

$$\varepsilon(0) - \varepsilon_\infty = \frac{N\mu^2}{3k_B\epsilon_0 TV} G_K \tag{4.23}$$

Here G_K is the finite system Kirkwood g-factor (see section 2.4). G_K can be calculated as:

$$G_K = \frac{\left\langle \sum_{i,j} \boldsymbol{\mu}_i \cdot \boldsymbol{\mu}_j \right\rangle}{N\langle \mu^2 \rangle} \tag{4.24}$$

This is equivalent to the integral:

$$G_K(r) = 1 + 4\pi\rho \int_{\text{box}} h_\Delta(r') g_{\text{OO}}(r') r'^2 dr' \tag{4.25}$$

Here $h_\Delta(r)$ gives the average cosine between two dipoles at radius r and g_{OO} is the normal oxygen-oxygen radial distribution function. Note that domain of integration is the entire box.[1]

As shown in figures 4.7 and 4.8 the integration equation should be preferred as it yields a lower error.

Based on these results, somewhat suprisingly, the calculation of $\varepsilon(0)$ to within 5 - 10 percent seems possible with a 20 ps DFT simulation.

The averaging time required to calculate $\varepsilon(0)$ varies with temperature, as can be seen in figures 4.9 (330 K) and 4.10 (370 K)

[1] Expressions with an integral over a spherical volume appear in the literature[95] but are incorrect.

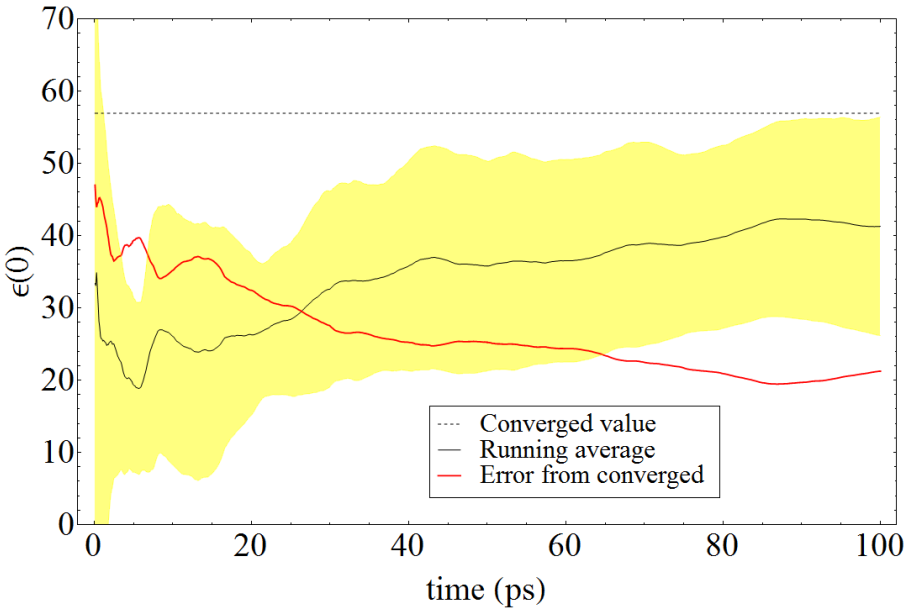

Figure 4.7: Running average of $\varepsilon(0)$ over ten runs calculated from the Kirkwood G-factor (eqn. 4.24).

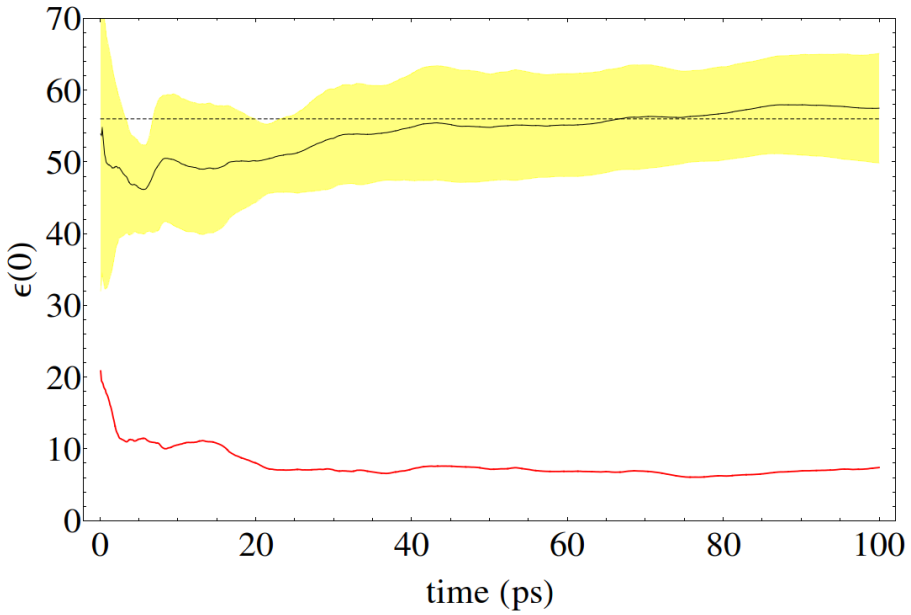

Figure 4.8: Running average of $\varepsilon(0)$ at 298 K over ten runs calculated from the Kirkwood G-factor found using the integration method (eqn. 4.25). Interestingly, this method converges faster.

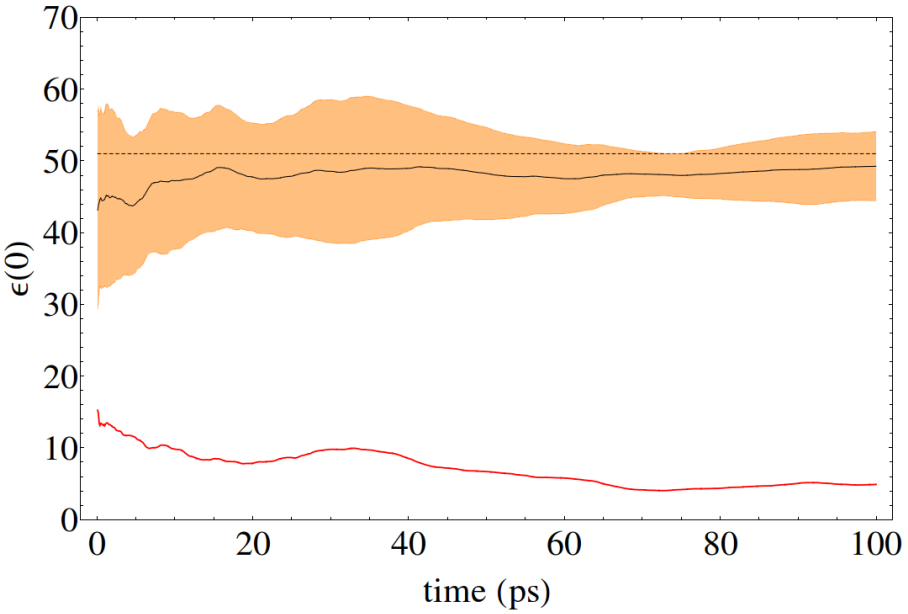

Figure 4.9: Running average of $\varepsilon(0)$ at 330 K over ten runs calculated from the Kirkwood G-factor found using the integration method (eqn. 6.19).

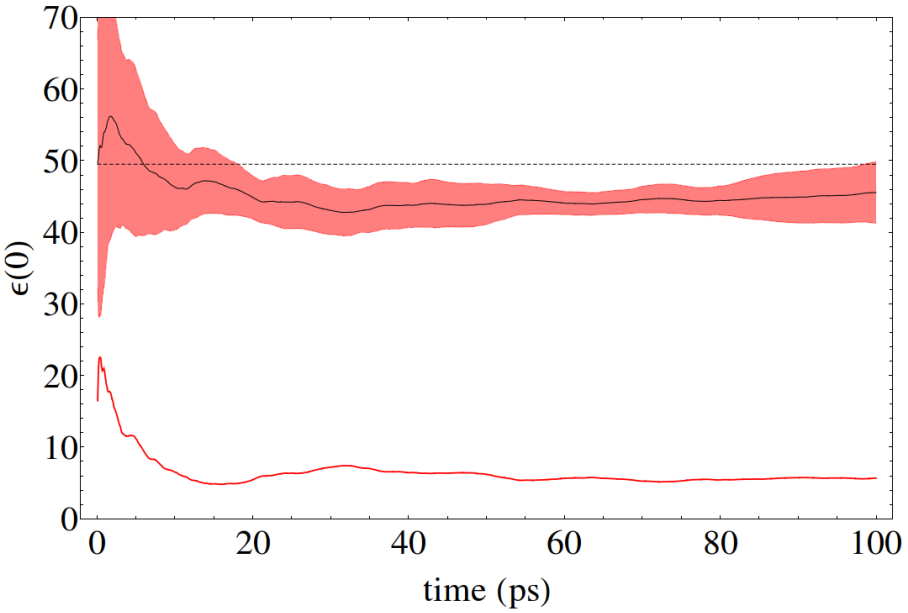

Figure 4.10: Running average of $\varepsilon(0)$ at 370 K over ten runs calculated from the Kirkwood G-factor found using the integration method (eqn. 6.19).

4.5.3 Method III: applied electric field

The third method we considered is to simply use the defining equation of dielectric constant:

$$\boldsymbol{P} = \epsilon_0(\varepsilon(0) - 1)\boldsymbol{E} \tag{4.26}$$

This equation is only valid when $\boldsymbol{\mu} \cdot \boldsymbol{E} \ll k_B T$ since as the electric field increases the response becomes nonlinear (dielectric saturation). We found that the strictly linear regime only holds between 0 - 0.5 V/nm (fig. 4.11). The relaxation time of the system after the field is introduced depends strongly on the strength of the field, as shown in fig. 4.12. Within the linear regime rather long simulations are needed ($>$ 100 ps) to allow for proper relaxation and averaging over the polarization fluctuations of the system. By contrast, at higher electric field strengths ($>$ 1 V/nm) only very short runs ($<$ 10 ps) are needed. Ideally we would like to be able to run several simulations at high electric fields (.5 - 5 V/nm) to extract $\varepsilon(0)$ with the least amount of simulation time.

The $P(E)$ curve is well described by the Langevin function:

$$P(E) = A\left(\coth(BE) - \frac{1}{BE}\right) \tag{4.27}$$

The linear term in the Taylor of expansion of the Langevin function is $AB/3$, which can be used to find $\varepsilon(0)$. A better fit to the full data in fig. 4.11 could only be obtained with a 7th order polynomial. The benefit of the Langevin expression is that it has a theoretical motivation and contains only two fitting parameters. Using all of the data in fig. 4.11 we found $\varepsilon(0) = 51$ for the Langevin function, $\varepsilon(0) = 62$ for the polynomial fit and $\varepsilon(0) = 52$ for the linear fit. The actual value is $\varepsilon(0) = 57$. In conclusion, it does not appear that this method can be made any more efficient than method II, although it is definitely more computationally efficient than method I.

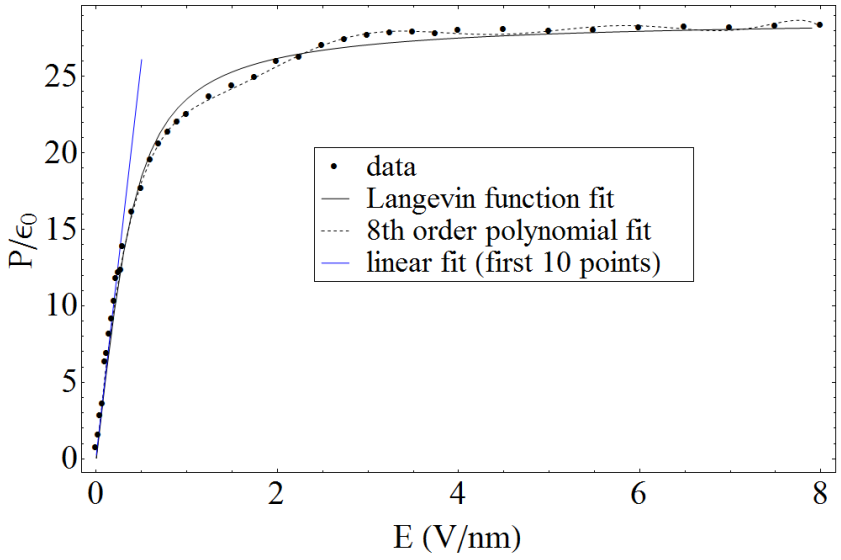

Figure 4.11: P vs E curve for 64 TIP4P/2005 molecules at 298 K. Each simulation was run for 1 ns to ensure adequate convergence of all the points.

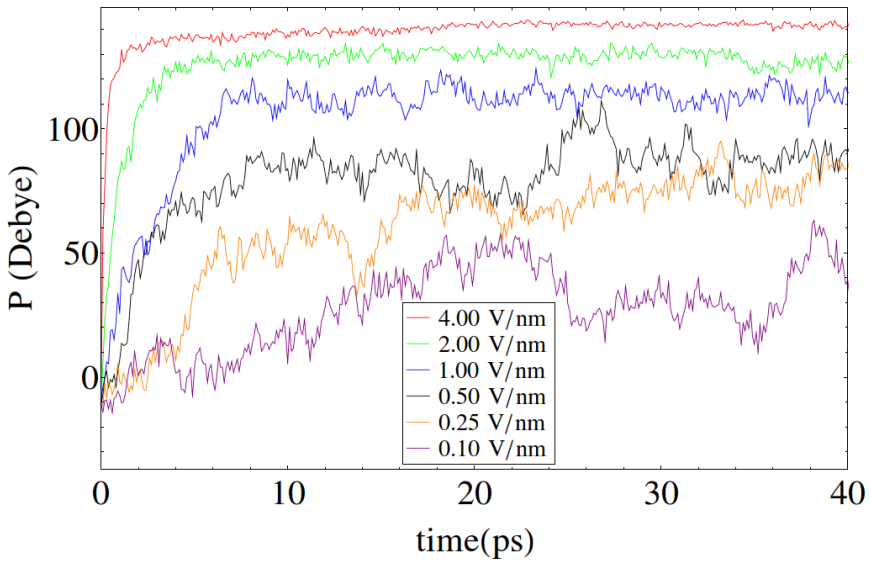

Figure 4.12: Polarization of the box vs time for different electric field strengths for 64 TIP4P/2005 at 298 K. The electric field was in the x-direction so only the x component of the polarization is shown.

4.6 Method of calculating the dielectric function

The dielectric function can be calculated from the total box dipole autocorrelation function $\Phi(t)$ using eqn. 2.107. Time correlation functions of dynamical quantities are known to converge very slowly.[59] For this reason it is essential to fit an exponential to the $\Phi(t)$ obtained from the simulation in order to properly calculate the long time part when computing $\varepsilon(\omega)$. To prevent artifacts in $\varepsilon(\omega)$ due to poor joining of the data and fit we used a cubic spline with a length of ≈ 1 ps. The short time parts (0 - .5 ps) of $\Phi(t)$ exhibit a rapid decrease and oscillatory behavior due to rapid librational and vibrational motions. To preserve these features, the spline must be started after 5 ps. Even with a spline we found that the joining of the fit introduces noise in $\varepsilon(\omega)$ in the range 10^{13} to 10^{14} Hz. This noise can be reduced by increasing or decreasing the length of the smoothing spline but is hard to eliminate completely. Similar noise appears in the $\varepsilon(\omega)$ plots of van der Spoel, et al.[62]

4.7 Conclusion

In section 4.5 we compared three methods for computing the dielectric constant. Somewhat counter-intuitively, the amount of simulation time required varies significantly depending on the method employed. We found that method II, using the Kirkwood g-factor G_K, requires significantly less simulation time to compute $\varepsilon(0)$. Convergence to 1% still takes 1+ ns, but convergence to 5% can be done in ≈ 20 ps. Method III, applying an electric field, was less efficient than method II but more efficient than method I, the traditional linear response method. Of the two methods we compared to compute G_K, the integration method was the most efficient. It is therefore no surprise that this was precisely the method used by Sharma, et al. [96] to calculate $\varepsilon(0)$ from DFT simulation, which is one of the only studies to do so. From only 20 ps of simulation with the PBE functional they found $\varepsilon(0) = 67 \pm 6$ at 330 K, in agreement with the experimental value of 68 at 330 K. We performed an identical analysis with TIP4P/2005f at 330 K (see fig. 4.9) and found a very similar error bar (± 8 for 20 ps), confirming that their error bar is indeed appropriate. These findings are good news for DFT practitioners and open the door to comparing the dielectric constants of different DFT functionals, something which has not yet been done.

Before closing this chapter we should discuss the recent work of Zhang & Sprik (2015),citePhysRevB.93.144201 who calculate the dielectric constant at constant dielectric displacement. They criticize method III, since it requires

carefully fitting the non-linearity of the response. Recall equation 2.12 which says that the longitudinal dielectric susceptibility relates $\boldsymbol{P}$ to $\boldsymbol{D}$. The Debye LST relation (eqn. 7.33) indicates that longitudinal fluctuations are faster than transverse by a factor of $\varepsilon(0)/\varepsilon_\infty$. Since the longitudinal susceptibility at $k = 0$ is related to the dielectric constant, by simulating at constant $\boldsymbol{D}$, in principle one can calculate ε faster. Such an approach has been discussed by Vanderbilt and others in their development of the modern theory of polarization. Zhang & Sprik show that there is an increase in efficiency, but only a modest one, and not one that justifies the difficulty of implementing their method rather than method II (using G_k).[97]

Chapter 5

Comparison of rigid, flexible, & polarizable models

In this chapter we study what the effects of water model geometry, flexibility and polarization are on the dielectric constant & dielectric function. The usefulness of adding flexibility to water models has been investigated before with mixed results,[98, 99, 100, 101, 102] and many polarizable models have likewise been created and investigated.[103, 104, 105, 106, 107, 108, 109, 110, 111, 112, 113] Critical comparisons of rigid vs. flexible and/or polarizable models have been done before with a focus on reproducing the density anomaly,[114] IR spectra,[115] water clusters,[116] and H-bond dynamics.[117] To perform our comparison we choose three models with similar geometries - the rigid and flexible versions of TIP4P/2005 and TTM3F, which is flexible and polarizable.

5.1 General overview of water models

Typically empirical models are optimized to reproduce experimental values for easily computable quantities such as the density, enthalpy of vaporization, the location of peaks in radial distribution functions and possibly one or two other variables. These optimizations have led to a considerable range of dielectric constants, as shown in table 5.1. Reparametrization to fix the dielectric constant has been done for SPC/E[94] and TIP4Q.[118] Recently Fennell, et. al. reparametrized the SPC/E model to better reproduce the dielectric constant at 298 K. To do this required increasing the dipole moment about 7%. A similar re-parametrization was done to the TIP4Q model, requiring a 12% increase in dipole moment.[118]

# sites	model	$\mu(D)$	$Q_T(D\text{Å})$	$\varepsilon(0)$	$\varepsilon(0)/\mu^2$	τ_D (ps)	τ_s(ps)	g_K	$\frac{d\varepsilon}{dT}\|_{300K}$ (K^{-1})	refs
1	uAMEOBA	1.802	2.803	76(1)						[119]
	SSD	2.35		76(3)						[120, 121, 122]
	SPC	2.274	1.969	65(2)	12.69	11(1)	5.0(5)	2.6	.09(1)	[94, 100, 123]
	SPC/E	2.351	2.038	74(2)	12.86	11(1)		2.7	.09(1)	[94, 100, 123, 100]
	SPC/DC	2.42		78(6)	13.69				.09(1)	[94]
	SPC/fw	2.39	2.017	78(2)	13.67	9.50		2.67		[124, 100]
3	SPC/Fd	2.47		102(3)	16.68	11.23		3.26		[100]
	q-SPC/Fw	2.465		90(3)	14.81					[?]
	TIP3P	2.347	1.720	97(5)	17.06	5.91		3.58	7.3(7)	[125, 100, 123]
	TIP3P/Fs	2.57		194(5)	29.24	16.08		5.53		[100]
	NEMO^p	2.9		90(4)	10.70	18(2)	9(2)	3		[126]
	F3C	2.46		102(3)	15.44	11.9		3.27		[100]
	ST2	2.353		72(10)	13.00					[127]
	MCY	2.19		46(11)	7.14	3.8		1.38	.06	[128, 110]
	MCYna	2.92		71(4)	8.15					[110]
	TIP4P	2.18	2.345	51(3)	10.84	6.32			.19(1)	[125, 129]
	TIP4P-Ew	2.32		63(9)	11.68				.23(1)	[130]
	TIP4Q	2.44		81(2)	13.54					[118]
4	TIP4P/2005	2.305	2.514	62(4)	11.37				.2(1)	[131, 130]
	TIP4P/2005f	2.319	2.561	56(4)	10.28	12		2.14	.2(1)	[132]
	TTM2F	2.66		78(7)						[16]
	TTM2.1-F	2.67		67	9.43					[88]
	TTM3F	2.75	1.986	94	8.95	12			.46	[15]
	TTM4F	2.81		72(11)						[16]
	AMEOBA	1.808	2.408	81.4(1)						[111, 119]
5	TIP5P	2.29	1.565	87(5)	15.63	7		3.22	.31(1)	[125, 133, 14, 134]
	TIP5P-Ew	2.29		92(14)	17.94				.30(1)	[14]
-	Expt.	2.95[21, 18]	2.565*[135]	78.6[?]	9.02	8.3[6, 100]	≈ 1	1.77	.40 [?]	

Table 5.1: Dielectric properties for some popular empirical water models at 298/300 K. Where multiple values for something were available, they were averaged. Numbers in parenthesis refer to the estimated error in the last reported digit. The magnitude of the quadruple moment for water is well quantified by the tetrahedral quadrupole moment $Q_T = 1/2(|Q_{\text{xx}}|+|Q_{\text{yy}}|)$.[14] The ST2 $\varepsilon(0)$ value was extrapolated from 373 K. *The experimental value for Q_T is for the gas phase geometry, as liquid phase quadrupole data from experiment does not seem to be available.

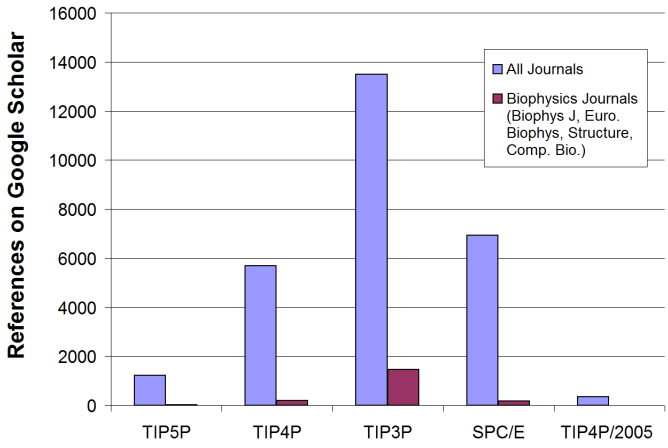

Figure 5.1: The popularity of various water models, based on a keyword search of journal articles on Google Scholar. The 3-site models TIP3P and SPC/E are predominant in biophysics since they're slightly more computationally efficient. However, they poorly capture the dielectric properties (and phase diagram) compared to 4-site models.

5.1.1 Sensitivity to water model geometry

The degree of dipole correlation and resulting $\varepsilon(0)$ is extremely sensitive to the equilibrium bond angle $\theta^{\text{eq}}_{\text{HOH}}$ and r_{OH} distance. These two parameters, along with the hydrogen charge q_{H} determine the dipole moment and quadrupole moment of the molecule for a three site model. Four and five site models contain additional geometric parameters. In general $\varepsilon(0)$ increases as μ^2 and decreases with an increasing quadrupole moment Q_T, which disrupts dipole-dipole correlations.[14] To a very good approximation the quadrupole tensor of water can be represented as a tetrahedral quadrupole (fig. 5.2) of the form

$$\boldsymbol{Q}_T = \begin{bmatrix} -Q_T & 0 & 0 \\ 0 & Q_T & 0 \\ 0 & 0 & 0 \end{bmatrix} \tag{5.1}$$

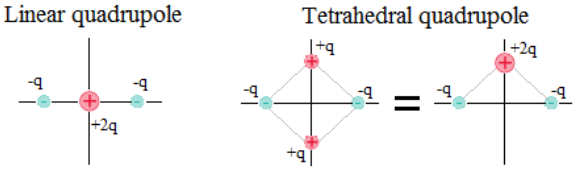

Figure 5.2: The linear and tetrahedral quadrupoles.

For a system of hard spheres with point dipoles and point quadrupoles analytic theory shows that the tetrahedral quadrupole is more effective than the linear quadrupole at suppressing dipolar correlations.[136] Increasing r_{OH} increases both the dipole moment and quadrupole moment, leading to only modest increases in $\varepsilon(0)$, since these changes act in opposite directions. Increasing $\theta^{\mathrm{eq}}_{\mathrm{HOH}}$ decreases the dipole moment and increases the quadrupole moment, both of which act in the same direction to decrease $\varepsilon(0)$. Increasing $\theta^{\mathrm{eq}}_{\mathrm{HOH}}$ also reduces the degree to which the H-bonded shells contribute to $\varepsilon(0)$ (see eqn. 3.29), which further decreases the dielectric constant. Overall, the differences in dielectric constant between rigid models can be largely accounted for by differences in θ_{HOH} and q_{H}.[123] It is important to bear in mind that even small changes in $\theta^{\mathrm{eq}}_{\mathrm{HOH}}$ and q_{H} can have a larger effect on $\varepsilon(0)$ than the introduction of flexibility or polarizability to a model.

5.2 Details of the simulations that were run

To determine the effect of flexibility we choose to compare the TIP4P/2005 model of Abascal & Vega[131] and the TIP4P/2005f model of Gonzalez & Abascal.[132] Although its value for $\varepsilon(0)$ is less accurate than other more popular empirical models (like SPC/E or TIP4P) TIP4P/2005 was recently scored as best overall among five popular rigid models.[125] In particular, it is better at reproducing the liquid structure, density-temperature curve and phase diagram. Although the value of $\varepsilon(0)$ of TIP4P/2005 is not as good as other models, it more accurately describes the variation of the dielectric constant with temperature (table 5.1).

Our TIP4P/2005 simulations were performed with the GROMACS molecular dynamics package (versions 3.3.3 and 4.5.5).[137] All of our GROMACS runs used a Nosé-Hoover thermostat with $\tau = 1$ ps or $\tau = .1$ ps. For rigid simulations we used a timestep of 2 fs and for flexible simulations we used a timestep of .5 fs. The GROMACS simulations with 512 molecules (used for all dielectric constant calculations) employed a Coulomb cutoff of 1.2 nm and a shifted VdW cutoff of 1.1 nm. For the long range part of the Coulomb interaction particle mesh Ewald (PME) was employed.

For a polarizable model we choose the TTM3F model of Fanourgakis & Xantheas, the details of which were discussed in section4.2.[15] It is a four site model, so it has a similar geometry to TIP4P/2005. Our TTM3F runs used a Nosé-Hoover thermostat with $\tau = .1$ ps, a timestep of .5 fs and Coulomb and VdW cutoffs of .7 nm. The VdW cutoff was switched off using the "GROMACS switch"[138] and long range VdW corrections to the energy were applied. Ewald summation was used, where the smeared dipoles and charges are

considered as point dipoles and point charges. The polarization dipole was calculated using a convergence tolerance of 10^{-5} D per molecule. A fourth order predictor was used to provide the first guess for each iteration, reducing the number of required iterations per timestep from 15 to 2 - 3.

We ran all of our simulations in the NVT ensemble. We decided not to use a barostat largely for simplicity but also to prevent the possibility of the barostat interfering with the dynamics of the system. The NVT ensemble also allows us to analyse the effects from changes in density and effects from changes in temperature separately.

5.3 Dielectric constant

Figure 5.3 shows the dielectric constants of the three models. Detailed data is presented in table 5.3. In all cases the errors are calculated by finding the RMS variation of the running value of $\varepsilon(0)$ during the later half of the simulation. To simulate at $\rho = .9$ kg/L, a Parrinello-Rahman barostat was employed to prevent the formation of cavities. The density .9 kg/L is of interest because it is close to the density of low density amorphous ice (LDA). The experimental $\varepsilon(0)$ values along the 1.00 kg/L and 1.20 kg/L isochores shown in fig. 5.3 are taken from the $\varepsilon(0)$ vs. pressure tables developed by Uematsu and Frank.[3] The dependence of $\varepsilon(0)$ on pressure is very close to linear, so a linear extrapolation of the Uematsu & Frank data was used to estimate $\varepsilon(0)$ at 1.2 kg/L. The pressure required to achieve 1.0 kg/L or 1.2 kg/L at different temperatures were taken from the ASME Steam Tables based on the IAPWS-1997 formulation,[139] which are freely accessible at wolframalpha.com. We also plotted experimental data taken along the 1 bar isobar.[**?** 1]

At all state points the dielectric constant of TIP4P/2005 is nearly equal to that of TI4P/2005f. This lack of change should be contrasted with the changes in $\varepsilon(0)$ observed in flexible versions of the SPC model. The flexible model of Wu, Tepper & Wolf (SPC/Fw) yields a dielectric constant which is 23% larger than SPC at STP,[124] and the flexible model of Dang & Pettit (SPC/Fd) yields a dielectric constant which is 54% larger.[100]

In developing TIP4P/2005f, the flexibility was added in a careful manner to ensure that the geometry of TIP4P/2005 was well preserved. The percent differences in the liquid HOH angle and r_{OH} distance are only .26 % and 1 %.[132][1] In the SPC/Fw model of Wu et al. the flexibility was parametrized specifically to reproduce the experimental $\varepsilon(0)$ and diffusion constant D_s. As a result of this SPC/Fw has a smaller liquid phase $\theta^{\mathrm{eq}}_{\mathrm{HOH}}$ (107.7° vs. 109.47°)

[1]The only other change they made was to make the Leonard-Jones σ parameter in TIP4P/2005f a little bit (.002%) smaller.

system	ρ (kg/L)	T (K)	P (bar)	length (ns)	$\varepsilon(0)$	% chg	τ_D (ps)	τ_s (ps)
		220	1035	120	88 ±3		535	271
		240	805	30	76 ±1		125	59
		270	333	30	63.8±.7		26	13
512 TIP4P/2005	1.00	300	512	30	59.3±.4		13	6.0
		330	881	10	52.8±.3		5.8	3.2
		370	1452	18	46.7±.2		3.2	1.9
		400	1983	18	43.6±.1		2.3	1.4
		220	6105	60	98.7±.2	12.1	76	46
		240	6562	24	93.8±1	23.4	44	24
		270	7307	15	78.4±.9	22.9	15	8.2
512 TIP4P/2005	1.2	300	8134	12	72.4±.40	22.1	8	4.3
		330	9025	10	65.0±.3	23.1	7.6	4.3
		370	10303	10	57.1±.1	22.1	2.7	1.5
		400	11300	8	52.7±.1	20.8	2.0	1.1
		220	1223	100	±2		280	
		240	795	30	69.8±.4		124	
		270	498	20	63.6±.7		30	16.7
512 TIP4P/2005f	1.00	300	545	20	58.8±.42		12	6.4
		330	815	20	51.8±.3		5.9	3.4
		370	1392	20	45.1±.1		3.0	1.9
		400	1921	20	42.0±.2		2.1	1.4
		240	6680	24	88.8±.7	27.2		
		270	7406	15	75.2±.7	18.2		
		300	8203	12	70.8±.5	20.4		
512 TIP4P/2005	1.2	330	9076	10	63.7±.4	23.0		
		370	10325	10	55.3±.1	22.6		
		400	11309	8	52.3±.1	24.5		
		220	803		137±4			143
		240	450	43	134±2		108	53
		270	200	40	108±2		26	
128 TTM3F	1.00	300	150	30	94.4±.4		12	5.7
		330	312	10	84 ±1		6.4	3.1
		370	695	27	69.3±.2		3.1	1.9
		400	1083	10	61.7±.2		2.1	1.2
		220	5866	30	197±3	34	89	51
		240	6242	19	170±3	26	31	18
		270	6808	3	139±2	28	13	6.6
128 TTM3F	1.20	300	7441	24	124±.5	31	6.4	3.6
		330	8083	9	109±.5	31	4.0	2.2
		370	9066	10	93.0 ±.3	34	2.3	1.4
		400	9830	9	83.6 ±.5	35	1.7	1.2
		240	500	54	68	-1.0		
		270	500	30	63	-1.4		
512 TIP4P/2005	.9	300	500	12	55	-6.3		
		330	500	10	51	-1.1		
		330	500	30	52.2±.2	-.02		
512 TIP4P/2005	.9965	300	-82	2.0	58.3±4			
512 TIP4P/2005	.9581	370	670	.5	41.3±5			
512 TIP4P/2005	.9014	450	566	.5	33.7±3			
1000 SPC/E	1.004	300	242	20	71.8±1			

Table 5.2: Details of the simulations. "% change" refers to the change in $\varepsilon(0)$ from 1.0 kg/ L.

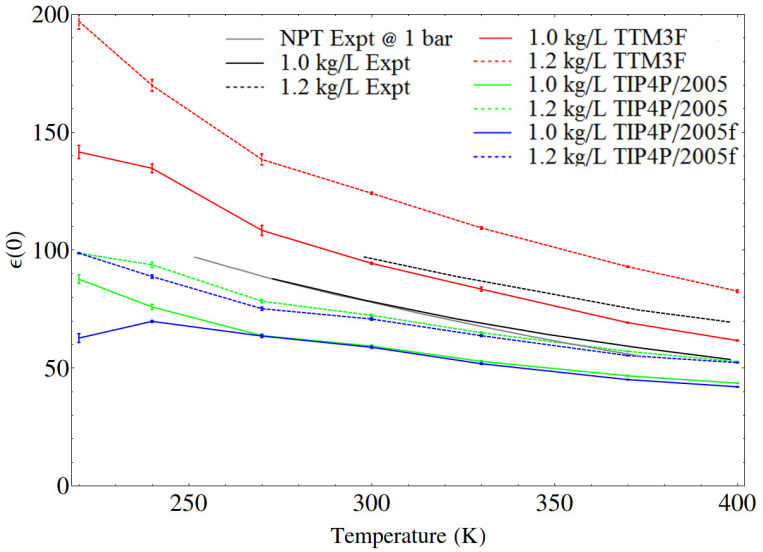

Figure 5.3: Dielectric constants for TIP4P/2005, TIP4P/2005f and TTM3F at 1 kg/L and 1.2 kg/L. The experimental values along the 1.0 kg/L isochore were taken by interpolating the tables given by Uematsu and Frank.[3] The experimental values at 1.2 kg/L were obtained by extrapolating the same tables to higher pressure.

and a longer r_{OH}, changes of 1.6% and 4 %. This resulted in SPC/Fw having a larger average dipole moment ($2.39D$ vs. $2.275D$ - an increase of 5 %). The same is true in SPC/Fd, but to an even greater extent, yielding a dipole of $2.47D$. By contrast the average dipole of TIP4P/2005f is only slightly larger than that of TIP4P/2005 ($2.319D$ vs. $2.305D$ - an increase of .6 %). Another difference is that the HOH bending potential in both SPC/Fw and SPC/Fd allow greater flexibility, since the coefficient K_θ is 14% smaller in both models.

TTM3F has a larger dielectric constant than TIP4P/2005, despite having a slightly larger θ_{HOH} angle (105.13° vs 104.52°), which by itself would decrease the dielectric constant by a few percent.[100] The increase is clearly due to a larger overall dipole moment and greater dipole-dipole correlation (discussed in chapter 6).

Increasing the density increases $\varepsilon(0)$ as can clearly be seen from equation 4.23. Table 5.3 shows the percentage increase in $\varepsilon(0)$ for the three models when the density is increased to 1.20 kg/L. For both rigid and flexible TIP4P/2005 the increase is around 22% at nearly all temperatures. From equation 4.23 one sees that this linear increase with density is consistent with G_K not increasing with density. With TTM3F, the increase is significantly larger than 20%, indicating that G_K increases with density. Although TTM3F overesti-

	Temperature (K)					
	240	270	300	330	370	400
TIP4P/2005	23	23	22	23	22	21
TIP4P/2005f	27	18	20	23	23	25
TTM3F	31	28	31	31	34	35
Expt	-	-	23	26	27	30

Table 5.3: Percentage increase in dielectric constant going from 1 kg/ L to 1.2 kg / L.

mates this increase when compared to experiment, it captures the temperature dependence of the increase correctly.

5.3.1 Dipole moments

density (kg/L)	0.80	1.00	1.05	1.10	1.15	1.20	% diff. (1→1.2)
TIP4P/2005f dipole		2.319±0.14				2.323±0.14	.1
TTM3F total dipole	2.738±0.18	2.750±0.19	2.763±0.21	2.769±0.22	2.780±0.23	2.785±0.24	1.2
TTM3F polarization dipole	0.817±0.15	0.827±0.16	0.839±0.16	0.844±0.16	0.854±0.16	0.857±0.16	3.6
TTM3F geometric dipole	1.921	1.922	1.924	1.925	1.927	1.927	.2

Table 5.4: Average dipole moments and their standard deviations for TIP4P/2005f and TTM3F.

Table 5.3.1 shows the average dipole moments of TIP4P/2005f and TTM3F at several different densities. The increase in going from a density of 1 to 1.2 kg/L is summarized in the last column. The increase in the dipole moment of TTM3F with density is almost completely due to an increase in the polarization dipole. The total dipole vs temperature is plotted in fig. 5.4.

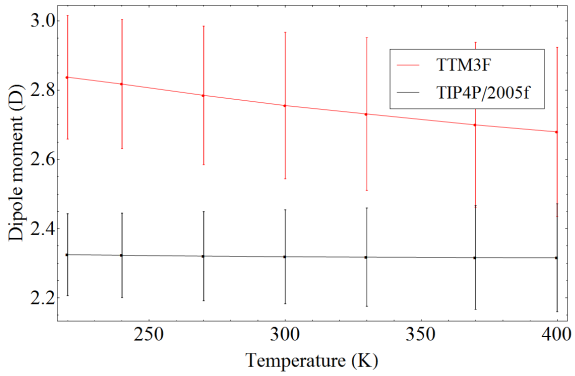

Figure 5.4: Average dipole moments for TTM3F and TIP4P/2005f vs. temperature at a fixed density of 1 kg/L. The bars show the standard deviations of the dipole moment distributions. The addition of polarization leads to a temperature dependent dipole moment, even when the density is fixed.

5.3.2 Temperature derivative of $\varepsilon(0)$

The temperature derivative of $\varepsilon(0)$ is an important quantity which has been largely neglected in studies of water models. The temperature derivative is directly proportional to the change in entropy of the liquid under the application of an electric field.[68][140] Thus an accurate value of $d\varepsilon(0)/dT$ is important for capturing the change in the entropy (ordering) of the liquid around ions and predicting the solvation free energy of charged species.[140] For this reason $d\varepsilon(0)/dT$ at 298/300K is compared for some popular water models in table 5.1. Interestingly, SPC/E greatly underestimates $d\varepsilon(0)/dT$ while TIP3P overestimates it. SPC/E and TIP3P have a 90% market share in the biophysics community (based on keyword searches of popular biophysics journals using Google Scholar). Of the water models listed, TTM3F most accurately captures the slope at 300 K.

It is also useful to look at the temperature dependence of G_K when comparing the models (see figure 5.5). All three models overestimate the degree of correlation but TTM3F yields the correct monotonic decrease in G_K with increasing temperature, while TIP4P/2005 and TIP4P/2005f show an unphysical increase in G_K with temperature between 240 and 300 K and then little change at higher temperatures. TTM3F exhibits temperature dependence of μ even at fixed density, as shown in figure 5.4. This is likely the distinguishing factor which allows TTM3F to have a better temperature derivative compared to the other models.

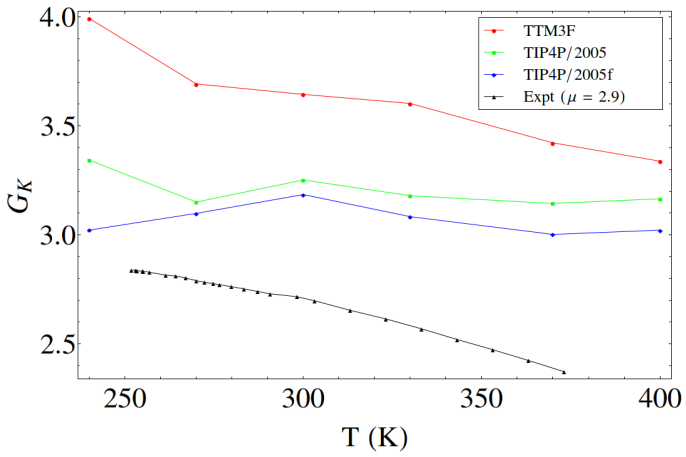

Figure 5.5: $G_K(r)$ for the models at different temperatures, calculated using $\varepsilon(0)(T)$ and $\mu(T)$. The experimental data was calculated using experimental $\varepsilon(0)$[**?** 1] using eqn. 4.23 and $\mu = 2.9$.

5.4 Dielectric function

Figure 5.6 shows the real and imaginary dielectric functions. The experimental points between 50 - 33,333 cm^{-1} (1.5×10^{11} - 10^{15} Hz) is derived from index of refraction data using the relation $\varepsilon(\omega) = n^2(\omega)$.[9] Of particular interest is the the feature centered at 180-200 cm^{-1} which is most clearly present in $\varepsilon''(\omega)$. Neumann noted that this feature is absent in the dielectric spectra of TIP4P and proposed that it must be due to polarization effects.[129] Raman and FIR spectra of water also show a band between 170-190 cm^{-1}.[141, 142, 143, 144] The exact nature of the 180 cm^{-1} Raman band has been the subject of some controversy.[142] The prevailing view is that it is due to the stretching vibrations of nearly-linear hydrogen bonds.[2] If the feature at 180-200 cm^{-1} is indeed due to the stretching of hydrogen bonds, then it will only appear in $\varepsilon(\omega)$ if polarization is included, as the geometric dipoles of two H-bonded molecules do not change during H-bond stretching. Indeed, the TTM3F spectrum shows a shallow peak in this region, while the flexible TIP4P/2005 shows nothing. The fact that the TTM3F peak is smaller than experiment makes sense considering that the hydrogens are not polarizable in TTM3F and the only polarization dipole is located on the m-site. At high frequencies we see that both TTM3F and TIP4P/2005f do a good job of reproducing the librational resonances and the bending (v_2) and symmetric

[2] In support of this view, the 170 cm^{-1} (and 60 cm^{-1} feature) show only small shifts with deuterium substitution (2-3 cm^{-1}) and larger shifts (10 cm^{-1}) with ^{18}O substitution.[142]

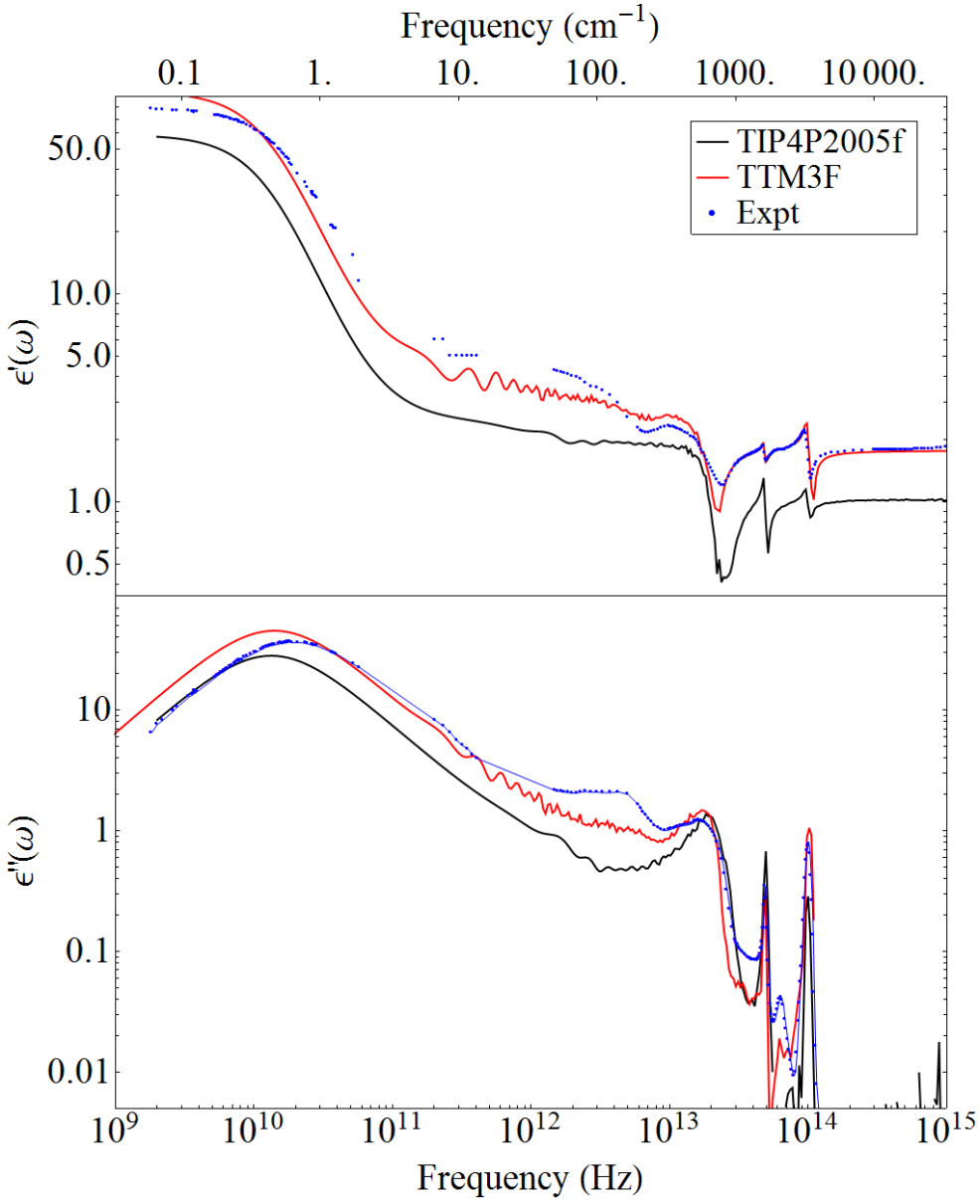

Figure 5.6: Real part (top) and imaginary part (bottom) of the dielectric spectra at 300 K. The region between 10 to 100 cm^{-1} is plagued by noise from the fitting process.

& antisymmetric modes ($v_1 + v_3$), with TTM3F performing noticeably better in reproducing $\varepsilon''(\omega)$. Using the Clausius-Mossotti equation we calculated ε_∞ for TTM3F to be 1.76 using the polarizability of the polarization dipole only. The molecular polarizability from flexibility was estimated by calculating the change in dipole due to bending in an electric field oriented along the HOH bisector. For TIP4P/2005f we found $\varepsilon_\infty \approx 1.04$.

5.5 Conclusion

Our results indicate that the addition of flexibility to a model, when no other reparameterizations are done, has little effect on the dielectric properties except at high frequencies. The effect of reparametrization of a flexible model, which results in changes to the model geometry, has a larger effect than the flexibility itself. The introduction of polarization, however, does have a significant effect in several regards. Firstly, it introduces significant temperature and density dependence to the the dipole moment resulting in better values for $d\varepsilon(0)/dT$ and $d\varepsilon(0)/dV$. An accurate value for $d\varepsilon(0)/dT$ ensures that the entropy change in an electric field is described accurately, even at fixed temperature. Secondly, polarization causes H-bonding features to appear in the dielectric function, especially the 200 cm^{-1} H-bond stretching and 60 cm^{-1} H-bond bending peaks.

Chapter 6

Dipole-dipole spatial correlation

In the first half of this chapter we discuss different correlation functions that can be used to quantify dipole-dipole spatial correlation. We discuss the presence of artificial enhancement in long range dipole-dipole correlation that arises from the artificial periodicity imposed on the system from the use of periodic boundary conditions and Ewald summation. This artifact, which is usually quite subtle, is largely unknown to most researchers in the field. In the second half of this chapter we calculate various spatial correlation functions and compare several rigid models with our flexible and polarizable models of choice, TIP4P/2005f and TTM3F. We find important differences between polarizable and nonpolarizable models, especially in the temperature dependence of dipole-dipole spatial correlations.

6.1 Introduction

Fully capturing the correlations between molecules requires calculating the full pair correlation function $g(1,2)$ which has (for a rigid non-linear molecules) seven dimensions - a distance r and three angles for each molecule (for instance, Euler angles). Visualization of this full correlation function has actually been attempted, but the results are not very enlightening unless one is interested in looking at the fine details of the shell structure of water.[61] Since seven dimensional spaces are impossible for humans to visualize, some reduction of dimensions is called for. The first obvious reduction is only consider the directions of the dipole moments of the molecules - the resulting function $g_d(1,2)$ is then five dimensional. As a next step it is possible to expand $g_d(1,2)$ in terms of either Wigner rotation matrices or spherical harmonics - this is rather complicated, but is necessary to properly compare with some experiments.[145] Spherical harmonic correlation functions are also extracted

by Soper (1994) from partial structure factors, allowing for extraction of the density of molecules in the first shell as a function of angle.[146] If we switch to considering the relative orientations between molecules (assume isotropy) and ignore one azimuthal angle, then we can reduce the number of variables to four (r, θ_1, θ_2 and ϕ), which are sufficient to calculate the dipole-dipole interaction energy. Using Matthias & Tavan's notation, we designate this set of angular variables as $\Omega \equiv (\theta_1, \theta_2, \phi)$.[4] In their analysis of dipolar correlation Matthias & Tavan use a basis introduced by Wertheim:[147]

$$\begin{aligned} S &\equiv 1 \\ \Delta &\equiv \hat{\mathbf{p}}_1 \cdot \hat{\mathbf{p}}_2 \\ D &\equiv 3(\hat{\mathbf{p}}_1 \cdot \hat{r})(\hat{\mathbf{p}}_2 \cdot \hat{r}) - \hat{\mathbf{p}}_1 \cdot \hat{\mathbf{p}}_2 \end{aligned} \tag{6.1}$$

These functions are basis functions under the inner product operator $\langle \quad \rangle_\Omega$, which is an angular average over Ω. If Cartesian coordinates are used, then these functions are orthogonal in the sense that $\langle S\Delta \rangle_\Omega = \langle SD \rangle_\Omega = \langle \Delta D \rangle_\Omega = 0$ but they are not orthonormal ($\langle S^2 \rangle_\Omega = 1$, $\langle \Delta^2 \rangle_\Omega = 1/3$, $\langle D^2 \rangle_\Omega = 2/3$).[4]

6.2 1D correlation functions

In this section we introduce several 1D correlation functions. The first we call the "cosine function", which simply gives the average cosine of the angle between the dipole moments of two molecules as a function of r:

$$\phi_\Delta(r) = \langle \cos(\theta) \rangle(r) = \frac{1}{N_r} \sum_{i,j}{}' \frac{\boldsymbol{\mu}_i \cdot \boldsymbol{\mu}_j}{|\boldsymbol{\mu}_i||\boldsymbol{\mu}_j|} \quad r < r_{ij} < r + \Delta r \tag{6.2}$$

The prime on the summation indicates that we do not include $i = j$. Here N_r is the number of molecules of molecules found in the shell between r and $r + \Delta$. In everything that follows, angle brackets indicate an ensemble average.

Another 1D correlation function is based on the angular part of the interaction energy:

$$\begin{aligned} D &= 3(\boldsymbol{\mu}_1 \cdot \hat{\boldsymbol{r}})(\boldsymbol{\mu}_1 \cdot \hat{\boldsymbol{r}}) - \boldsymbol{\mu}_1 \cdot \boldsymbol{\mu}_2 \\ \phi_D(r) &= \langle D \rangle(r) \end{aligned} \tag{6.3}$$

The algorithm for calculation of either of these correlation functions would be:

1. create n distance bins, each with width Δr.
2. for each pair of molecules in the trajectory, find either Δ or D and put

the value into the proper distance bin.

3. normalize each bin by the total number of molecules placed in the bin, ie. find the average for that bin.

Finally, we have introduce what we call the dipole-dipole spatial correlation function:

$$\begin{aligned}\phi(r) &= \frac{1}{N_{\text{gas}}(r)} \sum_{i,j}{}' \boldsymbol{\mu}_i \cdot \boldsymbol{\mu}_j \quad r < r_{ij} < r + \delta r \\ &= \langle \boldsymbol{\mu}_1 \cdot \boldsymbol{\mu}_2 \rangle (r) g_{\text{OO}}(r)\end{aligned} \tag{6.4}$$

Here $N_{\text{gas}}(r)$ is the number of molecules that would be found in a shell of thickness δr at radius r for a homogeneous "gas" ($N_{\text{gas}}(r) = 4/3\pi[(r+\delta r)^3 - r^3]N/V$).

6.3 2D spatial correlation functions

Mathias chose to introduce the following 2-dimensional correlation functions.[4] In their notation:

$$\begin{aligned} g_s(r,\theta) &\equiv \langle g_d(1,2) S \rangle \\ h_\Delta(r,\theta) &\equiv \frac{\langle g_d(1,2)\Delta \rangle}{g_s} \\ h_D(r,\theta) &\equiv \frac{\langle g_d(1,2) D \rangle}{g_s} \end{aligned} \tag{6.5}$$

These quantities can be averaged over a set of pairs of molecules in the system (for instance, the set of pairs separated by a distance between r and $r+\Delta$) to make correlation functions. In delta function notation:

$$\begin{aligned} g_s(r,\theta) &\equiv \frac{V}{N^2} \left\langle \sum_{ij} S \delta(r - r_{ij}) \delta(\theta - \theta_{ij}) \right\rangle \\ h_\Delta(r,\theta) &\equiv \left\langle \sum_{ij} \Delta_{ij} \delta(r - r_{ij}) \delta(\theta - \theta_{ij}) \right\rangle \\ h_D(r,\theta) &\equiv \left\langle \sum_{ij} D_{ij} \delta(r - r_{ij}) \delta(\theta - \theta_{ij}) \right\rangle \end{aligned} \tag{6.6}$$

The function g_s is a two dimensional radial distribution function, h_Δ is a two dimensional analog of cosine function and h_D gives the angular dependence of the energy of interaction (positive h_D correspond to lower energies).

6.4 2D correlation functions for a point dipole in a homogeneous dielectric continuum

Later, we will want to compare to the case of a point dipole in a homogeneous dielectric media, to gauge how far out the inhomogeneous effects of H-bonding extend. The field produced by a point dipole $\boldsymbol{p_1}$ in a homogeneous dielectric medium with relative dielectric constant ε is :

$$\boldsymbol{E}(\boldsymbol{r}) = \frac{p_1}{4\pi\varepsilon\epsilon_0}\frac{3\hat{\boldsymbol{r}}(\hat{\boldsymbol{r}}\cdot\hat{\boldsymbol{p}}_1)-\hat{\boldsymbol{p}}_1}{r^3} \tag{6.7}$$

In such a situation the polarization response is isotropic and linear $\boldsymbol{P}(\boldsymbol{r}) = \epsilon_0\chi\boldsymbol{E}(\boldsymbol{r})$ and is:

$$\boldsymbol{P}(\boldsymbol{r}) = \frac{p_1\chi}{4\pi\varepsilon}\frac{3\hat{\boldsymbol{r}}(\hat{\boldsymbol{r}}\cdot\hat{\boldsymbol{p}}_1)-\hat{\boldsymbol{p}}_1}{r^3} \tag{6.8}$$

Obviously, $g(r) = 1$ in this case - in other words, the density of dipoles is fixed through all of space. To make an analogy with water, let us assume that this density is the average density of water molecules. Then the dipole unit vector $\hat{\boldsymbol{p}}_2$ is given by $\hat{\boldsymbol{p}}_2 = \frac{\boldsymbol{P}}{p_1 n}$, where n is the number density. We define:

$$\lambda \equiv \frac{\chi}{4\pi\varepsilon n} \tag{6.9}$$

To calculate ϕ^c_Δ and ϕ^c_D we substitute the above expressions into 6.1. Setting $\hat{\mathbf{r}}\cdot\hat{\mathbf{p}}_1 \equiv \cos(\theta)$ we get:

$$h^c_\Delta(r,\theta) = \frac{\lambda}{r^3}(3\cos^2\theta - 1) \tag{6.10}$$

$$h^c_D(r,\theta) = \frac{\lambda}{r^3}(3\cos^2\theta + 1) \tag{6.11}$$

The angle θ_c where h^c_Δ changes from positive to negative can be solved for by setting eqn. 6.10 to zero and solving for θ. One finds:

$$\theta_c = \arccos\left(\frac{1}{\sqrt{3}}\right) = \arcsin\left(\sqrt{\frac{2}{3}}\right) \approx 54.74\,\text{deg} \tag{6.12}$$

The correlation function $\phi^c_\Delta(r)$ can be found by the appropriate spherical average over θ:

$$\phi^c_\Delta(r) = \frac{1}{2}\int_0^\pi \frac{\lambda}{r^3}(3\cos^2\theta - 1)\sin\theta d\theta = 0 \tag{6.13}$$

We see that the spatial correlation function $h^c_\Delta(r)$ is zero because the regions of correlation and anti-correlation precisely cancel out in the dielectric continuum case. However, we can focus on the $\theta = 0$ direction:

$$h^c_\Delta(r, \theta = 0) = \frac{2\lambda}{r^3} \tag{6.14}$$

The dielectric constant can be related to λ (eqn. 6.9) using $\chi = \varepsilon - 1$:

$$\begin{aligned} \lambda &= \frac{\varepsilon - 1}{4\pi n \varepsilon} \\ \varepsilon &= \frac{1}{1 - \lambda 4\pi n} \end{aligned} \tag{6.15}$$

Note that using $\chi_L = 1 - 1/\varepsilon$ we have

$$\lambda = \chi_L 4\pi n \tag{6.16}$$

In their paper Matthias & Tavan show that in water h_Δ begins to behave like h^c_Δ when r is larger than ≈ 15Å. At these distances they were able to fit their data to $h^c_\Delta(r, \theta = 0)$ and found that $\lambda = 2.36 \pm .1$Å. Substituting $n = .0333\text{Å}^{-3}$ for water this yields $\varepsilon = 95.9 \pm 385$. The actual value is 71 ± 4 for SPC/E. Unfortunately there is a very large error because $\frac{d\varepsilon}{d\lambda}$ becomes very large near $\lambda 4\pi n = 1$. In fact, within the error bar for λ given by Mathias & Tavan, the error in ε goes to infinity. Therefore, finding ε by fitting the correlation function to eqn. 6.13 at large distances and solving for λ does not appear to be a useful method, nor is it clear exactly how rigorous this method is.

6.5 Distance dependent Kirkwood function

Perhaps the most physically meaningful measure of dipole correlation is the distance dependent Kirkwood function, since it can be directly related to the dielectric constant via equation 4.23. For a single molecule, $G_K(r)$ is given by:

$$G^1_K(r) = \frac{\sum_j \boldsymbol{\mu}_1 \cdot \boldsymbol{\mu}_j}{\langle \mu^2 \rangle}, \quad r_{1j} < r \tag{6.17}$$

Averaged over N molecules and all timesteps, $G_K(r)$ becomes:

$$G_K(r) = \frac{\left\langle \sum_{i,j} \boldsymbol{\mu}_i \cdot \boldsymbol{\mu}_j \right\rangle}{N \langle \mu^2 \rangle}, \quad r_{ij} < r \tag{6.18}$$

The previous two dipole correlation functions become very small beyond the second shell in water. However, even small correlations beyond the second shell may be important as the number of molecules participating in these correlations grows as r^2. The Kirkwood correlation function accounts for this by reporting the total correlation of dipoles in a sphere of radius r normalized only by the dipole moment of the central molecule.

Another way of calculating $G_K(r)$ is from $h_\Delta(r)$:

$$G_K(r) = 1 + 4\pi\rho \int_0^r h_\Delta(r') g_{\mathrm{OO}}(r') r'^2 dr' \tag{6.19}$$

In practice, the calculation of $G_K(r)$ using equation 6.19 is significantly faster than using 6.18.

6.5.1 Axial and equatorial components

Since $h^c_\Delta(r) = 0$, from eqn. 6.19 $G^c_K(r) = 1$ for the homogeneous continuum. However, one can break $G_K(r)$ into axial and equatorial components:[4]

$$G_K(r) = G^a_K(r) - G^e_K(r) \tag{6.20}$$

The axial component comes from integrating over the region of positive correlation, while the equatorial component comes from integrating over the region of negative correlation. As was just shown, the two regions are separated by a conical surface at an angle of $\theta_c = \arcsin\left(\sqrt{\frac{2}{3}}\right) \approx 54.74\,\mathrm{deg}$. When analyzing these quantities for the homogeneous case, one runs into the issue of the a singularity at $r = 0$. To avoid this singularity we must start the integration at a cutoff distance r_c with $0 < r_c < r$. One arrives at the following equations:

$$G^{ac}_K(r) = 1 + \frac{8\pi}{3\sqrt{3}}\rho\lambda \ln\frac{r}{r_c} \tag{6.21}$$

$$G^{ec}_K(r) = \frac{8\pi}{3\sqrt{3}}\rho\lambda \ln\frac{r}{r'_c} \tag{6.22}$$

Note that we choose different cutoff radii for the axial and equatorial components. Mathias & Tavan found this to be necessary in order to fit these functions to the simulation data. Changing r_c is equivalent to adding or subtracting an arbitrary constant.[1]

[1] Technical note: Mathias & Tavan incorrectly refer to these as "integration constants". They separate part outside the natural log using the log identity $\ln(a/b) = \ln a - \ln b$ but

6.6 The artificial enhancement of dipole correlation from periodic boundary conditions

Dipolar interactions are very sensitive to how long range interactions are treated. As we saw in chapter 2, different equations for $\varepsilon(0)$ are required depending on what method is used (eqn. 2.62). Neglect of long range Coulomb interactions leads to severe artifacts - a simple cutoff to the Coulomb interaction leads to the formation of artificial layered phases with layers of dipoles pointing in alternate directions.[148, 149, 4, 150] Strikingly, these layered phases *increase* in magnitude as the cutoff is increased. Usually, artifacts decrease with increasing cutoff. This fact emphasizes that the dipolar order in water is due to long-range interactions. Using shift or switch functions on the spherical cutoff more or less reduces the layering artifact, but leads to other artifacts. The most popular way to treat long range interactions is particle-mesh Ewald summation (PME), which is capable of exactly treating the long range interactions for a periodic version of the system. However, as pointed out by Mathias & Tavan, even with use of PME there is still an artificial increase in $G_K(r)$. The presence of the artifact is perhaps not surprising since one is imposing periodicity on a non-periodic system.

Electrostatic artifacts from periodic repetition are extremely important for physical chemists who work to calculate the solvation free energy of ions. For a Na^+ ion, using Born theory (a simple electrostatic theory that treats water as a dielectric continuum) one finds that to calculate solvation free energy to within .5% accuracy, a sphere of radius 34 nm is required.[151] One must also increase the sphere to remove the perturbation of the water-vacuum boundary, which causes it's dimension to swell to 35-37 nm. Such a sphere would contain 10^6 molecules, and it is estimated that with Moore's law scaling, a processor that could simulate such a system (with classical MD) in one month will not be available until 2045. Thus, physical chemists are stuck with simulating ions in smaller periodically-repeated systems, and correction factors have been developed for use with such simulations.[151] If we replace the sodium ion with a water molecule it is clear that electrostatic artifacts from periodic repetition may have consequences for the simulation of pure water as well.

Dipolar artifacts are most easily seen in the distance dependent Kirkwood factor $G_K(r)$. Locally the PME artifact is quite small, corresponding to a slight enhancement of correlation, but it appears large in $G_K(r)$ since it is integrated. When PME is used, $G_K(r)$ begins to artificially grow beyond a certain point which we found is usually around half the minimum image distance ($r_m = L/2$

must retain part of r_c inside the log in order for the log to remain dimensionless.

for a cubic box).[2] A representative case of this is shown in fig. 6.2. When the reaction field method is used, a large artificial minimum appears in $g_K(r)$ at a distances around $0.8 - 0.9r_m$. These artifacts are obscured because the equations for the dielectric constant (eqn. 2.62) automatically correct for the effect of the artifact. Therefore one may obtain correct dielectric constants using both PME and reaction field, assuming one uses the correct equation.[3] However, one must bear in mind that the dipole correlation in such systems has a small unphysical component. To obtain a physically accurate $G_K(r)$ simulations of at least a few ns should be run in a box containing at least 5,000 molecules to cleanly separate the artifact from the correct (physical) $G_K(r)$, which exhibits features out to ≈ 1.5 nm.

Mathias & Tavan suggest that this artifact that appears with PME is due to the PME technique. However, a nearly identical artifact appears when using a switched cutoff and no PME.[149] This suggests the artifact is more due to the nearest image cells introduced by periodic boundary conditions, rather than the long range periodicity introduced by PME.

[2]The fact this is an artifact should be clear from the fact that it shifts position in proportion to L.

[3]In addition to yielding fairly accurate dielectric constants, reaction field also yields reasonable dielectric spectra and relaxation times.[129, 149, 59]

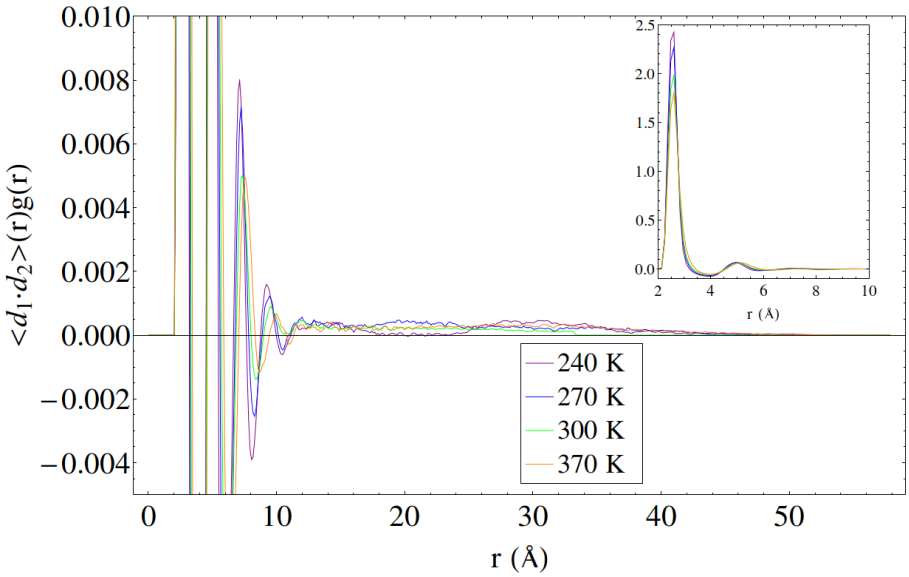

Figure 6.1: Dip-dip correlation function for 10,0000 TIP4P/2005 at different temperatures. The artificial enhancement of dip-dip correlation causes the function to remain slightly larger than zero at large distances. Note that the artifact is of nearly constant magnitude as a function of r.

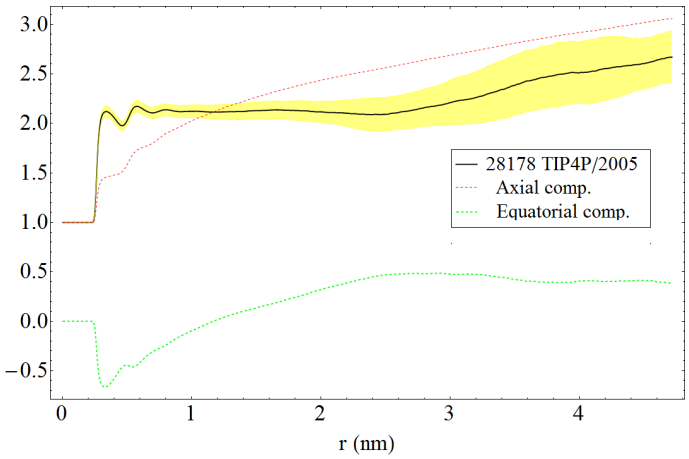

Figure 6.2: $G_K(r)$ function for a large box of TIP4P/2005 with $L = 9.45$ nm. Estimated error is shown in yellow (RMS fluctuation of last 30% of the averaging time). The axial (red) and equatorial (green) components of $G_K(r)$ are shown. The artifact contributes equally to both components, with the axial component becoming more correlated and the equatorial component becoming less anti-correlated.[4]

6.6.1 Dependence of the artifact on box shape

type	volume	$\frac{V_{\text{ins.}}}{V}$	$\frac{V_{\text{circ.}}}{V}$	sphericity
cube	d^3	.52	2.72	.806
truncated octahedron	$\frac{4}{9}\sqrt{3}d^3 \approx .770d^3$	.68	1.46	.909
rhombic dodecahedron	$\frac{1}{2}\sqrt{2}d^3 \approx .707d^3$	.74	2.09	.905

Table 6.1: Properties of the three most common box types. d is the distance between lattice points and equals twice the minimum image distance ($d = 2r_m$). $\frac{V_{\text{ins.}}}{V}$ is the ratio of the volume of an inscribed sphere (a sphere with $r = r_m$) to the volume of the polyhedra. $\frac{V_{\text{circ.}}}{V}$ gives the ratio of volume of a circumscribed sphere to the volume of the polyhedra.

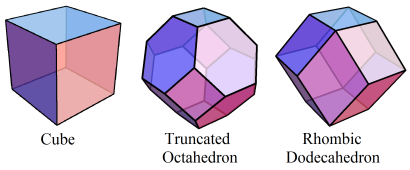

Figure 6.3: Three space-filling polyhedra used in simulations. Visualized with *Mathematica*.

We were interested in seeing if the artifact could be reduced by changing the box shape, or equivalently, the space lattice of Ewald summation. Out of the five types of polyhedra which fill space on a regular lattice in a similarly-situated manner [152] three are frequently used in computer simulation: the cube, truncated octahedron and the rhombic dodecahedron. The cube clearly corresponds to a cubic lattice, whereas the rhombic dodecahedron and truncated icosahedron correspond to the FCC and BCC lattices respectively. It has been hypothesized that the FCC & BCC lattices yield more accurate simulations because they better reproduce the spherical symmetry of liquid water. Some relevant properties of these three polyhedra are summarized in table 6.6.1. Sphericity is a mathematical measure of how spherical a polyhedra is – it is defined as the ratio of the surface area of a sphere with the same volume as the polyhedra to the surface area of the polyhedra. According to the ratio of the circumscribed volume and the sphericity, the truncated octahedron is the most spherical. The rhombic dodecahedron is less spherical but has the advantage of yielding a larger r_m for a given number of molecules. The cube is usually employed for simplicity, although codes for the rhombic dodecahedron and truncated icosahedron PBCs are readily available.[153, 59] The PBC code

type	# of mol.	d
cube	28178	9.446
truncated octahedron	21747	9.486
rhombic dodecahedron	20000	9.459

Table 6.2: The three large simulations performed to compare the polyhedra. The lattice spacing parameter d was kept nearly identical for comparison. All three simulations had a density of exactly 1.0 kg/L.

is shortest for the cube and grows in number of operations for the truncated octahedron and rhombic dodecahedron.[59] Although it has the longest code, the rhombic dodecahedron is often chosen for simulations of biomolecules, as the number of required solvent molecules is reduced due to a high value of $\frac{V_{\text{ins.}}}{V}$. Additionally we noticed that Mathias & Tavan used a rhombic dodecahedron box and they observed an artifact starting at $\approx .75\ r_m$ in two simulations with $r_m \approx 6.0$ nm (39,999 mol) and $r_m = 4.0$ nm (11,522 mol), in contrast to the artifact we observed in the cube which starts around $\approx .5 r_m$.

To compare the three polyhedra, we choose to keep the lattice spacing fixed, rather than the number of molecules.

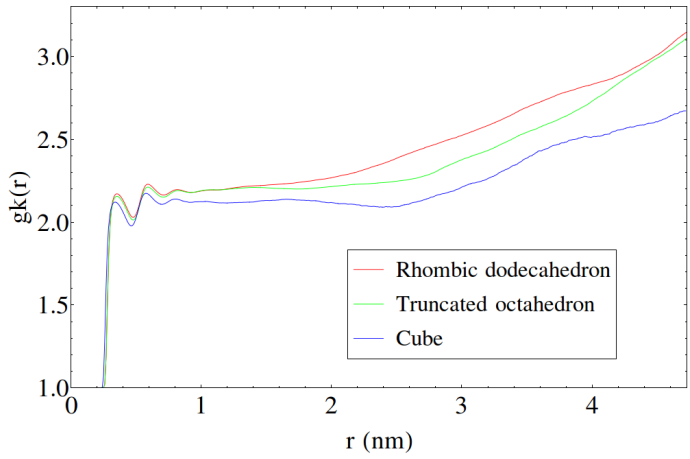

Figure 6.4: $g_K(r)$ functions for the three polyhedra. Overall the three polyhedra exhibit similar artifacts.

The simulations were run for 1 ns with output every 0.2 ps. Figure 6.4 shows $G_K(r)$ for the three types of boxes. The three polyhedra exhibit similar artifacts in $G_K(r)$, all starting around 0.5 $r_m \approx 2.4$ nm. The results show that the rhombic dodecahedron has a slightly larger artifact compared to the cube. In retrospect, this can be rationalized by considering that the rhombic

dodecahedron has a smaller longest diagonal. In other words, although the cube has a highly nonspherical placement of its periodic images, it also has a longer diagonal along which the periodic images are further spaced.

6.7 1D correlation functions for water

Cosine functions for water computed using our three models are shown in fig. 6.5. Oxygen-oxygen RDFs are shown for reference to emphasize that the peaks in the cosine function do not necessarily overlap with the RDF peaks, since the cosine function does not contain any information about the density of molecules. We clearly see that TTM3F has much larger correlation, especially in the first shell.[4]

The dip-dip correlation function for the different models at 300 K is shown in figure 6.8. Figures 6.9 and 6.10 show different contributions to the dip-dip correlation function, including the positive and negative components and (for TTM3F) the contribution of the induced dipoles.

From inspection of the first peak we see that the first H-bonded shell contributes a large positive component as expected. The region of the second H-bonded shell (4 - 5 Å) contains both positive and negative contributions. In such plots it is difficult to distinguish the contributions from H-bonded shells and non H-bonded shells, since they overlap considerably. It appears that the first interstitial shell contributes significantly to the minimum at 4 Å.

Figures 6.11 and 6.12 compare the dip-dip correlation functions at different temperatures for TTM3F and TIP4P/2005f. TTM3F exhibits more dramatic temperature dependence and a more clearly pronounced 3rd peak. By contrast, the third peak is almost non-existent in TIP4P/2005f. The expected temperature dependence of the dipole correlation is in the expected direction in TTM3F – ie. enhanced correlation at lower temperatures. This behaviour is not captured by either TIP4P/2005 or TIP4P/2005f, which shows less correlation in the 2nd shell at lower temperatures.

The polarization dipoles in TTM3F contribute mainly in the first shell, where they have a large positive component. Beyond that the polarization dipoles contribute nearly equal positive and negative components which nearly cancel out. The result is a small positive contribution to the second peak and almost zero contribution to the third peak.

[4]Interestingly, the molecules with the smallest H-bonds contribute positively with TTM3F and negatively with TIP4P/2005. The number of molecules at such small distances is very small, so it is not clear how significant this result is.

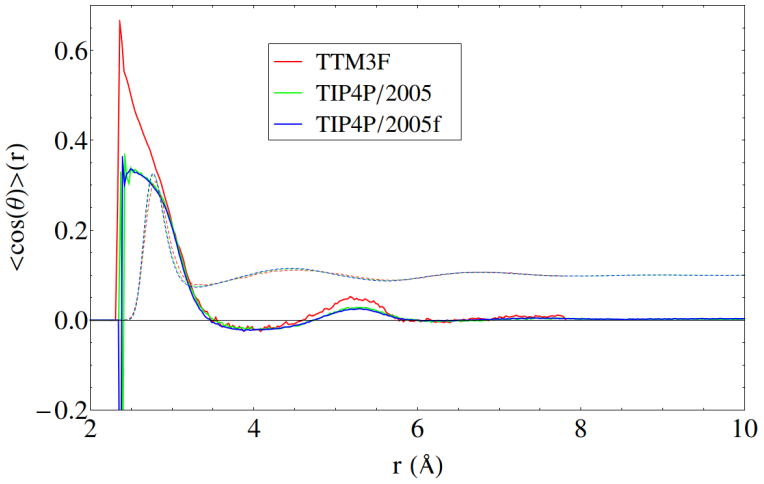

Figure 6.5: $\langle\cos(\theta)\rangle$(r) for the three models at 300 K. The O-O RDFs (rescaled by a factor of .1) are shown for comparison.

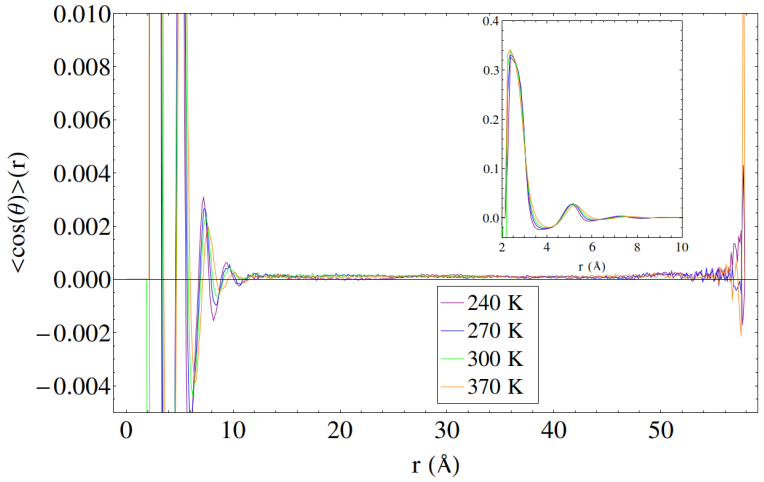

Figure 6.6: Cosine function for 10,0000 TIP4P/2005 at different temperatures. Again we see the artifact causing the function to be nonzero at large distances.

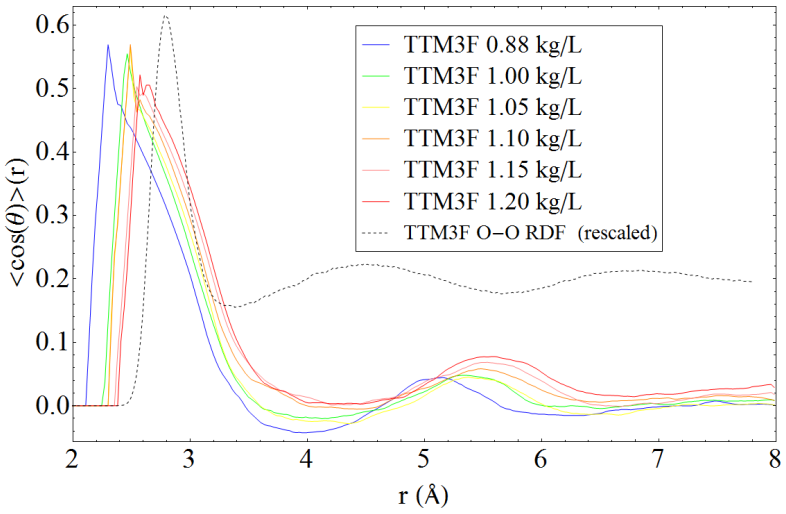

Figure 6.7: Cosine function for 128 TTM3F at different densities. Smoothing was applied to remove noise.

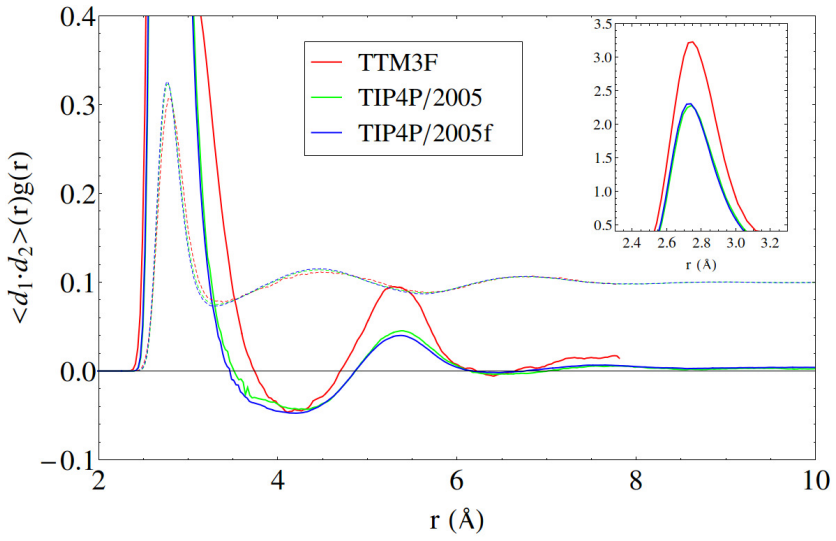

Figure 6.8: The dip-dip correlation function defined by equation 6.4. The O-O RDFs (rescaled by a factor of .1) are shown for comparison.

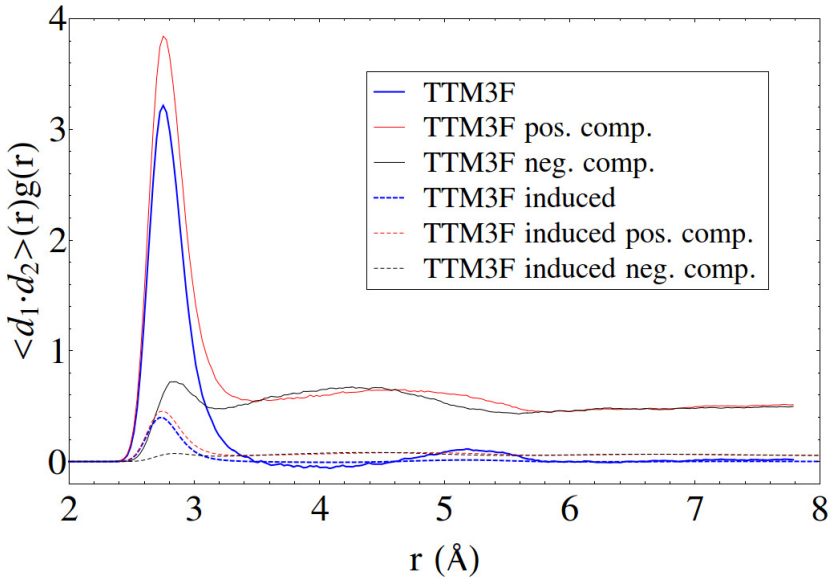

Figure 6.9: Positive, negative and induced components of the dip-dip correlation function for TTM3F.

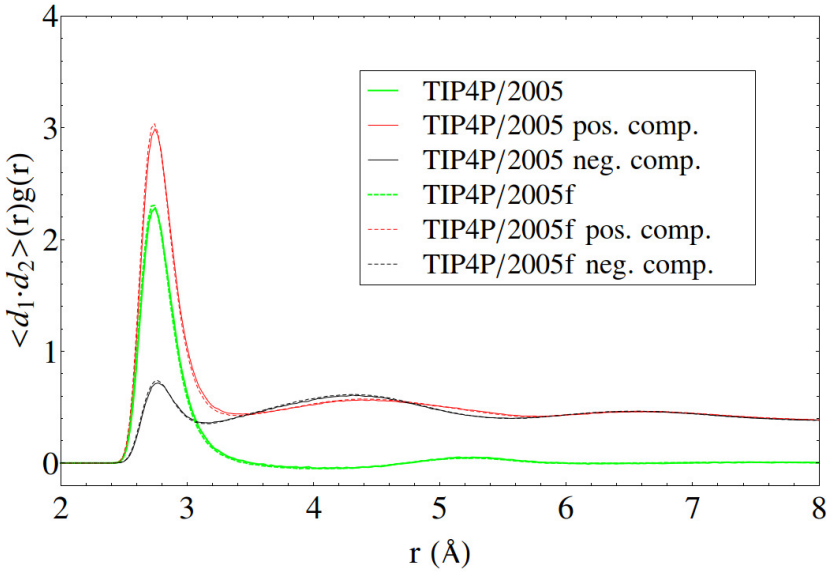

Figure 6.10: Positive and negative components of the dip-dip correlation function for the rigid (solid) and flexible (dashed) versions of TIP4P/2005. The rigid and flexible curves nearly overlap.

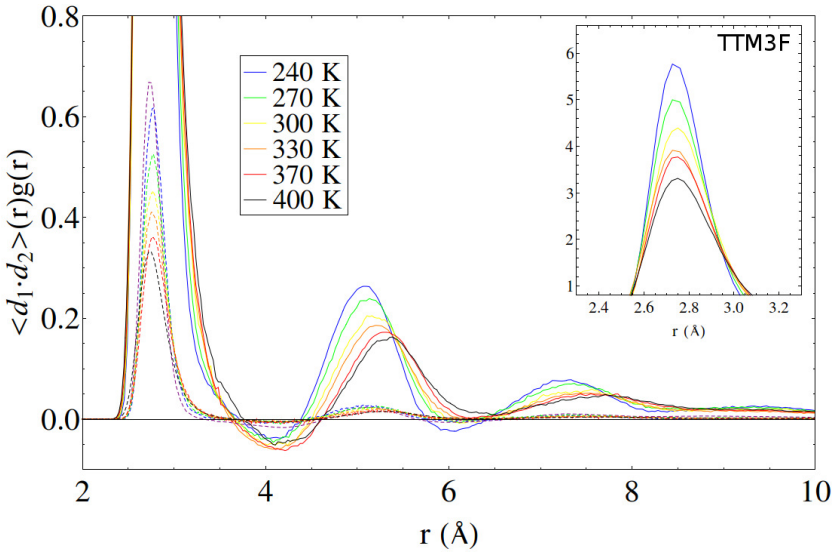

Figure 6.11: Dip-dip correlation function at different temperatures for TTM3F. Dashed lines show the contribution of the polarization dipoles.

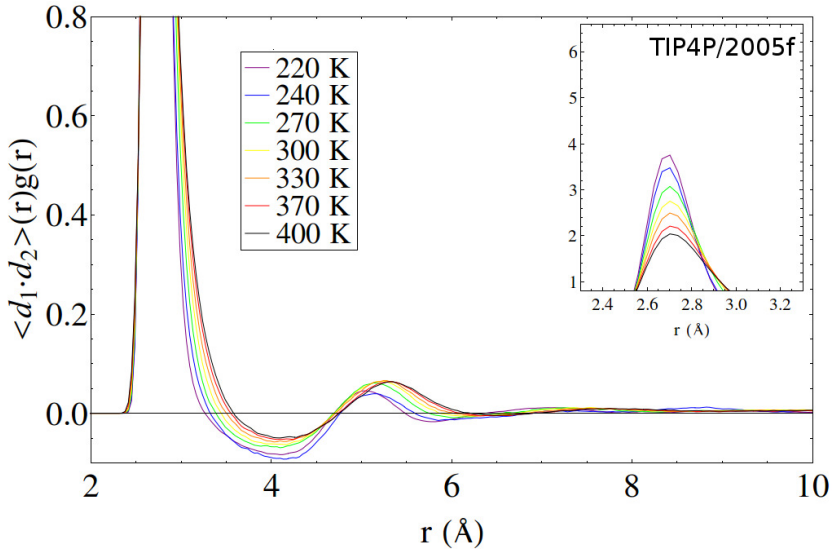

Figure 6.12: Dip-dip correlation function at different temperatures for TIP4P2005f.

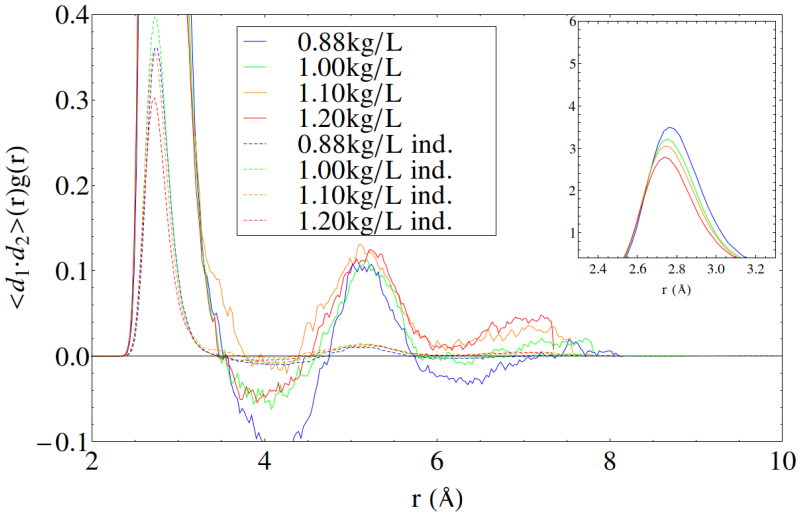

Figure 6.13: Dip-dip correlation function for 128 TTM3F at different densities, showing the contribution of the induced molecules. Note that while the overall correlation of the first shell decreases with density the induced exhibits non-monotonic behaviour, with greater correlation at 1.00 kg/L compared with 0.88 kg/L

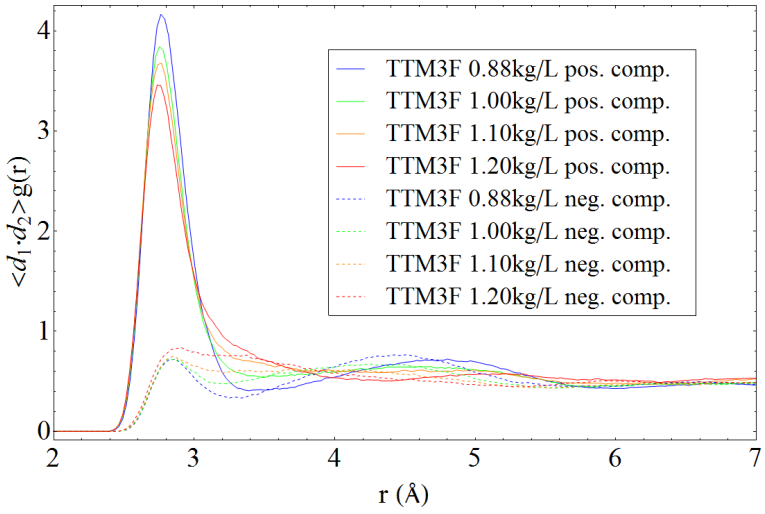

Figure 6.14: Dip-dip correlation function for 128 TTM3F at different densities, showing the positive (solid) and negative (dashed) components.

6.8 Kirkwood function of water

Simulations of 1,000 molecules were run with TTM3F for 1.8 ns and for TIP4P/2005 and TIP4P/2005f for 8 ns to compute $G_K(r)$. With 1000 molecules all $G_K(r)$ data beyond $\approx$ 10Å is unphysical. The $G_K(r)$ data clearly show the relative contributions from different H-bonded shells to G_K and therefore to the dielectric constant. Flexibility decreases $G_K(r)$ slightly in TIP4P/2005, which might be due to a weaker H-bond network. On the other hand, TTM3F $G_K(r)$ exhibits larger $G_K(r)$ values and displays a more pronounced contribution from the second shell. The third and fourth shells do not contribute to G_K in any of the models but appear more pronounced in TTM3F. Unlike the continuum case, the equatorial component is *correlated* (negative) in water out to about 1.2 nm due to the H-bond network (fig. 6.8). In our simulations with 1,000 molecules the equatorial component remains negative even at large distances due to the artifact.

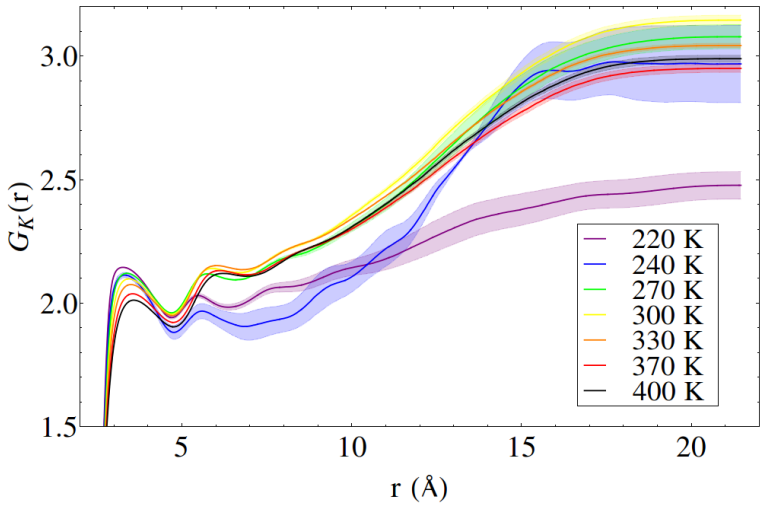

Figure 6.15: $G_K(r)$ for 512 TIP4P/2005f at different temperatures exhibiting the wrong temperature dependence in $G_K(T)$.

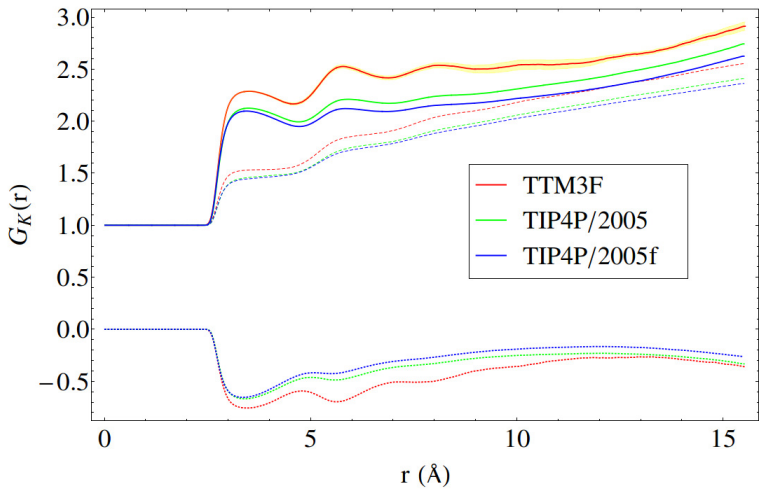

Figure 6.16: $G_K(r)$ functions for the three models showing the axial (dashed) and equatorial (dotted) components. Estimated errors are shown in yellow for TTM3F (the other errors were negligible). All $G_K(r)$ data beyond $\approx$ 9Å is due the artifact discussed in secction. 6.6

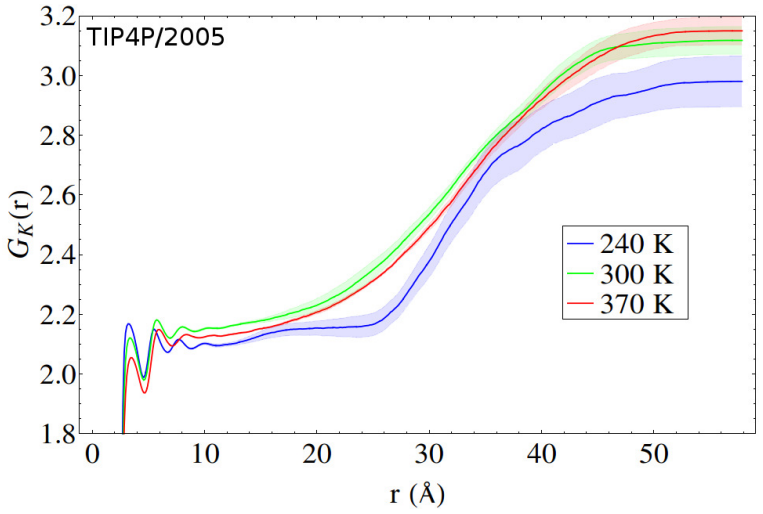

Figure 6.17: $G_K(r)$ function at three different temperatures for 10,000 TIP4P/2005 (L = 66.11Å). The shaded regions show the estimated error. The dipolar ordering becomes longer ranged at lower temperatures, but in the end decreases in magnitude, exhibiting the wrong temperature dependence.

6.9 2D angular correlation function of water

The one dimensional angular correlation functions are useful for measuring the overall correlation in each shell but do not contain any information about the structure within shells. To better understand the structure we use follow the approach of Mathias & Tavan[4] to produce 2D plots. These 2D correlation functions depend on two variables - a radial distance $r = |\boldsymbol{r}_{ij}|$ between molecules and the angle θ, which is the angle between the dipole moment of molecule i and $\boldsymbol{r}_{ij}$. Here $\theta = 0$ corresponds to the direction of the dipole moment (axial direction), which is called the "z" axis. The "x" axis lies in the plane perpendicular to the z axis (the equatorial plane).

As we explained in section 6.3 $g_s(r, \theta)$ is a two dimensional radial distribution function, $h_\Delta(r, \theta)$ is a two dimensional analog of cosine function and $h_D(r, \theta)$ gives the angular dependence of the energy of interaction (positive h_D correspond to lower energies). Figure 6.18 shows a comparison of the 2D correlation functions for TTM3F and TIP4P/2005f. The rigid and flexible versions of TIP4P/2005 are not compared here since they are nearly identical in appearance. Perhaps the most striking thing about these plots is their similarity – differences in magnitude are not very visible here. Several small differences can be observed, however. The first shell in TTM3F is more spread out and thus has a smaller maxima (6.52 vs. 9.35). The TTM3F 2D cosine function exhibits slightly more structure and anti-correlation in the interstitial regions.

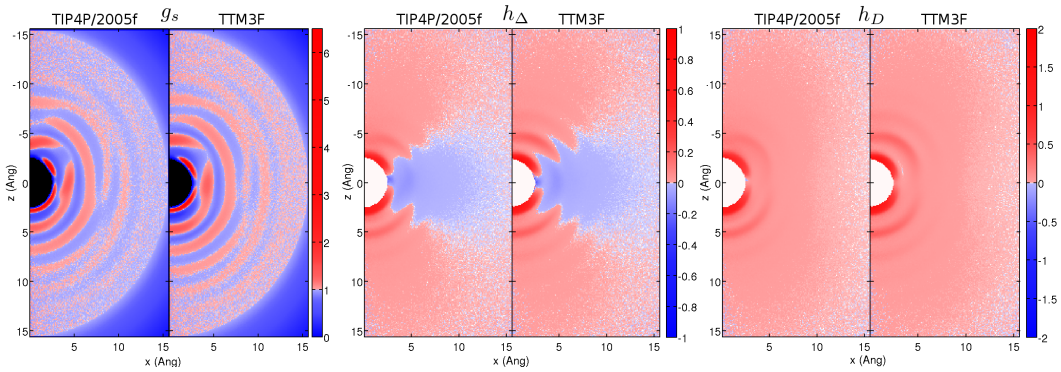

Figure 6.18: Comparison of 1000 TIP4P/2005f (left panels) with 1000 TTM3F (right panels). The three 2DRDFs correspond to the 2D O-O RDF (left), the 2D cosine function (middle) and the 2D dipole-dipole energy function (right). Each pixel represents a square histogram bin with $L = .1$Å.

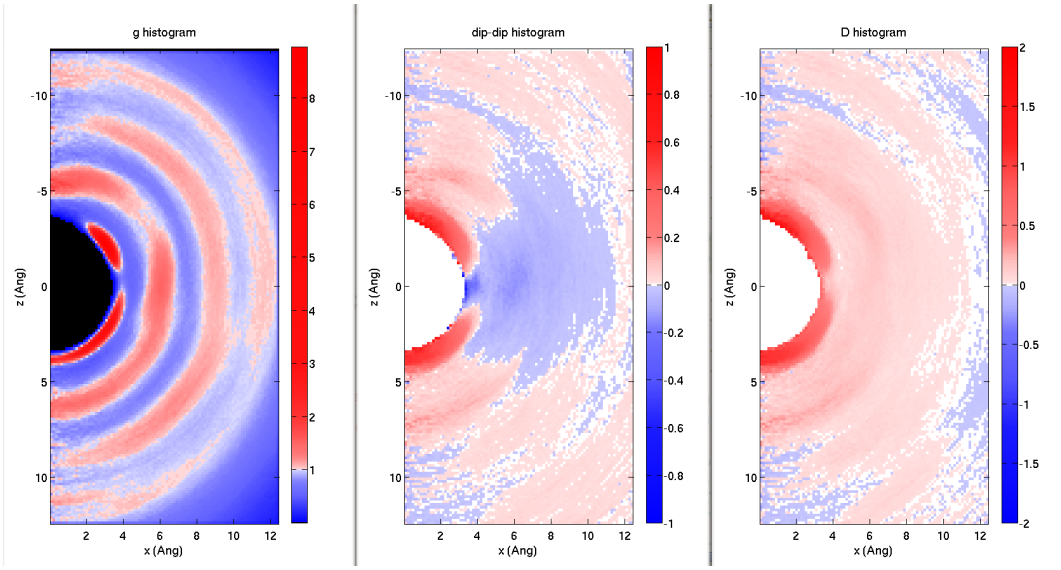

Figure 6.19: 2D correlation functions for 200 molecules simulated with the VV functional, with dipoles calculated by a simple placement of point charges on each atom. If the dipoles are calculated with TTM3F, the resulting figures are nearly the same.

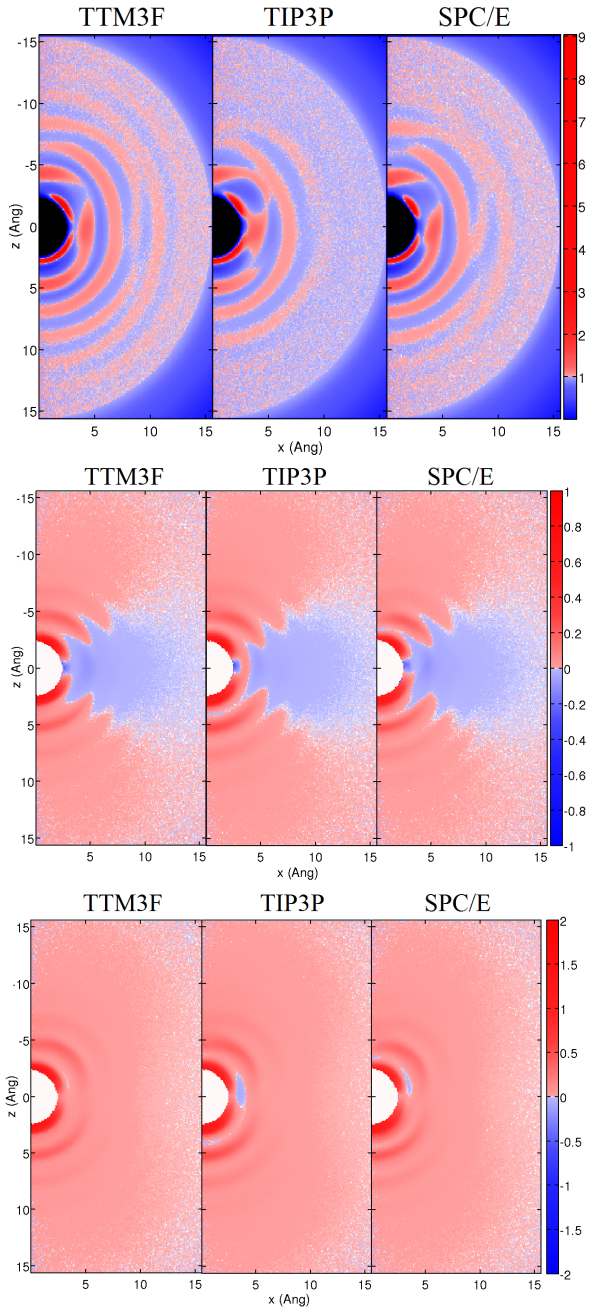

Figure 6.20: 2D correlation functions for 1000 TTM3F, SPC/E, and TIP3P. (top) 2D O-O RDF (middle) 2D dip-dip function (bottom) 2D energy function.

6.10 Conclusion

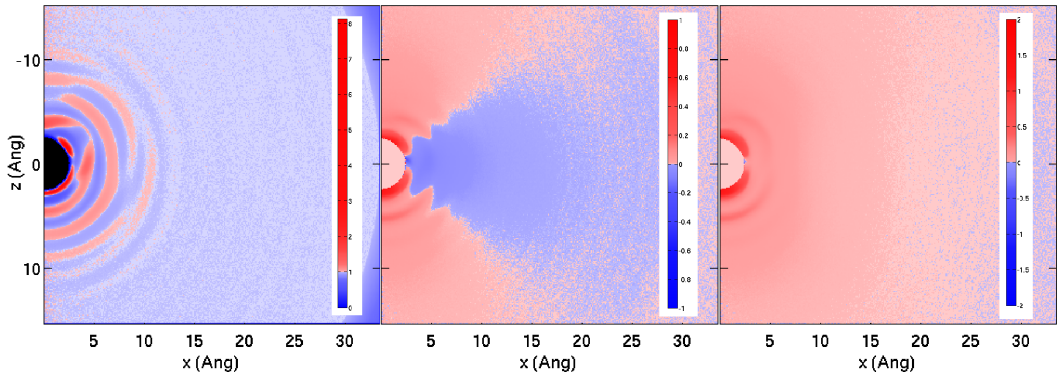

Figure 6.21: Bonus figure showing the 2D correlation functions for a large box of 10,000 TIP4P molecules.

In all five of the models presented the dipole correlations resemble a dielectric continuum at distances larger than 1.5 nm, confirming the findings of Mathias & Tavan. We propose that this distance corresponds to the largest possible radius of the polar nanoregions, which will be discussed in the next chapter. Polarization enhances dipole correlation and leads to a more physically accurate change in dipole correlation with temperature. This indicates that *ab initio* molecular dynamics simulation of liquid water will have even more enhancement of dipole correlations. The temperature dependence of the dipole-dipole correlation shows that TTM3F captures the expected increase in correlation in the second and third peaks at lower temperature, while TIP4P/2005 shows the opposite behavior. This problem is reflected in the temperature dependence of G_K which is flat for TIP4P/2005 but experimentally G_K increases at lower temperature. This highlights another reason that the temperature dependence of the dielectric constant is poorly captured by rigid/flexible TIP4P/2005 – in addition to the dipole remaining fixed, the change in the dipolar structure of the liquid with temperature is wrongly captured. This deficiency is not captured with traditional atom-atom RDFs.

Chapter 7

Dielectric relaxation of water

"The treatment of dielectric relaxation and its relationship to molecular phenomena is a subtle subject, one that has been fraught with uncertainty, error, and controversy." - Harold Friedman & Daniel Kivelson, 1989

7.1 The most commonly used dielectric functions are all related

Recall eqn. 2.110:

$$\varepsilon(\omega) - \varepsilon_\infty = (\varepsilon(0) - \varepsilon_\infty) \int_0^\infty dt - \dot{\Phi} e^{i\omega t} \tag{7.1}$$

Different assumptions about the nature of the correlation function yield to different dielectric functions, which we also call lineshapes in reference to the absorption peaks found in the imaginary part. In this section, we summarize the most commonly used dielectric functions and show how they relate to one another.

Debye

If we assume:

$$\Phi(t) = \exp(-t/\tau_D) \tag{7.2}$$

then we get the Debye equations:

$$\begin{aligned}\varepsilon(\omega) &= \frac{\varepsilon(0)-\varepsilon_\infty}{1-i\omega\tau_D}+\varepsilon_\infty \\ \varepsilon(\omega)' &= \frac{\varepsilon(0)-\varepsilon_\infty}{1+(\omega\tau_D)^2}+\varepsilon_\infty \\ \varepsilon(\omega)'' &= \frac{(\varepsilon(0)-\varepsilon_\infty)\omega\tau_D}{1+(\omega\tau_D)^2}\end{aligned} \tag{7.3}$$

Damped harmonic oscillator

Let us instead assume:

$$\Phi(t) = fe^{-t/\tau}e^{i\omega_0 t} \tag{7.4}$$

This assumption yields the dielectric function for the damped harmonic oscillator:

$$\begin{aligned}\varepsilon(\omega) &= \frac{f\omega_0^2}{\omega_0^2-\omega^2-i\omega\gamma}+\varepsilon_\infty \\ \varepsilon(\omega)' &= \frac{f\omega_0^2(\omega_0^2-\omega^2)}{(\omega_0^2-\omega^2)^2+\omega^2\gamma^2}+\varepsilon_\infty \\ \varepsilon(\omega)'' &= \frac{f\omega_0^2\gamma\omega}{(\omega_0^2-\omega^2)^2+\omega^2\gamma^2}\end{aligned} \tag{7.5}$$

Lorentzian lineshape

We consider the limit where $\omega \approx \omega_0$. We define $\Delta\omega \equiv \omega_0 - \omega$ and then note that $\omega_0^2 - \omega^2 = (2\omega + \Delta\omega)\Delta\omega = 2\omega\Delta\omega + (\Delta\omega)^2$. In the limit that $\Delta\omega$ becomes small, the $(\Delta\omega)^2$ term can be disregarded, and $\omega_0^2 - \omega^2 \approx 2\omega(\omega_0 - \omega)$. Using this approximation, eqn. 7.5 becomes:

$$\begin{aligned}\varepsilon(\omega) &= \frac{f\omega_0^2}{2\omega(\omega_0-\omega)-i\omega\gamma}+\varepsilon_\infty \\ \varepsilon(\omega)' &= \frac{f(\omega_0^2+\gamma^2/4)}{\omega_0^2}\frac{(\omega_0-\omega)}{\omega[(\omega_0-\omega)^2+\gamma^2/4]}+\varepsilon_\infty \\ \varepsilon(\omega)'' &= \frac{f(\omega_0^2+\gamma^2/4)}{2\omega_0^2}\frac{\gamma}{\omega[(\omega_0-\omega)^2+\gamma^2/4]}\end{aligned} \tag{7.6}$$

This lineshape is often used in IR spectra, because the IR absorption $\alpha(\omega) \approx \omega\varepsilon''(\omega)/cn$ is Lorentzian. The half width of the Lorentzian lineshape is $\gamma/2$

Plasma

Consider the high frequency limit ($\omega >> \omega_0$) of eqn. 7.5, and set $\varepsilon_\infty = 1$. Then one obtains the dielectric function for a plasma:

$$\begin{aligned} \varepsilon(\omega)' &= 1 - \frac{\omega_p}{\omega^2} \\ \varepsilon(\omega)'' &= \frac{\gamma\omega_p}{\omega^3} \end{aligned} \tag{7.7}$$

Here we have introduced the plasma frequency $\omega_p^2 = f\omega_0^2$. Note that when $\omega < \omega_p$ the real part of the dielectric function becomes negative. This corresponds to a situation where electromagnetic waves cannot enter the material and are perfectly reflected. Above the plasma frequency, the material becomes transparent.

Van Vleck-Weisskopf lineshape

The damped harmonic oscillator is symmetric around ω_0. At low frequencies, though, experimental lineshapes become asymmetric. For one thing, the imaginary part of the dielectric function must go to zero as $\omega \to 0$, and this is violated in the DHO lineshape. The problem can be traced to the form of the correlation function (eqn. 7.4). The correlation function contains an imaginary part. The appearence of an imaginary part here corresponds to the use of a driving field described by a complex exponential, a common assumption used in derivations that start from the differential equation for the DHO. A more physical correlation function is:

$$\Phi(t) = fe^{-t/\tau}\cos(\omega_0 t) \tag{7.8}$$

Using this one obtains:

$$\begin{aligned} \varepsilon(\omega) &= \frac{f}{2}\left(\frac{1 - i\omega_0\tau}{1 - i(\omega + \omega_0)^2\tau} + \frac{1 + i\omega_0\tau}{1 - i(\omega - \omega_0)^2\tau}\right) + \varepsilon_\infty \\ \varepsilon''(\omega) &= \frac{f}{2}\left(\frac{\omega\tau}{1 + (\omega + \omega_0)^2\tau^2} + \frac{\omega\tau}{1 + (\omega - \omega_0)^2\tau^2}\right) \end{aligned} \tag{7.9}$$

This lineshape was first introduced by Van Vleck and Weisskopf.[154, 155] In contrast to the standard damped harmonic oscillator, the Van Vleck-Weisskopf lineshape is asymmetric with a maximum at $\omega_{\max} = \sqrt{1 + (\omega_0\tau)^2}/\tau$. This equation has several nice properties. First of all, the Debye equations are seen to correspond to the case where $\omega_0 = 0$. Next, when $\omega_0 >> 0$ the usual damped harmonic oscillator equations (eqn. 7.5) are recovered. Seeing this

algebraically is quite tricky. The Van-Vleck-Weisskopf lineshape is really the "master lineshape" in the sense that the Debye, DHO, Plasma, and Lorentz lineshapes are all special cases of it.

Gaussian lineshape

For freely rotating molecules (ie. gas phase), Gaussian relaxation is often observed:

$$\Phi(t) = Be^{-(t/\tau)^2} \tag{7.10}$$

Via equation 2.110 this leads to:

$$\begin{aligned} \varepsilon'(\omega) &= (\varepsilon(0) - \varepsilon_\infty)B\frac{\sqrt{\pi}}{2}\omega\tau^2 e^{-\frac{1}{4}\tau^2\omega^2} + \varepsilon_\infty \\ \varepsilon''(\omega) &= (\varepsilon(0) - \varepsilon_\infty)B(\tau - \tau^2\omega F(\omega\tau/2)) \end{aligned} \tag{7.11}$$

where $F()$ is Dawson's integral.

7.2 More generalized lineshapes

Broadening: Brendel & Voigt lineshapes

In amorphous systems, one encounters broad peaks which can not be fit with a standard DHO lineshape. For such cases Brendel & D. Bormann have proposed the following dielectric function:[156]

$$\varepsilon(\omega) = \frac{1}{\sqrt{2\pi}\sigma}\int_{-\infty}^{\infty} e^{-\frac{(x-\omega_0)^2}{2\sigma^2}} \frac{\omega_p^2}{x^2 - \omega^2 + i\omega\gamma} + \varepsilon_\infty \tag{7.12}$$

this can be calculated analytically in terms of complex error functions, making it easy to evaluate numerically.[156] The Brendel model has similarities with the popular Voigt lineshape which is used in IR spectroscopy to describe Doppler broadening and other sources of inhomogeneous broadening. The Voigt lineshape is obtained by with the exact same assumption of a Gaussian distribution of frequencies, but with the Lorentzian lineshape in the integrand rather than the DHO lineshape.

Relaxation time distributions

It is also possible to describe $\varepsilon(\omega)$ as a sum of Debye relaxations or an integral over a distribution of relaxation times $G(\tau)$:[157]

$$\begin{aligned}
\phi(t) &= f\int_0^\infty G(\tau)\exp\left(-\frac{t}{\tau}\right)d\tau \\
\varepsilon(\omega) &= f\int_0^\infty \frac{G(\tau)}{1-i\omega\tau}d\tau + \varepsilon_\infty \\
\varepsilon(\omega)' &= f\int_0^\infty \frac{G(\tau)}{1+(\omega\tau^2}d\tau + \varepsilon_\infty \\
\varepsilon(\omega)'' &= f\int_0^\infty \frac{G(\tau)\omega\tau}{1+(\omega\tau)^2}d\tau
\end{aligned} \tag{7.13}$$

Unfortunately, the extraction of $G(\tau)$ from experimental data on $\varepsilon(\omega)$ or $\phi(t)$ is an ill-posed problem. It is easier to work in terms of $k = 1/\tau$. Then the "obvious" way of calculating $G(k)$ is to take the inverse Laplace transform:

$$G(k) = \frac{1}{2\pi i}\int_\Gamma \Phi(t)\exp((-ikt)\,dt \tag{7.14}$$

where Γ is a path of integration in the complex plane going from $-i\infty$ to $i\infty$ chosen such that all the singularities in the integrand lie on the left side. Using this approach, simple expressions for $G(\tau)$ (like a Gaussian) result in difficult to evaluate expressions for $\Phi(t)$ and $\varepsilon(\omega)$, and vice-versa. An exception is a distribution in the shape of a rectangle:

$$G(\tau) = g_0[H(\tau - k_1) - H(\tau - k_2)] \tag{7.15}$$

where $H(k)$ is the Heaviside step function. Then it is easy to confirm that

$$\Phi(t) = \frac{g_0}{t}\left[\exp\left(-k_1 t\right) - \exp\left(-k_2 t\right)\right] \tag{7.16}$$

Implementing an inverse Laplace transform numerically is difficult and also not very well defined. An easier way is to use a nonlinear fitting to fit $G(\tau)$ to $\varepsilon(\omega)$ via eqn. 7.13. However, such least-squares fitting is massively undetermined, so many $G(\tau)$ can fit the same data within the error bars of the data. Still, this type of fitting have been used,[158] but better methods exist which force $G(\tau)$ to be smooth using Tichonov regularization.[159, 160, 161, 162, 163] Perhaps the best description of how to perform the regularized deconvolution numerically is given by Macutkevic (2004).[164] Macutkevic et al. (2006) used

their program to find broad distributions of relaxation times in the archetypal relaxor PMN.[165]

Havriliak-Negami function

There are several phenomenological models that are widely used, which can be summarized in what is called the Havriliak-Negami (HN) formula:

$$\varepsilon(\omega) - \varepsilon_\infty = \frac{f}{[1 + (i\omega\tau_D)^\alpha]^\beta} \qquad \begin{cases} \alpha \geq 0, \beta \leq 1 & \text{HN} \\ \alpha = 1, \beta = 1 & \text{Debye} \\ \alpha \neq 1, \beta = 1 & \text{Cole-Cole} \\ \alpha = 1, \beta \neq 1 & \text{Cole-Davidson} \end{cases} \tag{7.17}$$

For completeness, we reproduce the real and imaginary parts here, although the result is cumbersome:[166]

$$\begin{aligned} \varepsilon(\omega)' &= \frac{\cos(\beta\phi)}{[1 + 2(\omega\tau)^\alpha \sin(\pi/2(1-\alpha)) + (\omega\tau)^{2\alpha}]^{\beta/2}} + \varepsilon_\infty \\ \varepsilon(\omega)'' &= \frac{\sin(\beta\phi)}{[1 + 2(\omega\tau)^\alpha \sin(\pi/2(1-\alpha)) + (\omega\tau)^{2\alpha}]^{\beta/2}} \end{aligned} \tag{7.18}$$

where

$$\phi = \arctan\left[\frac{(\omega\tau)^\alpha \cos(\pi/2(1-\alpha))}{1 + (\omega\tau)^\alpha \sin(\pi/2(1-\alpha))}\right] \tag{7.19}$$

Note that α is a "stretching exponent" since it "stretches" τ in exactly the same way as β does in the stretched exponential. This had lead many authors to speculate that there is a relation, perhaps even an equivalence, between the stretching exponent β and the exponents α and β in the HN expression. The necessary inverse-Laplace transform to obtain $\Phi(t)$ from eqn. 7.17 is difficult to compute. Hilfer (2002) performed the necessary calculation and showed that $\Phi(t)$ must be expressed in terms H-functions, which are in turn defined by contour integrals on the complex plane.[167] Hilfer also showed that there is no simple relation between the stretched exponential and HN relation, and that previous empirical work describing such a relation is not mathematically valid. The distribution $G(\tau)$ can be calculated analytically for NH relaxation.[166] The distribution is qualitatively similar to the distribution for stretched exponential relaxation.[166] In the case of Cole-Cole relaxation, $G(\tau)$ is symmetrical and can be approximated by a Gaussian function. In the case of Cole-Davidson relaxation, the distribution is asymmetric.

Power law "universal" relaxation

Although Debye relaxation describes the observed $\varepsilon(\omega)$ very well around the loss peak, in a very large class of complex materials it fails to give the correct description of the high frequencies and low frequency "wings". These wings are described by power laws, as was pointed out by Jonscher:[168]

$$\begin{aligned} &\varepsilon(\omega)' \propto \varepsilon(\omega)'' \propto \omega^{m} \quad 0 < m < 1 \quad \text{at low frequencies } (\omega \ll 2\pi\tau_D^{-1}) \\ &\varepsilon(\omega)' \propto \varepsilon(\omega)'' \propto \omega^{-n} \quad 0 < n < 1 \quad \text{at high frequencies } (\omega \gg 2\pi\tau_D^{-1}) \end{aligned} \tag{7.20}$$

In contrast the Debye expression gives $m = 2$ for $\varepsilon(\omega)'$ and $m = 1$ for $\varepsilon(\omega)''$ in the low frequency case and $n = 2$ for $\varepsilon'(\omega)$ and $n = 1$ for $\varepsilon''(\omega)$ in the high frequency case. These power law wings were coined "universal relaxation laws" by Jonscher because of their presence in an extremely diverse set of complex materials (metals, polymers, aqueous solutions, etc).[168] Attempts to explain this type of non-Debye behavior in terms of a general theory have so far been unsuccessful. However, one similarity that such systems share is the presence of moving charges or rotating dipoles which are "hopping" over barriers of different heights.[168] In small water clusters, MD simulation shows $\varepsilon \propto 1/\omega$, reflecting the complex energy landscape of the hydrogen bond network.[169]

Debye function with power law tail

In the context of studying the Debye peak in water-glycerol mixtures, Punkenko, et. al. introduce the following dielectric function:[170]

$$\begin{aligned} \varepsilon(\omega) &= \frac{f[1 + f(\omega)]}{(1 + i\omega\tau_D)^{\beta}} + \varepsilon_{\infty} \\ &\text{where} \\ f(\omega) &= \begin{cases} 0 \text{ if } \omega < \omega_c \\ A(\omega\tau)^{q} \text{ if } \omega > \omega_c \end{cases} \end{aligned} \tag{7.21}$$

A cutoff frequency ω_c is required, since otherwise this expression violates the Kramers-Kronig relations. In practice, we found this cutoff could be set to the lowest frequency being analyzed – in other words, one can ignore the cutoff. Putting the cutoff on at the center of the Debye peak results in an unphysical discontinuity in the fit function. The interpretation of A and q is not clear.

7.2.1 Power law relaxation

Let us consider for a moment a relaxation function described by a power law.

$$\Phi(t) = At^{-n} \tag{7.22}$$

This ansatz is not crazy, since powerlaw terms are often found in the correlation functions of systems exhibiting self-similarity.[1] Eqn. 7.22 is known as Curie-von Schwiedler relaxation, proposed by Curie in 1889 and von Schwiedler in 1907, making it even older than the Debye relaxation law of 1912. If one tries to substitute this into equation 7.1 for $\varepsilon(\omega)$ one finds that the integral does not converge for $n > 0$. The case $n < 0$ is clearly unphysical. What is the $G(\tau)$ distribution for eqn. 7.22? It is:

$$G(k) = \frac{A\tau^{n-1}}{\Gamma(n+1)} \tag{7.23}$$

This is non-normalizable. The problem is that the power law contains unphysically high and unphysically low frequency modes. Power laws are often multiplied by an exponential or a stretched exponential, which presumably helps with this issue. An especially simple case occurs when $n = 1$ ($\Phi(t) = t^{-1}$). Then

$$G(k) = \begin{cases} 0 \text{ if } k < 0 \\ 1 \text{ if } k \geq 0 \end{cases} \tag{7.24}$$

In other words, this decay contains exponential relaxations at all timescales, all with equal weight.

7.3 The physical mechanism of Debye relaxation in water

The Debye relaxation peak dominates the dielectric absorption spectrum of water. The peak is centered at $\approx$ 20 GHz (.66 cm^{-1}) and spans 6 decades of frequency. The large oscillator strength of the Debye peak (73 at 25 C°) is the main contributor to water's exceptionally high static dielectric constant, and thus understanding this mode is critical to understanding the dielectric

[1] The most famous example is in velocity-velocity correlation function which universally exhibits a power law tail in all liquids, including water.[59] Consider an particle (or molecule) which starts off with a large velocity. As it collides with molecules in front of it, it slows down. However, some of this lost momenta loops around and returns to the particle because of hydrodynamic "swirling" motion. Not surprisingly, such power tails are universal in systems undergoing turbulence.

liquid	τ_D	τ_2	ref
butanol	478	26.2	[171]
1-propanol	316(40)	2.9(1.1)	[172]
ethanol	161(21)	3.3(1.3)	[172]
methanol	48(4)	1.25(55)	[172]
acetonitrile	3.506(114)	0.177(18)	[173]
Nitromethane	4.18(12)	0.16(0)	[173]
Nitroethane	5.67(14)	0.29(3)	[173]

Table 7.1: Primary (τ_D) and secondary (τ_2) Debye relaxation times (ps) for some polar liquids, all at 298 / 300 K.

response of water around solutes, including proteins.[174] Debye absorption peak is used in microwave ovens, and is important in satellite-based sensing of ice, water, and soils.[175, 176, 177] Debye absorption is also one of the absorption processes which overlaps with protein dynamics.

In this chapter we show that the Debye relaxation is a collective process. We are not the first to show this, but we feel this point needs to be emphasized to clear up the confusion about the topic. In our survey of the existing literature, we found many authors link Debye relaxation to a particular mechanism involving the breaking and reforming of hydrogen bonds. Debye peaks and a high frequency excess are a universal feature polar liquids, irrespective of whether they contain hydrogen bonding (table 7.3).

Hydrogen bond rearrangement happens at shorter timescales (.5 - 5 ps), and H-bond rearrangement dynamics are stretched and not well-characterized by a single time constant like the Debye relaxation is.[2]

Reconciling the non-exponential dynamics of the H-bond network with the pure exponential character of the Deybe relaxation has been cited as an important unresolved question.[180] Shiratani & Sasai (1996) describe the problem as follows: *"Uniexponential decay has been interpreted to be the evidence that the network is rearranged through a single kind of relaxation process. A mystery is the inconsistency between this temporal homogeneity with the single time constant and the network inhomogeneity with various molecular environments."*[181]

Saito and Ohme used molecular dynamics to study the collective dipole reorientation dynamics of a large water cluster. Surprisingly, they found that the relaxation is significantly different than the bulk, exhibiting a stretched

[2]The applicability of Havriliak-Negami form (eqn 7.17) to water has been tested several times before. For instance Kaatze (1993) found $\alpha = .989(2)$ and $\beta = .959(4)$.[178] Vij et al. (2004) report $\alpha = 1$, $\beta = 1$.[179] Thus the distribution of relaxation times, if any, is very narrow.

long-time tail.[182] The pure exponential character of the Debye relaxation stands in opposition to the idea that water contains an inhomogeneous mixture of nanometer scale high-density liquid and low-density liquid regions, for if this was the case, a distribution of times would be expected, as is found with the stretched exponential relaxation in relaxor ferroelectrics.

7.4 Wrong conceptions of the Debye relaxation

7.4.1 Models based off the temperature dependence

We first consider Debye's original theory from 1929.[80] Debye considers a thermal ensemble of *non-interacting* molecules in an applied electric field, and considers what happens when the field is turned off. He assumes that each dipole undergoes Brownian rotational motion. He then solves the linearised diffusion equation in spherical coordinates, finding that the average moment decays exponentially with time, leading directly to the Debye equations (eqns 7.3). Debye points out that the relaxation time τ_D is related to the rotational friction constant ζ via $\tau_D = \zeta/2k_BT$. Stokes showed that for a sphere of radius a rotating in a medium with shear viscosity η, the rotational friction is given by $\zeta = 8\pi\eta R^3$. Thus, τ_D can be estimated as

$$\tau_D(T) \propto \frac{4\pi\eta(T)R^3}{k_BT} \tag{7.25}$$

Using the value of $R = 1.44$Å (inferred from data at 0 C°) and experimental data for $\eta(T)$ yields remarkably good agreement with $\tau_D(T)$.[183, 184] Many have noted this agreement, and from it have concluded that τ_D corresponds to the rotational relaxation of single molecules. The same Stokes model also says that the (translational) diffusion constant is given by

$$\frac{1}{D(T)} = \frac{6\pi\eta(T)R}{k_BT} \propto \tau_D(T) \tag{7.26}$$

Experimentally $\tau_D(T)$ and $\frac{1}{D(T)}$ obey Arrhenius temperature dependencies with very similar rate coefficients. The agreement only breaks down in the supercooled region.[1, 184] Bertolini argues that the Arrhenius temperature dependence must be due to a barrier hoping process. The diffusion constant of water also has an Arrhenius temperature dependence, suggesting a relation between the two.[7] Agmon builds his theory for τ_D on this fact, suggesting that Debye relaxation is due to translational hopping, in particular, a motion he calls "tetrahedral displacement".[184] Tetrahedral displacement has a

"hopping distance" of 3.3 Å, which is "the separation between an occupied and unoccupied corners of a cube binding the pentawater tetrahedron".[184] On the basis of the temperature dependence of τ_D, Buchner proposed that τ_D depends on the production rate of "free molecules", which are molecules having only 1 or 0 H-bonds.[12] We will argue later that neither Agmon or Buchner's models can be correct, because they do not explain the collective nature of the relaxation.

7.4.2 The Debye relaxation is purely due to rotational motions

Debye relaxation is often described as "rotational". Agmon notes that the effect of isotopic substitution can yield insight into the dynamics at play.[184] For purely rotational dynamics, one expects a ratio of $\tau_{D_2O}/\tau_{H_2O} = \sqrt{2} = 1.41$, while for translational dynamics, one expects $\tau_{D_2O}/\tau_{H_2O} = 1.05$. The experimental ratio for the Debye relaxation is $\approx$1.15,[**?**], suggesting that both rotational and translational dynamics are at play. Interestingly, this ratio increases at lower temperatures and becomes very close to 1.05 near the boiling point.[**?**]

7.5 Mean-field theories

Despite its empirical validation, the Debye-Stokes model is clearly flawed, since it ignores interactions between molecules- notably dipole-dipole forces and H-bonding interactions. The effects of dipole-dipole interaction can be approximated using mean-field theory. The simplest mean-field theory is obtained by moving Debye's Brownian-perturbed dipole into a homogeneous medium described by a frequency dependent dielectric function $\varepsilon(\omega)$. The dipole then feels an additional "internal field" due to the polarization of the medium. After solving the system self-consistently, one again obtains the Debye equations for $\varepsilon(\omega)$, but now:[185]

$$\frac{\tau_D}{\tau_s} = \frac{\varepsilon(0) + 2}{\varepsilon_\infty + 2} = 10.8 \tag{7.27}$$

In other words, the relaxation time for the polarization of the entire system, as measured through $\varepsilon(\omega)$, is greater than the relaxation time for the single dipole τ_S. Here ε_∞ can be understood as the excess oscillator strength not described by Debye relaxation. We use the experimental values $\varepsilon(0) = 78.6$ and $\varepsilon_\infty = 5.4$ to obtain a ratio of 10.8. The actual ratio is close to 8. The relatively good

agreement of Debye theory is quite surprising, because the same exact theory gives a completely wrong estimate of $\varepsilon(0)$, and predicts that water exists in a ferroelectric phase at room temperature (see eqn. 3.12).

The Onsager mean-field model, consisting of a dipole in a cavity, is considered a significant improvement over Debye's model. Glarum extended Onsager's model to the time-dependent case,[67] recovering the Debye equations with:

$$\frac{\tau_D}{\tau_s} = \frac{3\varepsilon(0)}{2\varepsilon(0) + \varepsilon_\infty} = 1.46 \tag{7.28}$$

A similar theory by Powles yields:[186]

$$\frac{\tau_D}{\tau_s} = \frac{3\varepsilon(0)G_K}{2\varepsilon(0) + \varepsilon_\infty} \tag{7.29}$$

More sophisticated mean field theories have been developed, the details of which we will not recount here.[187, 188, 185, 189, 185] A common outcome of these models is that dipole-dipole correlations lead to the macroscopic dipole relaxation time being longer than the molecular one.

7.6 The high frequency excess

There is considerable controversy on how to fit the high frequency tail of the Debye relaxation, between 1 - 100 cm^{-1}, where there is unaccounted for excess response. Traditionally, this excess response has been fit by introducing a second Debye mode, characterized by a time constant τ_2. While the value of τ_D has been very well characterized, values for τ_2 vary considerably in the experimental literature. Recently it has been proposed that a 3rd Debye relaxation (τ_3) is also required to properly fit this region.[197, 198] An additional problem, noted by Benduci, is that the data on the temperature dependence of τ_2 is contradictory - Barthel et. al. find it increasing with temperature while Ronne, et. al. find it decreasing.[197]

As with the primary Debye mode, different authors have different hypotheses about the microscopic mechanisms that would underly the secondary and tertiary Debye modes. Traditionally, τ_2 has been associated with the hydrogen bond lifetime, which is known to be around 1 ps. However, hydrogen bond dynamics are very non-exponential, so in this light of this, the use of 1 or 2 additional exponentials is very *ad-hoc*. We argue that a distribution of Debye and resonance processes contribute to the excess response. The wide variation in experimental fits is explained by the fact that each experiment only measures a certain window of frequencies, and fitting varies accordingly.

τ_D(ps)	τ_2(ps)	$\tau_3)(ps)$	f_1	f_2	f_3	range (cm^{-1})	method	ref
8.3	1.0		72	1.69(3)		.03 - 3	DRS	Barthel, 1990[190]
8.4	1.1		72	1.75		.006 - 14	DRS	Buchner, 1997[12]
8.4	0.91		72(1)	1.77(6)		.075 -10	DRS	Peacock, 2009[191]
8.3	0.39		75	1.67(3)		.2 - 4	DRS	Sato, 2008[192]
8.3	0.36		72	2.12		6 - 83	ATR	Möller,2009 [193]
	0.248(8)		75(1)	1.67(3)			ATR	Yada, 2008[194]
7.0(3)	9.20(6)		70(1)	2.0(3)		2 - 66	TDS	Ronne, 1997[183]
8.3	0.42		73	2		.001 - 3	TDS	Fukasawa, 2005[195]
8.24(4)	0.18(14)		73	1.9(5)		2-50	fLS	Kindt, 1996[172]
8.8(6)	0.21(6)		73	1.5(8)		3-55	fLS	Venables, 1998[173]
7.8	0.2		73	1.6		.16-33	var	Liebe, 1991 [196]
8.21	0.39(5)		73	2.5(2)		.1 - 33	var	Benduci, 2007[197]
8.31	1.0*	0.10**	71.5	2.8	1.6	50-220	dFTS	Vij, et al. 2004[179]
8.26(3)	1.1(5)	0.14(4)	73	2.2(2)	1.3(3)	.1 - 33	var	Benduci, 2007[197]
8.5	0.93	0.08				.03-800	var	Ellison, 2007[6]
8.4(3)	1.05(15)	0.18(5)				0.02-37	var	Vinh, et al., 2015[198]

Table 7.2: Reported two-Debye and three-Debye fits for experimental data taken at 298 K (25 C). DRS = microwave dielectric relaxation spectroscopy, ATR = THz attenuated total reflectance spectroscopy, TDS = THz time domain reflection spectroscopy, fLS - femotosecond laser spectroscopy, dFTS = dispersive Fourier Transform Spectroscopy * HK model, $\alpha = 1, \beta = .77$ ** HK model, $\alpha = .9, \beta = .8$

Dielectric relaxation spectroscopy (DRS) experiments can only probe the low frequency part (.0001 - 2 cm^{-1}), while THz or microwave time-domain reflection spectroscopy (TDS) probes the"middle" frequencies (1 - 10 cm^{-1}, as does a variation known as attenuated total reflectance spectroscopy (ATR).[193] Finally, Fourier transform infrared spectroscopy (FTIR) can cover the region above 10 cm^{-1}.

7.6.1 Hydrogen bond network modes

Non-exponential H-bond dynamics have been analyzed by Luzar & Chandler,[200] who emphasize the coupling of H-bond dynamics to diffusion. Laage & Hynes

approx freq. (cm^{-1})	description	ref
50-65	H-bond bending	[184]
70	H-bond torsion	[184]
80-150	assymetric umbrella mode	[199]
150	H-bond sym stretch ("breathing")	[184]
180	H-bond asym stretch	[184]

Table 7.3: Some of the H-bond network modes.

found that after H-bonds break, water molecules undergo angular "jumps" rather than small-angle Brownian diffusion.[201] Molecular dynamics simulation by Kumar et. al. (2006) show that the relaxation of individual water molecules is described by the stretched exponential relaxation function:

$$\phi(t) = \exp\left[-\left(\frac{t}{\tau}\right)^{\beta}\right] \tag{7.30}$$

The stretched exponential corresponds to a distribution of relaxation times. Note that τ is not easily related to the mean relaxation time.[202] This is confirmed by femtosecond spectroscopy of HDO, where it has reported that single molecule relaxation has two components - fast (≈.7 ps) and slow (≈13 ps).[203]

7.6.2 Overlap of hydrogen bond network modes and inertial relaxation

Another point that is not appreciated in the contemporary literature is that a high frequency excess is a general feature of all dipolar liquids, both H-bonding and non H-bonding. Debate about the nature of this excess goes back to 1955, when Poley first noticed that an excess around 10 cm^{-1} (.3 THz) exists in many dipolar liquids.[204] To explain this so called "Poley absorption", Hill and others proposed that it was due to inertial motion.[205, 46] Physically, inertial motion can be pictured as either fast "rattling" of molecules within their potential energy wells or as nearly-free rotation over small angles.[206, 207] In water, this inertial absorption overlaps with hydrogen bond network vibrations. Inertial relaxation can be understood from a theoretical standpoint by considering a free rigid dipole subjected to Brownian kicks. In that case the relaxation function can be computed exactly:[205]

$$\phi(t) = \exp\left[-\frac{t}{\tau_1} + \frac{\tau_2}{\tau_1}\left\{1 - \exp\left(-\frac{t}{\tau_2}\right)\right\}\right] \tag{7.31}$$

where $\tau_1 = \xi/2k_BT$, $\tau_2 = I/\xi$, and ξ is the "friction constant" (units $N \cdot s$). In either the limit that the friction goes to zero or $t \to 0$ (limits corresponding to the inertial regime), one obtains a relaxation function which has the Gaussian form (eqn. 7.10). Inertial relaxation can be seen in the "polar structure plots" described in chapter 10 (fig. 10.6). Inertial modes only occur in the self part. The intensity of the inertial response is greatly enhanced at high temperature and suppressed at low temperature. Instantaneous normal mode analysis of water shows a broad spectrum of translational modes, extending

from very 1-400 cm^{-1} and peaked around 100 cm^{-1}.[208, 169, 172, 172] Spectroscopy of aqueous solutions can also provide clues. Monoatomic ions always decrease τ_D. Increases are observed for a glucose, ethanol, and other sugars and alcohols.[209] These solutes have the common that they contain hydroxyl groups which can form H-bonds. Increases in τ_D are also observed in non H-bonding solutes such as urea[209] and $CdSO_4$.[210]

7.7 Using the gLST relation as a novel constraint to fit the dielectric function of water

Fitting a spectrum with many overlapping peaks is a tricky business. Within the error bars of the data, many possible multiple possible fits may be equally valid. Additionally, as the size of the fitting parameter space grows, optimization methods may get caught in local minima. In this section we argue that the generalized LST relation can be used to determine the physicality of proposed fit functions. Taking $\omega = 0$ in the Kramers-Kronig relations (eqn. 2.113) yields the f-sum rule, which can be used as a constraint during fitting:

$$\sum_i f_i = \varepsilon(0) - \varepsilon_\infty \tag{7.32}$$

where f_i is the oscillator strength of the ith mode.

Barker shows how the generalized LST relation can also be derived from the Kramers-Kronig relation.[211] For a dielectric function described by a single Debye relaxation, the LST relation is:[211]

$$\frac{\omega_L}{\omega_T} = \frac{\tau_T}{\tau_L} = \frac{\varepsilon(0)}{\varepsilon_\infty} \tag{7.33}$$

This equation can be derived on very general grounds from electromagnetic theory as is described by Kivelson, et. al. (1989).[212] For a single damped harmonic oscillator mode, the gLST relation is:

$$\frac{(\omega_L^2 + \gamma_L^2)}{\omega_T^2} = \frac{\varepsilon(0)}{\varepsilon_\infty} \tag{7.34}$$

The dampening factor appears in the numerator since the longitudinal frequency is complex $\bar{\omega_L} = \omega_L + i\gamma_L$. The generalized LST relation for N Debye

modes and M damped harmonic oscillator modes reads:[211]

$$\sum_{i}^{N} \frac{\tau_{Ti}}{\tau_{Li}} \sum_{j}^{M} \frac{(\omega_{Lj}^2 + \gamma_{Lj}^2)}{\omega_{Tj}^2} = \frac{\varepsilon(0)}{\varepsilon_\infty} \tag{7.35}$$

This is an exact relation, and thus can be also be used as a constraint while fitting. One starts with a dielectric function of the form:

$$\varepsilon(\omega) = \sum_{i}^{N} \frac{f_i}{1 - i\omega\tau_{Di}} + \sum_{j}^{M} \frac{f_j \omega_{Tj}^2}{\omega_{Tj}^2 - \omega^2 - i\omega\gamma_j} + \varepsilon_\infty \tag{7.36}$$

This dielectric function can be rearranged into the following form:

$$\varepsilon(\omega) = \varepsilon_\infty \prod_{i}^{N} \frac{(\omega - i\omega_{Li})}{(\omega - i\omega_{Ti})} \prod_{j}^{M} \frac{\omega_{Lj}^2 - \omega^2 - i\omega\gamma_j}{\omega_{Tj}^2 - \omega^2 - i\omega\gamma_j} \tag{7.37}$$

The longitudinal frequencies correspond to points where $\varepsilon(\omega) = 0$. Solving for the longitudinal frequencies requires factoring a very messy $(N + 2M)$th degree polynomial, which is cumbersome but possible to do using numerical libraries that are available in Python or Matlab. An easier alternative method is to simply invert 7.37

$$\frac{1}{\varepsilon(\omega)} = \frac{1}{\varepsilon_\infty} \prod_{i}^{N} \frac{(\omega - i\omega_{Ti})}{(\omega - i\omega_{Li})} \prod_{j}^{M} \frac{\omega_{Tj}^2 - \omega^2 - i\omega\gamma_j}{\omega_{Lj}^2 - \omega^2 - i\omega\gamma_j} \tag{7.38}$$

By symmetry it should be easy to see that the dielectric function for $\frac{1}{\varepsilon(\omega)}$ has the same form as for $\varepsilon(\omega)$, but with the transverse frequencies changed to the longitudinal frequencies. Thus, we can do a separate fit of $\frac{1}{\varepsilon(\omega)}$ using the same dielectric function given in eqn. 7.36 (with the change of $\varepsilon_\infty \to \frac{1}{\varepsilon_\infty}$) to obtain the longitudinal frequencies.

This method of fitting allows us to use the gLST equation as a constraint.

To test this method of fitting, we use the experimental refractive index data compiled by Segelstein (1981).[10] While dated, the Segelstein dataset has the benefit that it covers the entire frequency range from $.001 - 200,000$ cm^{-1} We first did an interpolation of the Segelstein data on a logarithmic grid up to 18 cm^{-1} and a linear grid from 18-4000 cm^{-1}, to prevent biasing the fitting towards the Debye mode. We perform the fitting by minimizing the

sum of the relative errors squared:

$$\text{Cost} = \sum_i \left(\frac{\text{fit}_i - \text{data}_i}{\text{data}_i} \right)^2 \tag{7.39}$$

7.7.1 A new code for fitting dielectric spectra

A object oriented Python program was written github.com/delton137/spectrum_fitter that fits both $\varepsilon(\omega)$ and $\frac{1}{\varepsilon(\omega)}$. It can perform the fits separately using using just the f-sum rule constraint or together using the gLST relation.

We tried several different optimization algorithms using the SciPy Python library. First we used the differential evolution method, a type of genetic algorithm with each parameter constrained to a specified range. The advantage of this method is it suited for searching large parameter ranges, while the disadvantage is runs much slower than other methods we tried. The code currently uses differential evolution followed by additional fast optimization with the truncated Newton's method (TNC) and Sequential Least SQuares Programming (SLSQP).

7.7.2 Results of fitting f-sum and gLST constraints

Figure 7.7.2 shows a fit with 3 Debye relaxations, 2 Brendel peaks for H-bond stretching and H-bond bending, and 3 Brendel peaks for the librational region. Under this model, the LHS of the gLST relation is 456 while the RHS is 48.15. The 1st Debye relaxation contributes a factor of 1.55 to the gLST relation, while the 2nd Debye relaxation contributes a factor of 5.49 and the 3rd Debye relaxation contributes a factor of 6.48. In every type of fit we tried, inclusion of the 3rd Debye relaxation resulted in larger departure from the the gLST equation. If only 2 Debye relaxations are used in this model, the gLST LHS becomes 21.921, and the RMS error increases slightly from 0.120 to 0.125.

Figure 7.7.2 shows a fit with 3 Debye relaxations, 1 DHO peak for H-bond stretching and 3 DHO peaks for the librational region. Under this model, the LHS of the gLST relation here is 284 while the RHS is 48.15. The 2nd Debye relaxation contributes a factor of 7.11 and the 3rd Debye relaxation contributes a factor of 4.2 to the gLST relation. Interestingly, in this fit we gave the fitting procedure the option of suppressing the 3rd Debye relaxation. It was completely suppressed in the transverse case, further suggesting that it is not physical. We found that if we tried to include an additional Brendel or DHO linehsape between 10 and 100 cm^{-1} for the H-bond bending peak was completely suppressed by the fitting procedure ($f \to 0$).

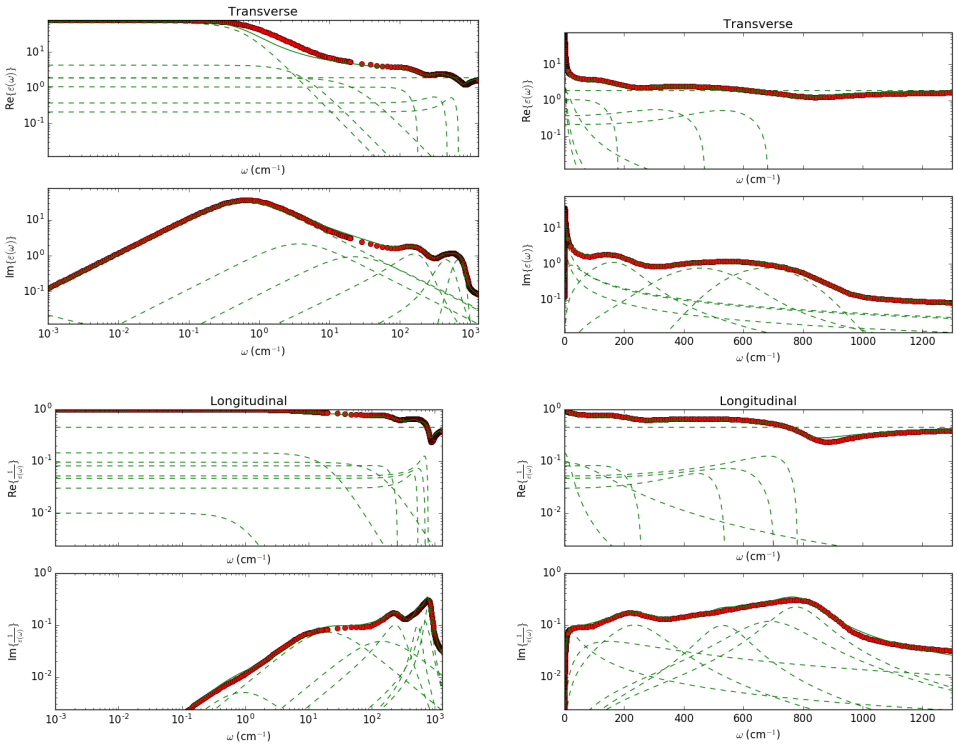

name	f	ω_0 (cm^{-1})	τ (ps)	γ (cm^{-1})	σ (cm^{-1})
Debye	0.01000	0.93	5.72		
2nd Debye	0.14439	20.33	0.26		
3rd Debye	0.09583	145.67	0.04		
Brendel Hbond Str	0.31331	258.58	0.129	221.05	2.85
Brendel L1	0.18003	704.24	0.047	283.57	12.11
Brendel L2	0.20105	781.90	0.043	183.49	7.20
Brendel L3	0.11668	538.43	0.062	162.55	21.65
eps inf L	0.44988				
name	f	ω_0 (cm^{-1})	τ (ps)	γ (cm^{-1})	σ (cm^{-1})
Debye	65.00000	0.60	8.88		
2nd Debye	4.27669	3.71	1.43		
3rd Debye	1.86412	22.47	0.24		
Brendel Hbond Str	3.43599	179.52	0.186	117.10	53.15
Brendel L1	1.28716	474.27	0.070	107.30	120.22
Brendel L2	0.74710	691.09	0.048	10.50	150.00
Brendel L3	0.01000	689.28	0.048	226.87	46.80
eps inf	1.88946				

Figure 7.1: Example longitudinal (top) and transverse (bottom) parameters. The fit contained 3 Debye relaxations, 1 Brendel peak for H-bond stretching, and 3 Brendel peaks for the librational region. The RMS error was 0.120.

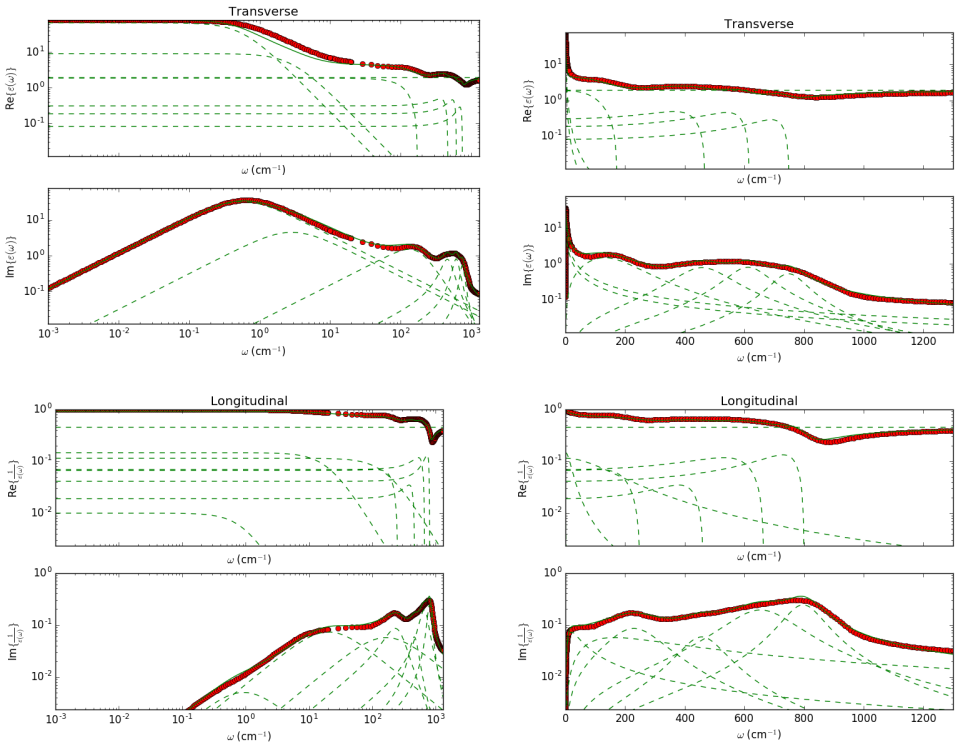

name	f	ω_0 (cm^{-1})	τ (ps)	γ (cm^{-1})	σ (cm^{-1})
Debye	0.01000	0.93	5.70		
2nd Debye	0.14537	20.36	0.26		
3rd Debye	0.11372	165.02	0.03		
Hbond Str	0.06641	250.01	0.021	203.29	
L1	0.01900	463.06	0.011	151.27	
L2	0.06915	665.03	0.008	240.08	
L3	0.04104	800.00	0.007	135.46	
eps inf L	0.45016				
name	f	ω_0 (cm^{-1})	τ (ps)	γ (cm^{-1})	σ (cm^{-1})
Debye	65.00000	0.57	9.32		
2nd Debye	8.97173	2.86	1.85		
3rd Debye	0.00001	39.25	0.14		
H-bond str.	1.85030	172.53	0.031	242.44	
L1	0.30808	467.75	0.011	184.65	
L2	0.18609	616.40	0.009	141.73	
L3	0.08187	750.00	0.007	115.23	
eps inf	1.91308				

Figure 7.2: Example longitudinal (top) and transverse (bottom) parameters. The fit contained 3 Debye relaxations, 1 DHO peak for H-bond stretching and 3 DHO peaks for the librational region. The RMS error was 0.124.

7.7.3 Collective nature of the relaxation

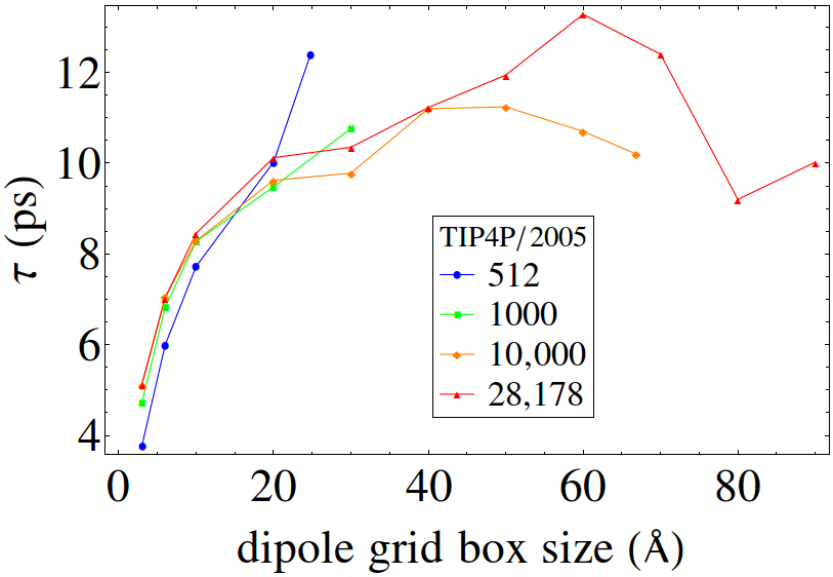

Figure 7.3: Debye relaxation calculated with different box sizes. This clearly shows that Debye relaxation is a collective phenomena, as box sizes of ≈ 2 nm are required for convergence.

A point that we wish to stress is that Debye relaxation is a collective phenomena. This is most easily seen by looking at the relaxation of sub-boxes of different sizes (fig. 7.7.3) and computing average relaxation times for the boxes. This dipole relaxation time does not converge to the bulk value until the box size is increased to ≈ 2 nm and therefore must involve the collective motion of hundreds of molecules. This appears to be inconsistent with the model for Debye relaxation proposed by Agnom[184] and similar H-bond breaking models that have been endorsed by some experimentalists.[198] Such models link the Debye relaxation time to the time for molecules to jump an energy barrier and undergo a particular type of rearrangement, which is inconsistent with the box-size dependence of the relaxation. Fig. 7.7.3 shows how the Debye peak exhibits dispersion with k, which confirms its collective nature. This dispersion was measured by Arbe et al. (2016) through neutron scattering,[213] where they found that the k dependence indicates diffusion but is not consistent with an interpretation in terms of a single hopping process, as in Agnom's model. Interestingly, Arbe et al. also found that the secondary Debye relaxation does not exhibit dispersion with k, and is therefore a local process.

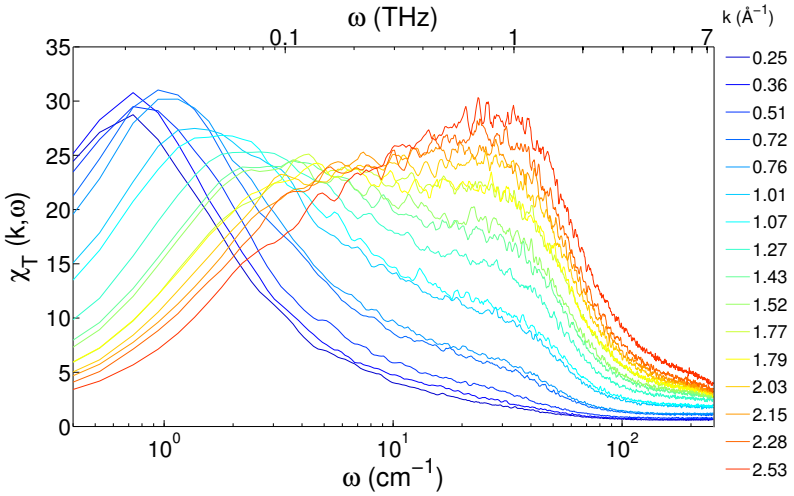

Figure 7.4: k dependence of the Debye relaxation (the peak on the left) for TIP4P/2005f.

7.8 Appendix: Relaxation at ultra low frequencies

Only a few studies report $\varepsilon(\omega)$ below 1 GHz.[214, 215, 216, 217] Ultra low frequency measurements of $\varepsilon(\omega)$ are complicated by the presence of charge build up on the electrodes, which leads to the Maxwell-Wagner-Sillars polarization response. Additionally, at very low frequencies (less than 1 kHz), the non-zero conductivity of water contributes to the dielectric function with a $\propto 1/\omega$ term. In 2010, Jansson, et. al. reported $\varepsilon(\omega)$ between 10^{-2} to 10^{6} Hz.[215, 216] A clear Maxwell-Wagner peak spans the interval between 10^{1} - 10^{5} Hz. They also report an ultra-slow Debye relaxation at $\approx 5\times10^{6} Hz$. Such "ultra slow" peaks have been observed in many alcohols. The work of Richert, et al. (2011) indicates that this ultra slow response is due to microscopic bubbles in the liquid.[218] Alternatively, the work of Casalini & Roland suggest that the low frequency peak is due to volatile non-polar contaminants.[219] It is possible both mechanisms were at play in Jansson's experiments, since they observe two ultra low frequency Debye peaks. New techniques which eliminate Maxwell-Wagner polarization and the ionic contribution promise to shed more light onto the situation.[220]

D.P. Shelton has reported a very slow relaxation time of 50 ns in liquid water from hyper Rayleigh scattering (HRS) at 280 nm.[221, 222, 223] Shelton interpreted these slow relaxations as being due to the relaxation of large scale

dipolar domains with sizes on the order of 200nm. In 2014, Shelton offered a new interpretation in terms of orientational coupling to long range acoustic modes.[224] In a more recent work, Shelton shows that the HRS measurements are consistent with the expected asymptotic limit $\propto r^{-3}$ in the orientational spatial correlation function on scales up to 2000 nm, which seems to indicate that his earlier interpretation of the experimental data in terms of domains was incorrect.[225]

7.9 Appendix: relevance to biology

There is growing interest in the use of terahertz spectroscopy to identify protein samples,[226] probe protein folding and dynamics,[227] and to study the dynamics of protein solvation water.[228, 229] Proteins exhibit large-scale collective modes in the low THz (between .01 - 10 THz or .3 - 330 cm^{-1}).[229, 230, 228] This is the same region of frequency disussed in this chapter. Recently computer simulations have shown that there exists "dynamical coupling" between a protein and its hydration water which may allow for biologically-relevant coupling between proteins that are physically separated by up to a nanometer or more. The extent of the dynamical hydration shell is the subject of current debate, with recent computer simulation suggesting it extends 5 - 10 Å, ie. at least 2-3 water layers.[231] The THz dynamics of proteins can be studied in anhydrous protein crystals as well. The biological relevance of frozen protein activity is questionable, though since the water is not included. An alternative is to study proteins frozen in glassy water. Starting from cryogenic temperatures, the temperature can be increased to analyze the thermal activation of different modes. Many cryogenic studies are focused on understanding the protein dynamical transition, which seems to be a type of glass transition that occurs between 100-200 K.

7.10 Appendix: cross-correlation time

This section is based on material in Brot, 1980.[232] We define the normalized cross correlation function:

$$\phi_{\mathrm{cc}}(t) \equiv \frac{\langle \boldsymbol{\mu}_1(0) \cdot \sum_{i \neq 1} \boldsymbol{\mu}_i(t) \rangle}{\langle \boldsymbol{\mu}_1(0) \cdot \sum_{i \neq 1} \boldsymbol{\mu}_i(0) \rangle} \tag{7.40}$$

Now consider the equation for $\Phi_D(t)$, recalling equation 2.63 ($g_K = \frac{\langle M^2 \rangle}{N\mu^2}$):

$$\begin{aligned}
\Phi_D(t) &= \frac{\langle (\sum_i \boldsymbol{\mu}_i(0)) \cdot \left(\sum_j \boldsymbol{\mu}_j(t) \right) \rangle}{\langle M^2 \rangle} \\
&= \frac{\langle \sum_i \boldsymbol{\mu}_i(0) \cdot \boldsymbol{\mu}_i(t) \rangle + \langle \sum_{i \neq j} \sum_j \boldsymbol{\mu}_i(0) \cdot \boldsymbol{\mu}_j(t) \rangle}{\langle M^2 \rangle} \\
&= \frac{1}{N \langle \mu^2 \rangle g_K} \left(N \langle \boldsymbol{\mu}(0) \cdot \boldsymbol{\mu}(t) \rangle + N \langle \boldsymbol{\mu}_1(0) \cdot \sum_{i \neq 1} \boldsymbol{\mu}_i(t) \rangle \right) \\
&= \frac{\phi(t)}{g_K} + \langle \boldsymbol{\mu}_1(0) \cdot \sum_{i \neq 1} \boldsymbol{\mu}_i(0) \rangle \frac{\phi_{cc}(t)}{\langle \mu^2 \rangle g_K} \\
&= \frac{\phi(t)}{g_K} + \frac{g_K - 1}{g_K} \phi_{cc}(t)
\end{aligned} \tag{7.41}$$

Where we used the relation $\langle \boldsymbol{\mu}_1(0) \cdot \sum_{i \neq 1} \boldsymbol{\mu}_i(0) \rangle = \langle \mu^2 \rangle (g_K - 1)$. We now integrate both sides from 0 to ∞ to get the following relation:

$$\tau_D = \frac{\tau}{g_K} + \frac{g_K - 1}{g_K} \tau_{cc} \tag{7.42}$$

Brot notes "It is reasonable to assume that, in structured liquids, whatever the nature of the correlations, parallel or antiparallel, their lifetime is larger than the correlation time τ of an individual molecule".[232] If we assume $\tau_{cc} > \tau$ (ie. $\tau_{cc} = \tau + \Delta$) then it is easy to prove that following inequalities hold:

$$\begin{aligned}
&\text{if } g_K > 1 \quad \tau_D > \tau \\
&\text{if } g_K < 1 \quad \tau_D < \tau
\end{aligned} \tag{7.43}$$

Also, if we have g_K, τ_D and τ from a simulation, we can calculate τ_{cc} using:

$$\tau_{cc} = \frac{\tau_D g_K - \tau}{g_K - 1} \tag{7.44}$$

Cross correlation times and g_k for TIP4P/2005 are shown in table 7.10.

Temp. (K)	τ (ps)	τ_D/τ	g_K (finite system)	τ_{cc}/τ
220	236	1.97	3.52	2.36
240	52	2.10	3.29	2.59
270	13	1.97	3.26	2.40
300	5.5	2.20	3.07	2.78
330	2.9	1.81	3.16	2.19
expt. at 300	1-2	5-10	2.9	9

Table 7.4: Relaxation times and g_K observed in a simulation of 512 TIP4P/2005 at 1kg/L

7.11 Appendix: the dipole randomization time

When one interprets "relaxation times" it is always with the understanding that one is dealing with an exponential function which actually exhibits correlations at times far greater than the relaxation time. The choice of defining the relaxation time as the time by which the correlation decays by a factor of e is a very useful convention but is actually quite arbitrary, corresponding to time when the correlation function is $\approx 63\%$ decayed. As an alternative method for quantifying correlation times, the dipole randomization time τ_r has been proposed.[5] The dipole randomization time τ_r is the sampling period at which dipole variables resemble uncorrelated random variables. To calculate τ_r one samples the normalized dipole moment $\boldsymbol{\mu}$ with a sampling period δt. At a large enough sampling period two samples $\boldsymbol{\mu}(t_i)$ and $\boldsymbol{\mu}(t_j) = \boldsymbol{\mu}(t_i + \delta t)$ will be independent (ie. $\langle \boldsymbol{\mu}(t_i) \cdot \boldsymbol{\mu}(t_j) \rangle = 0$ if $i \neq j$, where $\langle \quad \rangle$ denotes averaging over all the molecules and intervals). Any finite time average will have some variance from zero, however. If we have N samples with a sampling period of δt with $\delta t > \tau_r$ then the average for a single molecule is:

$$\bar{\boldsymbol{\mu}} = \frac{1}{N} \sum_{k=1}^{N} \boldsymbol{\mu}(t_k) \tag{7.45}$$

where $t_k \equiv k\delta t$. The total sampling time is denoted by $\Delta t = N\delta t$. The variance of this average will be:

$$\sigma^2 = \langle \bar{\boldsymbol{\mu}}^2 \rangle - \langle \bar{\boldsymbol{\mu}} \rangle^2 \tag{7.46}$$

The first term is the mean square, and is equal to:

$$\mu_{\text{MS}} = \frac{1}{N^2} \left\langle \sum_{i,j} \boldsymbol{\mu}(t_i) \cdot \boldsymbol{\mu}(t_j) \right\rangle = \frac{1}{N} \tag{7.47}$$

The root mean square of the average is given by

$$\mu_{\text{RMS}} = \frac{1}{\sqrt{N}} = \sqrt{\frac{\delta t}{\Delta t}} \quad \text{if } \delta t > \tau_r \tag{7.48}$$

What about the case when $\delta t < \tau_r$? One can show that for large enough Δt one still obtains $\mu_{\text{RMS}} \propto \frac{1}{\sqrt{\Delta t}}$.[5]

Thus the definition of τ_r becomes:

$$\mu_{\text{RMS}} \propto \frac{1}{\sqrt{\Delta t}} \begin{cases} \text{for any } \Delta t & \text{if } \delta t \geq \tau_r \\ \text{for } \Delta t \gg \tau_r \end{cases} \tag{7.49}$$

At this point hopefully it is clear that calculation of τ_r is somewhat ambiguous and more time consuming than calculation of τ. To start, one must calculate μ_{RMS} at different δt with varying Δt. To resolve ambiguities the authors introduce a fitting convention and cutoff.[5] Although this cutoff is somewhat arbitrary this does not mean this approach is a dead end. The authors find that $\tau_r = 5.1\tau$ for a wide range of temperatures (220 - 300 K). This suggests that meaningful correlations persist 5 x longer than τ. Perhaps this is not such a surprising result though, since at $t = 5\tau$ an exponential has decayed 99.3%, and the remaining .7% correlation may still be meaningful. For example, such small correlations may be what are showing up in the long time (100 ps) dipole-grid averaging procedure of Higo, et. al.[233]

Looking at μ_{RMS} as a function of Δt can also give some insight. One can take $\delta t = dt$ where dt is the timestep. The proceeding discussion still holds, so that at large Δt, $\mu_{\text{RMS}} \propto \frac{1}{\sqrt{\Delta t}}$. We can consider how μ_{RMS} will change as a function of box size - if we are averaging over many uncorrelated boxes, then $\mu_{\text{RMS}} \propto 1/\sqrt{N} \propto 1/\sqrt{V}$ where N is the number of molecules.[5] Figure 7.5 shows $\mu_{\text{RMS}} * V^{1/2}$ for several different boxes at 300 K and 220 K.

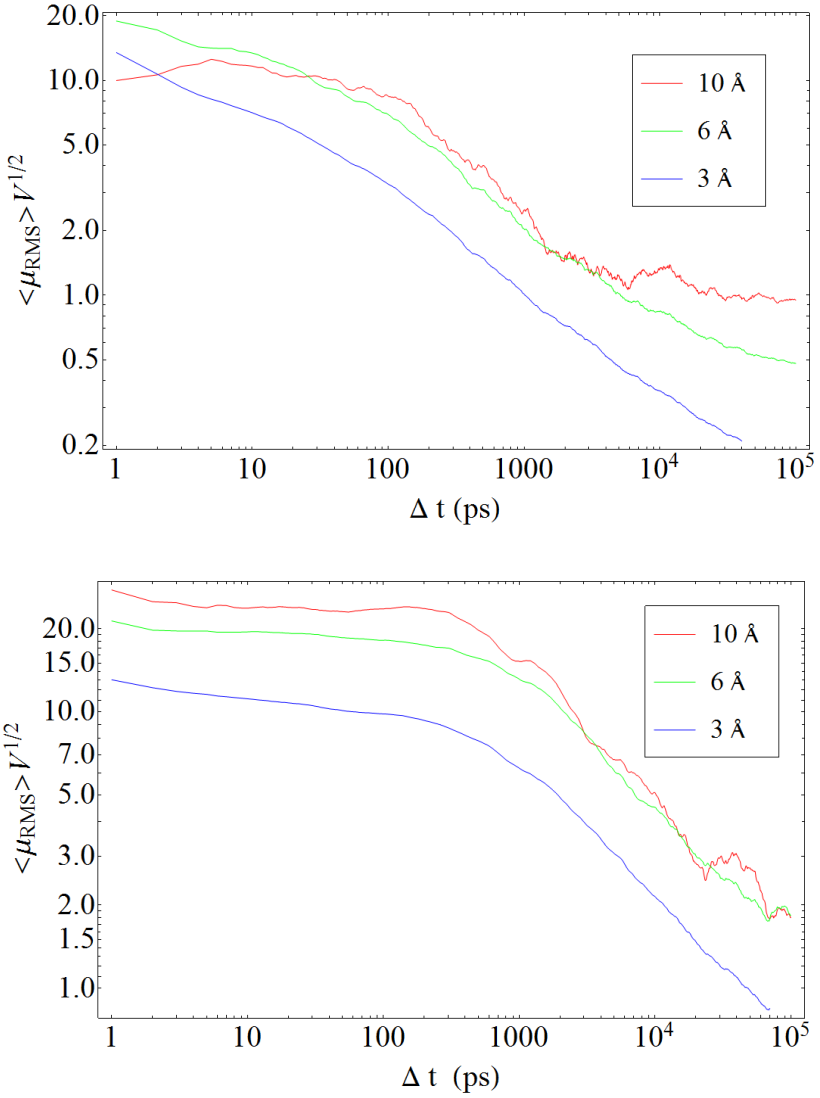

Figure 7.5: μ_{RMS} for different values of Δt at 300 K (top) and 220 K (bottom). As expected, the graphs approach $\frac{1}{\sqrt{\Delta t}}$ behaviour at large Δt, which appears as a slope of $\approx -1/2$ on this logarithmic plot. The fact that the 6Å and 10Å curves overlap at 300 K and 220K implies that dipole correlations do not persist much further than 6Å. This is different than the results previously reported for SPC/E, where it was found that all three curves overlapped at 300 K, suggesting very little spatial correlation.[5]

Chapter 8

Water as a relaxor ferroelectric

"That which can be destroyed by the truth should be." - P. C. Hodgell

This chapter explores interesting connections between the dielectric properties of water and relaxor ferroelectric ferroelectric materials. Water exhibits a wide variety of ordered phases. Most strikingly, Ice XI is a proton-ordered ferroelectric phase which forms when Ice Ih is cooled below 72 K. It has been observed that ferroelectrically ordered domains are preserved when Ice XI is transformed into Ice Ih, leading to easier reformation of Ice XI upon recooling.[234] Experimental evidence also suggests that films of ferroelectric ice grow on the 111 surface of platinum between 120 and 137 K under certain conditions of vapor deposition.[235] Water confined in carbon nanotubes is believed to exhibit ferroelectric order, as demonstrated in simulations of TIP5P-E water in 1.1-1.2 nm diameter nanotubes,[236] and in simulations of TIP4P ice in 1.1-1.33 nm diameter nanotubes.[237] Likewise, water that is confined in very narrow carbon nanotubes or membrane channels can form one dimensional "water wires" held together by hydrogen bonds.[238] In some special cases, water may form an extended hydration shell around proteins, beyond the typical shell thickness of 2-3 water diameters. Such extended shells, with thicknesses of 3-5 water diameters, were described as "ferroelectric" by one author.[239]

8.1 Background on relaxors

Relaxors show residual polarization after the applied field is turned off and thus are not true ferroelectrics. At high temperatures, relaxors exist in a paraelectric state, but unlike traditional ferroelectrics as the temperature is cooled they do not undergo a macroscopic phase transition. Instead, relaxor

properties gradually occur as the temperature is lowered (the onset of the relaxor phase is sometimes demarcated with the Burns temperature T_B). Key universal properties of relaxor ferroelectrics are:[240, 241]

1. high polarizability & dielectric constant
2. a broad peak in $\varepsilon(0, T)$ (loosely referred to as a "diffuse phase transition")
3. a peak in $\varepsilon(\omega, T)$ with respect to T and shifting of this peak with frequency.
4. strong deviation from the Curie-Weiss behavior $\varepsilon(0) = C/(T - T_0)$ except at very high T.
5. absence of spontaneous polarization and structural macroscopic symmetry breaking
6. ferroelectric-like response arising after cooling with an applied field to low temperature

At low temperatures, relaxors fall into two distinct categories. In "incipient relaxors", such as PSN ($Pb(Sc_{1/2}Nb_{1/2})O_3$), PST ($Pb(Sc_{1/2}Ta_{1/2})O_3$), or PZN ($Pb(Zn_{1/3}Nb_{2/3})O_3$) the relaxor ferroelectric transforms into a conventional ferroelectric at low temperature. Incipient relaxors are distinguished from "ordinary relaxor"' such as PMN ($Pb(Mg_{1/3}Nb_{2/3})O_3$) which form a glassy state at low temperature which is characterized by zero net moment and very low susceptibility. The theoretical underpinnings of such behavior has not been fully worked out, but experiments are offering new insights. It has been shown that an incipient relaxor can be transformed into a glassy relaxor by the introduction of vacancies. It is believed that vacancies create random fields in the crystal which "pin" domains upon cooling, leading to the glassy state. It has also been shown that hydrostatic pressure can reversibly transform an incipient relaxor such as PSN into a normal relaxor.

Experiments on a variety of perovskite materials indicate that relaxor ferroelectrics contain polar nanoregions.[240] In some relaxors these regions are embedded in a dielectric 'host' medium, while in others they fill all of space. The size of these regions depends greatly depends on the specific material in question – sizes ranging from $\approx 1 - 100$ nm have been reported.[242, 240] In one of the most famous relaxors, $Pb(Mg_{1/3}\ Nb_{2/3})O_3$ (PMN), they are believed to range in size from ≈ 2 nm at 400 K to ≈ 10 nm at 160 K. Measuring the precise size of polar nanoregions is difficult because they are too small to be

detected by optical diffraction measurements but usually too large to be detected by either high energy x-ray or neutron probes.[240] Thus the existence of these domains is usually inferred from a combination of electro-optical and dielectric measurements, or in rare cases, by direct measurement via transmission electron microscopy. In the case of incipient relaxors, it is widely believed that at low temperature PNRs coalesce to form macroscopic domains, leading to the ferroelectric state.

PMN is probably the most studied relaxor. PMN has the archetypal Perovskite structure with Mg^{2+} and Nb^{5+} ions randomly occupying the B sites. This disorder creates random crystal fields leading to displacement of the Pb atom in some direction. This, along with vacancies and other defects, creates local fields which greatly influence the formation and dynamics of the polar nanoregions.

A near-universal feature of relaxors is compositional disorder on the B site, which makes them very challenging to simulate. Supercells must be used and many different variations of disorder are possible, so conventional DFT simulation is usually impractical. Burton, et al. study PSN using a molecular dynamics simulations of a first principles based effective Hamiltonian designed for PSN.[242] They implement 40x40x40 unit cells corresponding to 320,000 atoms. With this system they performed 80,0000 MD steps corresponding to $\approx$ 70 ps. They also adapt their PSN effective Hamiltonian to study PMN by introducing local fields appropriate for PMN. They artificially introduce chemically ordered regions ("CORS") with B-site order and chemically disordered regions ("CDR"s) with B site disorder, and then look at the dielectric constant of the CDRs vs the CORs. They find (not surprisingly) that CORs have higher dielectric constants, smaller local fields and more dipolar correlation.

The concept of polarized nanoregions was questioned recently by Takenaka, Grinberg, and Rappe, who study PMN-PT (75% $PbMg_{1/3}Nb_{2/3}O_3$- 25% $PbTiO_3$) using classical MD simulation.[243] They argue that their results contradict the conventional picture of polar nanoregions. Their central argument revolves around their finding that the B atom vibrational displacements are large and spatially anisotropic, being very weak in the 110 and 111 directions. This contradicts the naive picture of spherically symmetric PNRs. They also argue that in order for the displacements to be as large as they are, they must highly correlated in space, otherwise they would incur too large of an energy cost. At high T, the thermal energy is high enough to disrupt this correlation, leading to paraelectric behavior dominated by dipole-dipole interactions. However, upon cooling they argue that larger and larger correlated structures emerge, and that the formation of these structures overwhelms dipole-dipole interactions. Strikingly, they draw an analogy to water, where the presence

of a hydrogen bond network frustrates dipole-dipole interactions. They say that a "coupling network mediated by the O atoms plays the role of the H bonds in water".[243] The PMN-PT system is probably not representative of most relaxor ferroelectrics, since it has additional compositional disorder. In their paper they do not give a motivation for studying PMN-PT as opposed to PMN, but their work builds off an earlier work on the same system.[244] The presence of discrete PNRs seems firmly established in PMN.

8.2 Temperature dependence of $\varepsilon(\omega)$

Plots of the real part of the dielectric function as a function of temperature are an important part of relaxor phenomenology and are often pointed to when characterizing materials as relaxors. Figure 8.1 shows the temperature dependence of the real part of the dielectric constant $\varepsilon'(\omega, T)$ at different frequencies for water. Strikingly, these plots exhibit the hallmarks of relaxor phenomenlogy - a large temperature dependent peak, (although at much higher frequencies than in relaxors). Of particular interest is the temperature dependence of the peak, which is best captured by TTM3F.

Prior to this work, to our knowledge such plots have only appeared once before, on the website of M. Chaplin.[2] Following the way Chaplin made his plot, we use a previously published two-Debye fit function for $\varepsilon(\omega, T)$ derived from experimental data by Meissner and Wentz.[**?**] This fit function contains 11 parameters and was developed to help make better climate models. The full fit function is:

$$\begin{aligned}
\varepsilon(\omega, T) &= \frac{\varepsilon_0(T) - \varepsilon_1(T)}{1 + i\frac{\omega}{2\pi}\tau_1(T)} + \frac{\varepsilon_1(T) - \varepsilon_\infty(T)}{1 + i\frac{\omega}{2\pi}\tau_2(T)} + \varepsilon_\infty(T) \\
\varepsilon_0(T) &= a_0 + a_1 T + a_2 T^2 \\
\tau_1(T) &= \frac{a_3 + a_4 T + a_5 T^2}{T_s + T} \\
\varepsilon_\infty(T) &= a_6 + a_7 T \\
\tau_2(T) &= \frac{a_8 + a_9 T + a_{10} T^2}{T_s + T}
\end{aligned} \tag{8.1}$$

It was shown that this fitting function well reproduces the experimental data for $\varepsilon'(\omega, T)$ between 273 and 373 K. In this fit the temperature dependence of τ_1 and τ_2 is computed using a modified Speedy expression with $T_s = 228$ K (-45 C). The use of the Speedy equation causes $\varepsilon'(\omega)$ to go to 0 at T_s.

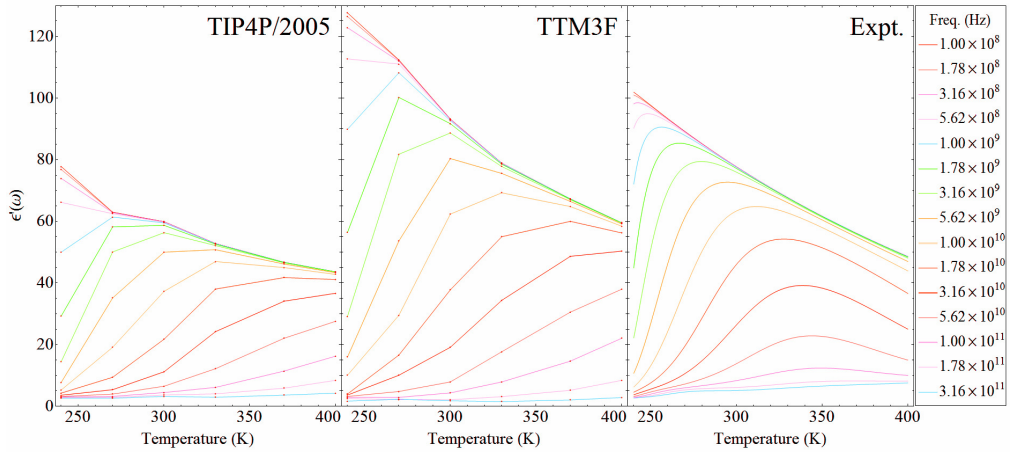

Figure 8.1: The temperature dependence of $\varepsilon'(\omega)$ at different frequencies. The experimental data actually a plot of a two-Debye fit function $\varepsilon'(\omega, T)$ derived from experimental data by Meissner and Wentz.[**?**] It was shown to very accurately reproduce experimental measurements between 273 and 373 K.

8.2.1 VFT temperature dependence and Adams-Gibbs theory

As shown in fig. 8.2 the temperature dependence of both τ_D is best described by the Vogel-Fulcher-Tammann (VFT) equation:

$$\tau = \tau_\infty \exp\left(\frac{DT_{\mathrm{VFT}}}{T - T_{\mathrm{VFT}}}\right) \tag{8.2}$$

VFT temperature dependence is a universal feature of both relaxor ferroelectrics and dipolar glasses.[245, 246] The underlying origin of the VFT equation is not very well understood, but most theories assume a distribution of relaxation environments within the bulk. Vilgis showed that a VFT-like expression results from two simple assumptions: a Gaussian distribution of energy barriers and a Gaussian distribution of the number of nearest neighbors.[247][1] A phenomenological theory by Tagantsev shows that near T_{VFT} VFT temperature dependence is a consequence of a very wide distribution of relaxation times

[1]The applicability of Vilgis's model to water is very questionable. If we take the 'number of nearest neighbors' to be the number of H-bonds per molecule, then the resulting distribution is better described by a binomial distribution (with $p_{\mathrm{HB}} \approx .9$), not a Gaussian distribution. Vilgis's derivation relies heavily on nice mathematical properties of the Gaussian function, which is the limit of the Binomial distribution when $p \to 0$. If one substitutes a binomial distribution into the derivation of Vilgis it is not that a clear that a VFT-like expression results.

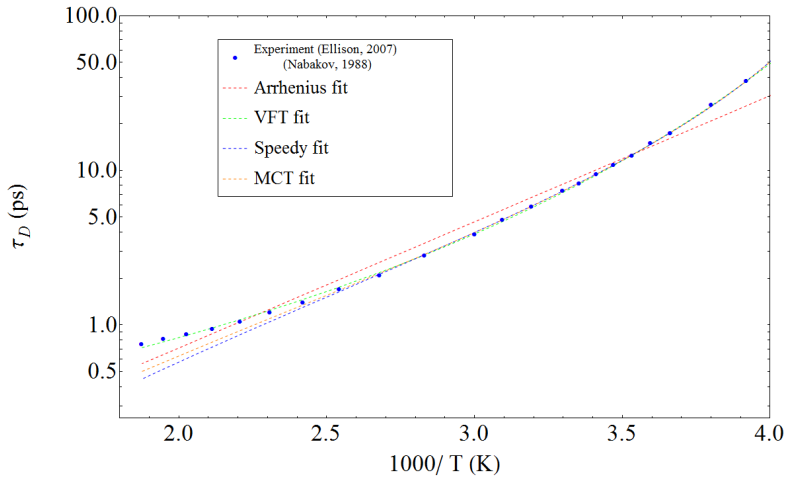

Figure 8.2: Arrhenius plot of $\tau_D(T)$ from experimental data,[6, 7] showing several fit functions. Only the VFT relaxation equation is capable of reproducing the experimental data over the full temperature range. In this fit, $T_{\mathrm{VFT}} = 126$ K

in the system which decreases in width as the temperature is increased.[248] At T_{VFT} the width of the distribution becomes infinite.[248] An very general theory for the VFT equation is the Adam-Gibbs model, which assumes the existence of cooperatively rearranging regions (CRRs).[249] In the Adam-Gibbs model relaxation assumes the following form:

$$\tau = \tau_\infty \exp\left(\frac{A}{k_B T S_{\mathrm{conf}}(T)}\right) \tag{8.3}$$

$S_{\mathrm{conf}}(T)$ can be found from the temperature dependence of the specific heat :

$$S_{\mathrm{conf}}(T_b) - S_{\mathrm{conf}}(T_a) = \int_{T_a}^{T_b} \left(\frac{C_p}{T}\right) dT \tag{8.4}$$

Recovering the VFT law requires that the specific heat of the liquid is independent of temperature, which is experimentally known to hold for water at low temperature. Adam & Gibbs argue that the configuration entropy reaches zero at precisely the glass transition temperature (T_g), so

$$S_{\mathrm{conf}}(T) = \int_{T_g}^{T} \left(\frac{C_p}{T}\right) dT \tag{8.5}$$

In addition to predicting VFT relaxation in glassy systems (and thus predicting the glass transition itself), the AG model solves the "Kauzmann paradox" by predicting that $T_k = T_g = T_{\mathrm{VFT}}$,[2] a fact which has been verified in many experiments.[250] Despite these successes, it is important to note that the physical plausibility of the CRRs in the AG model is still controversial.[250] One particular difficulty is that experimental studies attempting to measure the configurational entropy suggest that the CRRs are very small (4-8 molecules) even at very low temperatures close to the glass transition.[250] Such small regions cannot be considered as independent entities, as is assumed by Adams & Gibbs. In an analysis of supercooled water using the SPC/E model it has been suggested that the CRRs correspond to clusters of higher mobility which range in size from 2 - 12 molecules.[251] Clearly there are similarities between cooperatively rearranging regions and polar nanoregions.

8.3 Stretched exponential relaxation

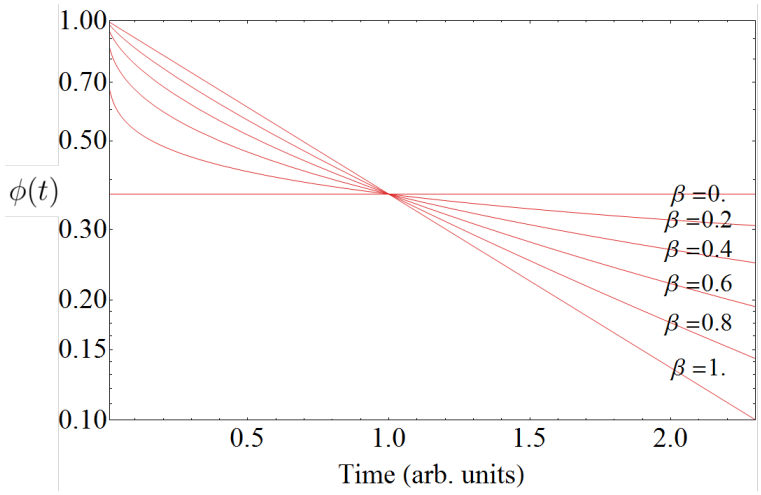

Figure 8.3: The stretched exponential function for various values of β.

The presence of PNRs of different sizes leads to a broad distribution of relaxation times, which leads to relaxation which is well characterized by a

[2]Here T_k is the Kauzmann temperature, which is the temperature that the entropy difference between the supercooled liquid and the crystalline state equals zero. The possibility of supercooling below T_k gives rise to the Kauzmann paradox, which is an apparent violation of the third law of thermodynamics.

stretched exponential:[252, 253]

$$\phi(t) = A \exp\left[-\left(\frac{t}{\tau_{\text{str}}}\right)^{\beta}\right] \tag{8.6}$$

Stretched exponential relaxation is very common in many materials.[3] Some have gone as far as to call it a "universal relaxation law" – in 1993 Bömer listed stretching exponents for over 70 materials, obtained by viscoelastic, calorimetric, dielectric, optical, and other response measurements. In the field of dielectric spectroscopy it is often referred to as the Williams-Watts (WW) or Kohlrausch-Williams-Watts (KWW) function after a paper by Williams & Watts in 1970.[255] The dielectric function corresponding to stretched relaxation does not have a closed form expression in terms, but Hilfer (2002) gives expressions for it in terms of an H-function.[167]

Klafter identifies three separate models which yield a stretched exponential relaxation – the Förster energy transfer model, the hierarchically constrained dynamics picture and the "defect diffusion model" – and he shows that all three share mathematical similarities.[256] Models yielding stretched exponential relaxation can generally be divided into two types - serial and parallel.[257] In a serial model, relaxation proceeds through a number of steps separated by barriers of different heights. In a parallel model, each molecule is relaxing exponentially through a single barrier, but there are different barrier heights for different molecules.

[3]Rudolf (Hermann Arndt) Kohlrausch (≈1809 - 1858) first proposed the stretched exponential in 1854 to describe the relaxation of charge from a glass Leiden jar.[254] He came to expression 8.6 by assuming that the decay rate $k = 1/\tau$ was not constant but deceased with time as $t^{-\beta-1}$.

8.3.1 stretched exponential relaxation distribution function

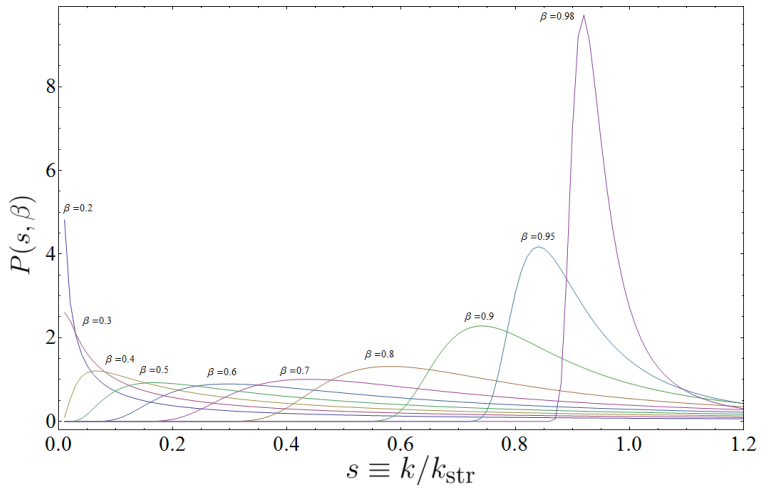

Figure 8.4: $G(k)$ distribution for various values of β.

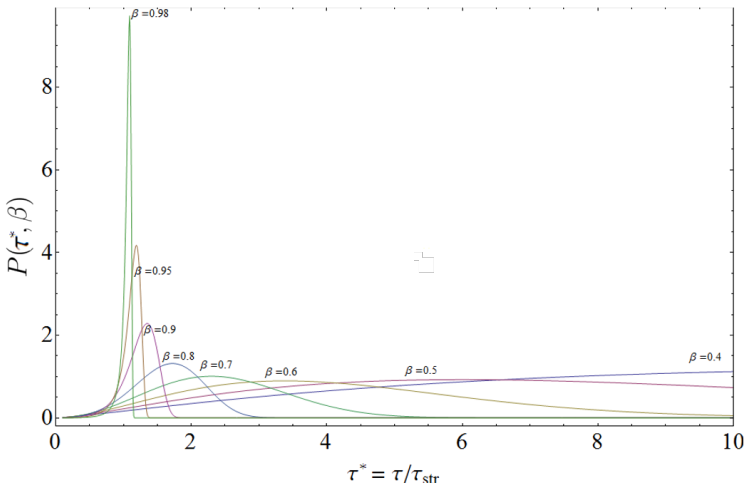

Figure 8.5: Same data as in fig. 8.3.1 but showing $G(\tau)$ for various values of β. (It appears that the normalization was lost during the transformation)

The stretched exponential can be understood as a continuous sum of exponential decays via the following transformation:

$$\exp\left[-\left(\frac{t}{\tau_{\text{str}}}\right)^{\beta}\right] = \int_0^\infty P(s,\beta)\exp\left(-s\frac{t}{\tau_{\text{str}}}\right)ds \tag{8.7}$$

Here s is defined as the dimensionless variable $s = k/k_{\text{str}} = \tau_{\text{str}}/\tau$.

Equation 8.7 is an example of a Laplace transform, thus, to recover $P(s,\beta)$ requires taking the inverse Laplace transform:

$$P(s,\beta) = \frac{1}{2\pi i}\int_\Gamma e^{-x^\beta}e^{sx}dx \tag{8.8}$$

Where Γ is a path from $-i\infty$ to $i\infty$ such that all the singularities in the integrand lie on the left. A change of variables $u = ix$ allows one to write this as a Fourier transform:

$$P(s,\beta) = \frac{1}{2\pi}\int_{-\infty}^{\infty} e^{-(iu)^\beta}e^{isu}du \tag{8.9}$$

$P(s,\beta)$ is a probability distribution normalized to one. Mathematically, there is a one-to-one correspondence between the space of asymmetric Lévy stable distributions and the space of functions of the form $\exp((kt)^\beta)$ where $\beta \in (0,2)$. Just as the central limit theorem says that independent identically distributed ("idd") random variables sampled from distributions with finite variance will eventually converge to a Gaussian, the generalized central limit theorem says that iid variables taken from distributions with power law tails of the form $|x|^{-\beta-1}$ ($\beta \in (0,2)$) will lead to asymmetric Lévy stable distributions.[258] This fact shows that the ubiquity of the stretched exponential in nature is related to the fact that power law distributions are also ubiquitous.

A few different formulae have been derived for calculating $P(s,\beta)$ for arbitrary β. One is a summation formula:

$$P(s,\beta) = \frac{1}{\pi}\sum_{n=1}^{\infty}\frac{(-1)^{n+1}\Gamma(n\beta+1)}{n!s^{n\beta+1}}\sin(n\pi\beta) \tag{8.10}$$

The convergence of this series appears to be very slow – to produce good plots $\approx$ 10,000 terms were required, thus making use of this formula very cumbersome even on a fast machine. A better equation can be obtained by looking at the real and imaginary parts of equation 8.9. It can be shown that the imaginary part is exactly zero (which is good because imaginary

probabilities don't make much sense). The real part is:[202, 259]

$$P(s,\beta) = \frac{1}{\pi}\int_0^\infty e^{-u^\beta \cos(\pi\beta/2)} \cos[su - u^\beta \sin(\pi\beta/2)]du \tag{8.11}$$

Equation 8.11 evaluates much faster – the production of a plot of $P(s,\beta)$ at $\approx$ with 1000 points takes about 1.5 minutes distributed over four 2.2 GHz i7 cores, using *Mathematica*.

It is also possible to obtain so-called "closed form expressions" (in terms of Airy, Bessel, Gamma, hypergeometric, and complex error functions) from eqn. 8.9 for rational values of β ($\beta = n/m$, where n and m are integers) although these expressions rapidly increase in complexity as with larger m. A particularly nice closed form expression is obtained for $\beta = 1/2$:[255]

$$P(s,\frac{1}{2}) = \frac{1}{\sqrt{4\pi s^3}} \exp\left(-\frac{1}{4s}\right) \tag{8.12}$$

8.3.2 Stretched relaxation in water

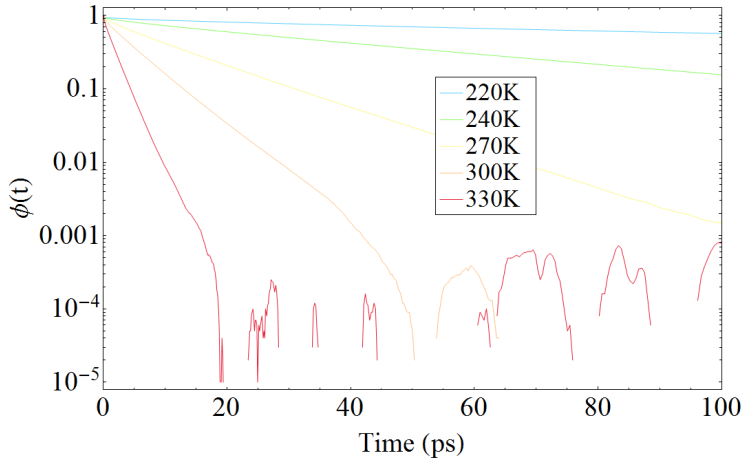

Figure 8.6: Single molecule correlation functions for TIP4P/2005.

Intriguingly, while the Debye autocorrelation function is perfectly Debye - ie. perfectly exponential, the single particle correlation $\phi(t)$ is better fit with a stretched exponential function.

T (K)	τ_D^{str} (ps)	β_D	τ_s^{str}	β_s
220	536	0.99	236	0.81
240	127	0.97	52	0.89
270	27	0.95	13	0.90
300	13	0.96	5.5	0.88
330	5.9	1.0	3.0	0.93
370	3.2	1.0	1.6	0.91
400	2.3	1.0	1.1	0.92

Table 8.1: Fit values for TIP4P/2005.

	τ_D (ps)	τ_D^{str} (ps)	β_D
1000 TIP4P			
3 Å	5.0	1.1	0.57
6 Å	5.3	2.8	0.74
10 Å	5.6	4.1	0.77
20 Å	7.6	5.5	0.76
1000 SPC/E			
3 Å	6.0	1.3	0.52
6 Å	6.7	4.2	0.75
10 Å	7.6	6.0	0.80
20 Å	9.3	8.7	0.89
256 q-TIP4P/2005f[?]			
3 Å	6.3	2.5	0.53
6 Å	7.1	6.9	0.59
10Å	10.0	8.5	0.78
512 TIP4P/2005			
3 Å	4.7	2.6	0.69
6 Å	6.1	6.1	0.93
10Å	8.8	8.0	0.92

Table 8.2: Fit values for τ_D, τ_D^{str} and β for various box sizes at 300 K.

Table 8.3.2 shows some values of of β found when fitting correlation functions from TIP4P/2005. These values are consistent with values previously reported for SPC/E.[5, 260]

Close inspection of fits reveals there are four regions to each correlation function:

1. (0 - .75 ps) - a short time decay corresponding to rapid librational/vibrational motions and hydrogen bond breaking/reformation, sometimes

collectively refereed to as the "second Debye relaxation".

2. (.75 ps - 3 ps) - a small "shoulder" region
3. (3 - 5 ps) - near exponential behaviour.
4. (5 ps -) - stretched exponential region

As shown in table 8.3.2, the Debye relaxation is very well characterized by an exponential ($\beta = 1$), although we observed some evidence of stretched behaviour at 220K and 240 K. The cross-over from exponential to stretched-exponential can be observed by analyzing boxes of different sizes (table 8.3.2).

8.3.3 Serial or parallel relaxation?

Normally $\phi(t)$ is computed by averaging over all the molecules in the system ($\phi_s(t) = \frac{1}{N}\sum_i^N \phi_i(t)$). As mentioned before, one can distinguish between two physical scenarios that can yield stretched exponential relaxation - parallel ("heterogeneous") relaxation different molecules go through different exponential relaxation processes with different τ and serial ("homogeneous") relaxation where each molecule's relaxation process is intrinsically stretched. Heterogeneous relaxation corresponds to a spatial distribution of Arrhenius energy barriers, whereas homogeneous relaxation corresponds to a relaxation process where each molecule has to relax through multiple barriers of different heights. Distinguishing these two cases is difficult and both relaxation processes may be combined. One might be able to distinguish heterogeneous from homogeneous relaxation by comparing a short time average over many molecules with a long time average $\phi(t)$ over a single molecule. If the short time averages are exponential with a broad distribution, then the relaxation is heterogeneous. The challenge is to do a long enough time average to obtain exponential fit, while at the same time not going too long since by the ergodic theorem, the same $\phi(t)$ will be obtained if one averages a bunch of short time averages from many molecules or a long time average from a single molecule. The fact that the long-time averages have finite width indicates the degree of error in the computation of β and τ_{str}.

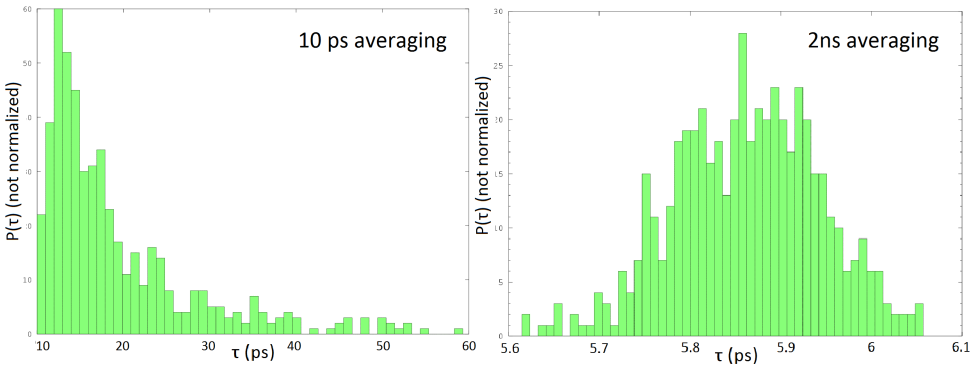

Figure 8.7: Distribution of τ when the correlation function for each molecule is analyzed separately for 512 TIP4P/2005 at 300 K for 10 ps (left) and 2ns (right).

Figure 8.3.3 shows the distribution of τ obtained from a 10 ps simulation with 512 molecules. Clearly, there is some heterogeneous relaxation present in the system. However, these correlation functions were not very well converged, so much of the distribution may be due to error in fitting. Figure 8.3.3 also shows the same distribution for a 2ns simulation. The distribution is much narrower, but still has some spread, suggesting a source of error in the fitting procedure.

8.4 Conclusion

In this chapter we explored several intriguing connections between the dielectric properties of water and relaxor ferroelectrics. In summary the similarities are:

- Ferroelectric phase at very low temperature.
- A peak in $\varepsilon'(T, \omega)$ and dispersion of the peak with frequency.
- VFT relaxation law

These similarities suggest the existence of polar nanoregions in water. However, water does not exhibit stretched dielectric relaxation, suggesting that discrete polar nanoregions of different sizes do not exist in water. Single molecule relaxation is stretched,[200] this is likely due to heterogeneity in the hydrogen bond network, although we were not able to clearly distinguish between homogeneous and heterogeneous relaxation processes.

Chapter 9

Nonlocal dielectric response

In a local dielectric, the relation $\boldsymbol{P}(\boldsymbol{r}) = \epsilon_0 \chi_e \boldsymbol{E}(\boldsymbol{r})$ holds at every point in space. In a nonlocal dielectric, this is not the case - the polarization at a given point depends not just on the electric field at that point but on the electric field at other points.[1] Any system with spatial correlations between dipoles will be nonlocal in space. Similarly, any system with temporal correlations between dipoles will be nonlocal in time. In this chapter we review the basic equations of nonlocal response and how one calculates the nonlocal response from a molecular dynamics simulation. Despite nonlocal response being nearly ubiquitous, studying the nonlocal response is unusual, partially because it is difficult to probe experimentally. However, the nonlocal response yields great insight into the structure and dynamics of water. The nonlocal dielectric function is also an important component in modeling solvation with nonlocal electrostatics, a technique currently being developed to efficiently calculate solvation free energies for ions and biomolecules.

9.1 Theory of the nonlocal response

To analyze the nonlocal case, we switch to the "nonlocal nomenclature" (see eqns 2.12 and 2.13). Therefore, χ will now denote a relation between $\boldsymbol{P}$ and $\boldsymbol{D}$, instead of between $\boldsymbol{P}$ and $\boldsymbol{E}$. The most general equation which is linear in the electric field is:

$$P_\alpha(\boldsymbol{r}, t) = \int_V \int_{-\infty}^{t} d\boldsymbol{r}' dt' \epsilon_0 \chi_{\alpha\beta}(\boldsymbol{r} - \boldsymbol{r}', t - t') D_\beta(\boldsymbol{r}', t') \tag{9.1}$$

[1] The speed of this non-local interaction is limited by the speed of light, but this is not usually factored in explicitly.

We assume spatial isotropy, so χ only depends on $\boldsymbol{r} - \boldsymbol{r}'$ and not on the absolute positions of $\boldsymbol{r}$ and $\boldsymbol{r}'$. This expression simplifies significantly when we take both the spatial and temporal Fourier transforms. Equation 9.1 is almost a convolution, except for the fact that, because of causality, the dt' integral only goes to t instead of to infinity. One can show though, by interchanging the order of integration in a similar way as done when proving the convolution theorem, that

$$\mathbf{P}(\mathbf{k},\omega) = \epsilon_0 \overleftrightarrow{\boldsymbol{\chi}}(\mathbf{k},\omega)\mathbf{E}(\mathbf{k},\omega) \tag{9.2}$$

Very few authors attempt to analyze the full response tensor $\overleftrightarrow{\boldsymbol{\chi}}$. For isotropic systems, the tensor can be decomposed into longitudinal and transverse components:

$$\overleftrightarrow{\boldsymbol{\chi}}(\boldsymbol{k},\omega) = \chi_L(k,\omega)\hat{\boldsymbol{k}}\hat{\boldsymbol{k}} + \chi_T(k,\omega)(\boldsymbol{I} - \hat{\boldsymbol{k}}\hat{\boldsymbol{k}}) \tag{9.3}$$

The easiest starting point for deriving microscopic expressions for $\chi_L(k,\omega)$ and $\chi_T(k,\omega)$ is the classical Kubo formula:[261]

$$\chi_{L/T}(\boldsymbol{k},\omega) = \frac{\beta}{\epsilon_0}\int_0^\infty dt \frac{d}{dt}\langle \boldsymbol{P}_{L/T}(\boldsymbol{k},t)\cdot\boldsymbol{P}^*_{L/T}(\boldsymbol{k},0)\rangle e^{i\omega t} \tag{9.4}$$

This expression relates the susceptibility to the time correlation function of the polarization in equilibrium. The longitudinal part of the polarization can calculated by Fourier transforming the defining expression for the the polarization:

$$\begin{aligned} \nabla\cdot\boldsymbol{P}(\boldsymbol{r},t) &= -\rho(\boldsymbol{r},t) \\ i\boldsymbol{k}\cdot\boldsymbol{P}(\boldsymbol{r},t) &= -\rho(\boldsymbol{k},t) \end{aligned} \tag{9.5}$$

$$\hat{\boldsymbol{k}}\cdot\boldsymbol{P} = \frac{i\rho(\boldsymbol{k},t)}{k} = P_L \tag{9.6}$$

Substitution of this into eqn. 9.4 allows one to calculate the longitudinal part of the response:

$$\chi_L(\boldsymbol{k},\omega) = \frac{\beta}{\epsilon_0 k^2}\int_0^\infty dt \frac{d}{dt}\langle \rho(\boldsymbol{k},t)\rho^*(\boldsymbol{k},0)\rangle e^{i\omega t} \tag{9.7}$$

For a system composed of point charges, the charge density is :

$$\rho(\boldsymbol{r},t) = \frac{1}{V}\sum_i\sum_\alpha q_{i\alpha}\delta(\boldsymbol{r} - \boldsymbol{r}_i(t) - \boldsymbol{r}_{i\alpha}(t)) \tag{9.8}$$

Here the index i runs over the molecules, α runs over the atomic sites on each molecule, $\boldsymbol{r}_i$ is the position of the center of mass of molecule i and $\boldsymbol{r}_{i\alpha} = \boldsymbol{r}_i - \boldsymbol{r}_\alpha$.

The charge density in k-space becomes:

$$\rho(\boldsymbol{k},t) = \frac{1}{V}\sum_i \sum_\alpha q_\alpha e^{-i\boldsymbol{k}\cdot(\boldsymbol{r}_i+\boldsymbol{r}_{i\alpha})} \tag{9.9}$$

To calculate the transverse part of the polarization we use the method of Raineri & Friedman to find the polarization vector of each molecule.[262] First we introduce a molecular polarization density $\boldsymbol{p}_i(\boldsymbol{k})$ so that we have

$$\boldsymbol{P}(\boldsymbol{k}) = \sum_i \boldsymbol{p}_i(\boldsymbol{k}) e^{-i\boldsymbol{k}\cdot\boldsymbol{r_i}} \tag{9.10}$$

We utilize the relation $i\boldsymbol{k}\cdot\boldsymbol{p}(\boldsymbol{r}) = -\rho(\boldsymbol{k})$ so we can write $\boldsymbol{p}_i$ as

$$i\boldsymbol{k}\cdot\boldsymbol{p}_i(\boldsymbol{k}) = -\sum_\alpha q_\alpha e^{-i\boldsymbol{k}\cdot\boldsymbol{r}_{\alpha i}} \tag{9.11}$$

As before $\boldsymbol{r}_{\alpha i}$ is the distance from each atomic site to the center of mass of molecule i. We now use the identity

$$e^x = 1 + x\int_0^1 ds e^{xs} \tag{9.12}$$

and taking into account the charge neutrality of each molecule we obtain

$$\boldsymbol{p}_i(\boldsymbol{k}) = -\sum_\alpha q_\alpha \boldsymbol{r}_{\alpha i}\int_0^1 ds e^{-i\boldsymbol{k}\cdot\boldsymbol{r}_{\alpha i}s} \tag{9.13}$$

$$\boldsymbol{p}_i(\boldsymbol{k}) = \sum_\alpha \frac{q_\alpha \boldsymbol{r}_{\alpha i}}{i\boldsymbol{k}\cdot\boldsymbol{r}_{\alpha i}}\left(e^{i\boldsymbol{k}\cdot\boldsymbol{r}_{\alpha i}} - 1\right) \tag{9.14}$$

The transverse part is then calculated as $\boldsymbol{P}_T = \hat{\boldsymbol{k}}\times\boldsymbol{P}$.

For ease of comparison and analysis, we define normalized time correlation functions:

$$\Phi_{L/T}(\boldsymbol{k},t) \equiv \frac{\langle \boldsymbol{P}_{L/T}(\boldsymbol{k},t)\cdot\boldsymbol{P}^*_{L/T}(\boldsymbol{k},0)\rangle}{\langle \boldsymbol{P}_{L/T}(\boldsymbol{k},0)\cdot\boldsymbol{P}^*_{L/T}(\boldsymbol{k},0)\rangle} \tag{9.15}$$

Substituting this into eqn. 9.4 and taking into account the isotropy of water we obtain:

$$\chi_{L/T}(k,\omega) = \chi_{L/T}(k,0)\int_0^\infty \dot{\Phi}_{L/T}(k,t)e^{i\omega t}dt \tag{9.16}$$

An alternate expression may be obtained by integrating by parts:

$$\chi_{L/T}(k,\omega) = \chi_{L/T}(k,0)\left(i\omega\int_0^\infty \Phi_L(k,t)e^{i\omega t}dt - 1\right) \tag{9.17}$$

This can be split into real and imaginary components:

$$\begin{aligned}\mathrm{Re}\{\chi_{L/T}(k,\omega)\} &= \chi_{L/T}(k,0)\left(\omega\int_0^\infty \Phi_{L/T}(k,t)\sin(\omega t)dt - 1\right)\\ \mathrm{Im}\{\chi_{L/T}(k,\omega)\} &= \chi_{L/T}(k,0)\omega\int_0^\infty \Phi_{L/T}(k,t)\cos(\omega t)dt\end{aligned} \tag{9.18}$$

The relations between $\chi_L(k,\omega)$ and $\chi_T(k,\omega)$ to the dielectric function in the infinite wavelength limit are as follows:[263, 264]

$$\varepsilon_L(k,\omega) = (1-\chi_L(k,\omega))^{-1} \quad \varepsilon_T(k,\omega) = 1+\chi_T(k,\omega) \tag{9.19}$$

$$\lim_{k\to 0}\varepsilon_T(k,\omega) = \lim_{k\to 0}\varepsilon_L(k,\omega) = \varepsilon(\omega) \tag{9.20}$$

$$\chi_L(k,\omega) = 1 - \frac{1}{\varepsilon_L(k,\omega)} \tag{9.21}$$

$$\chi_T(k,\omega) = \varepsilon_T(k,\omega) - 1 \tag{9.22}$$

Note that the transverse susceptibility is the k space generalization of what one normally calls "susceptibility". The dielectric function $\varepsilon(\omega) = \varepsilon'(\omega) + i\varepsilon''(\omega)$ is related to the infrared absorption coefficient through the following equations:

$$\alpha(\omega) = \frac{\omega\varepsilon''(\omega)}{cn(\omega)} \qquad n(\omega) = \sqrt{\varepsilon(\omega)} = \sqrt{\frac{|\varepsilon(\omega)| + \varepsilon'(\omega)}{2}} \tag{9.23}$$

9.2 Multipolar expansion of intramolecular part

The following section shows how the k-dependent polarization vectors (as computed above) are different than the k-dependent dipole moments of the molecules. Note that eqn. 9.9 for the charge density in k space can be Taylor expanded as:

$$\begin{aligned}\frac{\rho(\boldsymbol{k},t)}{k} &= \frac{1}{k}\sum_i\sum_\alpha q_\alpha \sum_n \frac{(-i\boldsymbol{k}\cdot\boldsymbol{r}_{i\alpha}(t))^n}{n!}\\ &= \boldsymbol{M}(\boldsymbol{k},t) + \boldsymbol{\mathcal{Q}}(\boldsymbol{k},t) + \boldsymbol{\mathcal{O}}(\boldsymbol{k},t) + \cdots\end{aligned} \tag{9.24}$$

Here $\boldsymbol{M}(\boldsymbol{k},t)$, $\boldsymbol{\mathcal{Q}}(\boldsymbol{k},t)$, $\boldsymbol{\mathcal{O}}(\boldsymbol{k},t)$ are contributions due to the molecular dipoles, quadrupoles and octupoles. In the limit $k \to 0$ from eqn. 9.7 it can be seen that only the dipole term contributes to the susceptibility. One obtains

$$\chi_L(k,\omega) \approx \frac{\beta}{3\epsilon_0 V}\int_0^\infty dt \frac{d}{dt}\langle \boldsymbol{M}_L(\boldsymbol{k},t)\cdot\boldsymbol{M}_L^*(\boldsymbol{k},0)\rangle e^{i\omega t} \tag{9.25}$$

with

$$\boldsymbol{M}_L(\boldsymbol{k},t) = \sum_{i=1}^{N_{\text{mol}}} \hat{\boldsymbol{k}}\cdot\boldsymbol{\mu}_i(t)e^{i\boldsymbol{k}\cdot\boldsymbol{r}_i(t)} \tag{9.26}$$

This expression has been used previously as an approximate expression at small k.[265, 266] However, Kornyshev shows quite convincingly that for water the higher order multipole terms are very important, even at the smallest k available in computer simulation.[267] Neglect of the higher order terms leads to severe consequences at large k, and in the limit $k \to \infty$ one will not recover the correct answer of $\chi_K = 1$. Instead, one gets the so-called "Onsager limit" for point dipoles:

$$\lim_{k\to\infty}\chi_L(k) = \frac{n\mu^2}{3\epsilon_0 k_B T} \tag{9.27}$$

The Onsager limit is approximately 13.5 if a point dipole of 3 D is used.

9.3 Calculation of $\varepsilon(k,0)$ from scattering experiments

The longitudinal response may be calculated as:

$$\begin{aligned}\chi_L(k) &= \frac{\langle\rho_q(k)\rho_q(-k)\rangle}{\epsilon_0 k^2 V k_B T}\\ &= \frac{S_q(k)}{\epsilon_0 k^2 V k_B T}\end{aligned} \tag{9.28}$$

The quantity $S_q(k)$, known as the static charge-charge structure factor, can be calculated from pair distribution functions that can be obtained from x-ray or neutron scattering data. It should not be confused with the normal structure factor, which depends on mass density. It is not our intent to go into a detailed description of scattering theory here. Instead, we will focus on some key results. In particular, let us consider a substance to have only one type of atom. Then one can observe a relation between the structure factor (be it

mass-mass or charge-charge) and the pair distribution function:

$$\begin{aligned} S(\boldsymbol{k}) &= \left\langle \frac{1}{N} \sum_{ij} \exp(-i\boldsymbol{k}\cdot\boldsymbol{r}_i) \exp(i\boldsymbol{k}\cdot\boldsymbol{r}_j) \right\rangle \\ &= 1 + \left\langle \frac{1}{N} \sum_{i,j\neq i} \exp(-i\boldsymbol{k}\cdot(\boldsymbol{r}_i - \boldsymbol{r}_j) \right\rangle \\ &= 1 + \left\langle \frac{1}{N} \sum_{i,j\neq i} \int\int \exp(-i\boldsymbol{k}\cdot(\boldsymbol{r}-\boldsymbol{r}'))\delta(\boldsymbol{r}-\boldsymbol{r}_i)\delta(\boldsymbol{r}'-\boldsymbol{r}_j) d\boldsymbol{r} d\boldsymbol{r}' \right\rangle \\ &= 1 + \left\langle \frac{1}{N} \int\int \exp(-i\boldsymbol{k}\cdot(\boldsymbol{r}-\boldsymbol{r}'))\rho(\boldsymbol{r}-\boldsymbol{r}') d\boldsymbol{r} d\boldsymbol{r}' \right\rangle \\ &= 1 + \rho \left\langle \int g(r) \exp(-i\boldsymbol{k}\cdot\boldsymbol{r}) d\boldsymbol{r} \right\rangle \end{aligned}$$

(9.29)

Here $g(r)$ is the radial distribution function and ρ is the number density.[2]

$$S(\boldsymbol{k}) = 1 + \rho \int (g(r) - 1) \exp(-i\boldsymbol{k}\cdot\boldsymbol{r}) d\boldsymbol{r} \tag{9.30}$$

If the system is isotropic then it is easy to show (by switching to spherical coordinates) that

$$S(k) = 1 + 4\pi\rho \int dr r^2 \frac{\sin(kr)}{kr} (g(r) - 1) \tag{9.31}$$

Now let's consider a molecular fluid. In particular, consider an interaction site model, where molecules consist of atomic sites carrying point charges arranged in a fixed geometry. Molecules will be labelled with the indices i, j and the atomic sites will be labelled with the indices α, β. We now calculate the charge-charge structure factor, assigning each atom a charge q_α. The distance

[2]Technically there is an issue with this equation however, which is that as $r \to \infty$ $g(r) \to 1$, so that the Fourier transform of $g(r)$ diverges at $r = 0$. This yields an extra term $\rho\delta(0)$. Experimentally, this term is of no use, since in a scattering experiment it corresponds to light which passes through the material without scattering. Therefore, it is conventional to drop the delta function.

vector for each atom from the molecular center will be designated $\boldsymbol{l}_{i\alpha}$.

$$S_q(\boldsymbol{k}) = \langle \frac{1}{N}\rho(\boldsymbol{k})\rho(-\boldsymbol{k})\rangle$$
$$= \frac{1}{V}\left\langle \left[\sum_i \sum_\alpha q_\alpha \exp(-i\boldsymbol{k}(\boldsymbol{r}_i + \boldsymbol{l}_{i\alpha})\right]\left[\sum_j \sum_\beta q_\beta \exp(i\boldsymbol{k}(\boldsymbol{r}_j + \boldsymbol{l}_{j\beta})\right]\right\rangle \tag{9.32}$$

It is standard to separate $S(\boldsymbol{k})$ into self ($i = j$) and distinct ($i \neq j$) parts so that $S(\boldsymbol{k}) = S^s(\boldsymbol{k}) + S^d(\boldsymbol{k})$. These are also called the *intra*molecular and *inter*molecular parts. We choose our molecular center to be on the oxygen atom. We will not go through the details of the expansion of this equation, which results in many factors. For each factor, a derivation similar to eqns 9.29 - 9.31 can be performed. The result for the distinct part is:

$$S_q^d(\boldsymbol{k}) = \frac{4Nq_H^2}{V}\int dr 4\pi r^2 \frac{\sin(kr)}{kr}[g_{OO}(r) + g_{HH}(r) - 2g_{OH}(r)] \tag{9.33}$$

The self part is:

$$S_q^s(k) = \frac{2Nq_H^2}{V}\left(3 + f_{\mathrm{HH}}(k)\frac{\sin(kd_{HH})}{kd_{HH}} - 4f_{\mathrm{OH}}(k)\frac{\sin(kd_{OH})}{kd_{OH}}\right) \tag{9.34}$$

More generally the charge-charge structure factor can be obtained from the pair correlation functions h_{ij} via:[268]

$$S_q^L(k,0) = \frac{N}{V}\sum_{ij} q_i q_j f_{ij}(k) w_{ij}(k) + \frac{N^2}{V^2}\sum_{ij} q_i q_j h_{ij}(k) \tag{9.35}$$

Here the first term is the self part, and

$$w_{ij} = \delta_{ij} + (1 - \delta_{ij})\frac{\sin(kl_{ij})}{kl_{ij}} \tag{9.36}$$

In eqn. 9.34 $f_{\alpha\beta}(k)$ are atomic form factors which depend on the details of the charge distribution around each atom. They are usually approximated as Gaussian functions with a characteristic width $\sigma_{\alpha\beta}$.[269] Experimentally, $f_{\alpha\beta}(k)$ may be further modified by Debye-Waller factors that take into account thermal motion. Often, the intramolecular charge distribution is modeled as a set of point charges, for which $f_{\alpha\beta}(k) = 1$. In our view, this explains the exceptionally good agreement found by Kornyshev when comparing his simulation results (for a point charge MD model) to neutron scattering data. In real water, charge is delocalized over the entire molecule and further delo-

calized between molecules along hydrogen bonds, so properly describing the intramolecular part is a challenge which is currently being addressed by several workers.

Clearly eqn. 9.35 can be employed in computer simulation to obtain $\chi_L(k)$. However, it has been shown that eqn. 9.35 performs poorly at reproducing small k values, largely due to the truncation of the Fourier transform at finite r. In neutron and x-ray scattering experiments a very similar problem occurs (in addition to other difficulties) so such data usually is not reliable at small k ($k < 1\text{Å}^{-1}$).

We also note in passing that there is a close similarity between eqn. 9.28 for $\chi_L(k,0)$ and the differential cross section of x-ray scattering.[270] The x-ray scattering cross section can be written as:[270]

$$\frac{d\sigma}{d\Omega} = \left\langle \left| \sum_j^{N_e} b_e e^{i\boldsymbol{Q}\cdot\boldsymbol{r}_j} \right|^2 \right\rangle \tag{9.37}$$

Where b_e is the scattering length for a single electron, N_e is the number of electrons in the sample and $\boldsymbol{Q}$ is the scattering vector. The expressions for the x-ray scattering cross section and $\chi_L(k,0)$ are nearly identical but differ in the charge contribution from each atom. In x-ray scattering the charge is proportional to the number of electrons on each atom. Since oxygen contains many more electrons than hydrogen, the oxygen atoms contribute much more to x-ray scattering and the hydrogen contribution is very small. The fact that x-ray scattering probes the electrons, which are mostly around the Oxygen, causes the relative weight of the peaks to change - in the x-ray cross section the peak at 3 Å^{-1} is suppressed and the peak at 2 Å^{-1} is enhanced relative to how the peaks appear in $\chi_L(k,0)$. It has been shown that smearing the charge on the oxygen atoms in a simulation increases the peak at 2 Å.[271]

9.3.1 A very peculiar equation for $\varepsilon(0)$

It was shown by Kornyshev, Kossakowski & Vorotyntsev that utilizing eqn. 9.35 to find $\varepsilon(k)$ at low k is difficult in practice because the equation is extremely sensitive to details of the radial distribution function at large r.[272] Kornyshev et al. expand $1 - 1/\varepsilon(k)$ for small k:

$$\chi_L(k) = 1 - 1/\varepsilon(k) = Ak^{-2} + B + Ck^2 + \mathcal{O}(k^4) \tag{9.38}$$

Kornyshev, et. al. report the expansion to be:[272]

$$\begin{aligned} A &= \frac{(8\pi N)^2 q_H^2}{V^2 k_B T} R_2 \\ B &= \frac{4\pi N q_H^2}{3V k_B T}(4d_{OH}^2 + d_{HH}^2 + 8\pi \frac{N}{V} R_4) \\ C &= \frac{\pi N q_H^2}{15 k_B T V}(d_{HH}^2 - 4d_{OH}^2 + 8\pi \frac{N}{V} R_6) \end{aligned} \tag{9.39}$$

Here R_i refers to the ith moment of the function $H(r) = g_{OO}(r) + g_{HH}(r) - 2g_{OH}(r)$:

$$R_n = \int_0^\infty dR R^n H(R) \tag{9.40}$$

Recalling that $h_{\alpha\beta} \equiv g_{\alpha\beta} - 1$, note that the following identity holds:

$$\begin{aligned} H(R) &= h_{OO}(r) + 1 + h_{HH}(r) + 1 - 2(h_{OH}(r) + 1) \\ &= h_{OO}(r) + h_{HH}(r) - 2h_{OH}(r) \end{aligned} \tag{9.41}$$

From this it is easy to see that $R_2 = 0$ due to the way $h_{\alpha\beta}$ is defined. Thus B is the leading term in the expansion. When $k = 0$ only B survives and we are left with this peculiar formula for the dielectric constant:

$$1 - \frac{1}{\varepsilon(0)} = \frac{4\pi N q_H^2}{3V k_B T}(4d_{OH}^2 + d_{HH}^2 + 8\pi \frac{N}{V} R_4) \tag{9.42}$$

To yield a value of $\varepsilon(0) = 80$ for water, the RHS of 9.42 must be equal to .9875. Kornyshev, et. al. investigated the behaviour of R_4 as a function of the cutoff distance, finding that it was highly oscillatory in nature. They report that "a difference in the third digit of R_4 leads to the change of the dielectric constant from 80 to infinity!".[272] They go on to say "In solving this task on the basis of binary correlation functions one needs the data at distances up to 100 Å."[272]

9.4 Static nonlocal susceptibility of water

In this section we report the static nonlocal susceptibilities $\chi_L(k, 0)$ and $\chi_T(k, 0)$ for water. In nonmagnetic media, when frequencies are low then only the longitudinal part of the response tensor contributes to the polarization.[269][3]

[3]This follows from Maxwell's equation $\nabla \times \boldsymbol{E}(\boldsymbol{r}, t) = -(1/c)\partial_t \boldsymbol{B}(\boldsymbol{r}, t)$ which in frequency form is $\nabla \times \boldsymbol{E}(\boldsymbol{r}, \omega) = -(i\omega/c)\boldsymbol{B}(\boldsymbol{r}, t)$. This shows that in the limit $\omega \to 0$ the electric field

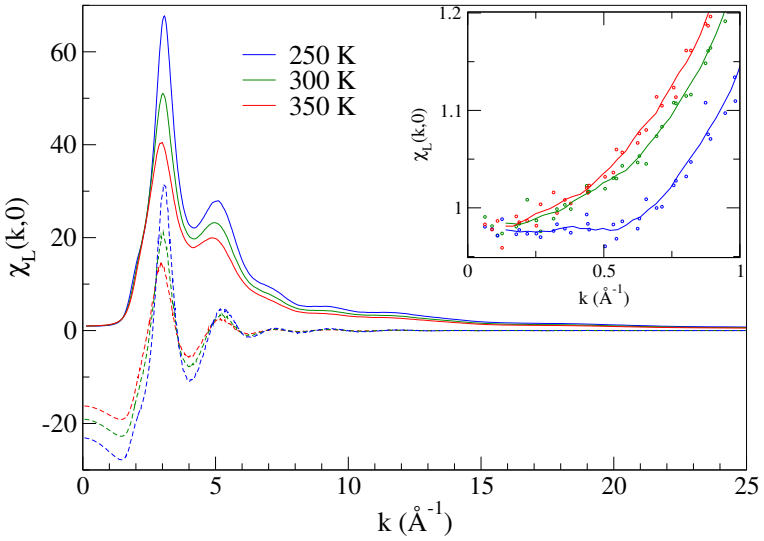

Figure 9.1: Static longitudinal susceptibility for a 10 nm box of TIP4P/ε (solid) and the distinct part (dashed). The behaviour at small k is shown in the inset. A running average is used to interpolate between the different k points. The scatter of the points is representative of size of the error bars we calculated (not shown).

The transverse static nonlocal susceptibility is therefore not of any direct physical import but has been referenced in theories of solvation.[262, 273]

Thermodynamic stability requires that $\chi_{L/T} > 0$.[274] This implies (see eqn. 10.1) that $\varepsilon(k)$ cannot be between 0 and 1. However, $\varepsilon(k)$ can be negative, a phenomena known as overscreening. A negative $\varepsilon(k)$ can lead to strange effects such as the attraction of like charges and the repulsion of opposite charges. Since $\varepsilon_L(k,0)$ cannot lie between 0 and 1, to pass from a positive value at $\varepsilon_L(0,0)$ to a negative value at finite k there must be a pole. Likewise, as $k \to \infty$ to pass from a negative value to the physical limit of $\varepsilon_L(\infty,0) = 1$ there must be another pole. Therefore the region of overscreening is always bounded by two poles in k space. These poles occur when $\chi_L(k,0) = 1$. Note that while a pole in $\chi_L(k,\omega)$ indicates a freely propagating mode, this is not the case for $\varepsilon_L(k,\omega)$, since $\varepsilon_L(k,\omega)$ is not a valid response function except at $k = 0$.[274, 267]

Overscreening was first found in computer simulation of molten salts.[275][4]

must become purely longitudinal, with no transverse component. The fact that only the longitudinal response contributes in electrostatics explains why the equations of electrostatics (ie. Gauss's law, etc) contain $1/\varepsilon$, as opposed to ε.

[4]The existence of negative $\varepsilon(\boldsymbol{k})$ took time to be accepted by the theoretical community,

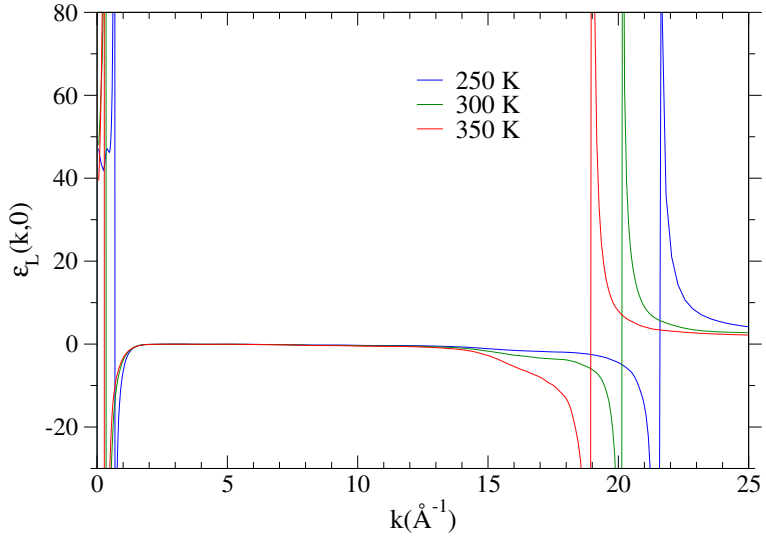

Figure 9.2: Static longitudinal dielectric function for a 10 nm box of TIP4P/ε, showing the overscreening (negative) region between $k^* \approx .5$Å^{-1} and $k \approx 20$Å^{-1}.

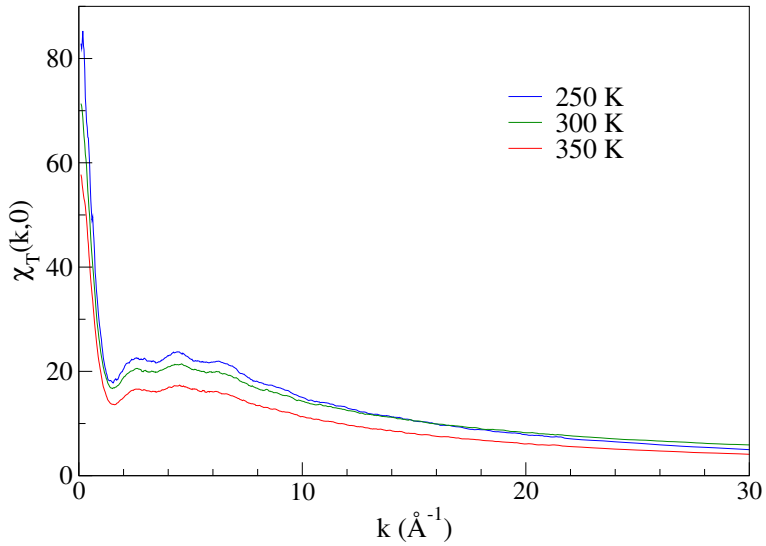

Figure 9.3: Static transverse susceptibility for a 10 nm box of TIP4P/ε.

It has been interpreted as being due to the presence of periodicity in the charge density at wavevector k.[267] In molten salts this periodicity may be due to alternating layers of charge. In water, it is due to the hydrogen bond network which creates dipole correlations. Additionally, in all molecular systems molecules automatically introduce charge periodicity on length scales corresponding to the molecular size. This contribution to $\chi_L(k,0)$ is contained entirely in the self part. Conversely, the distinct part contains k space information about the charge ordering among molecules.

Figure 9.1 shows $\chi_L(k,0)$ for a 10 nm box of TIP4P/ε. Most prominent is a peak at ≈ 3 Å^{-1} which corresponds to a wavelength of 2.1 Å – about the length of the hydrogen bond. While the H-bonded nearest-neighbor charge correlation is clearly a large contributor to this peak there is also a contribution from charge-charge correlation in the vicinity of the 3rd O-O shell (6 - 8 Å).[277] Also of interest is the peak at 2 Å^{-1} (compare with fig. 10.6) which becomes more prominent at lower temperatures.

The transverse susceptibility $\chi_T(k,0)$ is shown in figure 9.3. As $k \to 0$ it approaches $\varepsilon(0) - 1$. It also contains structure, but with peaks in different positions compared to the longitudinal case. At high k it converges very slowly to the limit $\chi_T(\infty,0) = 1$.

9.4.1 Behaviour at small k

We were very interested in the behaviour of $\chi_L(k,0)$ and $\varepsilon_L(k,0)$ at small k, since this is important for nonlocal theories of solvation. Assuming a spherical ion of charge q and radius a, the electrostatic contribution to the free energy of solvation can be approximated as:

$$\Delta F_{\text{elec}} = \frac{-q^2}{4\pi\epsilon_0}\int_0^\infty dk \frac{\sin^2 ka}{(ka)^2}\left(1 - \frac{1}{\varepsilon_L(k)}\right) \tag{9.43}$$

In actuality it has been shown that this equation performs worse than naive (local) Born theory.[**?**] However, the effective radii a can be reparametrized to make nonlocal Born theory more accurate than local Born theory.[**?**] The great shortcoming of nonlocal Born theory is that it does not take into account the reordering of the water molecules around the solute, which is obviously critical. In any case, to describe $\chi_L(k,0)$ a Lorentzian model has often been

many of whom had been working under the assumption that it was impossible. An influential proof that $\varepsilon(\boldsymbol{k},\omega)$ must always be greater than zero given by Landau & Lifshitz (1960) was shown to only be valid only in the limit $\boldsymbol{k} \to 0$.[276]

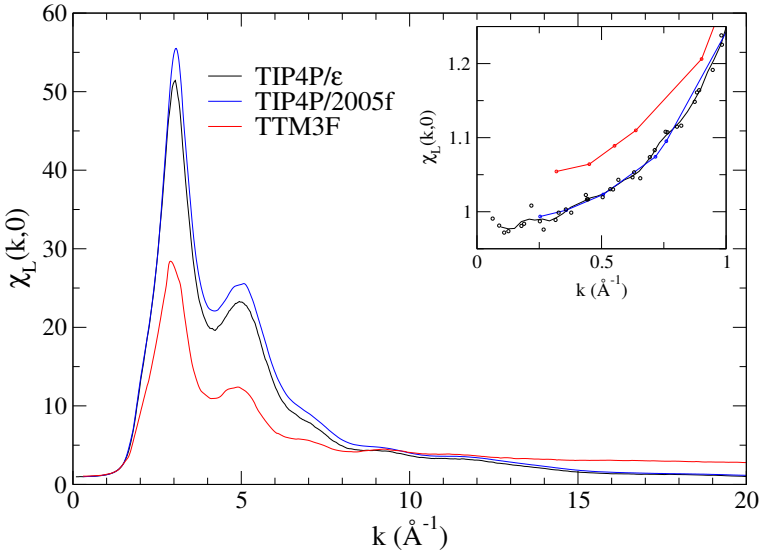

Figure 9.4: Static longitudinal susceptibility for three different models.

used:[278]

$$\chi_L(k) = \chi_{L\infty} - \frac{1}{\varepsilon_L(k)} = \frac{\chi_L(0) - \chi_{L\infty}}{1 + k^2\Lambda^2} + \chi_{L\infty} \tag{9.44}$$

Here Λ characterizes the length scale of dielectric screening. This function can be Fourier transformed analytically into real space:

$$\chi_L(R) = \frac{\chi_L - \chi_{L\infty}}{4\pi\Lambda^2}\frac{e^{-\frac{R}{\Lambda}}}{R} + \chi_{L\infty}\delta(R) \tag{9.45}$$

where $R \equiv |\boldsymbol{r} - \boldsymbol{r}'|$. Very similar equations also appear in the Thomas-Fermi theory of screening in the free electron gas, as well as in the linearised Poisson-Boltzmann theory of solvent screening around ions. The Lorentzian form is appealing because it's a simple function that processes the correct limits:

$$\begin{aligned} \chi_L(k) &\to \chi_L(0) \quad \text{as} \quad k \to 0 \\ \chi_L(k) &\to \chi_{L\infty} \quad \text{as} \quad k \to \infty \\ \chi_L(R) &\to \delta(R) \quad \text{as} \quad \lambda \to 0 \end{aligned} \tag{9.46}$$

Obviously, the Lorentzian model fails because it does not include the overscreening region which is ubiquitous for molecular liquids and spans a wide range of k in water. The presence of overscreening leads to an oscillatory structure in $\varepsilon(R)$, which indicates non-monotonic size dependence in the solvation energy of ions.[279] Somewhat confusingly, the same Lorentzian model

can also be applied to $\varepsilon_L(k,0)$, assuming one makes the transformation $\lambda = \sqrt{\frac{\varepsilon_\infty}{\varepsilon(0)}}\Lambda$.[279]

Despite the fact that it doesn't seem to be at all applicable, we would like to see if the Lorentzian model can be fit to $\varepsilon_L(k,0)$ at small k, and if so, an effective screening length can be determined. Computing $\varepsilon_L(k,0)$ at small k is very difficult, requiring large boxes and long simulation times. This so-called "small-k problem" has been discussed before.[280][267] We denote the position of the first divergence point as k^*. There are already a variety of results for k^*.[281, 267] We find $k^* = .68\text{Å}^{-1}$ at 250 K , $k^* = .34\text{Å}^{-1}$ at 300 K and $k^* = .27\text{Å}^{-1}$ at 350 K. We found that as longer and longer simulations are run and analyzed, k^* shifts to smaller and smaller k. For our longest simulation (65 ns) k^* becomes smaller than the smallest k available in the system ($k = .25\text{Å}^{-1}$). These results indicate that $\varepsilon(k)$ converges to $\varepsilon(0)$ much more slowly than previously reported. The fact that long wavelengths are required to obtain $\varepsilon(0)$ emphasizes the importance of long-range dipole dipole spatial correlation in determining $\varepsilon(0)$. Application of the Lorentzian model seems to be a complete loss. Interestingly, though, the Lorentzian model does seem appropriate for $\varepsilon_T(k,0)$ at small k. The physical interpretation of such "transverse screening" is unclear, however.

9.4.2 Effect of polarizability

As we discussed in chapter 5 the nonpolarizable model TIP4P/2005f does not capture the correct temperature dependence in dipole spatial correlation. This leads to the temperature dependence of the dielectric constant being poorly reproduced. This deficiency has been largely neglected in current analysis of the applicability of non-polarizable models. Figure 9.4.1 compares the nonlocal response of TTM3F with TIP4P/ε and TIP4P/2005f. TTM3-F contains one polarization dipole per molecule on the "M" site with $\langle\mu\rangle = 0.827$ D at 300 K. These dipoles are smeared ("Thole type") dipoles consisting of two Gaussian charge clouds that are brought infinitely close together. The polarization dipole can be incorporated into calculation of $\chi_L(k,0)$ simply by adding the longitudinal component to the geometric polarization. As is the case with point dipoles, the inclusion of smeared point dipoles results in a non-physical finite response at infinite k (see eqn. 9.27). For TTM3-F eqn. 9.27 yields $\chi_L(\infty,0) = 2.34$. The overall lower magnitude for TTM3F is due to the fact that model has about 50% less charge on each atom compared to TIP4P-like models.[271] TTM3F displays a larger overscreening region that is extended to smaller k, and the reason and significance of this is not clear.

9.4.3 Conclusion

Nonlocal electrostatics is a promising method for the calculation of solvation free energies for ions and biomolecules.[282] Contrary to earlier results, a recent study found that $\varepsilon(k)$ from the bulk may be sufficient for such calculations.[283] Correct nonlocal electrostatics for water requires including the divergences in $\varepsilon(k)$ using an analytic fit,[284] something which was ignored in many earlier studies. Overscreening is a result of both molecular structure and molecular ordering in the hydrogen bond network, and leads to the interesting phenomena of non-monotonic attraction or repulsion between ions in water. The development of fast algorithms that can solve the non-local Poisson equation in $k-$ space is a promising avenue for free energy calculations for computational drug design.

Chapter 10

Optical phonons in liquid water

10.1 Introduction

In this chapter we study the k dependence of the dielectric susceptibility, where $k = 2\pi/\lambda$. It has previously been shown that the librational peak in the longitudinal dielectric susceptibility of water is dispersive. The librational longitudinal mode we discuss is equivalent to the dispersive mode discovered by Ricci et al. (1989) in the spectrum of hydrogen density fluctuations.[285] Restat, Raineri and Friedman (1992) calculated $\chi_L(k,\omega)$ and found a dispersive "high frequency optical mode" in the librational part of the spectrum using the reference memory function approximation for TIP4P and SPC/E, but did not offer any specific theory for the origin of this mode.[286] Bopp & Kornyshev (1998) noted that the dispersion relation has the appearance of an optical phonon mode.[267] Hirata & Chong (1999) further investigated this mode using MD simulation,[287] and found that its basic phenomenology could be recovered from the Zwanzig-Mori formalism.[288]

k dependence in the dielectric spectra is hard to probe experimentally, requiring inelastic electron or neutron scattering experiments,[213] but in the limit of infinite wavelength ($k \to 0$) the longitudinal and transverse dielectric susceptibilities can be obtained from the dielectric function via the following relations:[263, 264]

$$\chi_L(k \to 0, \omega) = 1 - \frac{1}{\varepsilon(\omega)} \tag{10.1}$$

$$\chi_T(k \to 0, \omega) = \varepsilon(\omega) - 1 \tag{10.2}$$

As was discussed in chapter 2, the transverse susceptibility is what one normally calls susceptibility. The dielectric function can be obtained from the

index of refraction $n(\omega)$ and extinction coefficient $k(\omega)$ as:

$$\begin{aligned} \varepsilon'(\omega) &= n^2(\omega) - k^2(\omega) \\ \varepsilon''(\omega) &= 2n(\omega)k(\omega) \end{aligned} \tag{10.3}$$

These equations allow us to use previously published experimental data[8, 9] to calculate the imaginary part of the longitudinal response (see fig. 10.1).

Comparison of the peak positions in the longitudinal and transverse dielectric susceptibilities reveals longitudinal-transverse (LO-TO) splitting. LO-TO splitting indicates the presence of long-range dipole-dipole interactions in the system. One way to understand LO-TO splitting is through the Lyddane-Sachs-Teller (LST) relation:[289]

$$\frac{\omega_{\mathrm{LO}}^2}{\omega_{\mathrm{TO}}^2} = \frac{\varepsilon(0)}{\varepsilon_\infty} \tag{10.4}$$

Although this relation was originally derived for a cubic ionic crystal it was later shown to have very general applicability,[211, 290] and has been applied to disordered and glassy solids.[291, 292, 293] To apply this equation to water we must use a generalized LST relation which takes into account all of the optically active modes in the system and the effects of damping.[211] The generalized LST relation is:[211]

$$\prod_i \frac{\omega_{\mathrm{LDi}}}{\omega_{\mathrm{TDi}}} \prod_j \frac{|\bar{\omega}_{\mathrm{Lj}}|^2}{\omega_{\mathrm{Tj}}^2} = \frac{\varepsilon(0)}{\varepsilon_\infty} \tag{10.5}$$

Here the index i runs over the Debye peaks in the system and the index j runs over the number of damped harmonic oscillator peaks. The longitudinal frequencies of the damped harmonic oscillators must be considered as complex numbers ($\bar{\omega}_{Li} = \omega_{Li} + i\gamma_i$), where γ_i is the damping factor.

As shown by Barker, the generalized LST equation can be understood purely from a macroscopic point of view,[211] so by itself it yields little insight into microscopic dynamics. LO-TO splitting can be understood from a microscopic standpoint via the equation:[294, 295]

$$\omega_{Lk}^2 - \omega_{Tk}^2 = \frac{4\pi C}{3v} \left(\frac{\partial \boldsymbol{\mu}}{\partial Q_k} \right)^2 \tag{10.6}$$

Here v is the volume per unit cell, Q_k is the normal coordinate of mode k, and C is a prefactor which depends on the type of lattice and the boundary conditions of the region being considered (for an infinite cubic lattice, $C =$

1). More specifically, C can be related to the Lorentz field factor, which has been tabulated for many simple crystals.[295, 296] Equation 10.6 shows that LO-TO splitting is intimately related to crystal structure, and it has been used to evaluate the quasi-symmetry of room temperature ionic liquids.[297]. A full derivation of 10.6 is provided in appendix A, along with a description of how how C may be found for dipoles on simple lattices. Unfortunately, the relation between C and crystal structure is simple or one-to-one.

An overarching theme of this chapter is that the nonlocal dielectric susceptibility can be used to probe water's local structure and dynamics. We argue that water can support optical phonons that travel along the H-bond network of water. Our results indicate that not only does water exhibit LO-TO splitting, but also that its dependence with temperature is anomalous. We suggest that this measurement provides an alternative probe to evaluate structural changes in the hydrogen bond network of water as a function of temperature.

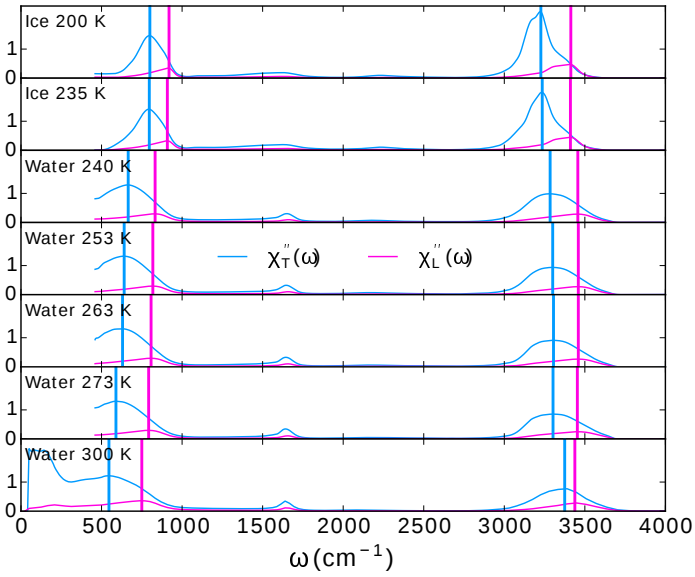

Figure 10.1: **Dielectric susceptibilities of ice and water.** Computed from index of refraction data using equations 10.1 and 10.3. data from 210 to 280 K comes from aerosol droplets[8] while the data at 300 comes from bulk liquid.[9]

10.2 The discrepancy in librational peak assignments

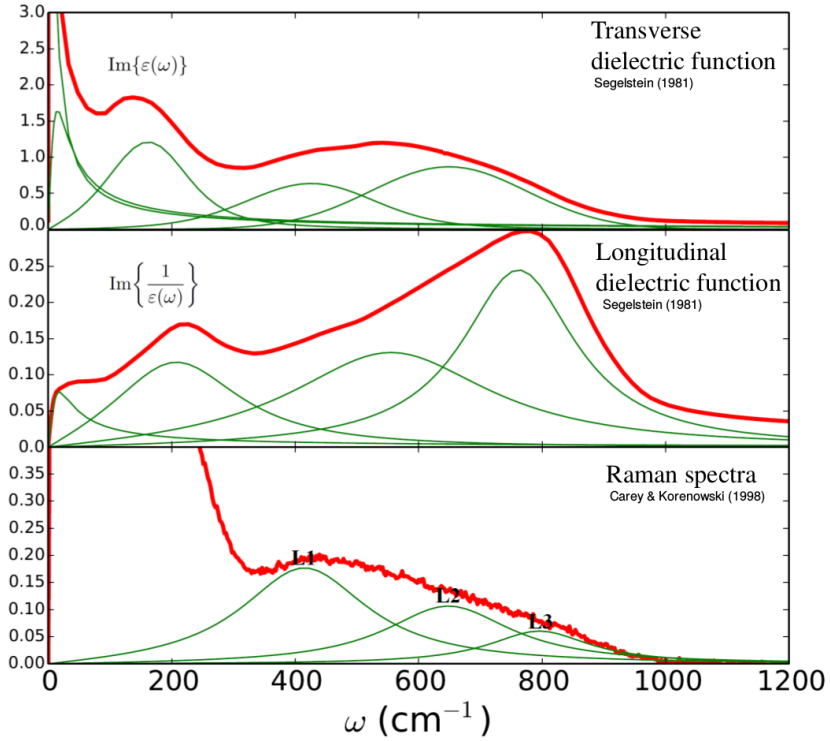

Figure 10.2: A figure highlighting the discrepancy in peak assignment. Dielectric functions derived from a compilation of experimental data by Segelstein,[10] with fits by D. C. Elton, while the Raman data comes from (Carey, 1998).[11] The Raman peaks are not fit but merely placed at the positions reported from Carey's fit.

We found that a previously unrecognised discrepancy exits between the peak assignments reported in Raman spectra with those reported in dielectric/IR spectra. Although early experimentalists fit the Raman librational band with two peaks,[298] it is better fit with three (See table 10.1).[11, 299, 300, 301, 302] Previously these three peaks were assigned to the three librational motions of the water molecule - twisting (≈ 435 cm^{-1}), rocking (≈ 600 cm^{-1}) and wagging (≈ 770 cm^{-1}).[11, 299, 301] However, when comparing these assignments to infrared and dielectric spectra, one runs into a serious discrepancy. One expects to find the two higher frequency modes to be present, since only the rocking and wagging librations are IR active. The twisting libration, consisting of a rotation of the hydrogen atoms around the C2 axis,

type	ω_{L1}	ω_{L2}	ω_{L3}	ref.
Raman	510	—	780	Bolla (1933) [308]
	450	—	780	Walrafen (1962) [309]
	400	—	700	Fukasawa, et. al. (2005)[195]
	430	650	795	Carey, et. al. (1998)[11]
	440	540	770	Castner, et. al. (1995)[302]
	450	550	725	Walrafen (1990)[299]
	424	550	725	Walrafen (1986)[301]
	439	538	717	Walrafen (1967)[300]
infrared	380	665	—	Zelsmann (1995) [303]
dielectric	420	620	—	Fukasawa, et. al. (2005)[195]

Table 10.1: Experimental Raman, dielectric, and IR spectra giving 2 peak and 3 peak fits to the librational region at 298 K.

is not IR active since it does not affect the dipole moment of the molecule. Instead, IR spectra show two peaks at 380 and 665 cm^{-1},[303] and similarly dielectric spectra show peaks at 420 and 620 cm^{-1},[195] in disagreement with this assignment (fig. 10.2).

The assignment of longitudinal optical phonon modes to Raman spectra can be made via the longitudinal dielectric susceptibility. This method has been used previously to assign longitudinal phonon modes to the Raman spectra of ice Ih,[304, 305, 291] ice Ic,[306] and vitreous GeO_2 and SiO_2.[307]

Later we present evidence that the lowest frequency librational Raman peak ($\approx$ 435 cm^{-1}) is a transverse optical phonon-like mode while the highest frequency peak ($\approx$ 770 cm^{-1}) is a longitudinal optical phonon-like mode. This explains why the highest frequency Raman mode does not appear in IR or dielectric experiments, since such experiments only report the transverse response.

10.3 Computational methods

The three water models we used were TIP4P/ε,[310] TIP4P/2005f,[132] and TTM3F.[15] A summary of the simulations that were run is shown in table 10.2. To simulate methanol and acetonitrile we used the General AMBER Forcefield (GAFF),[311] a forcefield with full intramolecular flexibility which has been shown to satisfactory reproduce key properties of both liquids.[312] Our TTM3F simulations were performed with an in-house code that uses the TTM3F force calculation routine of Fanourgakis and Xantheas. All other simulations were ran using the GROMACS package (ver. 4.6.5).[137] We

Model	Temp	N_{mol}	L(nm)	t(ns)	Δt_{out}(ps)
TIP4P/ε	250, 300, 350	33,049	9.96	6	1
TIP4p/ε	300	17,815	12x12x4	0.3	.012
TIP4p/ε	300	512	2.48	100	.1
TIP4p/ε	300	512	2.48	2	.002
TIP4P/2005f	300	2,228	4.05	0.18	.002
TIP4P/2005f	300	2,228	4.05	0.72	.008
TIP4P/2005f	250	512	2.48	1.2	.004
TIP4P/2005f	300, 350	512	2.48	0.6	.004
TIP4P/2005f	250	512	2.48	16	.008
TIP4P/2005f	300, 350	512	2.48	8	.008
TTM3F	300	256	1.97	2.5	.002
TTM3F	250, 350	256	1.97	1	.004
MeOH (GAFF)	300	1,000		1	.008
ACN (GAFF)	300	1,000		1	.008

Table 10.2: Details of the simulations that were run.

used particle-mesh Ewald summation for the long range electrostatics with a Coloumb cutoff of 2 nm for our 4+ nm simulations and a cutoff of 1.2 nm for our simulations with 512 molecules. Our TTM3F simulations used Ewald summation and a Coulomb cutoff of .9 nm. All simulations were equilibrated for at least 40 ps prior to outputting data. The principle TIP4P/2005f simulations contained 512 molecules and were 8 ns long ($\Delta t_{\mathrm{out}} = 8$ fs) and 0.6 - 1.2 ns long ($\Delta t_{\mathrm{out}} = 4$ fs). Other simulations were 1-2 ns long. Simulations with MeOH and ACN contained 1,000 molecules, while the TTM3F simulations contained 256 molecules. Small output steps (Δt_{out}) were required to avoid the complication of spectral folding, where spectral features higher than $f = 1/2\Delta t_{\mathrm{out}}$ are folded onto the spectrum. The combination of long runs, a small output step and large boxes requires a lot of disk space, so we utilized the .xtc compression feature of GROMACS. Because of periodic boundary conditions, the possible k vectors are limited to the form $\boldsymbol{k} = 2\pi n_x \hat{\boldsymbol{i}}/L_x + 2\pi n_y \hat{\boldsymbol{j}}/L_y + 2\pi n_z \hat{\boldsymbol{k}}/L_z$, where n_x, n_y, and n_z are integers. We calculated correlation functions separately for each $\boldsymbol{k}$ and then average over the results for $\boldsymbol{k}$ vectors with the same magnitude, a process we found greatly reduced random noise.

One can question whether a purely classical treatment is justified here because the librational dynamics we are interested have frequencies of 700-900 cm^{-1} for which $\hbar\omega \approx 3 - 4k_BT$ at 300 K. Previously it was shown that the widely-used harmonic approximation does not change the spectrum.[267] whereas applying the so-called standard approximation does. In either case,

such quantum correction factors do not shift the position of peaks, but only change their magnitude (and to a lesser extent their shape).[313] Furthermore, comparison of k resolved IR spectra taken from molecular dynamics and *ab-initio* DFT simulation show that they give qualitatively similar results for all frequencies below 800 cm^{-1}, at least when Wannier-center charges are used to describe the charge distribution.[314] For the OH stretching peak, however, quantum effects are known to be very important.

10.4 Fitting the librational band

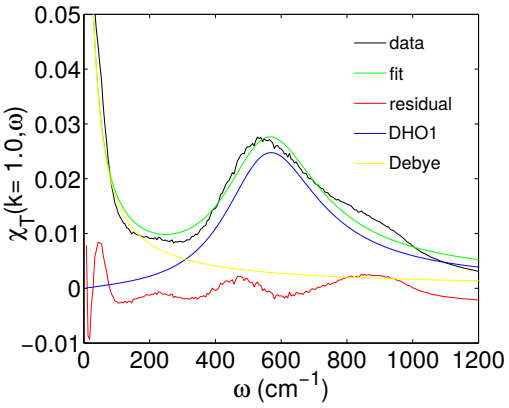

Figure 10.3: Examples of fitting the transverse susceptibility of TIP4P/2005f at 300K with a Debye function and one damped harmonic oscillator at $k = 1.0\text{Å}^{-1}$. The residual shows what is not captured by the fit.

To obtain resonance frequencies and lifetimes for the librational peak in the imaginary part of the response we used a damped oscillator model. A Debye peak overlaps significantly with the librational band in both the longitudinal and transverse cases and must be included in the peak fitting. Equation 9.16 can be used to relate the form of the time correlation function to the absorption peak lineshape. For Debye[80] response one has the following expressions:

$$\begin{aligned} \Phi(k,t) &= Ae^{-t/\tau_D} \\ \frac{\chi(k,\omega)}{\chi(k,0)} &= \frac{A}{1-i\omega\tau_D} \\ \frac{\text{Im}\{\chi(k,\omega)\}}{\chi(k,0)} &= \frac{A\omega\tau_D}{1+\omega^2\tau_D^2} \end{aligned} \tag{10.7}$$

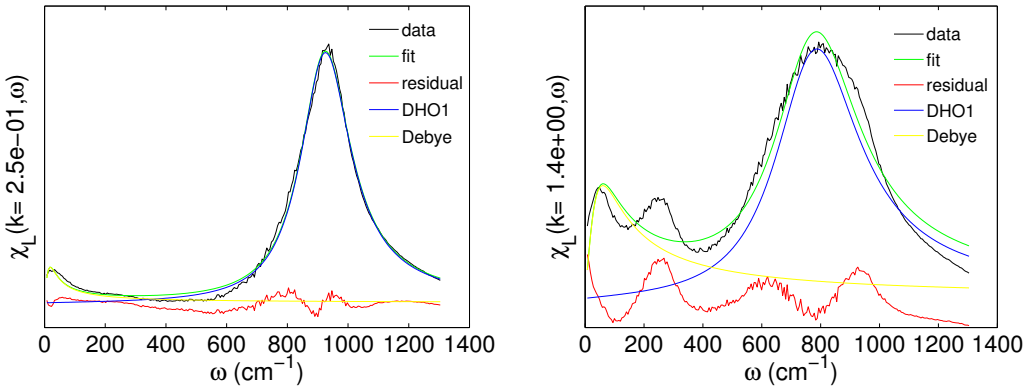

Figure 10.4: Examples of fitting the longitudinal susceptibility of TIP4P/2005f at 300K with a Debye function and one damped harmonic oscillator at $k = .25\text{Å}^{-1}$ and $k = 1.4\text{Å}^{-1}$. The residual shows the parts not captured by the fit. Two peaks appear in the residual - the lower frequency peak is dispersive, having the same dispersion relation as the fitted peak, suggesting that it is actually part of the dispersive peak lineshape that is not captured by our lineshape function. The higher frequency peak in the residual is non-dispersive and is in the same location for both the transverse and longitudinal susceptibility.

For resonant response with resonance frequency $\omega_0(k)$ and damping factor $\gamma \equiv 1/\tau$ we have:[267, 155]

$$\begin{aligned}
\Phi(k,t) &= Be^{-t/\tau}\cos(\omega_0 t) \\
\frac{\chi(k,\omega)}{\chi(k,0)} &= \frac{B}{2}\left(\frac{1-i\omega_0\tau}{1-i(\omega+\omega_0)^2\tau} + \frac{1+i\omega_0\tau}{1-i(\omega-\omega_0)^2\tau}\right) \\
\frac{\text{Im}\{\chi(k,\omega)\}}{\chi(k,0)} &= \frac{B}{2}\left(\frac{\omega\tau}{1+(\omega+\omega_0)^2\tau^2} + \frac{\omega\tau}{1+(\omega-\omega_0)^2\tau^2}\right)
\end{aligned}$$

This is the Van Vleck-Weisskopf lineshape, and is discussed in further detail in section 7.1. We found this lineshape yields τ, ω_0 results identical to the standard damped harmonic oscillator response for the range of τ, ω_0 values we fit. We found a two function (Debye + resonant) fit worked very well for fitting the librational peak in the longitudinal case. The H-bond stretching peak at $\approx$200 cm^{-1} overlaps with the librational band for $2 < k < 2.5$, and we found that it can be included in the fit using an additional damped harmonic oscillator, but usually this was not necessary. Because of this overlap and the broad nature of the fitting of the transverse band is approximate, especially

in the case of TTM3F and when looking at experimental data, so we do not report lifetimes for the transverse TTM3F response.

10.5 Polarization correlation functions

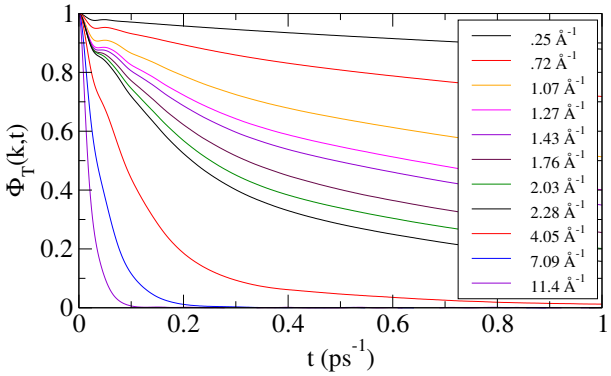

Figure 10.5: Transverse polarization relaxation functions for TIP4P/ε. The librational mode at small k is heavily damped.

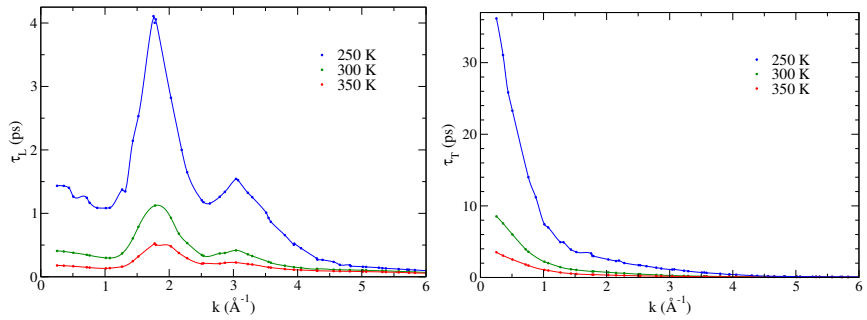

Figure 10.6: **Longitudinal (left) and transverse (right) relaxation times for 512 TIP4P/2005f.** Computed for the underlying exponential of the relaxation and interpolated by Akima splines. The transverse relaxation time at $k = 0$ is the Debye relaxation time ($\approx$ 11 ps at 300 K for TIP4P/2005f). Experimentally it is 8.5 ps.[12]

The longitudinal and transverse polarization correlation functions at small k are shown in figure 10.5 for TIP4P/ε, TIP4P/2005f, and TTM3F. Since TIP4P/ε is a rigid model, only librational motions are present. The addition of flexibility and polarizability add additional high frequency oscillations to the picture. In the small wavenumber regime ($k < 1.75$Å) there is a damped

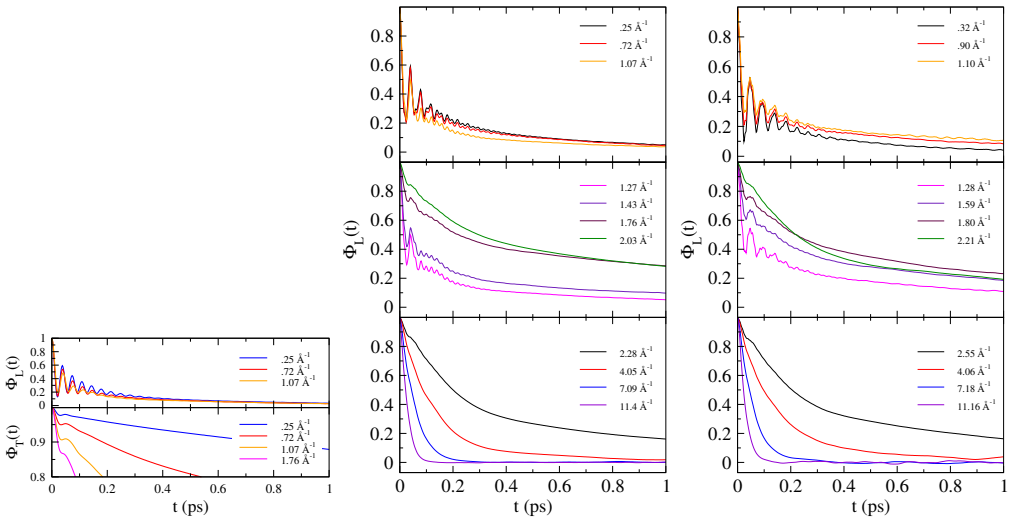

Figure 10.7: Longitudinal polarization relaxation functions for 512 TIP4P/ε (left), 512 TIP4P2005/f (middle) and 128 TTM3F (right) at 300 K. The oscillations at small k come from the collective librational mode.

oscillation which corresponds to the collective librational phonon mode. This damped oscillation is superimposed on an underlying exponential relaxation in both the transverse and longitudinal cases. In the longitudinal case the underlying exponential relaxation exhibits non-monotonic behaviour with k, reaching maximum at $k \approx 3\text{Å}^{-1}$. At wavenumbers greater than $k \approx 2.5$ only intramolecular motions contribute to the relaxation. Intriguingly, close inspection of the longitudinal correlation function at small k shows that small-magnitude librational oscillations persist for greater than one picosecond before eventually loosing coherence (fig. 10.8.

Relaxation times can be computed by fitting exponentials to the correlation functions. Figure 10.6 shows the longitudinal and transverse relaxation times of TIP4P/2005f at 300 K. We see that the longitudinal relaxation exhibits a peak at $k \approx 2\text{Å}^{-1}, \lambda = 2.1\text{Å}$) and a secondary peak at $k \approx 3\text{Å}^{-1}, \lambda \approx 3.1\text{Å}$. The first peak is close to a k corresponding to the O–H distance in the hydrogen bond, while the second is close to the H-bond O-O distance. The transverse relaxation decays monotonically with k.

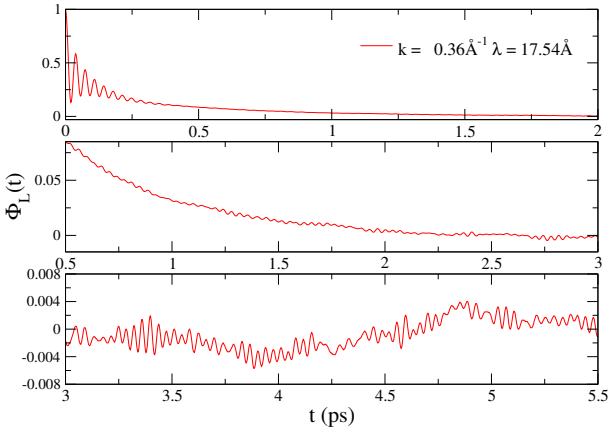

Figure 10.8: Fine features of the longitudinal polarization correlation function for 512 TIP4P/ε at 300 K. Coherent small-magnitude oscillations appear to persist for longer than 1 ps.

10.6 Polarization-polarization structure factors

To assist in visualizing $\chi_{L,T}(k,\omega)$ we introduce longitudinal and transverse "polarization-polarization structure factors":

$$S^{PP}_{L,T}(k,\omega) = \int_0^\infty \dot{\Phi}_{L,T}(k,t)e^{i\omega t}dt \tag{10.8}$$

Thus, $\chi_{L,T}(k,\omega) = \chi_{L,T}(k,0)S^{PP}_{L,T}(k,\omega)$. These structure factors are shown in fig. 10.6 because they provide a visual overview of the features in the nonlocal susceptibility. One new feature that appears in these plots is the low frequency acoustic-like mode originating at ≈ 60 cm^{-1}. This mode is purely intramolecular in nature and appears to be related to inertial rotation.[206, 207] At very high wavenumbers ($k > 8$)) the relaxation is described by a rapidly decaying exponential and a Gaussian function:[315]

$$\Phi_L(k,t) = A(k)e^{t/\tau_1(k)} + B(k)e^{-(t/\tau_2(k))^2} \tag{10.9}$$

The interpretation of the Gaussian form is that it is due to fast inertial relaxation. It has been suggested that such inertial relaxation is origin of the "Poley absorption" that has been found in some dipolar liquids (see section 7.6.2 for discussion).[205, 46, 206, 207]

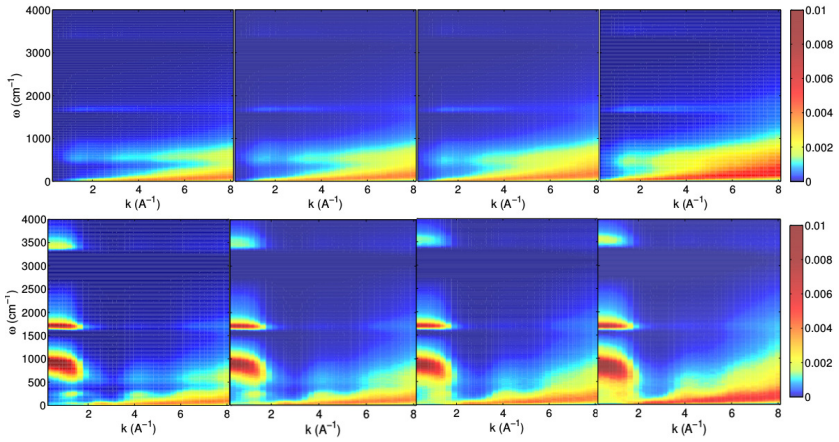

Figure 10.9: Imaginary part of the longitudinal (top) and transverse (bottom) polar structure factor for TIP4P/2005f at 250 K, 300 K, 350 K, and 400 K (left to right). Note the increased intensity of the low frequency, high wavenumber intramolecular mode at higher temperatures. This is likely due to weaker H-bonding and greater freedom for inertial motion, which is responsible for this band.

10.7 Dispersion of the librational peak

Figure 10.10 shows the imaginary part of the longitudinal and transverse susceptibility for TTM3F. In the longitudinal case the librational peak is clearly seen to shift with k. In the transverse case, the lower frequency portion of the band is seen to shift slightly with k. Dispersion relations for the longitudinal and transverse librational peaks are shown in fig. 10.7 for three different temperatures, using one peak fits. The dispersion relations appear to be that of optical phonons. In both the longitudinal and transverse case the damping factors remain less than the resonance frequencies, indicating an underdamped oscillation.

Resonance frequencies and lifetimes for the smallest k are shown in table 10.7. The speed of propagation of these modes was computed by finding the slope $d\omega/dk$ in the regime of linear dispersion. For TIP4P/2005f we found speeds of $\approx$ 2700 m/s and $\approx$ 1800 m/s for the longitudinal and transverse modes. These propagation speeds are above the speed of sound in water (1500 m/s) but below the speed of sound in ice (4000 m/s). The temperature dependence of the propagation speed was found to be very small.

In both the longitudinal and transverse cases, the residual of the peak fitting shows features not captured our Debye + one resonance fit of the librational peak. In both the longitudinal and transverse cases there is a non-

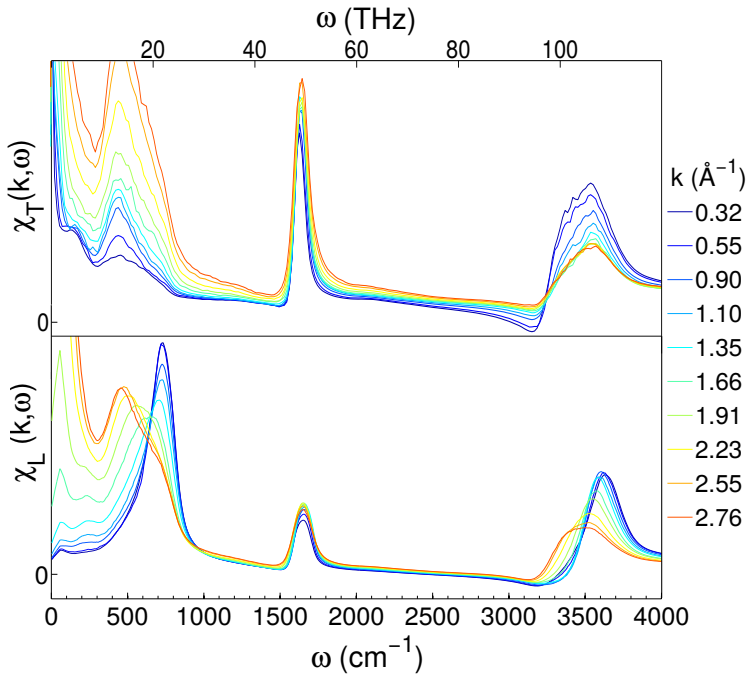

Figure 10.10: Imaginary part of the transverse (top) & longitudinal (bottom) susceptibility for TTM3F at 300 K. Both the librational ($\approx$ 750 cm^{-1}) and OH stretching peak ($\approx$ 3500 cm^{-1}) exhibit dispersion in the longitudinal case.

dispersive peak at higher frequency, located at $\approx$900 cm^{-1} for TIP4P/2005f and at $\approx$650 cm^{-1} in TTM3F. This peak is negligibly small in the $k = 0$ longitudinal susceptibility but appears as a shoulder as k increases. In the transverse case the overlapping peak persists at $k = 0$, so we found that the $k = 0$ transverse spectra is best fit with two peaks, in agreement with experimental spectra. As we describe later, the higher frequency transverse peak is largely due to the self part of the response and is associated with the wagging librations of single molecules.

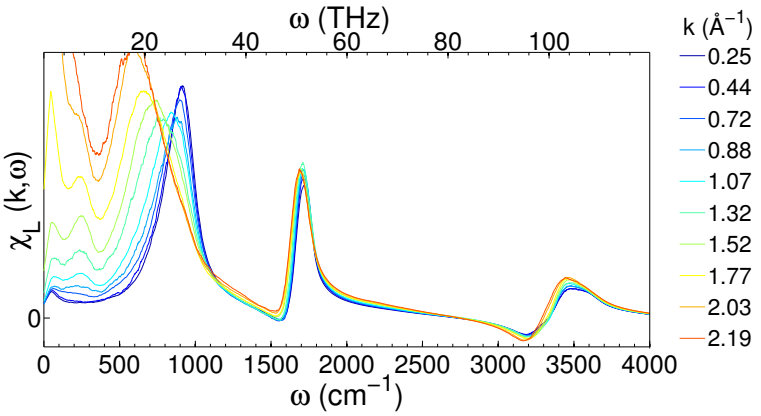

Figure 10.11: Imaginary part of the longitudinal susceptibility for TIP4P/2005f at 300 K. No dispersion is observed in the OH stretching peak.

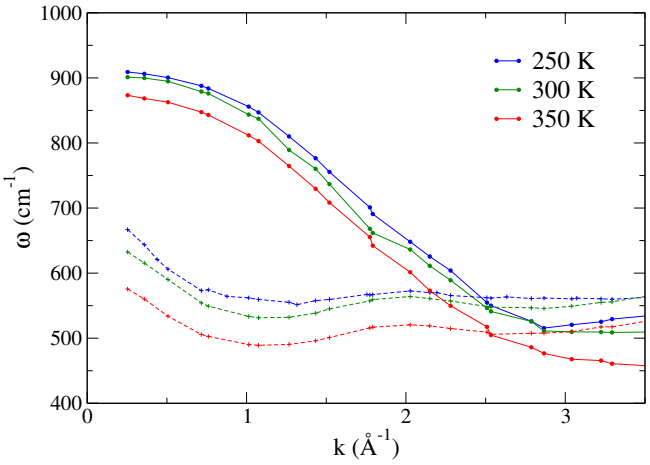

Figure 10.12: **Dispersion relations for the propagating librational modes.** For TIP4P/2005f at three different temperatures (squares = longutudinal, pluses = transverse). A similar plot was found for TTM3F, but with lower frequencies.

Model	Temp	ω_{LO}	τ_{LO}	ω_{TO}	τ_{TO}	$\omega_{LO} - \omega_{TO}$
TIP4P/2005f	250	905	.38	667	.23	233
	300	900	.44	632	.18	268
	350	871	.34	574	.18	297
	400	826	.25	423*	.17	400
TTM3F	250	757	.49	496		261
	300	721	.44	410		311
	350	710	.20	380		330
expt[8, 9]	253	820		641		179
	300	759		556		203

Table 10.3: Observed resonance frequencies (cm^{-1}) and lifetimes (ps) for the propagating modes at the smallest k in the system. The experimental values are approximate, based on the position of the max of the band. * Fitting questionable due to two broad overlapping peaks at 400 K.)

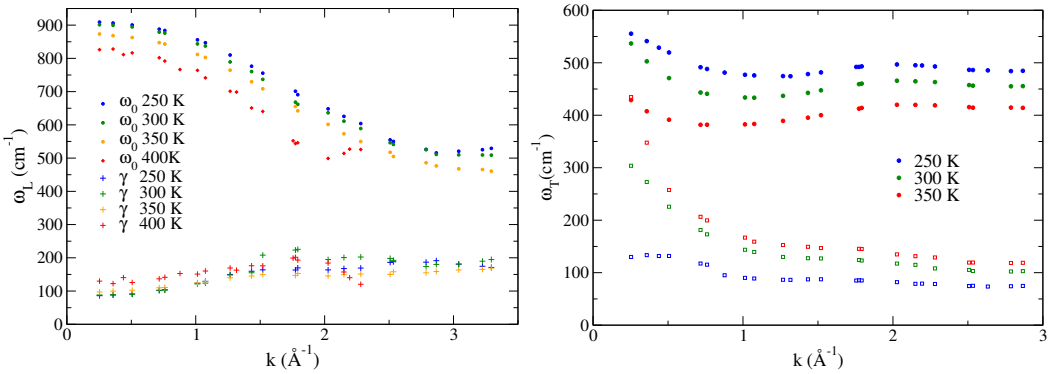

Figure 10.13: **Longitudinal (left) and transverse (right) dispersion relations (circles) and damping factors (squares) for 512 TIP4P/2005f.** These curves were obtained from a two peak (Debye + resonant) fit. In contrast to the longitudinal mode, the transverse mode is much more damped.

10.8 Importance of polarizability

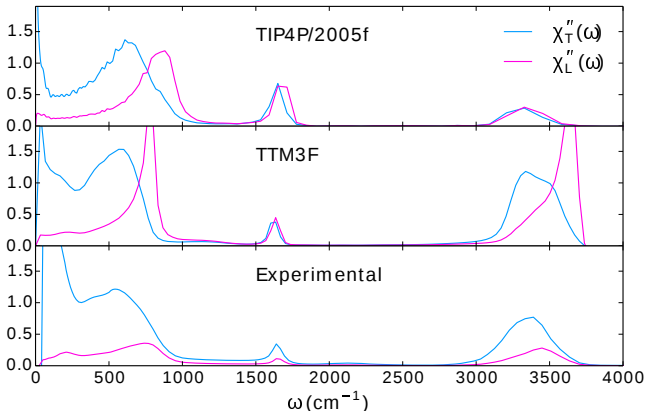

Figure 10.14: Imaginary parts of the static transverse and longitudinal dielectric susceptibility for TIP4P/2005f, TTM3F, and experimental data[9] at 298 K. The effects of polarization can be seen in the LO-TO splitting of the stretching mode and in the low frequency features.

There are several notable differences between TTM3F and the non-polarizable model TIP4P/2005f. First of all, the librational band of TIP4P/2005f is at higher frequency, in worse agreement with experiment. More importantly, we find that TTM3F exhibits dispersion in the OH stretching band in the longitudinal case while TIP4P/2005f does not. The transverse susceptibility of TTM3F does not exhibit such dispersion but the magnitude of the OH stretching band increases at small k, indicating long range intermolecular correlations. TIP4P/2005f does not exhibit this behavior. Similarly, at $k = 0$ TTM3F exhibits significant LO-TO splitting in the OH stretching band while TIP4P/2005f does not (fig.10.14). These findings are consistent with Heyden's results for the k-resolved IR spectra from *inito* simulation, where they concluded that polarization allows for intermolecular correlations at the OH-stretch frequency.[314]

These findings can be understood from the dipole derivative in eqn. 10.6. In the librational band the deriviative of the dipole moment with respect to normal coordinate is purely due to rotation, while in the OH-stretching band it is due to changes in the geometry of the molecule and electronic polarization of the molecule during the OH stretching. In principle there may also be coupling between the librational and stretching motions, but typically such rotational-vibrational coupling effects are negligibly small.[316] The

dipole moment surface (fluctuating charges) and polarization dipole incorporated in TTM3F account for the changes in polarization that occur during OH stretching motion. These results confirm the significance of polarization in capturing the OH stretching response of water.[314]

Figure 10.14 shows a comparison of TTM3F, TIP4P/2005f and experiment at $k = 0$. While the locations of peaks in TTM3F are in good agreement with the experimental data at 298 K, the magnitude of the longitudinal response is greatly overestimated. The degree of LO-TO splitting in the OH stretching peak is also overestimated in TTM3F. In general it appears that TTM3F overestimates the dipole derivative in eqn. 10.6 while TIP4P/2005f underestimates it. Figure 10.14 also shows the effect of polarization at low frequencies, in particular the appearance of an H-bond stretching response at ≈ 250 cm^{-1} in TTM3F which is absent in TIP4P/2005f.[317]

10.9 LO-TO splitting vs temperature

The frequencies of the librational and stretching modes are shown in table 10.7. Once again we compare our results to experimental data.[318, 9, 8] The comparison is imperfect since the TIP4P/2005f and TTM3F results were computed at nonzero k (the smallest k in the system). For all three systems (TIP4P/2005f, TTM3F, and experiment) the increase in the LO-TO splitting of the librational band is puzzling, since the right hand side of the LST relation predicts a decrease in splitting, corresponding to a smaller dielectric constant and weaker dipole-dipole interactions. We found verifying the generalized LST equation is difficult because water contains either two or three Debye relaxations which must be taken into account.[198, 319] Uncertainties in how to fit the region of 1 - 300 cm^{-1} (.2- 9 THz), which includes contributions from many H-bonding modes, precludes a direct application of the generalized LST relation to water. By ignoring this region, however, we were able to achieve an approximate validation of the generalized LST equation for TIP4P/2005f. A more detailed analysis of how to fit the low frequency region will be the focus of future work. Since the generalized LST equation is an exact sum rule it can be used to assist in testing the validity of different fit functions.

10.10 Relation to phonons in ice

Naturally we would like to find corresponding optical phonon modes in ice. As shown in figure 10.1 the dielectric spectra and LO-TO splitting of supercooled water resembles that of ice. Recently evidence has been presented

for propagating librational phonon modes in ice XI.[320, 321] Three of the twelve librational modes of ice XI are IR active (labeled WR1, RW1 and RW2) and all exhibit LO-TO splitting. The splittings have been found from Raman scattering to be 255, 135 and 35 cm^{-1}.[321] These modes all consist of coupled wagging and rocking motions. The WR1 mode, which has the largest infrared intensity, most closely matches our results. WR1 and RW2 have the same transverse frequency and RW1 has a smaller infrared intensity, which may help explain why the librational band is well fit by a single optical mode. LO-TO splitting in the OH-stretching modes of ice Ih has been discussed previously.[291]

10.11 Range of propagation and spatial decomposition of spectra

The range of propagation of these modes can be calculated as $R = \tau v_g$ where τ is the lifetime and $v_g = d\omega/dk$ is the group velocity. For TIP4P/2005f we find a range of propagation of $\approx$ 1.1 nm for the longitudinal librational mode and $\approx$ .3 nm for the transverse mode. Similar results hold for TTM3F.

To verify that the modes we observe are actually propagating and to further quantify the range of propagation we study the spatial extent of polarization dipole correlations as a function of frequency. We investigated several different methodologies that can be used to decompose a spectrum into distance-dependent components:

"Kirkwood" dipole-sphere method

This is the method we choose, which is a modification of the "sphere-sphere" method (see below). We start with the time-correlation function of interest :

$$\phi(t) = \left\langle \sum_i \boldsymbol{\mu}_i(0) \cdot \sum_j \boldsymbol{\mu}_j(t) \right\rangle \tag{10.10}$$

Here $\boldsymbol{\mu}$ can be replaced with any dynamical variable of interest, for instance $\boldsymbol{p}^T(\boldsymbol{k}, t)$ or $\boldsymbol{j}(t)$. We omit the k dependence for simplicity.

One simply limits the molecules around each molecule i to those in a sphere of radius R:

$$\phi(t, R) = \left\langle \sum_i \boldsymbol{\mu}_i(0) \cdot \sum_{j \in R_i} \boldsymbol{\mu}_j(t) \right\rangle \tag{10.11}$$

This is similar to the method employed by Bopp & Kornyshev. During the

the course of a simulation molecules enter and leave each sphere, which creates noise, requiring longer averaging times. This can be improved by utilizing a smooth cutoff function:

$$\phi(t,R) = \left\langle \sum_i \boldsymbol{\mu}_i(0) \cdot \sum_j P_{ij}(t)\boldsymbol{\mu}_j(t) \right\rangle \tag{10.12}$$

where

$$P_{ij} = \frac{1}{1+e^{(R_{ij}-R)/D}} \tag{10.13}$$

Here D is a "sharpness parameter" determining the relative sharpness of the cutoff. We choose not to use smoothing however, finding it to be unnecessary. The result is a spectrum $\chi(\boldsymbol{k},\omega,R)$ showing contributions from molecules up to radius R. The resulting function exhibits the expected $R \to 0$ limit, yielding only the self contribution. In the $R \to \infty$ limit, the original full response function is recovered. This function can then be numerically differentiated to show the contributions from shells of thickness ΔR centered at distance R.

Sphere-sphere method

In the limit $R \to 0$ only the self-term contributes. Results from this method must be interpreted with a bit of care since the calculation includes all cross-correlations between molecules within the sphere centered around the reference molecule. We found that this method is more sensitive to intermolecular correlations, in particular the H-bond stretching at $\approx$ 250 cm^{-1} (not shown). Altogether though we found the results from this method are complementary with our results from the dipole-sphere method.

We computed a distance-dependent IR spectra using the "sphere-sphere method" (see fig 10.15) with smoothing (D = .4Å). The IR spectrum is computed using the formula:

$$\alpha(\omega)n(\omega) = \frac{1}{4\pi\epsilon_0}\frac{2\pi\omega^2}{3Vk_BTc}\int_{-\infty}^{\infty} dt e^{-i\omega t}\langle \boldsymbol{M}(0)\boldsymbol{M}(t)\rangle \tag{10.14}$$

The IR spectrum is in qualitative agreement with the results of Heyden, et. al.[199] The main difference observed when using this method is that the H-bond stretching feature at 200 cm^{-1} is emphasized at $R \approx 3-6$Å.

Spatial grid method

To achieve higher resolution, Heyden, et al. also introduce a spatial grid method.[199] The method works by binning the molecular dipoles into grid

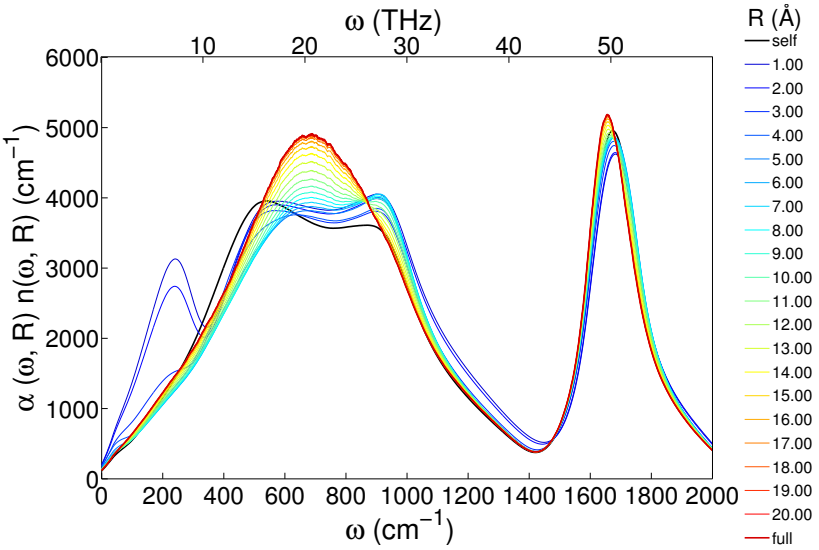

Figure 10.15: Distance decomposed IR spectra for TIP4P/2005f at 300 K using the technique of Heyden, et al. A smooth cut-off with a smoothing width $\sigma = .4$Å was applied. Again, the librational region is observed to have long-range contributions.

cells. To reduce noise caused by molecules moving in and out of bins the binning is Gaussian, meaning the dipoles are smeared with a Gaussian function. Unlike the other methods the spatial grid method does not yield the self part as $R \to 0$ so this limit requires special interpretation.

Results

Figure 10.16 shows the distance decomposed longitudinal and transverse susceptibilities for TIP4P/2005f in a 4 nm box at the smallest k available in the system. The entire region between 0 - 1000 cm^{-1} contains significant cancellation between the self and distinct parts, in qualitative agreement with a previous study.[322] In the longitudinal susceptibility, the self component has two peaks (at 500 and 900 cm^{-1} for TIP4P/2005f) representing the two IR active librational motions (rocking and wagging, respectively). The self part is the same in both the longitudinal and transverse cases, reflecting an underlying isotropy which is only broken when dipole-dipole correlations are introduced. Further insight into the self-distinct cancellation comes from the results of Bopp, et. al., who project the hydrogen currents into a local molecular frame, allowing them to study the cross correlations between the rocking and wagging librations.[267] They find that in the longitudinal case cross correlations between rocking and wagging contribute negatively in the region of 480 cm^{-1}

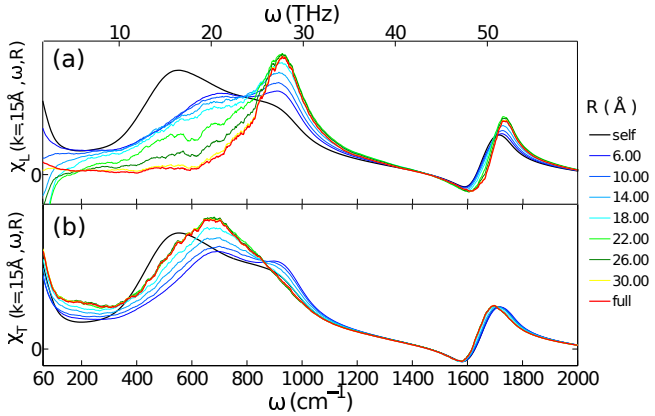

Figure 10.16: Distance decomposed longitudinal (top) and transverse (bottom) susceptibility for TIP4P/2005f at 300 K with a 4nm box, calculated at the smallest k vector in the system. Gaussian smoothing was applied. Long range contributions to the librational peak extending to $R = 2$ nm are observed.

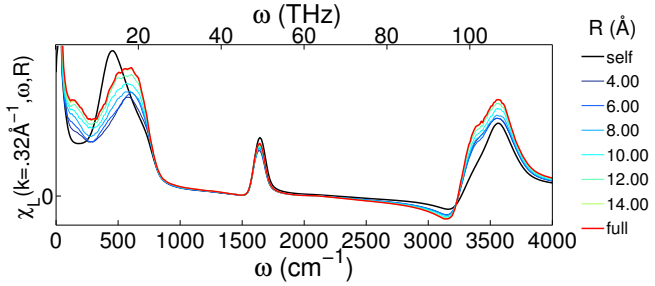

Figure 10.17: Distance decomposed longitudinal susceptibility for TTM3F at 300 K.

and positively in the region of 740 cm^{-1}, suppressing the lower frequency peak to zero and enhancing the higher frequency peak. In both the transverse and longitudinal cases as R increases a new peak emerges, corresponding to the propagating mode. Interestingly, there are very long range contributions to this peak. In our simulations with a 4 nm box of TIP4P/2005f contributions persist up to 3 nm in the longitudinal case and 2 nm in the transverse case. As noted, recent studies of ice suggest that the propagating modes consist of coupled wagging and rocking librations.[320, 321] The results for the transverse mode confirm this hypothesis, since the propagating mode peak lies between the rocking and wagging peaks. In the longitudinal case the propagating mode peak lies more on the wagging peak, suggesting a greater role for these type of librations in the longitudinal phonon.

10.12 Methanol & acentonitrile

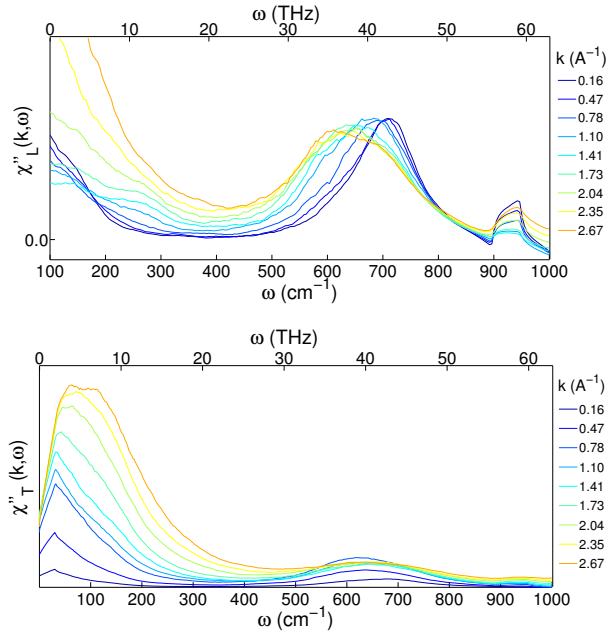

Figure 10.18: Longitudinal (top) and transverse (bottom) dielectric susceptibility for a simulation of 1,000 MeOH molecules. The longitudinal librational peak at $\approx$ 700 cm^{-1} clearly disperses with k, while the transverse peak at $\approx$ 600 cm^{-1} disperses slightly with k. The higher frequency peaks exhibit no dispersion. The static dielectric function $\varepsilon(k, 0)$ has not converged properly in the transverse case, so the magnitude of the peaks is not converged.

To provide further evidence that the optical mode propagate along the H-bond network of water we decided to repeat our analysis for other polar liquids, both H-bonding and non0H-bonding. As an H-bonding liquid we choose methanol (CH_3OH), which is known to contain winding H-bonded chains. According to results from MD simulation, most of these chains have around 5-6 molecules[323, 324], with a small percentage of chains containing 10-20 molecules.[325] Chain lifetimes have been estimated to be about .5 ps.[325] Therefore we expect methanol can also support a librational phonon mode that propagates along hydrogen bonds, but perhaps with a shorter lifetime and range than water. As a non H-bonding polar liquid we choose acetonitrile (CH_3CN), because it has a structure similar to methanol, but with the hydroxyl group replaced by a cyanide group (CN). Previous work using molecular dynamics simulation has shown that the time dependent solvation correlation

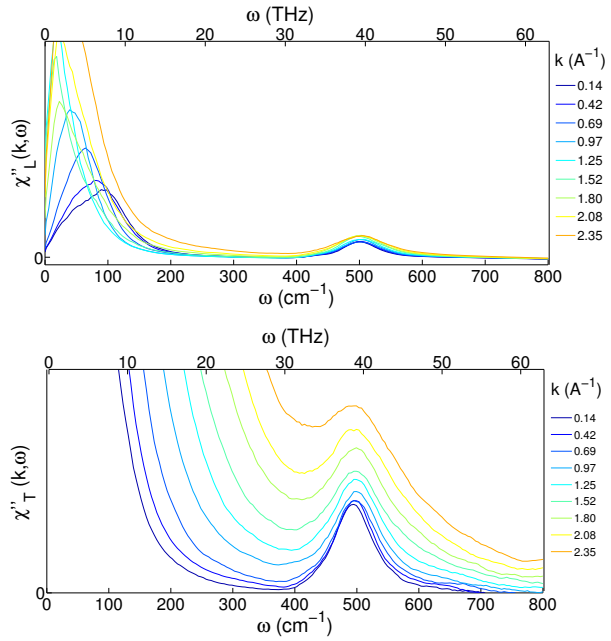

Figure 10.19: Longitudinal (top) and transverse (bottom) dielectric susceptibility for a simulation of 1,000 acetonitrile molecules. The broad band which peaks at 100 cm^{-1} exhibits dispersion. We hypothesize this dispersion is due entirely to the translational modes, however we cannot say for sure since the librational and translational modes overlap in this region. The peak at $\approx$ 500 cm^{-1} is due to CCN bending. The static dielectric function $\varepsilon(k, 0)$ has not converged properly, so the magnitude of the transverse peaks is not converged correctly, but the position of the peaks and dispersion can be seen.

functions of water and methanol exhibit fast oscillations, whereas acetonitrile and methyl chloride (CH_3Cl) do not.[326] This is perhaps not surprising since methanol contains a dangling OH group which can undergo fast librational motion, while acetonitrile and methyl chloride do not.

We find that the OH librational band of methanol ($\approx$ 700 cm^{-1}[327]) is indeed dispersive (fig. 10.18). As with water, the transverse spectrum also exhibits dispersion, but to a much lesser extent. LO-TO splitting of about 100 cm^{-1} is observed in the 700 cm^{-1} librational peak. The results for acetonitrile (fig. 10.19) are more ambiguous - we observe dispersion in the broad peak at $\approx$ 100 cm^{-1}, however this peak contains contributions from translational and (free) rotational modes, as well as the CH_3 torsion mode, and it is not clear which modes are responsible for the dispersion.

We mention in passing that there is experimental evidence for propagat-

ing/collective librational modes in ethanol (C_2H_5OH) an H-bonding liquid very similar to methanol. Infrared spectra of ethanol- acetonitrile mixtures show a shifting of the enthanol librational peak with increasing acetonitrile concentration.[328]

10.13 Esoteric aside: dipolar plasmon interpretation

A possible alternative to the optical phonon interpretation which we found warranted serious investigation is that the librational mode is a dipolar plasmon (also called, somewhat confusingly, the "dipolaron"). For systems of dipoles there is predicted to exist dipolar plasmon modes analogous to the plasmon mode found in one component plasmas such as the free electron gas.[329, 330] Dipolar plasmons have been claimed to be observed in molecular dynamics simulation of point dipoles with the Lennard-Jones interaction (the "Stockmayer system").[331, 332] As far as we know the possibility that the librational peak in the dielectric susceptibility of water is a dipolar plasmon peak has not been considered in detail before. The dipolar plasmon corresponds to different physics than the optical phonon picture. The theory of the dipolar plasmon is based on the dielectric function derived by Nee & Zwanzig[188] and separately Fatuzzo & Mason[333] using a dynamical version of the Onsager cavity mean field model. The model they employ makes no mention of molecular interactions such as H-bonds, and instead consists of a single molecular dipole interacting with a cavity reaction field and undergoing random Brownian motion. To obtain the dipolar plasmon, the dielectric function is modified by including inertial effects and by making the Brownian friction exponentially correlated instead of delta correlated. The physics of the dipolar plasmon is easiest to understand by picturing a dipole undergoing small librations and being driven by an external plane wave electric field (this picture is the starting point of Fatuzzo & Mason). In equilibrium the reaction field always points in the same direction as the dipole, but if the dipole is rotating the reaction field will exhibit a phase lag in time (whenever the imaginary part of the dielectric function is nonzero). The phase lagged reaction field acts to counter the rotation of the dipole, an effect called rotational dielectric friction. At high enough driving frequencies a resonance can be set up between the librating dipole and the phase-lagged reaction field response.

The Nee-Zwanzig theory of the dipolar plasmon appears to be very similar to the generalized Langevin equation (Mori-Zwanzig memory function) formalism used by Chong & Hirata to model collective excitations in water.[288] It

seems quite likely that the dispersive mode they observe is actually the dipolar plasmon, and not physically the same as the mode observed in MD simulation, as they suggest. The phenomenology of the dipolar plasmon is very similar to a propagating optical phonon mode, as we will see.

Computational studies of the Stockmayer system (a system of point dipoles) find a dispersive mode in the dielectric susceptibility, and this behaviour has been studied in detail and established to be due to the dipolar plasmon resonance.[331] The change in peak shape during dispersion is almost identical to the propagating phonon modes we observe. Furthermore, the dipolar plasmon mode exhibits LO-TO splitting, and the transverse counterpart in the Stockmayer system is heavily damped, also in agreement with our observations. The frequencies predicted by Lobo, et. al. for the dipolar plasmon resonances in water ($\omega_L = 636$ cm^{-1}, $\omega_T = 407$ cm^{-1}) are also in fairly good agreement with our findings for TTM3F and experiment. However, the frequencies predicted by dipolar plasmon theory shift significantly depending on the time constant τ chosen for the exponentially-correlated Brownian friction. Curiously, the dipolar plasmon only appears when the Brownian friction is exponentially correlated (frequency dependent), and disappears when the friction becomes delta correlated ($\tau \to 0$). There is no well-defined way to choose τ and it is not clear whether the argument given by Lobo, et. al. for their choice of τ (based on the hydrogen bond energy) makes sense. When there is no Debye relaxation dipolar plasmon theory predicts that the polarization time correlation function contains oscillations of around zero.[331, 329] Dipolar plasmon theory can easily be extended to include a Debye term, in which case the polarization time correlation functions consist of an oscillation superimposed on an exponential.

There is scant experimental evidence for dipolar plasmons in dipolar liquids. Experimental observations of a dipolar plasmon peak have been suggested for both nitromethane[334] and methyl chloride,[335] although the former result was questioned.[336] On the basis of a hydrodynamic theory, Bagchi and Chandra argue that whether a dipolar plasmon is present depends on the parameter $B = \frac{k_B T}{I D_R^2}$.[337, 338] Here I is the moment of inertia of the molecule and D_r is the rotational diffusion constant. They found that B must be less than 5 for dipolar plasmons to exist, implying that they are unlikely to exist in most dipolar liquids since the rotational diffusion constant required is much too fast. If we take $D_r \approx 1/\tau_s$ (τ_s being the relaxation time for a single molecular dipole) then we find $B \approx 800$ for water. However, this result does not conclusively rule out the existence of a dipolar plasmon in water since the hydrodynamic theory they employ is of questionable applicability to an H-bonding liquid like water. Bagri & Chandra also found that the dipolar

plasmon is enhanced by a large dielectric constant and by coupling between translational and rotational polarization relaxation, which has recently been found to be significant in water.[339] In some ways, the dipolar plasmon is very similar to an optical phonon. As with optical phonons, for the pure dipolar plasmon the longitudinal and transverse modes occur when $\varepsilon(\omega) = 0$ and $\varepsilon(\omega) = \infty$. The dispersion observed by Pollock & Adler is qualitatively similar to that of a phonon. The *pure* dipolar plasmon obeys an LST relation given by:[329]

$$\frac{\omega_L^2}{\omega_T^2} = \frac{\varepsilon(0)}{\varepsilon_\infty}\left(\frac{2\varepsilon(0)}{\varepsilon(0)+\varepsilon_\infty}\right) \tag{10.15}$$

Apart from the factor of $2\varepsilon(0)/(\varepsilon(0)+\varepsilon_\infty$ this is identical to the standard LST relation for a single damped harmonic oscillator mode.

A few other qualitative observations suggest a dipolar plasmon:

- The mode contains contributions from very long range correlations. This is an assumption of dipolaron theory, which assumes a molecule (or equivalently a collection of molecules) is surrounded by a cavity and interacts with the cavity reaction field created by long range electrostatics.

- The temperature dependence of speed of propagation of the mode is very small. This is expected since the strength of H-bonds changes significantly with temperature.

However, a key property of the dipolar plasmon resonance is that it is simultaneously a resonance of both the single dipole motion and the collective motion.[329] *This is not borne out when we compare the self and full response.* The underlying assumptions of the dipolar plasmon theory are also very questionable. The Onsager cavity picture neglects H-bonding and is known to give mediocre predictions for the dielectric constant. As mentioned, dipolar plasmon theory also contains a free parameter, τ, for which there is no rigorous justification. Small changes in τ change the frequencies predicted by the theory significantly. The objections raised by Bagchi & Chandra also represent a serious theoretical difficulty.[337, 338] The fact that dipolarons have not been unambiguously detected in other dipolar liquids (despite some efforts) confirms the assertion of Bagchi & Chandra that the moments of inertia found in dipolar liquids are too large.

There is also the broader issue of whether a dipolar plasmon in real materials would be in anyway distinct from a normal optical phonon mode. The idealized dipolar plasmon, occurring in a system of point dipoles, cannot exist in nature, unlike the plasmon, which can exist in the free electron gas in metals

or in a plasma. Any realization of the dipolar plasmon in real materials has to be due to the rotation of molecules, ie. the motion of nuclei. In our view, such collective oscillations of nuclei are better characterized as phonon modes. Nevertheless, the dipolar plasmon theory does offer some physical insight into the librational dynamics of water since there is no doubt that water molecules feel a reaction field as they undergo hindered rotation. The effect of this reaction field (dielectric friction) appears to be small, however, and the moment of inertia of water appears to be too high to allow for a dipolar plasmon.

10.14 Conclusion

In this work we have presented several lines of evidence for short lived optical phonons that propagate along the H-bond network of water. The longitudinal and transverse nonlocal susceptibility exhibit dispersive peaks with dispersion relations resembling optical phonons. As the temperature is lowered, the resonance frequencies and LO-TO splittings of these modes converge towards the values for phonons in ice Ih. By comparing our results with a recent study of ice XI we believe both modes likely consist of coupled wagging and rocking librations.[320, 321] This work fundamentally changes our understanding of the librational band in the Raman spectra of water by assigning the lower and higher frequency peaks to transverse and longitudinal optical modes. Our analysis of the self-distinct cancellation indicates that the middle Raman peak ($\approx$ 600 cm^{-1}) belongs to the remnant of the single molecule wagging response which remains after the cancellation. We are also led to a new interpretation of the librational region of the real part of the dielectric function. In the case of a lossless optical phonon the transverse phonon occurs where $\varepsilon'(\omega) = \infty$ while the longitudinal phonon occurs where $\varepsilon'(\omega) = 0$. The presence of damping smooths the divergence leading to a peak followed by a sharp dip. This is what is observed in the real part of the dielectric function of water between 300 - 500 cm^{-1} (the features are shifted to lower frequencies by the tail of the low frequency Debye relaxation).

One might wonder how our work relates to existing work on acoustic modes in water, in particular, the controversial "fast sound" mode.[340, 341] Acoustic modes, which are observable through the dynamic structure factor, have been explored as means of understanding the hydrogen bond structure and low temperature anomalies of water.[36] In this work we have argued that optical modes can also provide insight into water's structure and dynamics. The fast sound mode lies at much lower frequencies than the librational and OH stretch modes that we studied. The H-bond bending and stretching modes also primarily lie at at frequencies below the librational region. However,

normal mode analysis of liquid water and clusters shows that the H-bond stretching modes have a wide distribution of frequencies which overlaps with the librational modes, so some coupling between these modes is possible.[208, 342] Recently it was shown that there is coupling between the acoustic and optic modes in water - ie. between fluctuations in mass density and fluctuations in charge density.[339]

The large spatial range and coherent propagation of these modes is surprising and implies the existence of an extended hydrogen bond network, in contrast to earlier ideas about the structure of water which emphasize dynamics as being confined within small clusters.[343] Simulations with larger simulation boxes are needed to fully quantify the extent of the longitudinal modes. The ability of water to support propagating phonon modes may be relevant to biophysics, where such modes could lead to dynamical coupling between biomolecules, a phenomena which is currently only being considered at much lower frequencies.[227, 228, 230] Finally, these phonons likely play a role in water's unusually large thermal conductivity, which can be explained with a phonon theory, as in solids.[344] The methodology used in this paper to analyse LO-TO splitting opens up a new avenue to understanding the structure and dynamics of water. The fact that the librational LO-TO splitting increases with temperature instead of the expected decrease is likely due to significant changes in the structure of the liquid. One likely possibility is that the volume per "unit cell" term in equation 10.6 decreases with temperature. This could be caused by the local quasi-structure determined by H-bonding changing from a more ice-like structure (4 molecules per unit cell) to a more cubic structure (1 molecule per unit cell). More research is needed to understand the microscopic origin of the LO-TO splitting in water, both in the librational and stretching modes.

Chapter 11

Path Integral Molecular Dynamics

"The study of mathematics is apt to commence in disappointment... We are told that by its aid the stars are weighed and the billions of molecules in a drop of water are counted. Yet, like the ghost of Hamlet's father, this great science eludes the efforts of our mental weapons to grasp it." - Alfred North Whitehead, 1911.

The light mass of the hydrogen nucleus leads to nontrivial nuclear quantum effects (NQEs) in water such as quantum delocalization, quantum zero-point motion, and tunnelling. These effects subtly influence water's structure and dynamics, and lead to unexpected changes when deuterium is substituted. Path integral molecular dynamics (PIMD) is the primary method used to treat nuclei quantum mechanically in molecular dynamics simulation.

The path integral formulation of quantum mechanics was discovered by Richard Feynman in 1948.[345] In 1953, Feynman applied path integral techniques to understand the λ transition in liquid helium. The appendix to his 1953 *Phys. Rev.* paper contains the essential idea that underlies PIMD.[346] More often though the method is attributed to Chandler and Wolynes, who proposed using Feynman's method to study liquids in 1981.[347] Not long after, the first computer simulations using PIMD were performed by Parrniello and Rahman in 1984.[348]

11.1 Derivation of the PIMD method

We begin with the quantum partition function and apply path integral methods to it. The partition function is:

$$Z = \mathrm{Tr}\left[e^{-\beta\hat{H}}\right] \tag{11.1}$$

The Hamiltonian is

$$\hat{H} = \hat{T} + \hat{V} = \frac{\hat{p}^2}{2m} + V(\hat{q}) \tag{11.2}$$

We make use of the Trotter formula:

$$e^{\hat{A}+\hat{B}} = \lim_{n\to\infty}\left(e^{\frac{B}{n}}e^{\frac{A}{n}}\right)^n \tag{11.3}$$

$$Z = \lim_{n\to\infty}\mathrm{Tr}\left[\left(e^{-\beta_n\hat{T}}e^{-\beta_n\hat{V}}\right)^n\right] \tag{11.4}$$

Where we have defined $\beta_n \equiv \beta/n$. In the position basis the trace becomes:

$$Z = \lim_{n\to\infty}\int dq_1\langle q_1|\left(e^{-\beta_n\hat{T}}e^{-\beta_n\hat{V}}\right)^n|q_1\rangle \tag{11.5}$$

We now insert $n-1$ complete sets of position eigenstates

$$Z = \lim_{n\to\infty}\int dq_1 dq_2\cdots dq_n\prod_{j=1}^{n}\langle q_j|e^{-\beta_n\hat{T}}|q_{j+1}\rangle e^{-\beta_n V(q_{j+1})} \tag{11.6}$$

To evaluate each matrix element we insert a complete set of momentum eigenstates, to get:

$$\langle q_j|e^{-\beta_n\hat{T}}|q_{j+1}\rangle = \int dp\langle q_j|p\rangle e^{-\beta_n p^2/2m}\langle p|q_{j+1}\rangle \tag{11.7}$$

We use

$$\langle q|p\rangle = \frac{1}{\sqrt{2\pi\hbar}}e^{iqp/\hbar} \tag{11.8}$$

Which yields the Gaussian integral:

$$\langle q_j|e^{-\beta_n\hat{T}}|q_{j+1}\rangle = \frac{1}{2\pi\hbar}\int dp e^{-\beta_n p^2/2m - ip(q_j-q_{j+1})/\hbar} \tag{11.9}$$

this leads to

$$\langle q_j|e^{-\beta_n \hat{T}}|q_{j+1}\rangle = \left(\frac{\beta_n m\omega_n^2}{2\pi}\right)^{1/2} e^{\frac{1}{2}\beta_n m\omega_n^2(q_j-q_{j+1})^2} \tag{11.10}$$

where we defined $\omega_n \equiv 1/(\beta_n\hbar) = k_B T n/\hbar$.

Eqn. 11.6 becomes:

$$Z = \lim_{n\to\infty}\left(\frac{\beta_n m\omega_n^2}{2\pi}\right)^{n/2} \int dq_1 dq_2 \cdots dq_n \prod_{j=1}^{n} e^{-\beta_n \phi_n(q_j)} \tag{11.11}$$

where

$$\phi_n(q_j) = \sum_{j+1}^{n} \frac{1}{2} m\omega_n^2 (q_j - q_{j+1})^2 + V(q_j) \tag{11.12}$$

This form can be sampled by Monte Carlo simulation. However, to sample this with molecular dynamics we need to introduce momenta. To do this, we use the standard Gaussian integral:

$$\int_{-\infty}^{\infty} dp e^{-\beta_n p^2/2m'} = \left(\frac{2\pi m'}{\beta_n}\right)^{1/2} \tag{11.13}$$

Which yields

$$1 = \left(\frac{\beta_n}{2\pi m'}\right)^{1/2} \int_{-\infty}^{\infty} dp e^{-\beta_n p^2/2m'} \tag{11.14}$$

Using this we introduce momentum into each matrix element (eqn. 11.10):

$$\begin{aligned}\langle q_j|e^{-\beta_n \hat{T}}|q_{j+1}\rangle &= \frac{\beta_n\omega_n}{2\pi}\sqrt{\frac{m}{m'}}\int dp_k e^{-\beta_n\left(\frac{p_k^2}{2m}+\frac{m\omega_n^2}{2}(q_k-q_{k+1})^2\right)} \\ &= \frac{1}{2\pi\hbar}\sqrt{\frac{m}{m'}}\int dp_k e^{-\beta_n\left(\frac{p_k^2}{2m}+\frac{m\omega_n^2}{2}(q_k-q_{k+1})^2\right)}\end{aligned} \tag{11.15}$$

The path integral (eqn. 11.11) becomes:

$$Z = \lim_{n\to\infty}\left(\frac{1}{2\pi\hbar}\right)^n \left(\frac{m}{m'}\right)^{n/2} \int dq_1 dq_2 \cdots dq_n dp_1 dp_2 \cdots dp_n \prod_{j=1}^{n} e^{-\beta_n H(q_j,p_j)} \tag{11.16}$$

The Hamiltonian is

$$H = \sum_{k=1}^{n} \left[\frac{p_k^2}{2m} + \frac{m\omega_n^2}{2}(q_k + q_{k+1})^2 + V(q_k) \right] \tag{11.17}$$

The introduction of momentum (eqn. 11.14) involved a mass m' which is arbitrary and does not necessarily need to be the physical mass. Therefore, we write the PIMD Hamiltonian more generally as :

$$H = \frac{1}{2}\boldsymbol{p}^T \boldsymbol{M}^{-1}\boldsymbol{p} + \sum_{k=1}^{n} \left[\frac{m\omega_n^2}{2}(q_k + q_{k+1})^2 + V(q_k) \right] \tag{11.18}$$

Where $\boldsymbol{p} = (p_1, p_2, ..., p_n)$ is a vector of the bead momenta and $\boldsymbol{M}$ is the mass matrix. Any reasonable choice of mass matrix (real-symmetric and positive definite) will yield the same equilibrium averages for the system, but the dynamics will be changed. Normally, $\boldsymbol{M}$ is diagonal.

The same derivation can be generalized to an N body system in 3 spatial dimensions. The resulting Hamiltonian is

$$H = \sum_{i=1}^{N}\sum_{k=1}^{n} \left(\frac{(\boldsymbol{p}_i^k)^2}{2m_i'} + \frac{m_i\omega_n^2}{2}(\boldsymbol{q}_i^k + \boldsymbol{q}_i^{k+1})^2 \right) + \sum_{k=1}^{n} V(\boldsymbol{q}_1^k, \cdots, \boldsymbol{q}_N^k) \tag{11.19}$$

As should be clear, $i = 1...N$ is the particle index and $k = 1..n$ is the bead index. We have put a prime on m_i' to indicate that this mass may be different than the physical mass m_i.

11.1.1 Equivalence of two different formulations

From the β_n in eqn. 11.16 we see that the quantum system evolves at an effective temperature nT. Therefore in this scheme the beads should be thermostated at nT. Alternatively one can factor $\frac{1}{n}$ into the Hamiltonian, yielding

$$H = \sum_{i=1}^{N}\sum_{k=1}^{n} \left(\frac{(\boldsymbol{p}_i^k)^2}{2N_b m_i'} + \frac{m_i(\omega_n')^2}{2}(\boldsymbol{q}_k + \boldsymbol{q}_{k+1})^2 \right) + \frac{1}{n}\sum_{k=1}^{n} V(\boldsymbol{q}_1^k, \cdots, \boldsymbol{q}_N^k) \tag{11.20}$$

where $\omega_n' = \omega/\sqrt{n} = k_B T\sqrt{n}/\hbar$. Using this Hamiltonian the beads are thermostated at temperature T. The bead mass is changed to $N_b m'$ but as mentioned before, but this is of no consequence to the static properties.

The fact that two different schemes exist causes the literature to be very

confusing. Most contemporary work uses the $\beta = 1/k_B T$ scheme, but the RPMD method of Craig and Manolopoulos [349] and lecture notes by Markland use $\beta_n = 1/(k_B T N_b)$.

The code implements the "RPMD style" method with β_n. We have already described the "RPMD style" as thermostating the beads at a temperature of $N_b T$ instead of T. However, viewing it as a simulation at $N_b T$ can be confusing as we will show here. To better understand what is going on, one must use the the generalized virial theorem, sometimes also called the generalized equipartition theorem:

$$\left\langle x_i \frac{\partial \mathcal{H}}{\partial x_j} \right\rangle = \frac{1}{\beta} \delta_{ij} \tag{11.21}$$

This theorem is proved by doing integration by parts on the canonical partition function. This theorem provides the rigorous link between the temperature and the kinetic energy of the system. For the "RPMD" method the theorem yields:

$$\left\langle \sum_i^N \sum_j^{N_b} \frac{(\boldsymbol{p}_i^j)^2}{2m_i} \right\rangle = \frac{3NN_b^2 k_B T}{2} \tag{11.22}$$

Whereas in method 2 we obtain the more expected form:[1]

$$\left\langle \sum_i^N \sum_j^{N_b} \frac{(\boldsymbol{p}_i^j)^2}{2m_i} \right\rangle = \frac{3NN_b k_B T}{2} \tag{11.23}$$

Another way to look at what is going on is to look at the centroid virial theorem. For the "RPMD style" method the centroid equipartition theorem is

$$\left\langle \sum_i^N \frac{(\boldsymbol{p}_i^c)^2}{2m_i} \right\rangle = \frac{3Nk_B T}{2} \tag{11.24}$$

whereas for method 2 the centroid equipartition theorem is

$$\left\langle \sum_i^N \frac{(\boldsymbol{p}_i^c)^2}{2m_i} \right\rangle = \frac{3Nk_B T}{2N_b} \tag{11.25}$$

[1] From this equation we can see that at a given temperature the "RPMD style" method has N_b times the kinetic energy of method 1, (when simulating at the same T) suggesting that this method actually may have better ergodicity (can explore phase space faster). However, at the same time the spring constants are larger by a factor of N_b, so the system is more stiff. The two factors appear to cancel each other out, suggesting that both methods have the same ergodicity.

These relations can be proved easily using $\boldsymbol{p}_i^c = \frac{1}{N_b}\sum_k^{N_b} \boldsymbol{p}_i^k$ and equation 11.21. Therefore we see that in RPMD the centroid variables follow the classical virial theorem whereas in method 2 they do not. This can be confusing, because if one used the classical virial theorem on the centroids for method 2 one would find they have a temperature of T/N_b where T is the bead temperature. In conclusion, the difference between the two methods is best viewed as a mathematical difference, and not a difference in the physics of the system.

11.1.2 Evolution of the free ring polymer

The evolution of the free ring polymer would make a good undergraduate physics problem. We sketch the solution here. The bead index will be b and the spatial index (x,y,z) will be i.

The potential energy of the system is:

$$V = \sum_b \frac{1}{2} m\omega_n^2 (\boldsymbol{q}^b - \boldsymbol{q}^{b+1})^2 \tag{11.26}$$

Using Newton's 2nd law we find

$$\begin{aligned} \ddot{q}_i^b &= \omega_n^2 (q_i^b - q_i^{b+1}) + \omega_n^2 (q_i^{b-1} - q_i^b) \\ &= \omega_n^2 (q_i^{b+1} + q_i^{b-1} - 2q_i^b) \end{aligned} \tag{11.27}$$

This result can be recast as a matrix equation. The system can then be solved by finding the eigenvectors and eigenvalues of the matrix. However the general form of the eigenvectors and eigenvalues can be found for an arbitrary number of beads N_b, and with the general solution in hand there is no need to solve a matrix equation each time a number of beads is presented. Because there are N_b independent variables, the theory of ODEs tells us that there should be N_b linearly independent solutions. We assume a particularly simple form for these solutions:

$$q_i^b(t) = u_i^b (A\cos(\omega t) + B\sin(\omega t)) \tag{11.28}$$

Additionally, we assume that the amplitudes u_i^b have a sinusoidal spatial dependence $u_i^b = e^{-ibk}$:

$$q_i^b(t) = e^{-ibk} (A\cos(\omega t) + B\sin(\omega t)) \tag{11.29}$$

Other equivalent choices are possible here (for instance we could have chosen $u_i^b = \sin(bk)$). By plugging 11.29 into 11.27 we find that this solution works

as long as:

$$\Omega^2 = 2\omega_n^2(1 - \cos(k)) \tag{11.30}$$

We also require periodic boundary conditions ($q_i^b = q_i^{b+N_b}$), which restrict the possible k to $k = \frac{2\pi j}{N_b}$ where $j = 1, 2, \cdots N_b$. We can recast 11.30 into a nicer form for computation by using the identity $\cos(2x) = 1 - 2\sin^2(x)$, which leads to:

$$\Omega_j = \pm 2\omega_n \sin\left(\frac{\pi j}{N_b}\right) \tag{11.31}$$

These are the frequencies of the N_b normal modes. Note that for every frequency Ω_b there is another frequency $\Omega_k = -\Omega_j$ corresponding to a two-fold degeneracy in the spectrum. For a single free ring polymer in normal modes the Hamiltonian becomes:

$$H_i = \sum_{j=0}^{n-1} \frac{(\tilde{p}_i^j)^2}{2m_i'} + \frac{1}{2} m_i \Omega_j^2 (\tilde{q}_i^j)^2 \tag{11.32}$$

Since these normal modes have simple harmonic oscillator Hamiltonian, they evolve the same way. The textbook propagation equation is:

$$\begin{pmatrix} q(\Delta t) \\ \dot{q}(\Delta t) \end{pmatrix} = \begin{pmatrix} \cos(\Omega_j \Delta t) & 1/\omega_j \sin(\Omega_j \Delta t) \\ \omega_j \sin(\Omega_j \Delta t)) & \cos(\Omega_j \Delta t) \end{pmatrix} \begin{pmatrix} q(0) \\ \dot{q}(0) \end{pmatrix} \tag{11.33}$$

An arbitrary starting configuration of the ring polymer will consist of a linear combination of the normal mode solutions. To find this linear combination we do a projection into the normal mode vector space, which is precisely a discrete Fourier transform.[84] Once in Fourier space, the normal mode components are evolved a time Δt according to 11.33 and then the result is transformed back into real space. In our code the FFT has not yet been implemented. Instead we use a transformation matrix:

$$\begin{aligned} \tilde{q}_i &= \frac{1}{\sqrt{N_b}} \sum_{i=1}^{N_b} O_{ij} q_i \\ q_i &= \sqrt{N_b} \sum_{i=1}^{N_b} O_{ij}^T q_i \end{aligned} \tag{11.34}$$

11.2 CMD vs. PIMD vs. RPMD

The literature on path integral methods is very large and difficult to navigate, in part because there are several different methodologies. However,

what appear to be very different methodologies are actually very closely related, as we will show in this section. Witt et. al note that"Mathematically, only the choice of the fictitious mass matrix $\mathbf{M}$ and the use of thermostats set apart PIMD, CMD and PIMD, whereas conceptually the methods differ dramatically."[350] The difference between the methods really only amounts to a difference in mass rescaling. Differences in terminology obscure this fact, however.

Recall that when momentum was added (eqn. 11.14) the masses m'_j of the beads were arbitrary. The effect of changing the fictitious mass of the j^{th} normal mode can be seen by starting with the ring polymer Hamiltonian in normal mode space. For simplicity we consider a single ring polymer in free space:

$$H = \sum_{j=0}^{n-1} \frac{(\tilde{p}^j)^2}{2m'_j} + \frac{1}{2} m\Omega_j^2 (\tilde{q}^j)^2 \tag{11.35}$$

From Hamilton's equations ($\dot{q} = \partial H/\partial p$, $\dot{p} = -\partial H/\partial q$) we get the following equations of motion:

$$\dot{\tilde{q}}^j = \frac{\tilde{p}^j}{m'_j} \tag{11.36}$$

$$\dot{\tilde{p}}^j = -m\Omega_j^2 \tilde{q}^j \tag{11.37}$$

Now we set our artificial masses m'_j to $\sigma_j m$. We call σ_j the "mass rescaling factor". The effect of σ_j can be seen by looking taking the time derivative of 11.36 and substituting 11.37 into 11.36:

$$\ddot{\tilde{q}}^j + \frac{\Omega_j^2}{\sigma_j} \tilde{q}^j = 0 \tag{11.38}$$

This is the equation of motion of a harmonic oscillator with frequency

$$f_j = \frac{\Omega_j}{\sqrt{\sigma_j}} \tag{11.39}$$

Many different choices for σ_j are possible. These choices will be discussed in the following sections.

11.2.1 Path integral molecular dynamics

The authors of the original PIMD approach[348] choose to bring all of the non-centroid frequencies to the value of ω_n by setting

$$\sigma_j = \begin{cases} 1 & j = 0 \\ \Omega_j^2/\omega_n^2 & j \neq 0 \end{cases} \tag{11.40}$$

The frequency ω_n lies in the middle of the unscaled frequency spectrum. The other ingredient to PIMD is to attach thermostats to each degree of freedom to overcome the ergodicity problems first pointed out by Hall and Berne (1984).[351] This results in the introduction of a large number of extra degrees of freedom, especially when using Nosé-Hoover chains, where a chain length of 4 is typical. As an example, with 4 chains, 30 beads, and 128 H_2O molecules this results in $4 \times 30 \times 128 \times 3 \times 3 = 138,240$ extra degrees of freedom. Updating these degrees of freedom takes time, but the extra time is usually insignificant compared to the force calculation routine. For fast force routines, Langevin thermostating can be used instead.

11.2.2 Partially adiabatic centroid molecular dynamics

A large class of choices for σ_j fall under the heading of "partially adiabatic centroid molecular dynamics" or PA-CMD, first introduced by Hone, Rossky and Voth (2006).[352] In this approach, the frequencies of the normal modes are scaled above the highest frequency of interest in the system. This is done so that the normal mode frequencies will not contaminate the frequency spectrum of the system.

A possible choice of σ_j for PA-CMD was suggested by Haberhon, Fanourgakis and Manolopoulos (2008):[353]

$$\sigma_j = \begin{cases} 1 & j = 0 \\ \frac{(\Omega_j \beta\hbar)^2}{N_b^{2N_b/(N_b-1)}} & j \neq 0 \end{cases} \tag{11.41}$$

This choice brings the beads to a frequency of $f = N_b^{N_b/(N_b-1)}/\beta\hbar$ which satisfies $\hbar f > N_b k_B T$. Thus assuming that N_b is chosen to satisfy the convergence criteria, this also guarantees that f is above the highest frequency of interest in the system. They also note that this case keeps the determinant of the Parrinello-Rahman mass matrix the same, thus ensuring that Z_n retains the correct normalization.[353] (Other authors ignore the normalization of Z - it does not affect the form of estimators for thermodynamic properties.) Addi-

tionally, $f < 2\omega_n$, where $2\omega_n$ is the highest normal mode in the case that all the masses equal the physical mass. Thus, by using this prescription one can use the same timestep as one would normally use.

More generally, one can consider shifting the masses as

$$\sigma_j = \begin{cases} 1 & j = 0 \\ \gamma^2 \frac{\Omega_j^2}{\omega_n^2} & j \neq 0 \end{cases} \tag{11.42}$$

γ is called the adiabaticity parameter. γ rescales the frequencies to ω_n/γ. Here we use the original notation of Hone et al.[352] Confusingly, Witt et al. define the adiabaticity parameter to be $\gamma' = 1/\gamma$.

11.2.3 Ring polymer molecular dynamics

Craig and Manolopoulos (2004) argued that the best way to accurately capture quantum dynamics is to give each bead the physical mass:[349]

$$\sigma_j = \begin{cases} 1 & j = 0 \\ 1 & j \neq 0 \end{cases} \tag{11.43}$$

In this scheme each bead is supposed to capture the physical dynamics so thermostating is not recommended. To achieve ergodic sampling one must sample many different initial conditions, for instance by running a thermostated MD run and then using many frames from the trajectory to start RPMD runs. However, RPMD spectra are plagued by contamination by the normal mode frequencies which span the entire spectrum from 0 to ω_n

11.2.4 Centroid molecular dynamics

An entirely different way of formulating path integral MD based on the centroid variables was introduced by Cao and Voth (1996).[354][355] Cao and Voth reformulated quantum statistical mechanics in terms of the centroid which feels a force from a quantum effective potential, also called the potential of mean force. CMD corresponds to an idealized limit where $\gamma \to 0$ or in other words, a limit where the masses of the non-centroid modes go to zero and they become completely adiabatically decoupled. In this limit, the non-centroid modes sample the effective potential completely and generate the effective force on the centroid. In practice all CMD runs use a non-zero γ. Because the non-centroid modes are scaled to very high frequency, very short time steps are required, leading to a severe increase in computational cost. CMD is of interest among

those studying time correlation functions since it performs better compared to PIMD and RPMD.[352] It is often remarked that only CMD has been proven to yield the exact quantum correlation function in the limit $t \to 0$ for a general anharmonic potential (as the number of beads is increased to infinity). PA-CMD or RPMD have only been proven to yield the correct correlation function in the harmonic, classical and free particle limits, and not the $t \to 0$ anharmonic limit.[352] In our view PA-CMD is therefore preferable to RPMD, especially because it was shown to perform slightly better at longer times.[352] On the other hand, it was shown that RPMD has a smaller leading error in the short time limit for both harmonic and anharmonic potentials compared with CMD.[356] The issue of how accurately either RPMD or PA-CMD can capture quantum time correlation functions and remains a subject of debate,[352] and more accurate methods are under development.[357]

11.2.5 Comparison of methods

The PIMD code (discussed below) allows one to rescale the masses and test the different methods. Out of the four methodologies presented, in general we argue that PACMD is the best, since it removes the spurious normal mode frequencies from the system while still allowing one to use the same timestep as RPMD. All these methods have been proven to be exact in the classical and free particle limit and $t \to 0$ harmonic cases.

11.3 Convergence criteria

11.3.1 Number of beads

The case of a PIMD ring polymer in a harmonic potential at temperature T can be solved exactly in the $n \to \infty$ (full quantum) limit. Therefore, by evaluating the performance of PIMD method at reproducing the energy of the harmonic oscillator one can derive the following convergence criteria:

$$n > \frac{\hbar\omega_{\max}}{k_B T} \tag{11.44}$$

$$k_B(nT) > \hbar\omega_{\max} \tag{11.45}$$

Here $\omega_{\max}$ is the highest frequency in the system. The interpretation of this formula is that the thermal energy of each bead ($k_B(nT)$) must be greater than the harmonic oscillator level spacing of the highest frequency oscillation in the system. As n is increased the effective temperature of the bead is

increased until the dynamics of each bead becomes classical. In water, eqn. 11.44 suggests using $\approx 30 - 40$ beads for capturing the OH stretch motion. In the literature, however, many authors use less beads – older studies, which tend to focus on static properties, often only used about 5 beads.[358] A later study which looked at the interaction energy vs number of beads showed that at least $n = 25$ is required for convergence.[359]

11.3.2 Timestep

As far as the timestep, when one is using an analytic method to evaluate the propagation of the ring polymer (either normal mode variables or staging variables) then in principle one can use the same timestep one uses in a classical MD simulation (ie. 00.5 fs for flexible and 1-2fs for rigid models). However, in practice most practitioners reduce the timestep when running PIMD. This helps avoid resonance phenomena which occur when a normal mode frequency is close to the inverse timestep $1/\delta t$. Many different choices of timestep can be found in the literature, some as low as .001 fs. We found that TTM3F RPMD runs OK with a timestep of 0.5 fs with up to 16 beads but will encounter resonance issues with 32 beads, requiring reduction of the timestep to 0.25 fs. A resonance occurs suddenly and at random, and is catastrophic to the simulation. In one case, what is believed to be a transient resonance was observed when running 32 beads with $\delta t = 0.5$ fs, where the temperature suddenly increased to 3500 K before quickly falling back. Interestingly, we found a timestep of 0.5 fs is perfectly stable with 32 beads and PA-CMD, which is another reason we find this method to be superior to RPMD.

11.4 The curvature problem

We make a detour at this point to discuss an an issue with PIMD simulations which is rarely discussed but in principle is always present. The "curvature problem" is most easily visualized in the limit that the OH bond becomes very stiff, but it is not restricted to this case. In this case, the path integral beads are confined to the surface of a sphere whose radius is determined by the OH bond length (neglecting the H-H potential for simplicity). Due to the curvature of the sphere, the centroid will lie somewhere inside the sphere, effectively making the OH bond shorter as measured by the centroid. If one observes the infrared spectra of a single flexible water molecule one finds two regimes - a regime where the OH stretching peak shifts linearly with temperature and a regime at lower temperature where the shift becomes highly nonlinear. This nonlinear behaviour and an associated

broadening of the peak are due to the curvature problem.[350] Fortunately it only becomes problematic at low temperatures. For a single flexible water molecule, the threshold of the nonlinear regime is around 220 K.[350] For the case of rigid models it may be possible to rectify this issue through a modification of the method. For instance, a special formulation of PIMD in curvilinear coordinates was developed for the simulation of rigid rotors to solve this issue, but only through the painstaking addition of complicated coordinate transformations.[360] The curvature problem was investigated in detail by Paesani and Voth (2009).[350][361] The conclusion was that the curvature problem is greater in harmonic potentials and less of a problem in anharmonic problems. The reason for this is simply due to the fact that anharmonic potentials include a more physically realistic repulsive potential at small r_{OH}. The conclusion of Paesani & Voth is that the effects of the curvature problem (redshifting and broadening) are negligible for simulations at ambient temperature when an anharmonic OH potential is used.[361] For the purely harmonic potential SPC-f, we found that the curvature problem is problematic even at 300 K.

11.5 Calculating observables in PIMD

11.5.1 The radius of gyration

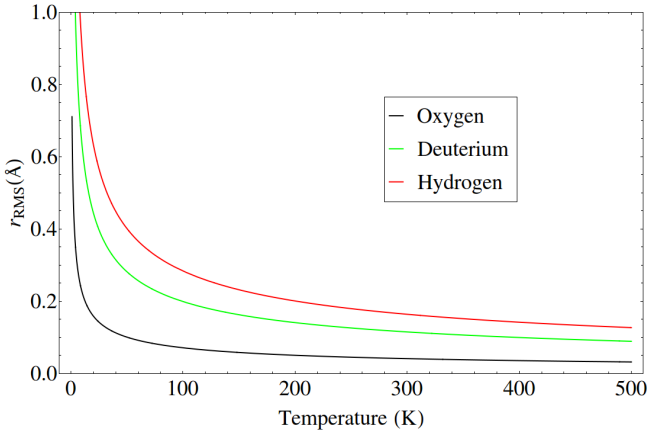

Figure 11.1: A plot of equation 11.48 for the radius of gyration vs. temperature.

The effective size of the ring polymer can be found by calculating the root mean square displacement of beads from the center of the ring, also called the "radius of gyration". The average radius of gyration can be calculated as:

$$r_{\text{gyr}} = \frac{1}{NN_b} \sum_{i=1}^{N} \sum_{j=1}^{N_b} ||\boldsymbol{r}_i^j - \boldsymbol{r}_i^c|| \tag{11.46}$$

In general, the beads will not be spherically distributed. To see this one can calculate a radius of gyration tensor[362]:

$$r_{lk}^2 = \frac{1}{N_b} \left\langle \sum_{j=1}^{N_b} (r_j^l - r_c^l)(r_j^k - r_c^k) \right\rangle \tag{11.47}$$

Where $l, k \subset x, y, z$. This tensor can be diagonalized into three principle components. This analysis has been done before to study how the hydrogen atom delocalizes in liquid water.[362] Not surprisingly, one finds that the hy-

drogen atom is mostly delocalized along the axis perpendicular to the OH and HH vectors. This direction is called the "flap" direction. The reason for this delocalization is clear when one considers that in the OH-bond direction, the hydrogen atom finds itself confined in a rather steep well. In the perpendicular direction in the HOH plane the hydrogen atom encounters repulsion from the other hydrogen atom. In the "flap" direction, however, there is only free space so naturally the ring polymer spreads most in this direction.

The radius of gyration for the free ring polymer at temperature T in the exact ($N_b \to \infty$) limit is:

$$r_{\text{gyr}} = \frac{\Lambda(T)}{\sqrt{8\pi}} \tag{11.48}$$

where $\Lambda(T)$ is the quantum thermal de Broglie wavelength :

$$\Lambda(T) \equiv \frac{h}{\sqrt{2\pi m k_B T}} \tag{11.49}$$

Equation 11.48 is plotted in figure 11.5.1 for hydrogen, deuterium and oxygen.

11.5.2 Estimators

A good description of estimators can be found in Tuckerman (2008).[84] Estimators follow from the equation

$$\langle \hat{A} \rangle = \frac{1}{Z} \text{Tr} \left[\hat{A} e^{-\beta \hat{H}} \right] \tag{11.50}$$

The energy estimator and pressure estimator can be derived using the thermodynamic relation

$$E = \frac{-1}{Z} \frac{\partial Z}{\partial \beta_n} \tag{11.51}$$

Using this relation results in the "primitive estimator" for the energy:

$$E_s = \frac{1}{N_b} \left[\frac{3NN_b k_B T}{2} - \frac{1}{2} \sum_{i=1}^{N} \sum_{k=1}^{N_b} m_i \omega_n^2 (\boldsymbol{r}_i^{k+1} - \boldsymbol{r}_i^k)^2 + \sum_{k=1}^{N_b} U(\boldsymbol{r}_1^k, \cdots, \boldsymbol{r}_N^k) \right] \tag{11.52}$$

The factor of $1/N_b$ in the front is only included for "RPMD style" PIMD, where $\beta_n = \beta/N_b$. the bead temperature is $N_b T$. The estimator for the kinetic energy is :

$$E_k = \frac{3NN_b k_B T}{2} - \frac{1}{2} \sum_{i=1}^{N} \sum_{k=1}^{N_b} m_i \omega_n^2 (\boldsymbol{r}_i^{k+1} - \boldsymbol{r}_i^k)^2 \tag{11.53}$$

The first term in eqn. 11.53 is the classical kinetic energy, so the second term is known as the "quantum kinetic energy".

The pressure estimator can be derived using

$$P = \frac{k_B T}{Z} \frac{\partial Z}{\partial V} \tag{11.54}$$

The volume dependence of Z can be made explicit by switching to scaled variables which are a canonical transformation :

$$\begin{aligned} \boldsymbol{s}_i^k &= V^{-1/3} \boldsymbol{q}_i^k \\ \boldsymbol{\pi}_i^k &= V^{1/3} \boldsymbol{q}_i^k \end{aligned} \tag{11.55}$$

These variables preserve the form of the phase space volume element. The resulting primitive estimator for the pressure can be found in (Cao, 1989).[363] It turns out the primitive estimators for energy and pressure converge extremely slowly. Therefore, "virial estimators" (derived from the virial equation) are preferred. The virial energy estimator is:

$$E_{\text{vir}} = \frac{3Nk_BT}{2} + \frac{1}{N_b} \sum_{k=1}^{N_b} \sum_{i=1}^{N} \frac{1}{2} \left(\boldsymbol{r}_i^k - \boldsymbol{r}_i^c \right) \cdot \frac{\partial U}{\partial \boldsymbol{r}_i^k} + \frac{1}{N_b} \sum_{k=1}^{N_b} U(\boldsymbol{r}_1^k, \cdots, \boldsymbol{r}_N^k) \tag{11.56}$$

The virial estimator for the pressure is :

$$P_{\text{vir}} = \frac{3Nk_BT}{V} + \frac{1}{N_b V} \sum_{i=1}^{N} \boldsymbol{r}_i^c \cdot \sum_{k=1}^{N_b} \frac{\partial U}{\partial \boldsymbol{r}_i^c} \tag{11.57}$$

The primitive pressure estimator and virial estimators for the energy and pressure involve calculation of the virial $\sum -\boldsymbol{r}_i^k \cdot \boldsymbol{\nabla} U$. One runs into a problem when trying to apply this formula to systems with periodic boundary conditions, which is that the coordinate $\boldsymbol{r}_i^k$ is not properly defined in an absolute coordinate system. Another way to see the problem is to note that there is no obvious notion of a surface term when using periodic boundary conditions, and the presence of a surface term in the virial equation of state is what makes the pressure nonzero.[59] Using a bit of algebra one can show the following relation:[59]

$$\sum_i \boldsymbol{r}_i \cdot \boldsymbol{F}_i = \frac{1}{2} \sum_{i,j,i \neq j} \boldsymbol{r}_{ij} \cdot \boldsymbol{F}_{ij} \tag{11.58}$$

By rewriting the virial in this way, we can properly compute it with periodic boundary conditions, where $\boldsymbol{r}_{ij}$ refers to the distance between $\boldsymbol{r}_i$ and the nearest image of $\boldsymbol{r}_j$.

A few other estimators not discussed here have been derived, for instance for the heat capacity.[364] To our knowledge no estimator for the dielectric susceptibility has been derived, although the early work of Parrinello & Rahman contains a derivation of an estimator for the magnetic susceptibility.[348]

11.5.3 The dipole moment

There are two ways to calculate the dipole moment – the first is to simply use the centroids:

$$\begin{aligned} \boldsymbol{\mu}_i &= \boldsymbol{\mu}(\bar{\boldsymbol{r}}_{\mathrm{O}}, \bar{\boldsymbol{r}}_{\mathrm{H1}}, \bar{\boldsymbol{r}}_{\mathrm{H2}}) \\ \bar{\boldsymbol{r}}_i &= \frac{1}{N_b} \sum_{j=1}^{N_b} \boldsymbol{r}_i^j \end{aligned} \tag{11.59}$$

The second way is to calculate it for each the beads in each "image" (or imaginary time slice) and then average them:

$$\boldsymbol{\mu}_i = \frac{1}{N_b} \sum_{j=1}^{N_b} \boldsymbol{\mu}(\boldsymbol{r}_{\mathrm{O}}^j, \boldsymbol{r}_{\mathrm{H1}}^j, \boldsymbol{r}_{\mathrm{H2}}^j) \tag{11.60}$$

For a linear dipole function the results are the same, but for a non-linear dipole function, such as in TTM3F, the results are not guaranteed to be the same. Habershon et al. note that "neither is particularly well justified" and choose method 1 since it is the one most commonly employed in CMD for non-linear operators. We implemented the second method because it was easier to implement - recalculating the dipole moment for TTM3F based on the centroids requires an additional dipole calculation. In practice no difference is observed between these two methods.[365]

11.6 The PIMD-F90 code

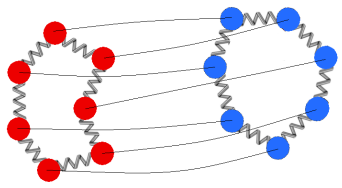

Figure 11.2: Illustration of the interaction of two atoms in PIMD, each represented by ring polymers.

A Fortran-90 code was written to implement the PIMD method described above. The code is open source and available at https://github.com/delton137/PIMD. The program uses a variable format input file, the specification of which are provided in appendix C. The force calculation routine was parallelized by performing the force calculations of each bead image on a separate processor. In the case that the number of beads is not equal to the number of processors, the work is divided accordingly.

11.6.1 Validation of energy & pressure

N_b	E_{gas}	E_{liq}	$E_{\text{liq}} - E_{\text{gas}}$	P (bar)
1	30.55 (30.55)	-7.1	-10.6(-10.7)	3.4 (54)
2	5.27 (5.18)	-40.5	-9.77(-10.0)	(-16)
3	6.84	-2.88	-9.8	-40
4	7.92 (7.82)	-1.89	-9.81 (-9.77)	-.75 (-116)
4		-1.61		
8	11.2 (11.0)	1.43	-9.77 (-10.0)	-53 (-138)
16	13.4 (130.5)		(-10.4)	(-152)
32	14.4 (14.6)	60.5	(-10.7)	-50 (-271)
48	15.0			
64	15.1			

Table 11.1: Data from runs of 128 molecules of TTM3F at 300 K in gas phase and liquid phase with a density of .997 kg/L. Values in parenthesis are the results from the original TTM3F paper.[15] All energies in kcal/mol. The energy converged quickly in 2-20 ps, but converging the pressure was much more difficult and required longer runs.

N_b	E_{gas}	E_{liq}	$E_{\text{liq}} - E_{\text{gas}}$	P (bar)	notes
1	3.62	-7.26	10.9	.27	$\rho = .994$ kg/L, 60 ps
1		-7.27		1.18	$\rho = .997$ kg/L, 177 ps
2	5.29			.08	
4	7.93				
8	110.25				
16	130.55				

Table 11.2: Data from runs of 128 molecules of SPC/F at 300 K in gas phase an in liquid phase with a density of .997 = kg/L unless otherwise specified.

The energy (computed via the primitive or virial energy estimator) provides one of the best gauges for the performance and convergence of a PIMD code.

Table 11.6.1 shows energies and pressures for different number of beads in the gas and liquid phases of TTM3F. There is good agreement with previously published results for TTM3F and convergence of the energy in gas phase is achieved with 32 beads. Table 11.6.1 shows similar results for SPC/f.

11.6.2 Radius of gyration

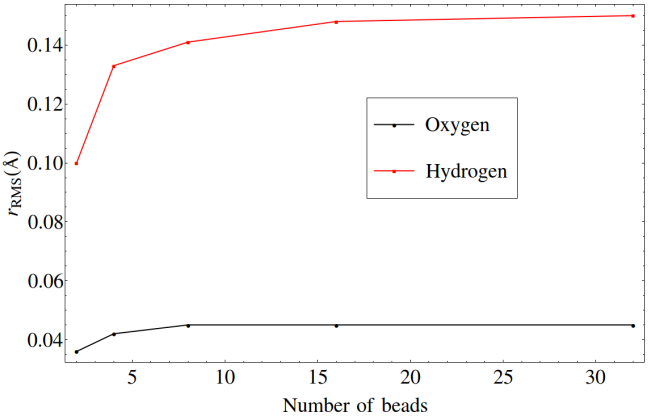

Figure 11.3: The radius of gyration vs. number of beads for TTM3F at 300 K.

Figure 11.6.2 shows the convergence of the radius of gyration with number of beads. We see that based on this measure as few as 8 beads can give a satisfactory degree of delocalization although at least 16 are needed for full convergence. Some early authors focused on this quantity alone and incorrectly assumed that 4-8 beads were an adequate number.

11.7 The effect of nuclear quantum effects in water

11.7.1 Literature overview

PIMD has now been used extensively to study structural quantities such as the molecular volume, bulk modulus, and bond lengths in water and ice. PIMD simulations can yield insights into how quantum delocalization and tunneling effect these properties and how they change under isotopic substitution. Herrero & Ramirez (2014) have written a detailed review of the PIMD simulation work that has been done on ice.[366]

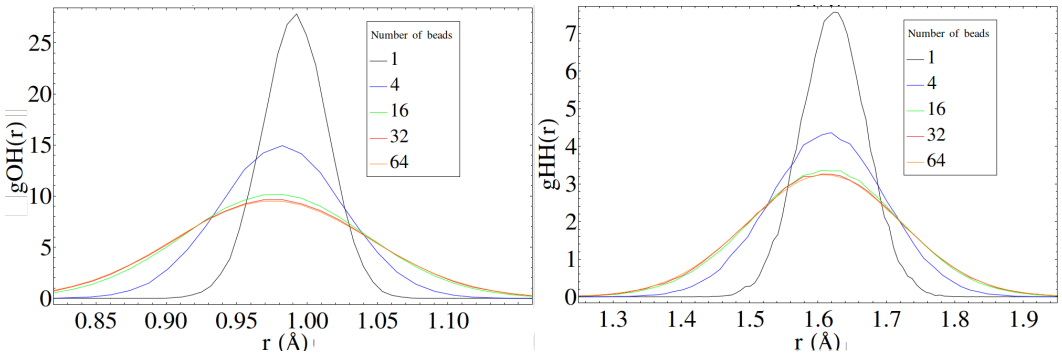

Figure 11.4: O-H (left) and H-H (right) RDFs for SPC/F, gas phase 300 K.

11.7.2 Radial distribution functions

The introduction of nuclear quantum effects via PIMD with a classical forcefield results in destructuring of the RDFs.[367, 368] The degree of destructuring in water at 300 K is small - for example the height of first and second O-O RDF peaks decrease by 1-3%. In ice at 220 K this increases to an 8% decrease.[369] There are also small (but very important) shifts in the spacing of the peaks, which signal changes in the density of the liquid and relative strength of OH and hydrogen bonds. When calculating RDFs with PIMD/CMD, it is important to calculate the RDF for the bead positions and not the centroid. Although the centroid is sometimes described as the "physical" coordinate, the centroid-centroid RDF does not correspond to the physical (quantum) RDF.[2]

Figure 11.4 shows the O-H and H-H RDFs for the SPC/F model of Toukan & Rahman (1985) vs number of beads.[371] The RDFs we computed for one bead matches the RDF in the original SPC/F paper fairly closely. As can be seen in the 1 bead RDF, SPC/F is a poor water model since it produces an understructured liquid. Figure 12.9.2 shows the OO, HH, and OH RDFs for TTM3F.

[2]This has been a point of confusion. For those wishing to do a deeper dive, the connection between the centroid RDF and the physical RDF is explained in detail by Blinov & Roy (2004).[370]

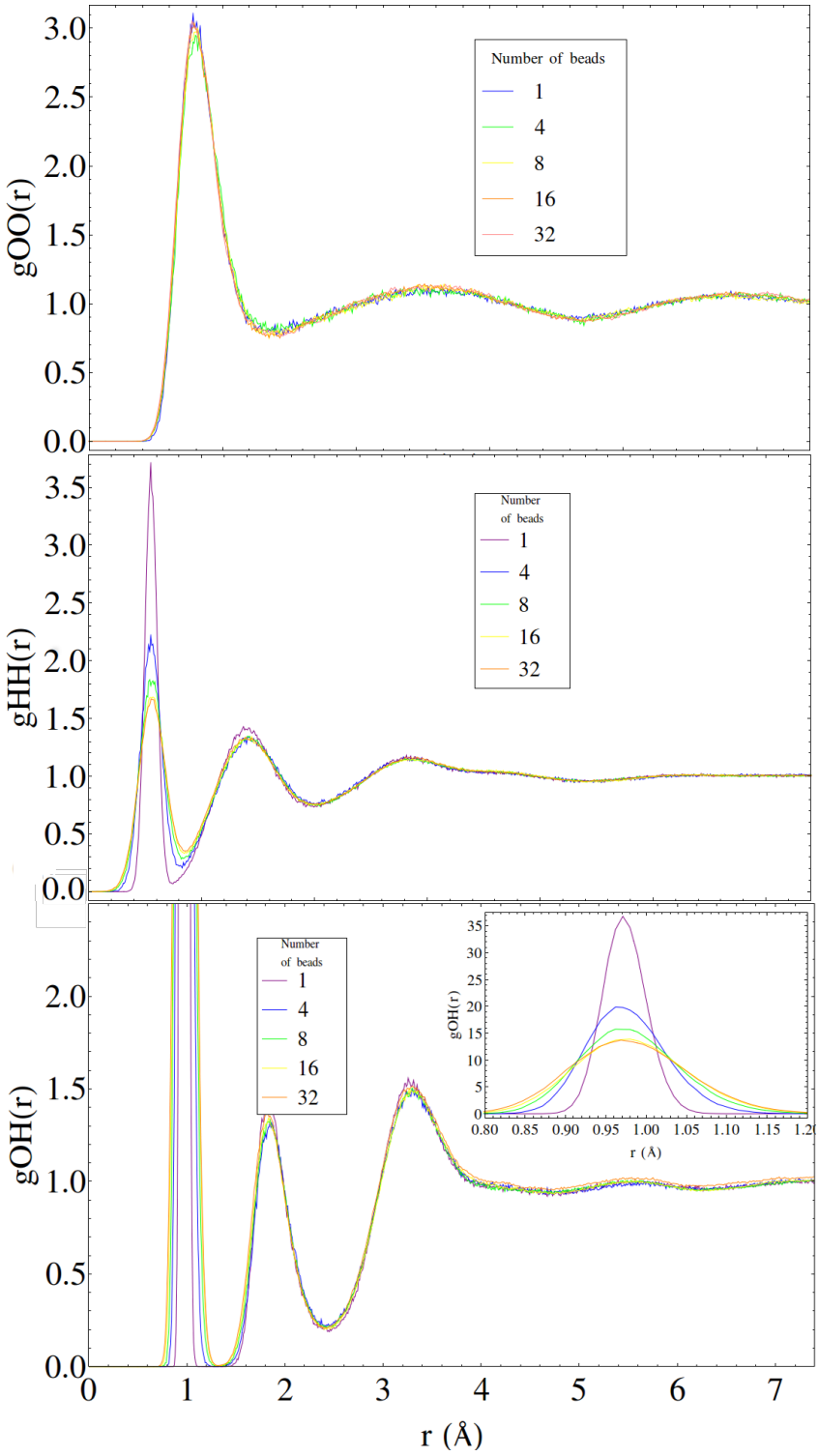

Figure 11.5: O-O (top), H-H (middle) and O-H (bottom) RDFs for TTM3F at 300 K vs number of beads.

11.7.3 Infrared spectra

Infrared spectra were calculated using the quantum harmonic correction, otherwise the magnitude is much too low.

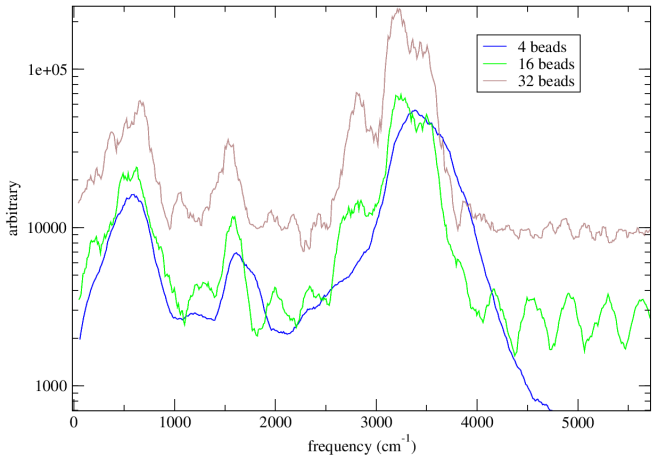

Figure 11.6: Preliminary simulations using TTM3F and RPMD. RPMD introduces normal mode contamination, as evidenced by the periodic bumps in the spectrum. For larger numbers of beads, the contamination appears to take the form of background noise in the smoothed spectrum.

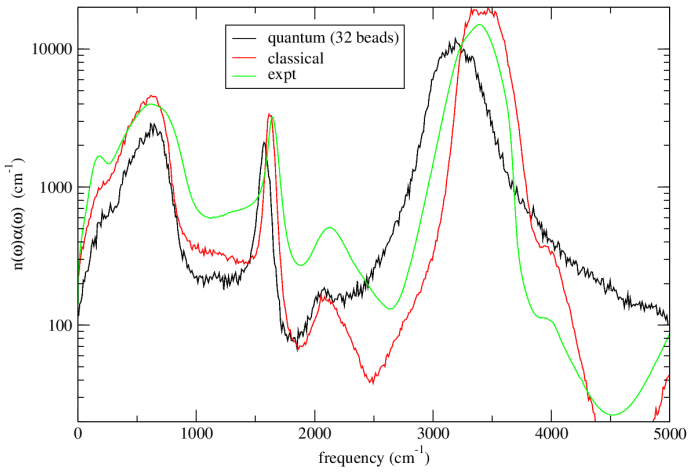

Figure 11.7: Infrared spectra for TTM3F at 300 K, plotted on a log scale to show detail. Experimental data from Bertie & Lan, 1996.[13] PA-CMD was used, with normal mode frequencies scaled to 5000 cm^{-1}.

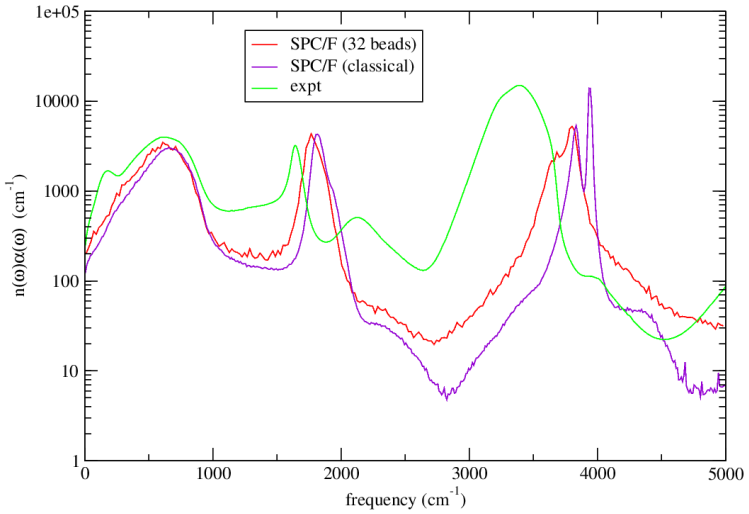

Figure 11.8: Infrared spectra for SPC/F at 300 K. Experimental data from Bertie & Lan, 1996.[13] PA-CMD was used, with normal mode frequencies scaled to 5000 cm^{-1}.

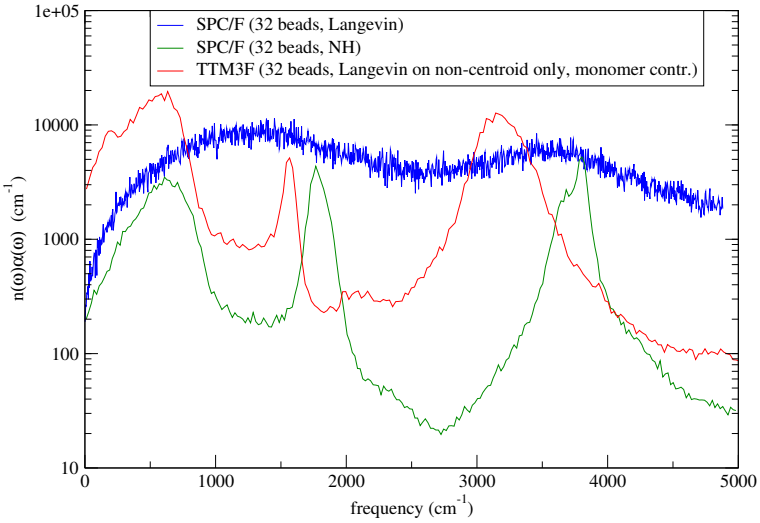

Figure 11.9: Infrared spectra for SPC/F at 300 K showing the dramatic difference between the use of Langevin and Nosé-Hoover bead thermostats. The Langevin thermostat samples PIMD phase space faster, but completely destroys the dynamics. However, when Langevin thermostating is done in normal mode space (such as the PILE thermostat) it can can be disabled on the centroid mode. In that case, the dynamics are preserved, as shown for TTM3F.

Figure 11.7.3 shows the infrared spectra for TTM3F. Since TTM3F is already so well tuned to reproduce such spectra, PIMD does not improve the model. The well known redshifting and broadening of the OH stretch mode due to NQEs is clearly visible.

11.7.4 Debye relaxation

As we showed earlier, TTM3F, TIP4P/2005f, and TIP4P/2005 all overestimate the Debye relaxation time by about 15%. It has been found that using PIMD simulation with rigid models typically results in a 10-30% reduction in the Debye relaxation times and single molecule reorientation times, yielding better agreement with the experimental values.[359] In TTM3F, however, the inclusion of quantum effects with 32 beads results in single molecule relaxation times which are essentially the same at room temperature, but which are faster at lower temperatures.[372]

11.7.5 Diffusion constant

Similar to the increase in dipole relaxation time, PIMD increases the diffusion constant by ≈40-50% at 300 K.[359, 373, 374, 369, 375, 376] Unfortunately, this increase in diffusion makes the models less physically accurate. The validity of prior studies using PIMD was questioned by Habershon, Markland, and Manolopoulos.[353] There are several reasons for this dramatic increase in diffusion. The oft-cited reason is the weakening of the H-bonds, which can be due to delocalization or due to a shorter OH distance, depending on the model being used. Another more general explanation is that PIMD results in effective smoothing of the potential energy surface, since the effective force on the centroid is an "average" of the forces experienced by different beads. This results in a potential energy surface with lower maxima and higher minima, and thus atoms (and molecules) have more freedom to move. The lowering of potential energy maxima is sometimes interpreted as "effective tunneling".[377]

11.8 The effects of isotopic substitution

The PIMD code contains an option to change the mass of hydrogen, which allows one to simulate the effects of the isotopic substitution of deuterium or tritium. In classical molecular dynamics, substituting deuterium for hydrogen does not change the structure of the liquid, and only slows the dynamics. In PIMD simulation, however, important changes to the structure and dynamics of the liquid can be observed.

	H2O	D2O	T2O	$\Delta_{H\rightarrow D}$	ref.
ice XI $\rightarrow$ ice Ih	70	76		6	[378, 379, 380, 379, 379]
melting point	273.15	276.96	277.64	3.81	[381]
boiling point	373.12	3740.55		1.46	[381]
critical temp	647.00	643.85		-30.25	[381]
temp max density	277.13	284.35	2860.55	7.22	

Table 11.3: Experimental values for various phase transition temperatures and the temperature of max density.

model	V^{clas}_{H2O}	V^{quan}_{H2O}	V^{quan}_{D2O}	ref.
q-TIP4P/2005f	30.98	32.30	32.13	ice, QHA [384]
TTM3F	31.66	31.67	31.67	ice, QHA [384]
TTM3F	30.08	29.43		liquid, 298 K [15]
TTM2.1F	280.54	29.15	28.92	liquid, 298 K [385]
expt.		29.94	29.99	liquid, 298 K

Table 11.4: Quantum effects on the volume (in $Å^3$) per molecule.

11.8.1 Thermodynamic properties

Isotopic substitution changes the phase transition temperatures of water, as shown in table 11.8.1. With the exception of the critical temperature, important points on the phase diagram are shifted to higher temperatures for D2O. This effect has been captured via PIMD simulation with the q-TIP4P/2005f model, where it is found that D2O increases the melting point of the model by 60.5 degrees.[382] q-TIP4P/2005f has been reparameterized for D2O and T2O to better capture the isotopic shifts in the melting point and temperature of maximum density.[383] Nuclear quantum effects increase the volume of ice by about 1% over the value expected from an extrapolation from higher temperatures. This "anomalous zero-point volume expansion" is found in many materials and is especially pronounced in atomic solids such as Neon. Recently, Pamuk, et al., showed that this anomalous volume expansion is itself anomalous in water.[384] According to the usual quantum volume expansion, D2O should have a smaller volume per molecule than H2O, since NQEs are less pronounced in D2O. However, experimentally at very low temperatures (10 K), the volume per molecule of D2O ice is greater than H2O by about 0.1%. Intriguingly, this effect becomes larger at higher temperatures – near the melting point of ice it D2O has a volume that is 40.5% higher. Lesser known is

that this same effect appears in liquid water - the volume per molecule of D2O water is about 0.1% larger than in H2O! This effect is not captured by classical models such as TIP4P/2005f or TTM3F.[384]

11.8.2 Dielectric properties of ice

The first reported measurements to compare the dielectric constants of H2O and D2O was performed by Auty & Cole (1952).[386] They found that the dielectric constant of D2O was somewhat smaller than H2O at all temperatures ($\approx 3\%$ smaller at -20 C). Johari & Jones (1976) found values of the dielectric constant for D2O to be about 8% larger than those measured by Auty & Cole.[387] The data of Auty & Cole was called into question, since their values for H2O ice were systematically lower than other authors by 3% to 5% (while the other authors agreed within 1%). Contrary to the finding of Auty & Cole, Johari & Jones found that D2O ice has a dielectric constant which is 7% higher, which may "indicate a 4% higher effective dipole moment in D2O ice compared with H2O ice". Johari & Jones found that the high frequency dielectric constant of D2O is about 3% smaller at all temperatures.[387]

The data of Kawada shows the isotopic effects found in other hydrogen-bonded systems - an increase in the Curie temperature and dielectric constant.[3] More specifically, T_C was raised from 46 K to 55 K, or in other words $T_C(D)/T_C(H) = 1.2$.[388] This value can be compared with normal order-disorder ferroelectrics, which typically have $T_C(D)/T_C(H) = 1.02 - 1.08$ and KDP materials, which have $T_C(D)/T_C(H) = 1.6 - 1.7$.[388] Early experimental data indicated a wide range of values for T_c, ranging from -146 to 30 K.[389] (A T_c below 0 indicates there is no ferroelectric transition.) The data of Johari and Jones (1976) yield $T_c = 27 \pm 1$ K for D2O.[390] A later study by Johari & Whalley (1981) found $T_C = 6.2 \pm 1.7$ K for H2O and their review of previous experiments up to 1981 found an average of $T_C = 15 \pm 11$.[391] Since Kawada et al. used single crystal samples, he was able to observe significant anisotropy in the dielectric constant. They found that upon isotopic substitution $\varepsilon_\perp$ does not change but $\varepsilon_\parallel$ increases, resulting in an increase in anisotropy.

Other differences between H2O and D2O are the ice-XI transition temperature (70 K for H2O and 76 K for D2O)[379, 378, 380, 392] and the dielectric relaxation time, which is about 40% slower in D2O ice.[390]

[3] To a good approximation the temperature dependence of the dielectric constant of ice follows the Curie-Weiss law:

$$\varepsilon - \varepsilon_\infty = \frac{A_c}{T - T_c} \tag{11.61}$$

11.8.3 Liquid structure

We find the q-TIP4P/2005f model shows an increase in *both* hydrogen bond length (1.82 → 1.84) and covalent bond length (.963 → .977) upon the inclusion of NQEs. As we explain in the next chapter, this is unphysical. Likewise, it shows a slight decrease in both hydrogen bond length (1.84 → 1.83) and covalent bond length (.977 → .974) upon isotopic substitution of deuterium. In figure 11.8.4 we compare the RDFs of H2O and D2O for TTM3F at 300 K with 32 beads.

11.8.4 Dipole moments & dielectric constant

	H2O	D2O	ref
ice Ih $\varepsilon(0)$(-25 C)	98	96	Auty & Cole, 1952 [386]
	103	110	Johari, et al. 1976 [387]
	103	107	Kawada, 1979 [388]
liquid $\varepsilon(0)$ (25 C)	78.39	78.06	Vidulich et al. 196 [393]
	78.39	78.06	Kawada et al. 1979 [388]
gas phase μ (D)	1.8546(4)	1.8545(4)	Dyke & Muenter, 1973[394]
	1.8546(6)	1.8558(21)	Clough, 1973 [395]
	1.85498(9)		Shostak, 1991 (IAPWS value) [396]
	1.84(1)	1.84(1)	Groves & Sugden, 1935 [397]
gas phase r_{OX} (Å)	0.9724	0.9687	Cook, 1974 [398]
gas phase θ_{XOX}	1040.50	104.3	Cook, 1974 [398]

Table 11.5: Experimental dielectric constants for H2O & D2O in the solid (polycrystalline ice Ih), liquid, and gas phases, and dipole moments and geometry in the gas phase.

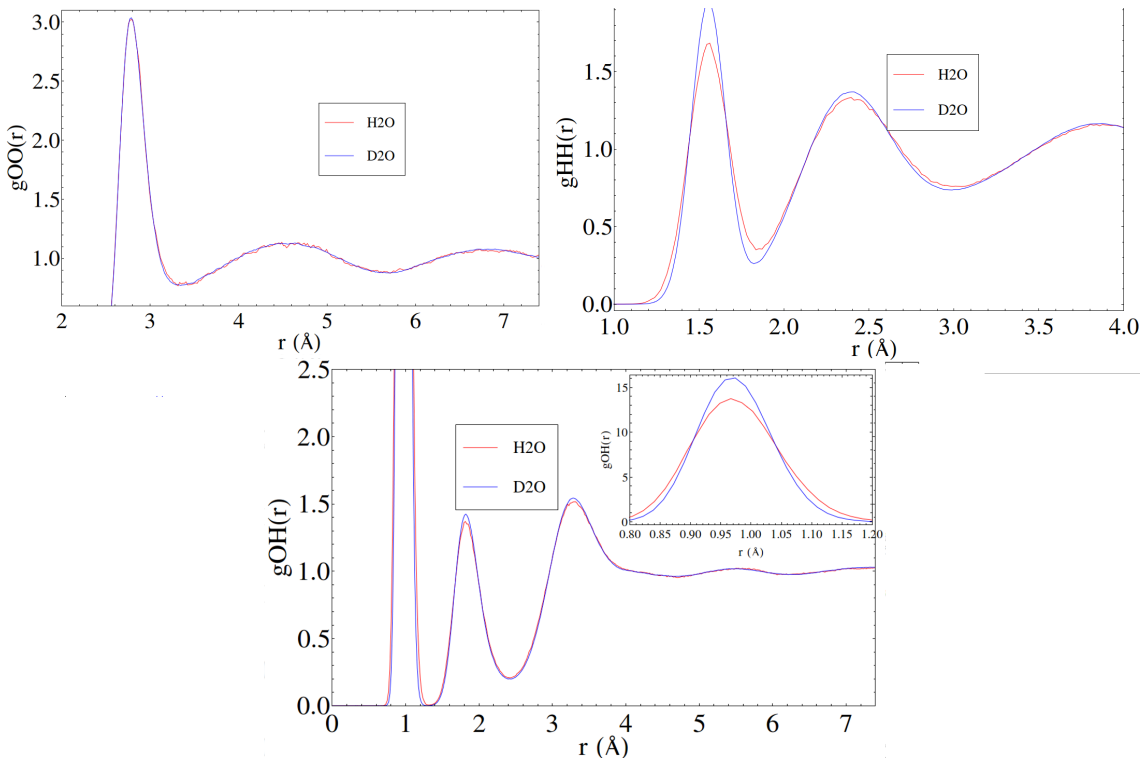

Figure 11.10: RDFs for TTM3F at 300 K comparing H2O and D2O. In these results the OH and OD bond lengths are nearly identical.

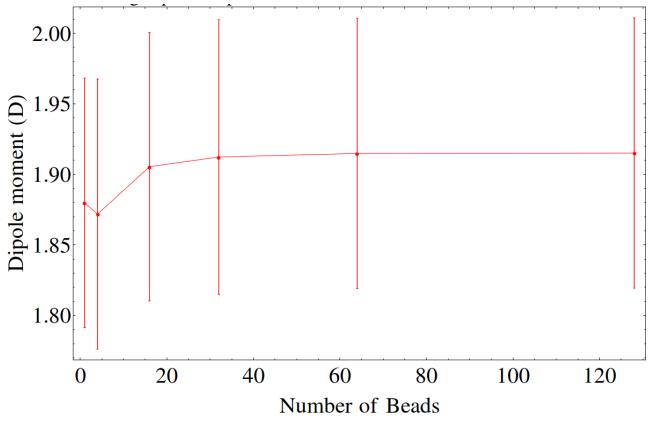

Figure 11.11: Gas phase dipole moments for TTM3F vs number of beads at 300 K.

model	temp	# beads	$\varepsilon(0)^{\text{clas}}_{\text{H2O}}$	$\varepsilon(0)^{\text{quan}}_{\text{H2O}}$	$\varepsilon(0)^{\text{quan}}_{\text{D2O}}$	
TTM3F	300	32	94±1	81±2		this work
SPC/F	300	32	82±1	60±1		this work
SPC/F	300	8	80±8	67±9		[399]
SPC/Fw	300	8	80±2	64±4		[400]
q-TIP4P/2005f	298	32	58±1	60±3		this work,[**?**]
q-SPC/Fw	298	32	60±3	90±3		[**?**]
q-SPC/Fw	298	32	60±3	86±4		[**?**]
RWK2	300	8	28±2	30±4		[16]
TTM2.1-F	298	32	67±10*	74±10*	71±10*	[385]

Table 11.6: Classical (1 bead) and quantum (32 bead) dielectric constants.*As pointed out by Burnham et al., the error bars in $\varepsilon(0)$ reported in the work of Paesani et al. appear to be too low by a factor of 5, so we have corrected them accordingly.[16]

phase	model	# beads	μ^{clas}	μ^{quan}	% diff	ref
gas, 300 K	SPC/F	32	2.271 ± 0.13	2.206 ± 0.14	-3	this work
	TTM3F	32	1.880 ± 0.09	1.912 ± 0.10	+1.7	this work
	q-TIP4P2005f	32 *	2.311	2.348	+1.6	Habershon, et al., 2009[**?**]
	MCDHO	24	1.869	1.922	+2.8	Bern & Stern, 2001[401]
liquid 298/300 K	SPC/F	32	2.419 ± 0.12	2.355 ± 0.13	-20.5	this work
	TTM3F	32	2.750 ± 0.19	2.836 ± 0.22	+3	this work
	TTM3F (D2O)	32	2.759 ± 0.21	2.814 ± 0.22	+2	this work
	q-TIP4P2005f	32	2.312	2.346	+10.5	this work
	q-TIP4P2005f	32*	2.311	2.348	+1.6	Habershon, et al., 2009[**?**]
	q-TIP4P2005f	20	2.312	2.346	+10.5	Ramirez, et al., 2010[382]
	q-TIP4P2005f (D2O)	32	2.312	2.338	+1.1	this work
	qSPC/Fw	32*	2.39	2.465	+3.1	Habershon, et al., 2009[**?**]
	qSPC/Fw	32	20.51	2.46		this work
	TIP3P/F	32	20.54	20.54	0.0	Burnham, et al. 2008[16]
	RKW2	32	1.92	1.89	-1.6	”
	TTM2-F	32	2.66	2.62	-10.5	”
	TTM2.1F	32	2.67	2.63	-10.5	Paesani, 2007[385]
	TTM4-F	32	2.81	2.83	+0.07	Burnham, et al. 2008[16]
	MCDHO	24	2.968(5)	3.011(3)	+1.4	Bern & Stern, 2001[401]
	BLYP DFT	16	3.04	3.18(1)	+4.6	Chen, et al., 2003 [402]
	BLYP DFT	32	2.83	2.83	+0.0	Morrone & Car, 2008[403]
ice, 269 K	TIP3P/F	32	20.52	20.55	+1.2	Burnham, et al. 2008 [16]
	RKW2	32	1.92	1.82	-50.5	”
	TTM2-F	32	2.78	2.72	-2.2	”
	TTM4-F	32	2.92	2.96	+1.4	”
ice, 100 K	PBE DFT	32	3.413(1)	30.56(1)	+4.3	Moreira, et al., 2015[404]

Table 11.7: Classical (1 bead) and quantum dipole moments and standard deviations. *Haberson, et al. use a ring polymer contraction scheme with a cutoff of 5Å.

Table 11.8.4 shows experimental values for $\varepsilon(0)$ for H2O and D2O. As expected the O-H distance is slightly longer than the O-D distance, and the HOH angle is slightly larger than the DOD angle. A larger O-X distance does not always imply a larger dipole moment. At some r_{OX}, the dipole moment must reach a maximum, since the charge on the isolated atoms is zero. In HCl, experimentally it appears that the maximum is close to the equilibrium bond length, so nuclear quantum effects actually cause the dipole moment to decrease. The dipole moment of HCl is smaller than DCl by about 0.5%.[405] An even larger effect ($\approx -5\%$) is seen when comparing the dipole moments of NH_3 and ND_3.

Does the dipole moment of the water molecule change with isotopic substitution? There are very few measurements of the dipole moment of D2O in the literature. The work of of Dyke & Muenter and Clough et al. (both using the Stark effect to infer the equilibrium dipole moment) both found that the dipole moment of D2O is slightly larger, but the increase is within the experimental error bar.[394, 395] The theoretical work of Kern & Matcha (1968) indicates that zero point motion decreases the equilibrium dipole moment of water, to a larger degree in H2O than D2O (-0.0171 vs. -0.0129).[406] Tables 11.8.4 and 11.8.4 show the effect of PIMD on the dipole moment and dielectric constant. The dielectric constant of D2O water is almost exactly the same as H2O, but is a tiny bit (.4%) smaller, which is consistent with the idea that the dipole moment of D2O should be a tiny bit smaller. However, as we will see, there are theoretical reasons to believe that isotopic substitution affect both the liquid phase dipole moment and liquid structure and the two effects may work in opposite directions.

Tables 11.8.4 and 11.8.4 show dipole moments and dielectric constants for H2O and D2O obtained from PIMD simulation. Clearly, the effect of isotopic substitution on these quantities varies with the model. SPC/F shows a reduction in both dipole moment and dielectric constant, consistent with the finds of Lombaugh et al.[399] This reduction may be related to the fact that in SPC/F the OH distance decreases when PIMD is used (see fig. 11.4) because of the curvature problem, which is greatly exacerbated by the use of a purely harmonic potential (see sec. 11.4). Lombaugh et al. subsequently reparameterized SPC/F to better reproduce the dielectric constant with PIMD, resulting in q-SPC/F.[399] In TTM2.1F, which has an anharmonic OH potential, the dipole moment is also seen to decrease with the inclusion of NQEs. Intriguingly, however, the dielectric constant of TTM2.1F is observed to increase slightly, although as pointed out by Burnham et al. the error bars are likely around ± 10 rather than the ± 2 that was reported, so the difference is not statistically significant.

For the first time, we computed the dipole moment and dielectric constant with TTM3F with PIMD. We find the dipole moment increases, but surprisingly, the dielectric constant decreases slightly.

11.8.5 Infrared spectra

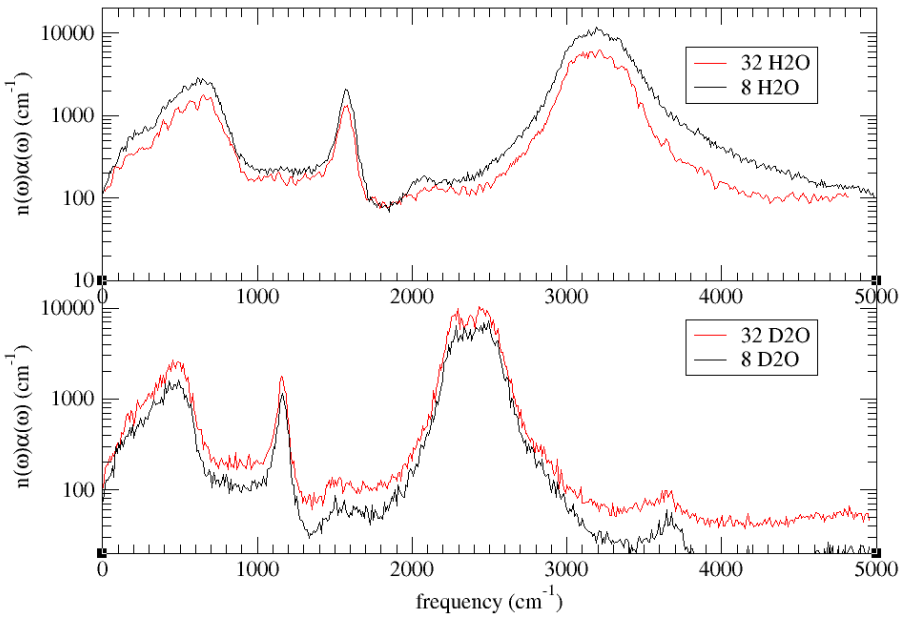

Figure 11.12: Infrared spectra from PIMD simulations of TTM3F at 300 K showing the effect of isotopic substitution. Number refers to number of beads (8 vs 32).

Figure 11.8.5 compares the infrared spectra of H2O and D2O for TTM3F. The first interesting thing to note is that the frequency shifts do not obey the relation for the simple harmonic oscillator $\omega^{\mathrm{H2O}}/\omega^{\mathrm{D2O}} = \sqrt{2} \approx 1.41$. More exactly, comparing the ratio of the reduced masses, one expects:

$$\frac{\omega^{\mathrm{H_2O}}}{\omega^{\mathrm{D_2O}}} = \sqrt{\frac{\frac{m_O m_D}{m_O+m_D}}{\frac{m_O m_H}{m_O+m_H}}} \approx 1.37 \tag{11.62}$$

In TTM3F we observe $\omega^{\mathrm{H2O}}_{\mathrm{str}}/\omega^{\mathrm{D2O}}_{\mathrm{str}} = 1.32$ and $\omega^{\mathrm{H2O}}_{\mathrm{bend}}/\omega^{\mathrm{D2O}}_{\mathrm{bend}} = 1.36$. The experimental values are 1.36 and 1.36 respectively. A different experimental study claims that the H2O spectra is shifted nearly uniformly from the D2O spectra by a factor of 1.347.[407] If correct, this uniformity of isotope shift would need to be explained. Theoretically, the shift should vary for different

modes depending on their degree of anharmonicity. Another interesting observation is that there is little difference between the use of 8 beads vs 32. This may be due to the use of PA-CMD with bead thermostats, indicating another way that PA-CMD is superior to RPMD.

Morse potential anharmonicity

The Morse potential is:

$$V(r) = D_r \left[1 - e^{-\beta(r - r\text{eq})}\right]^2 \tag{11.63}$$

The ground state frequency can be computed analytically as:

$$E_n = (n + 1/2)\hbar\omega_0 - (n + 1/2)^2\hbar\omega_0\chi \tag{11.64}$$

where the anhamonicity $\chi \equiv \frac{\hbar\omega_0}{4D_r}$. The frequency ratio is:[408]

$$\frac{\omega^{\text{H2O}}}{\omega^{\text{D2O}}} = \sqrt{2}\left(\frac{1 - 2\chi}{1 - \sqrt{2}\chi}\right) \tag{11.65}$$

where ω_0 is the harmonic zero-point frequency. Anharmonicity decreases the ratio. To estimate the corrected ratio, we can look at the model q-TIP4P/2005f of Gonzalez & Abascal, which uses the Morse potential to capture anharmonicity. They set $D_r = 4320.581$ kJ/mol. For $\omega_0 = 3600$ cm^{-1} this corresponds to an anharmonicity of $\chi \approx 0.004$, which is quite small, causing a reduction in the ratio of only 0.3%.

Chapter 12

"Monomer PIMD" for ab-initio simulation

"The underlying physical laws necessary for the mathematical theory of a large part of physics and the whole of chemistry are thus completely known, and the difficulty is only that the exact application of these laws leads to equations much too complicated to be soluble. It therefore becomes desirable that approximate practical methods of applying quantum mechanics should be developed, which can lead to an explanation of the main features of complex atomic systems without too much computation - Paul Dirac, 1930

12.1 Background on DFT

The non-relativistic Schrödinger equation is:

$$i\hbar\frac{\partial}{\partial t}\Phi(\{\boldsymbol{r}_i\},\{\boldsymbol{R}_I\};t) = \mathcal{H}\Phi(\{\boldsymbol{r}_i\},\{\boldsymbol{R}_I\};t) \tag{12.1}$$

The Hamiltonian operator for a system of nuclei and electrons is:

$$\begin{aligned}\mathcal{H} = &-\sum_I \frac{\hbar^2}{2m_I}\nabla_I^2 - \sum_I \frac{\hbar^2}{2m_e}\nabla_i^2 + \frac{1}{4\pi\epsilon_0}\sum_{i<j}\frac{e^2}{|\boldsymbol{r}_i-\boldsymbol{r}_j|} \\ &- \frac{1}{4\pi\epsilon_0}\sum_{I,i}\frac{e^2 Z_I}{|\boldsymbol{R}_I-\boldsymbol{r}_i|} + \frac{1}{4\pi\epsilon_0}\sum_{I<J}\frac{e^2 Z_I Z_J}{|\boldsymbol{R}_I-\boldsymbol{R}_J|}\end{aligned} \tag{12.2}$$

The electronic coordinates are $\{\boldsymbol{r}_i\}$ and the nuclear coordinates are $\{\boldsymbol{R}_I\}$. Let us suppose that we know the *electronic* eigenstates of the *time-independent* Schrödinger equation for arbitrary nuclei positions $\{\boldsymbol{R}_I\}$, which we denote $\Psi_l(\{\boldsymbol{r}_i\}, \{\boldsymbol{R}_I\})$. Born suggested that the wavefunction at time t can be expanded as:

$$\Phi(\{\boldsymbol{r}_i\}, \{\boldsymbol{R}_I\}; t) = \sum_{l=0}^{\infty} \Psi_l(\{\boldsymbol{r}_i\}, \{\boldsymbol{R}_I\}) \chi_l(\{\boldsymbol{R}_I\}; t) \tag{12.3}$$

The nuclear wavefunctions χ_l can be considered as time-dependent expansion coefficients. By placing this ansatz into the full *time-dependent* Schrödinger equation, one can obtained a coupled system of equations. The "adiabatic approximation" comes from simplifying this coupled set of equations by only considering the diagonal terms. Additionally, the mass of the nuclei is set to infinity, so the kinetic energy operator for the nuclei is dropped from the Hamiltonian. The result is that the motion of the nuclei does not change the quantum state of the electrons. The famous "Born-Oppenheimer" approximation comes from further simplifying the diagonal terms. It can be shown that the nuclei move according to classical mechanics in an effective potential. The effective potential energy is obtained by solving the time-independent Schrödinger equation.. From this potential energy surface, the forces on the nuclei can be obtained. This the basis of Born-Oppenheimer molecular dynamics (BOMD). Although widely used, a problem with BOMD is that the occupancy of electronic states does not change with time. Note also that we have not yet discussed how the time-independent Schrödinger equation for the electronic states should be solved.

The Hohenberg-Kohn theorems

The Hohenberg-Kohn theorems are:
Theorem I:

> If two systems of electrons, one trapped in a potential $V_1(\boldsymbol{r})$ and the other in $V_2(\boldsymbol{r})$, have the same ground-state density $n(\boldsymbol{r})$ then necessarily $V_1(\boldsymbol{r}) - V_2(\boldsymbol{r}) = C$, where C is a constant.

Corollary:

> The ground state density uniquely determines the potential (apart from a constant) and therefore uniquely determines the full wave function.

Theorem II:

A universal functional $F[n(\boldsymbol{r})]$ for the energy in terms of the density $n(\boldsymbol{r})$ can be defined, valid for any potential. For a particular potential the exact ground state energy is the global minimum of this functional, and the density that minimizes it is the ground state density.

The density functional is written as:

$$E[n, N_e] = F[n, N_e] + \int V_{\text{ext}}(\boldsymbol{r}) n(\boldsymbol{r}) d^3r \tag{12.4}$$

The first term contains the kinetic energy and electron-electron, electron-ion interactions. The second term is the interaction of the electrons with the external potential. With a functional $F[n]$ in hand applying the HK theorem requires solving the variational problem:

$$\frac{\delta}{\delta n(\boldsymbol{r})} \left[E[n, N_e] - \mu \left(\int n(\boldsymbol{r}) d^3r - N_e \right) \right] = 0 \tag{12.5}$$

The Lagrange multiplier μ is introduced to enforce the constraint :

$$\int n(\boldsymbol{r}) d^3r = N_e \tag{12.6}$$

This leads to

$$\frac{\delta E[n, N_e]}{\delta n(\boldsymbol{r})} + V_{\text{ext}} = \mu \tag{12.7}$$

μ is sometimes identified as the chemical potential, although this is not a rigorous identification. So far we have no idea either how to construct the density or the form of the density functional $F[n(\boldsymbol{r})]$. Kohn and Sham introduce a famous *ansatz*, which rests on two unproven assumptions:[409]

1. The ground state density can be represented as the ground state density of an auxiliary system of non-interacting electrons.

2. The auxiliary system has a Hamiltonian consisting of the usual kinetic energy operator and an effective local potential $V^{\sigma}_{\text{eff}}(\boldsymbol{r})$.

That is, Kohn and Sham suggest constructing the ground state density from from N_e single-electron states with the effective Hamiltonian:

$$H^{\sigma}_{eff} = \frac{1}{2}\nabla^2 + V^{\sigma}_{\text{eff}}(\boldsymbol{r}) \tag{12.8}$$

Assuming we have $N_e = N^{\uparrow} + N^{\downarrow}$ electrons, orbitals $\psi_i^{\sigma}(\boldsymbol{r})$ with the lowest energy eigenvalues in the single particle Shroedinger equation using the effective Hamiltonian 12.8 are filled.

Kohn & Sham write the energy functional as:

$$E_{\mathrm{KS}}[n(\boldsymbol{r})] = E_{\mathrm{KE}} + \int d^3\boldsymbol{r} V_{\mathrm{ext}}(\boldsymbol{r}) n(\boldsymbol{r}) + E_{\mathrm{Hartree}}[n(\boldsymbol{r})] + E_{\mathrm{xc}}[n(\boldsymbol{r})] + E_{II} \tag{12.9}$$

$$E_{\mathrm{KE}} = -\frac{1}{2}\sum_{i=1}^{N} \int |\nabla \psi_i|^2 d^3 r \tag{12.10}$$

$$E_{\mathrm{Hartree}}[n(\boldsymbol{r})] = -\frac{1}{2}\sum_{i=1}^{N}\sum_{j=1}^{N} \int \frac{n(\boldsymbol{r}) n(\boldsymbol{r}')}{|\boldsymbol{r} - \boldsymbol{r}'|} d^3 r d^3 r' \tag{12.11}$$

The external potential here is due to both the nuclei and any external fields. E_{KE}, $E_{\mathrm{Hartree}}[n(\boldsymbol{r})]$, and E_{II} are now well defined. The many body effects are contained in the exchange-correlation functional $E_{\mathrm{XC}}[n(\boldsymbol{r})]$. The exchange-correlation functional also contains difference between the true kinetic energy and the kinetic energy given by E_{KE}. To solve the variational problem given in eqn. 12.7 Kohn and Sham suggested the following method: from the orbitals, compute the density using:

$$n(\boldsymbol{r}) = \sum_{\sigma}\sum_{i=1}^{N^{\sigma}} |\psi_i^{\sigma}(\boldsymbol{r})|^2 \tag{12.12}$$

It can be shown that solving the variational problem given eqn. 12.7 amounts to solving the "Kohn-Sham equations":

$$(H_{KS}^{\sigma} - \epsilon_i^{\sigma})\psi_i^{\sigma} = 0 \tag{12.13}$$

$$H_{KS}^{\sigma} = \frac{1}{2}\nabla^2 + V_{\mathrm{KS}}^{\sigma}(\boldsymbol{r}) \tag{12.14}$$

$$V_{KS}^{\sigma}(\boldsymbol{r}) = V_{\mathrm{ext}}(\boldsymbol{r}) + \frac{\delta E_{\mathrm{Hartree}}[n(\boldsymbol{r})]}{\delta n(\boldsymbol{r}, \sigma)} + \frac{\delta E_{\mathrm{xc}}[n(\boldsymbol{r})]}{\delta n(\boldsymbol{r}, \sigma)} \tag{12.15}$$

These equations must be solved self consistently. The Kohn-Sham orbitals do not have any direct physical interpretation, since they are rather artificially introduced to help facilitate the construction of the density. An exception to this is the highest occupied state, since it can be shown that the eigenvalue of the highest occupied state yields the correct ionization energy of the system.

The exchange-correlation functional

We have not yet explained the exchange-correlation functional. Surprisingly, for many systems, local exchange-correlation functionals perform well. Local functionals have the form:

$$E_{\mathrm{xc}}[n(\boldsymbol{r})] = \int n(\boldsymbol{r})\epsilon_{\mathrm{xc}}(n(\boldsymbol{r}))d^3r \tag{12.16}$$

The sucess of local x-c functionals indicate that the Hartree term incorporates much of the long range electron-electron interaction. Separating out the Hartree term was one of the key insights of Kohn & Sham.

Force theorem

The force conjugate to any parameter in the system, such as the position of a nucleous $\boldsymbol{R}_I$ can be written :

$$\boldsymbol{F}_I = -\frac{\partial E}{\partial \boldsymbol{R}_I} \tag{12.17}$$

In first order perturbation theory, this can be written:

$$-\frac{\partial E}{\partial \boldsymbol{R}_I} = \langle\Psi|\frac{\partial H}{\partial \boldsymbol{R}_I}|\Psi\rangle - \langle\frac{\Psi H}{\partial \boldsymbol{R}_I}|\hat{H}|\Psi\rangle - \langle\Psi|\hat{H}|\frac{\Psi H}{\partial \boldsymbol{R}_I}\rangle - \frac{\partial E_{\mathrm{II}}}{\partial \boldsymbol{R}_I} \tag{12.18}$$

Since the ground state is a minima of the energy, the middle two terms are zero. Substituting in the DFT Hamiltonian, one obtains:

$$\boldsymbol{F}_I = -\int d^3r n(\boldsymbol{r})\frac{\partial V_{\mathrm{ext}}(\boldsymbol{r})}{\partial \boldsymbol{R}_I} - \frac{\partial E_{\mathrm{II}}}{\partial \boldsymbol{R}_I} \tag{12.19}$$

The force depends only on the motion of the nuclei, it does not depend on the change in the density. If the basis depends on the position of atoms, additional terms have to be added to eqn. 12.19. Additionally, if the basis is not complete (as is often the case), an additional term called the Pulay correction needs to be included in the case of orbital-based DFT. Finally, there is a correction due to lack of self-consistency.

authors / year	N	T	time(ps)	functionals	focus
Wang, et al. (2011) [410]	64	300	20	var vdW	density, detailed structure
Corsetti, et al. (2013) [411]	200	300	20	vdW-DF, VV10	compressibility, diffusivity
Romain, et al. (2011) [412]				various vdW	
Schmidt, et al. (2009) [413]	64	330	24-48	BLYP, PBE	density, pressure, RDFs
DiStasio. et al. (2014) [414]	128	300	25+	PBE0	
Gaiduk, et al. (2015) [415]				PBE, PBE0	
Lin, et al. (2009) [416]	64	330	30	BLYP, BLYP-D	
Guardia, et al. (2015) [417]	96	330	15	BLYP	
Giacomo et wal. (2015) [418]	64	300	25-35	PBE, rVV10	
Zhang, Wu, Galli, Gygi (2011)[419]	32	320+	20	DRSLLPBE, LMKLL, OptB88, PBE, PBE0	
Mongelgo (2011) [420]	64	300	10	PBE, optPBE-vdW, vdW-DF2	

Table 12.1: A sampling of some recent published simulations of water with various DFT functionals.

12.2 Incorporating nuclear quantum effects into DFT simulation

There is great interest in being able to accurately treat liquid water at the quantum mechanical level.[421] The most widely used methodology for this is density functional theory. However, most density functionals fail to accurately reproduce key thermodynamic properties of water such as its density, compressibility, and diffusion constant. Moreover, different density functionals fail in different ways. PBE creates a overstructured liquid, while some vdW functionals such as vdW-DF2 and optPBE-vdW create an understructured liquid.[420]

Most *ab-initio* techniques are based on the Born-Oppenheimer approximation and the assumption that nuclear dynamics can be treated classically. However, over the past two decades a wide range of studies have demonstrated that this is not a good assumption for water because the OH stretching mode of water is very quantum mechanical (zero point temperature $T_z = \hbar\omega/2k_b = 2600$ K).[422], and hydrogen nuclei are delocalized. Currently, many DFT simulations of water are done with D_2O, where NQEs are much smaller. However, the structure and dynamics of D_2O is different than H_2O, as can be seen from experiments that compare the two. In the primary isotope effect, the OH distance is observed to be longer than the OD distance. In the secondary isotope effect, also called the Ubbelöhde effect, the H-bond donor-acceptor (oxygen-oxygen) distance R changes open isotopic substitution. The magnitude and direction of the change depends on the strength of the hydrogen bond, due to competing quantum effects.[408, 423, 424, 425, 426, 427] In particular, the zero-point motion of hydrogen in the out-of-plane direction (a type of librational motion) acts to increase R while the zero point motion of the stretching mode acts to decrease R.[408] In materials with strong H-bonds, NQEs decrease the donor-acceptor distance (positive Ubbelöhde effect), while in materials with

weaker H-bonds the opposite effect occurs (negative Ubbelöhde effect). The crossover between from positive to negative Ubbelöhde effect has been estimated to be around $R = 2.6$Å[424] or $R = 2.7$Å.[408] Ice lies right at this crossover point (H-bond ≈ 2.74Å[428]) so relative to other H-bonding materials its secondary isotope effect is small.[421] The secondary isotope effect in ice is known to be positive (NQEs decrease R), leading to the anomalous isotope effects discovered by Pamuk et al. Surprisingly, the anomalous isotope effect reflected in the volume of water per molecule becomes greater at room temperature water - the volume per molecule of D_2O is slightly larger than H_2O, suggesting that H-bonds in H_2O water are stronger than in D_2O. The competition between the OH stretching and the bending+librational modes is clearly reflected in the Grüneisen constants reported by Pamuk et al - the OH stretch Grüneisen parameters are negative, while the librational Grüneisen parameters are positive. The HOH bending Grüneisen parameter is positive but very close to zero, showing that it has a much smaller role. Similarly, a study of liquid water showed that the competing quantum effects from libration are about 50% larger than those from bending.[408]

In biophysics, the strengthening of hydrogen bonds by NQEs is believed to very slightly increase protein stability.[429] The balance of competing quantum effects is very sensitive to the r_{OH} distance and degree of anharmonicity in the OH potential,[408, 424] which explains the broad spectrum of often conflicting results obtained from PIMD simulation of water with different forcefield models and DFT functionals.[402, 424] DFT functionals also show variation in monomer geometry (for instance PBE gives an r_{OH} that is too long) and likely have significant differences in anharmonicity as well. Therefore, a proper comparison of DFT functionals to each other and to experiment should include NQEs.

Currently many people introduce "effective NQEs" by raising the temperature of the simulation. This can be justified theoretically for weakly interacting systems such as gases or van der Waals bonding materials,[430] but the same justification does not apply to hydrogen bonded materials. Increasing the temperature can be useful for compensating for the overstructuring of GGA functionals, but should not be refereed to as an effective treatment of NQEs. Recently it was shown that colored noise thermostats tuned to quantum zero point temperatures of different modes in liquid water is a more rigorous and effective way of taking into account NQEs.[431] Still, the "gold standard" technique for treating NQEs is path integral molecular dynamics (PIMD).[432]

In PIMD, hydrogen nuclei become delocalized along H-bonds. This delocalization increases the probability of dissociation by several orders of magnitude,[433, 434, 435] and causes an excess proton in water to become delocalized over sev-

eral molecules.[436, 437] PIMD has proven useful to understanding proton tunnelling in acids,[438] enzymes,[439, 440] ice,[441, 437] unstable forms of the DNA base pairs,[442] and small water clusters.[443, 444, 445, 446, 447] PIMD has also proved useful for reproducing the *ab initio* spectra of water, protonated methane,[448] and the DNA base guanine.[449] NQEs decrease the band gap of diamond,[450] and were recently shown to significantly reduce the bandgap of water as well (by 0.6 eV).[435] Interestingly, GW-corrected DFT simulations result in a bandgap that is 0.4 eV larger than the experimental value – this overestimation is likely due to the lack of NQEs.[451] NQEs also play an important role in the heat capacity,[452] and surface structure of water.[453]

We note that classical forcefield models are not a rigorous way of studying NQEs because they are parametrized to experimental data, leading to a double counting of NQEs when used with PIMD simulation. Additionally, harmonic models do not allow for a change in the average OH distance from NQEs, and thus cannot capture primary or secondary isotope effects. Even worse, we have found that PIMD simulation with the harmonic model SPC-f[371] shows an unphysical *decrease* in r_{OH}, which is due to the "curvature problem" intrinsic to PIMD simulation. In the curvature problem, beads curve around a spherical shell of near constant r_{OH}, causing the centroid lies in the interior, leading to a shorter r_{OH}.[350, 361] This calls into question PIMD studies which have used the qSPC/Fw model.[454, 455] While classical forcefields have been reparametrized specifically for use with PIMD,[456, 457] and have also been parametrized from Born Oppenheimer ab-initio simulation using force matching,[458] and other approaches,[400] a more rigorous understanding of nuclear quantum effects can only come through DFT PIMD simulation.

12.3 Centroid molecular dynamics

The PIMD simulation methodology we use is called "partially adiabatic centroid molecular dynamics", denoted PA-CMD.[352] In this approach, the frequencies of the normal modes are scaled above the highest frequency of interest in the system, so that the normal mode frequencies will not contaminate the frequency spectrum of the system.[459, 353]

12.4 The many body expansion

The many body expansion gives an exact decomposition of the potential into 1-body, 2-body, 3-body, and higher order terms:

$$V(\{\boldsymbol{R}_I\}) = \sum_{I=1}^{N_{mol}} V_1(\boldsymbol{R}_I) + \sum_{I<J}^{N_{mol}} V_2(\boldsymbol{R}_I, \boldsymbol{R}_J) + \sum_{I<J<K}^{N_{mol}} V_3(\boldsymbol{R}_I, \boldsymbol{R}_J, \boldsymbol{R}_K) + \cdots \tag{12.20}$$

In our method, we first subtract off the DFT monomer energies using a monomer potential energy surface (described below) fitted to the DFT functional being used. In our method, intramolecular forces on the beads are calculated using the Partridge-Schwenke monomer potential energy surface,[460] which is a highly accurate surface derived from CCSD calculations. This can thought of as a monomer correction to the DFT potential:

$$V'(\{\boldsymbol{R}_I\}) = V_{\mathrm{DFT}}(\{\boldsymbol{R}_I\}) - \sum_{I=1}^{N_{mol}} V_{1\mathrm{DFT}}(\boldsymbol{R}_I) + \sum_{I=1}^{N_{mol}} V_{1\mathrm{PS}}(\boldsymbol{R}_I) \tag{12.21}$$

The intermolecular forces on the beads are all set set equal to the intermolecular forces computed from the bead centroids. Thus, in each timestep we only have to do one DFT calculation, using the centroid coordinates. Our method has the added advantage that it includes a monomer correction which increases the accuracy of the simulation. However, using the Partridge-Schwenke PES is not necessary, as the energy surface fit to the functional being used may be used instead, as may be desired for doing a full comparison of different functionals with PIMD.

12.5 Monomer potential energy surface

The form of the potential energy fitting function is:[460]

$$V(r_1, r_2, \theta) = V^a(r_1) + V^a(r_2) + V^b(r_{\mathrm{HH}}) + V^c(r_1, r_2, \theta) \tag{12.22}$$

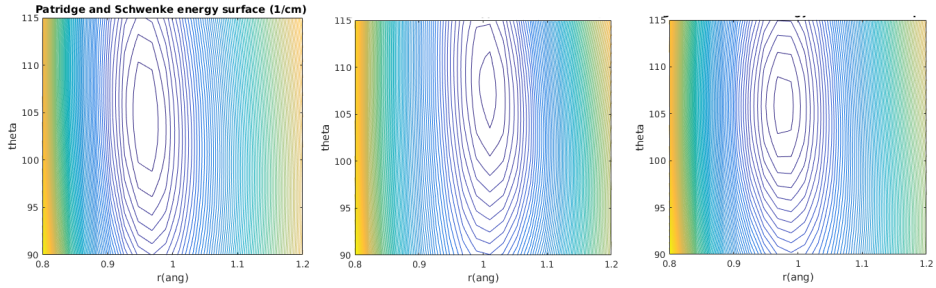

Figure 12.1: The monomer potential energy surface of Partridge and Schwenke (left) and a fit for PBE (middle) and BH (right).

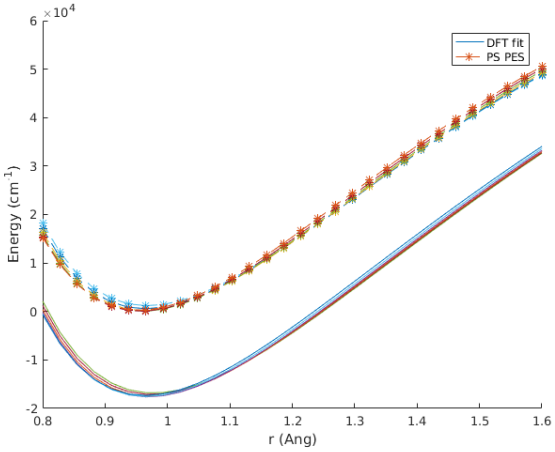

Figure 12.2: Energy vs r_{OH} for the case where $r_{\mathrm{OH1}} = r_{\mathrm{OH2}}$. Different HOH angles are shown in different colors. The PS energy surface is compared with a custom fit to PBE.

where

$$\begin{aligned} V^a(r) &= D[e^{-2a(r-r_0)} - 2e^{-a(r-r_0)}] \\ V^b(r) &= Ae^{-br} \\ V^c(r_1, r_2, \theta) &= c_{000} + e^{-\beta[(r_1-r_e)^2+(r_2-r_e)^2]} \\ &\quad \times \sum_{ijk} [(r_1 - r_e)/r_e]^i [(r_2 - r_e)/r_e]^j \\ &\quad \times [\cos(\theta) - \cos(\theta_e)]^k \end{aligned} \tag{12.23}$$

as in the work of Partridge & Schwenke we truncate the polynomial at $i+j \leq 8$ and $k \leq 14-(i+j)$ for a total of 245 c_{ijk}. The fit is performed with a training set of 550 monomer configurations.

12.6 Multiple timestep algorithm

The use of the monomer potential energy surface introduces a split between intramolecular and intermolecular forces which is similar to the type of split between long-range (slow) and short-range (fast) forces used in multiple time step (MTS) algorithms. Tcukerman, Berne, & Martyna derived an MTS integration algorithm which has the desirable properties of being phase space area-preserving (symplectic) and reversible.[461] The method is derived from the classical propagator $e^{iL\Delta t}$, which exactly evolves the system from an initial phase space point $\Gamma(t) = \{\sum \boldsymbol{r}, \sum \boldsymbol{p}\}$ at time t to a final point at $t + \Delta t$ through $\Gamma(t + \delta t) = e^{iL\Delta t}\Gamma(t)$. The Liouville operator L is written as

$$\begin{aligned} L &= L_\gamma + L_r + L_p^s + L_p^l \\ &= L_\gamma + \sum_i^{n_a} \frac{\boldsymbol{p}_i}{m_i} \cdot \frac{\partial}{\partial \boldsymbol{r}_i} + \sum_i^{n_a} \boldsymbol{F}_i^s \cdot \frac{\partial}{\partial \boldsymbol{p}_i} + \sum_i^{n_a} \boldsymbol{F}_i^l \cdot \frac{\partial}{\partial \boldsymbol{p}_i} \end{aligned} \tag{12.24}$$

The multiple timestep algorithm is derived by Trotter splitting the propagator with timestep Δt:

$$\begin{aligned} e^{iL\Delta t} \approx\ & e^{iL_\gamma \frac{\Delta t}{2}} e^{iL_p^l \frac{\Delta t}{2}} \\ & \times \left[e^{iL_p^s \frac{\Delta t}{2M}} e^{iL_r \frac{\Delta t}{M}} e^{iL_p^s \frac{\Delta t}{2M}} \right]^M \\ & \times e^{iL_p^l \frac{\Delta t}{2}} e^{iL_\gamma \frac{\Delta t}{2}} \end{aligned} \tag{12.25}$$

Here the inner timestep is $\frac{\Delta t}{M}$, where M is an integer. Expression 12.25 can be translated into an algorithm by reading the sequence of propagators from right to left. First, the global thermostat is applied for half the outer timestep, followed by a modification of the momentum by the slowly varying force. Next, the inner loop is performed M times consisting of an update of the momentum with the fast varying force, evolution of the free ring polymer (L_0) for a timestep $\delta t = \frac{\Delta t}{M}$. Finally, in a symmetric fashion one applies update of the momenta is performed with the slowly varying force, and an update of the thermostat. When using a multiple timestep method, one should be aware that resonances can occur between the fast timestep(s) and the slow timestep. The first resonance occurs when the outer timestep becomes larger than $t_{\max} = \tau/\pi$, where τ is the period of the fastest mode in the problem. For water, this would be the OH stretch frequency ≈ 3600 cm^{-1} which leads to a value of $\Delta t_{\max} = 2.95$ fs. However, in PIMD simulation one must also consider the highest frequency normal mode of the ring polymer + the OH potential which is $\sqrt{\omega_{\mathrm{RP,max}}^2 + \omega_{OH,max}^2}$. For a full PIMD simulation with 32

beads PIMD simulation this would yield a max frequency of 13,300 cm^{-1} and a resonance at $\Delta t = .8$ fs. If we instead scale the normal modes to 4100 cm^{-1} (as done here), then one obtains $\Delta t_{max} = 1.9$ fs. Additionally, Morrone, et al. have shown that the use of colored noise thermostats can stabilize resonances, offering the possibility of even higher outer timesteps.[462]

12.7 ab-initio PIMD implementation details

We scale all normal modes to 10000 cm^{-1}, well above the overtones found at 5260 cm^{-1} and 6800 cm^{-1}. The beads are thermostated with Nosé-Hoover chain thermostats, with a chain length of 4. Alternatively, our code allows for Langevin thermostats to be used. The thermostating is done in normal-mode space, with the thermostats optimally tuned to each normal mode as they are in the PILE thermostat scheme of Ceriotti et al.[463] The centroid mode is not thermostated, since doing so washes out the dynamics.

12.8 Comparison to other methods

Our method can be understood as an extension to ab initio MD of the ring polymer contraction method introduced by Markland and Manoloupolos for classical MD.[464, 465] In ring polymer contraction, long-range forces are analyzed using a contracted ring polymer with n' beads that are constructed by taking the n' lowest frequency ring polymer normal modes in Fourier space and transforming them into real space. Short range forces are analysed on all n beads. Our method corresponds to contraction to $n = 1$, namely the centroid mode (also called the 0th order mode), and a separation between long range and short range forces that corresponds to intermolecular vs intramolecular forces.

Because it is based on a separation of long range and short range forces, ring polymer contraction can be combined with a multiple time step (MTS) method. Recently a technique called basis set partitioning was developed to incorporated MTS into *ab-initio* simulation.[466] Luehr, Markland, and Martinez have demonstrated how MTS can be implemented in Hartree-Fock calculations for water clusters through a fragment-based approach.[467] Recently a number of papers have been published that combine ring polymer contracted PIMD with a MTS integrator and the idea of mixing forces[468] from higher level and lower level ab initio methods.[469, 470, 471] The lower level ab-initio technique can be used in conjunction with the short timestep & full ring polymer, while the higher level (more expensive) technique can be used with a long timestep

and the contracted ring polymer. For example, in two recent studies, MP2 was combined with DFT in this manner to study small gas phase molecular systems.[470, 471] A variation of this method called multilevel sampling was introduced and applied to FCC hydrogen, resulting in a 3-4x speedup.[472]

Recently, two separate groups have published a method called "quantum ring polymer contraction", which uses an "auxiliary potential" to perform PIMD at virtually no added cost.[457, 469] The method they employed, while couched in different language, is similar to the method we present here. The principal difference is that they use self consistent charge density functional tight binding (SCC-DFTB) as the auxiliary potential in place of the monomer PES we use here. Our method has the advantage of introducing a monomer correction.

12.9 Verification of the method

12.9.1 Methods

To verify that our method captures nuclear quantum effects with minimal losses in accuracy compared to a full PIMD simulation, we compare several observables - RDFs, infrared spectra, density of states, and OH distance histograms. The infrared spectrum is calculated using:[473]

$$n(\omega)\alpha(\omega) = \frac{\beta\omega^2}{6\epsilon_0 V c}\int_{-\infty}^{\infty} e^{-i\omega t}\langle \boldsymbol{P}(0)\cdot\boldsymbol{P}(t)\rangle dt \tag{12.26}$$

To calculate dipole moments for our DFT simulations, we calculate dipoles using the polarizable model TTM3F using the centroid coordinates. This method takes into account polarization, which we found is necessary to correctly capture the intensity of the OH-stretching peak relative to simply assigning fixed charges to each atom.

In addition we also calculate the "density of states" for hydrogen using the velocity-velocity autocorrelation function:

$$I(\omega) = \frac{1}{N_{\text{hyd}}}\int_{-\infty}^{\infty} e^{-i\omega t}\sum_{i=1}^{N_{\text{hyd}}}\langle \boldsymbol{v}_i^H(0)\cdot\boldsymbol{v}_i^H(t)\rangle dt \tag{12.27}$$

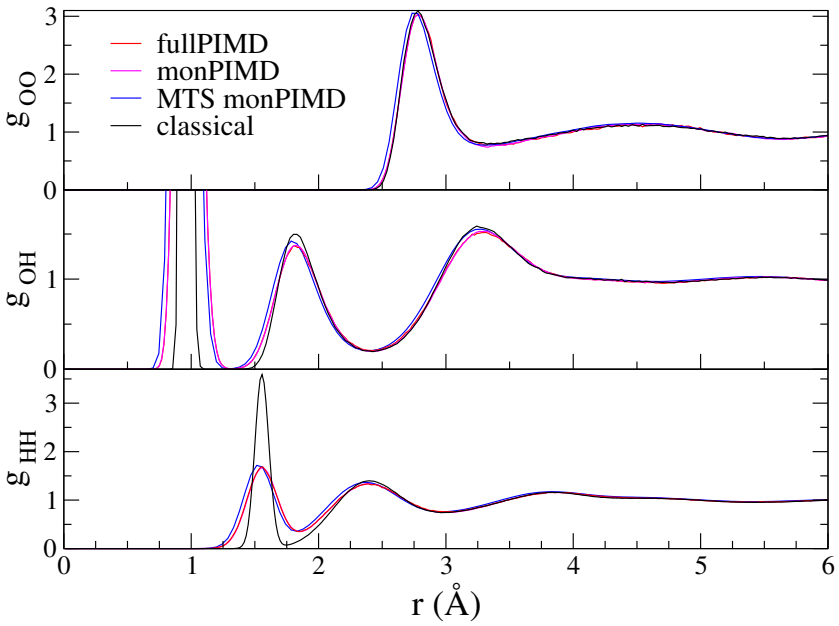

Figure 12.3: Validation with TTM3F: RDFs for the three methods at 300 K.

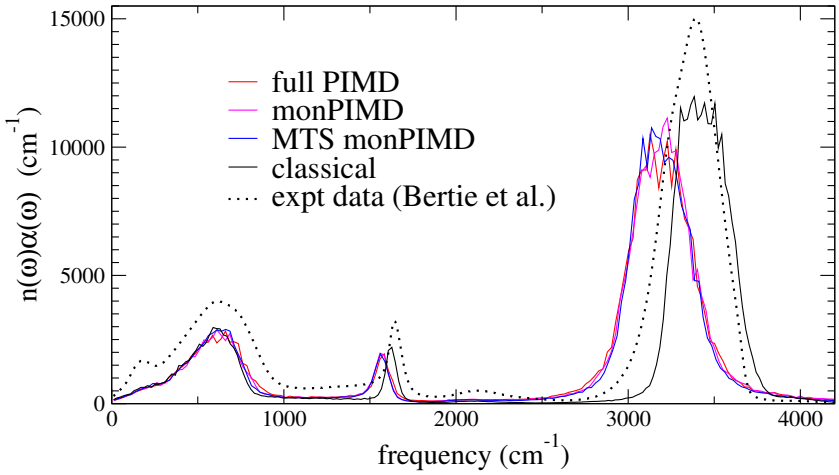

Figure 12.4: Validation with TTM3F: infrared spectra for the three PIMD methods compared to the classical spectra and experimental data at 300 K.[13]

	TTM3F			BH vdW		
property	class.	fullPIMD	monPIMD	class.	fullPIMD	monPIMD
$\langle r_{\mathrm{OH}} \rangle$	.986	.994/1.006	.996/	.994		.986/.997
$\langle \theta_{\mathrm{HOH}} \rangle$	105.43	105.4/105.2	105.66	104.6		105.02/104.798
$\langle \mu \rangle$	2.757	2.835	2.855	3.683		3.66
D (10^{-5} cm^2/s	2.7		2.9	2.3		
$\langle r_{\mathrm{gyr}} \rangle$	0.0	.1507	.1515	0.0		.1456
max bead r_{OH}	1.18	1.54	1.56	1.19		1.49
max cent. r_{OH}	1.18	1.13	1.23	1.19		1.19

Table 12.2: Note: distances for PIMD simulation are reported in the form centroid-centroid distance /bead-bead distance.

12.9.2 Initial tests with TTM3F

The first test we did was with the *ab initio* based polarizable TTM3F potential.[15] We used a system of 256 molecules, simulated for 200 ps with a 9 Å realspace Columb cutoff. RDFs for TTM3F are shown in fig. 12.9.2. As has been noted elsewhere, TTM3F exhibits only small primary isotope effect and very little or no secondary isotope effect,[474] due to a lack of anharmonicity in the r_{OH} potential and competing quantum effects. The monomer PIMD and full PIMD O-O RDFs are nearly the same, but the multiple time step monomer PIMD is noticeably shifted. Similar discrepancies are observed by Marsalek, et al. when applying their quantum ring polymer contraction method to RevPBE with D3 dispersion corrections.[469]

12.9.3 Tests with DFT

We next began tests with PBE[475] and the Berland-Hyldgaard (BH) functional,[476] which is a version of the DRSLL vdW functional introduced by Dion et al. with modified exchange.[477] A comparison of the RDFs for conventional PBE simulation and monomer-corrected PBE simulation is shown in fig. 12.9.3. The density of states spectra for conventional DFT simulation of the the BH monomer is shown in fig. 12.9.3. Density of states for the PBE monomer comparing conventional DFT with the monomer PIMD method are shown in fig. 12.9.3. The expected redshifting and broadening of the OH stretch band is observed. Histograms of the bead-bead and centroid-centroid distances for the BH monomer and BH pentamer cluster are shown in fig. 12.9.3.

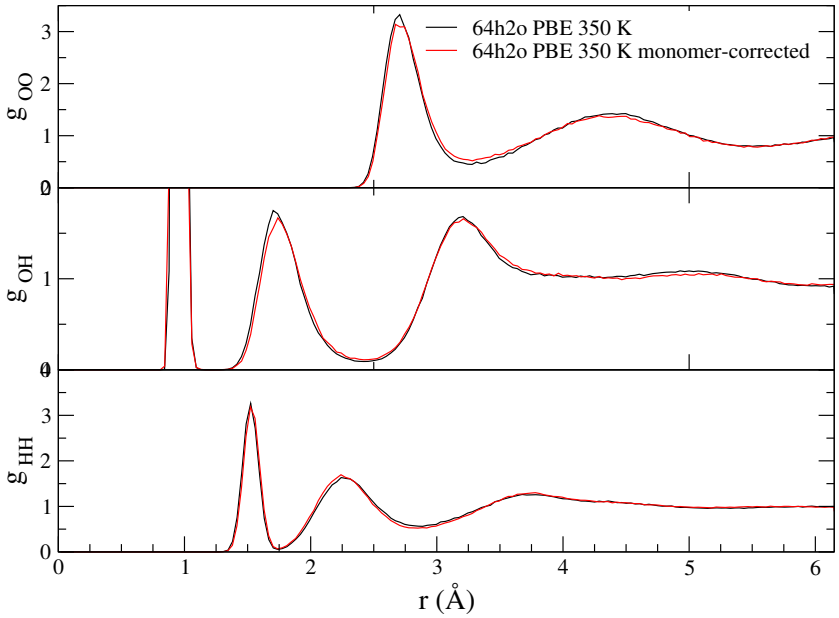

Figure 12.5: Comparison of RDFs for conventional PBE and monomer corrected PBE. The simulations had lengths of 35 and 27 ps, respectively.

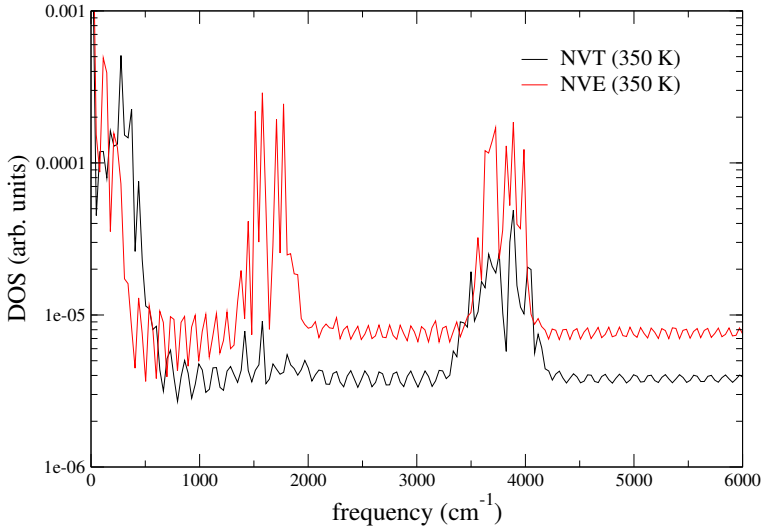

Figure 12.6: Density of states (eqn. 12.27) for a single molecule simulated with conventional DFT MD (1 bead) with Nosé-Hoover thermostating (NVT) (top) and without a thermostat (NVE) (bottom). An unexplained splitting appears in the HOH bending mode (≈ 1500 cm^{-1}).

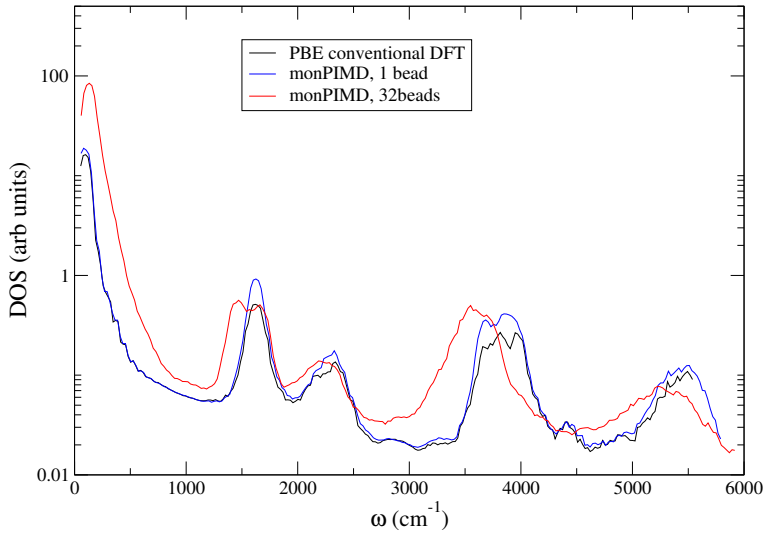

Figure 12.7: Density of states (eqn. 12.27) for a single molecule simulated with PBE at 350 K with conventional DFT (30 ps), and the monomer PIMD method with 1 and 32 beads (each 10 ps). Smoothing has been applied to the spectra.

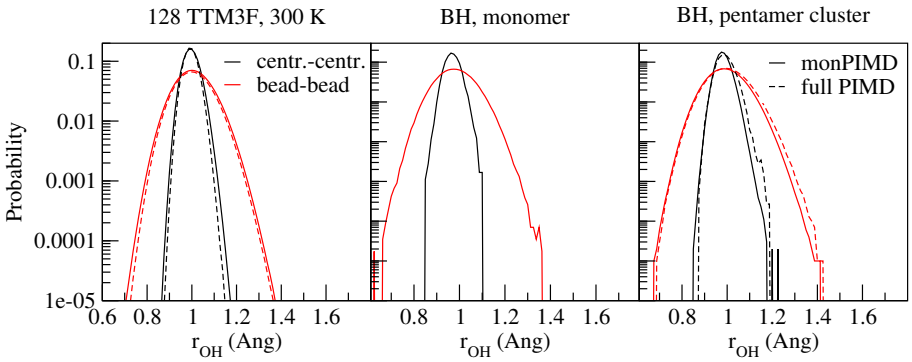

Figure 12.8: Histograms of the r_{OH} distance for a simulation of bulk water with TTM3F and simulation of a gas phase monomer and pentamer cluster with BH. Little difference is observed between full PIMD (solid lines) and the monomerPIMD method (dashed).

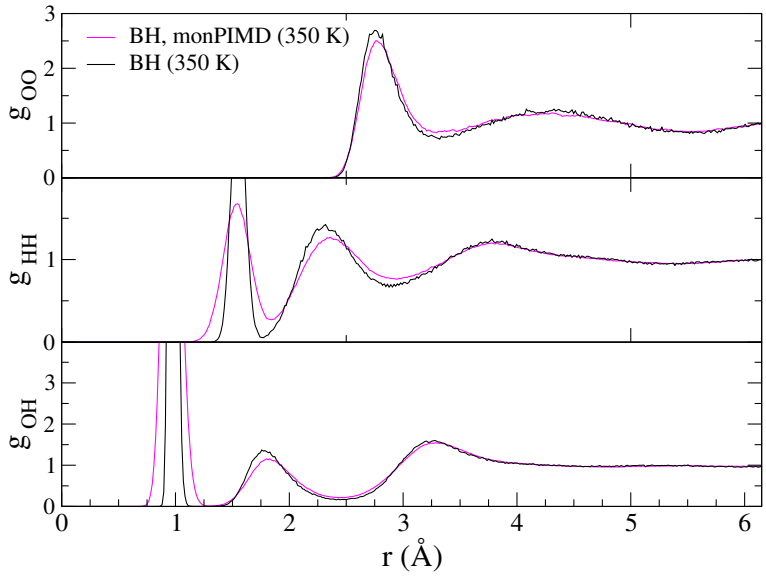

Figure 12.9: Comparison of BH simulated with the monomer PIMD method (with the monomer correction) compared to a conventional BH simulation. The simulation was performed at 350 K here to compare with PBE at the same temperature.

12.10 Conclusion

We have presented preliminary results for our "monomerPIMD" method using our custom PIMD code. This method was shown to capture the main effects of conventional PIMD simulation – redshifting of the OH stretching band and destructuring of the RDFs. The method provides a speedup of $\approx$ 30x when using the monomer correction, or 10-15x when using SIESTA for the monomer calculations. The code is open source and the latest version is available at https://github.com/delton137/PIMD.

Bibliography

[1] D. Bertolini, M. Cassettari, and G. Salvetti. The dielectric relaxation time of supercooled water. *J. Chem. Phys.*, 76(6):3285–3290, 1982.

[2] M. Chaplin. Water and microwaves, May 2012.

[3] M. Uematsu and E. U. Frank. Static dielectric constant of water and steam. *journal of Physical and Chemical Reference Data*, 9(4): 1291–1306, 1980.

[4] Gerald Mathias and Paul Tavan. Angular resolution and range of dipole-dipole correlations in water. *J. Chem. Phys.*, 120(9):4393–4403, 2004.

[5] Pradeep Kumar, Giancarlo Franzese, Sergey V. Buldyrev, and H. Eugene Stanley. Molecular dynamics study of orientational cooperativity in water. *Phys. Rev. E*, 73:041505, Apr 2006.

[6] W. J. Ellison. Permittivity of pure water, at standard atmospheric pressure, over the frequency range 0-25 thz and the temperature range 0-100 c. *J. Phys. Chem. Ref. Data*, 36(1):1, 2007.

[7] O.A. Nabokov and Yu.A. Lubimov. The dielectric relaxation and the percolation model of water. *Mol. Phys.*, 65(6):1473–1482, 1988.

[8] A. Y. Zasetsky, A. F. Khalizov, M. E. Earle, and J. J. Sloan. Frequency dependent complex refractive indices of supercooled liquid water and ice determined from aerosol extinction spectra. *J. Phys. Chem. A*, 109(12): 2760, 2005.

[9] George M. Hale and Marvin R. Querry. Optical constants of water in the 200-nm to 200-micrometer wavelength region. *Appl. Opt.*, 12(3): 555–563, Mar 1973.

[10] D. Segelstein. The complex refractive index of water. Master's thesis, University of Missouri, Kansas City, 1981.

[11] David M. Carey and Gerald M. Korenowski. Measurement of the Raman spectrum of liquid water. *J. Chem. Phys.*, 108(7):2669–2675, 1998.

[12] R. Buchner, Barthel, and journal Stauber. The dielectric relaxation of water between 0 c and 35 c. *Chem. Phys. Lett.*, 306(12):57, 1999.

[13] John E. Bertie and Zhida Lan. Infrared intensities of liquids xx: The intensity of the oh stretching band of liquid water revisited, and the best current values of the optical constants of H2O(l) at 25 C between 15,000 and 1 cm^{-1}. *Appl. Spectrosc.*, 50(8):1047–1057, Aug 1996.

[14] Steven W. Rick. A reoptimization of the five-site water potential (tip5p) for use with ewald sums. *J. Chem. Phys.*, 120(13):6085–6093, 2004.

[15] George S. Fanourgakis and Sotiris S. Xantheas. Development of transferable interaction potentials for water. v. extension of the flexible, polarizable, thole-type model potential (TTM3-F, v. 3.0) to describe the vibrational spectra of water clusters and liquid water. *J. Chem. Phys.*, 128(7):074506, 2008.

[16] C. J. Burnham, D. J. Anick, P. K. Mankoo, and G. F. Reiter. The vibrational proton potential in bulk liquid water and ice. *J. Chem. Phys.*, 128(15):154519, 2008.

[17] W.J. Ellison, K. Lamkaouchi, and J.-M. Moreau. Water: a dielectric reference. *J. Mol. Liq.*, 68(23):171 – 279, 1996.

[18] Anna V. Gubskaya and Peter G. Kusalik. The total molecular dipole moment for liquid water. *J. Chem. Phys.*, 117(11):5290–5302, 2002.

[19] John G. Kirkwood. The dielectric polarization of polar liquids. *J. Chem. Phys.*, 7:911, 1939.

[20] M. J. McGrath, J. I. Siepmann, I.-F. W. Kuo, and C. J. Mundy. Spatial correlation of dipole fluctuations in liquid water. *Mol. Phys.*, 105(10): 1411–1417, 2007.

[21] Y. S. Badyal, M.-L. Saboungi, D. L. Price, S. D. Shastri, D. R. Haeffner, and A. K. Soper. Electron distribution in water. *J. Chem. Phys.*, 112 (21):9206–9208, 2000.

[22] Enrique R. Batista, Sotiris S. Xantheas, and Hannes Jonsson. Molecular multipole moments of water molecules in ice ih. *J. Chem. Phys.*, 109 (11):4546–4551, 1998.

[23] Michiel Sprik. Hydrogen bonding and the static dielectric constant in liquid water. *J. Chem. Phys.*, 95(9):6762–6769, 1991.

[24] Noriyuki Yoshii, Shinichi Miura, and Susumu Okazaki. A molecular dynamics study of dielectric constant of water from ambient to sub- and supercritical conditions using a fluctuating-charge potential model. *Chem. Phys. Lett.*, 345(12):195 – 200, 2001.

[25] Udo Kaatze. The dielectric properties of water in its different states of interaction. *journal of Solution Chemistry*, 26:1049–1112, 1997.

[26] H. E. Stanley. Is there a second critical point in liquid water? *Physica A*, 205(1):122 – 139, 1994.

[27] R. J. Speedy and C. A. Angell. Isothermal compressibility of supercooled water and evidence for a thermodynamic singularity at -45 c. *J. Chem. Phys.*, 65(3):851–858, 1976.

[28] José L. F. Abascal and Carlos Vega. Widom line and the liquidliquid critical point for the TIP4P/2005 water model. *J. Chem. Phys.*, 133(23): 234502, 2010.

[29] Gaël Pallares, Mouna El Mekki Azouzi, Miguel A. Gonzalez, Juan L. Aragones, José L. F. Abascal, Chantal Valeriani, and Frédéric Caupin. Anomalies in bulk supercooled water at negative pressure. *Proceedings of the National Academy of Sciences*, 111(22):7936–7941, 2014.

[30] JA Sellberg, C Huang, Trevor A McQueen, Duane Loh, H Laksmono, D Schlesinger, RG Sierra, D Nordlund, CY Hampton, Dmitri Starodub, et al. Ultrafast x-ray probing of water structure below the homogeneous ice nucleation temperature. *Nature*, 510(7505):381–384, 2014.

[31] W. C. Rntgen. Ueber die constitution des flssigen wassers. *Annalen der Physik*, 281(1).

[32] Biswajit Santra, Robert A. DiStasio Jr., Fausto Martelli, and Roberto Car. Local structure analysis in ab initio liquid water. *Mol. Phys.*, pages 1–13, in press 2015.

[33] Jeffrey R. Errington and Pablo G. Debenedetti. Relationship between structural order and the anomalies of liquid water. *Nature*, 409:318–321, 2001.

[34] Niall J. English and John S. Tse. Density fluctuations in liquid water. *Phys. Rev. Lett.*, 106:037801, Jan 2011.

[35] C. Huang, K. T. Wikfeldt, T. Tokushima, D. Nordlund, Y. Harada, U. Bergmann, M. Niebuhr, T. M. Weiss, Y. Horikawa, M. Leetmaa, M. P. Ljungberg, O. Takahashi, A. Lenz, L. Ojame, A. P. Lyubartsev, S. Shin, L. G. M. Pettersson, and A. Nilsson. The inhomogeneous structure of water at ambient conditions. 106(36):15214–15218, 2009.

[36] Francesco Mallamace, Carmelo Corsaro, and H. Eugene Stanley. Possible relation of water structural relaxation to water anomalies. *Proc. Natl. Acad. Sci. USA*, 110(13):4899–4904, 2013.

[37] Christoph J. Sahle, Christian Sternemann, Christian Schmidt, Susi Lehtola, Sandro Jahn, Laura Simonelli, Simo Huotari, Mikko Hakala, Tuomas Pylkknen, Alexander Nyrow, Kolja Mende, Metin Tolan, Keijo Hmlinen, and Max Wilke. Microscopic structure of water at elevated pressures and temperatures. *Proc. Natl. Acad. Sci. USA*, 110(16): 6301–6306, 2013.

[38] Teresa Head-Gordon and Margaret E. Johnson. Tetrahedral structure or chains for liquid water. *Proceedings of the National Academy of Sciences*, 103(21):7973–7977, 2006.

[39] Felix Sedlmeier, Dominik Horinek, and Roland R. Netz. Spatial correlations of density and structural fluctuations in liquid water: A comparative simulation study. *journal of the American Chemical Society*, 133 (5):1391–1398, 2011.

[40] Gary N. I. Clark, Greg L. Hura, Jose Teixeira, Alan K. Soper, and Teresa Head-Gordon. Small-angle scattering and the structure of ambient liquid water. *Proc. Nat. Acad. Sci.*, 107(32):14003–14007, 2010.

[41] K. T. Wikfeldt, A. Nilsson, and L. G. M. Pettersson. Spatially inhomogeneous bimodal inherent structure of simulated liquid water. *Phys. Chem. Chem. Phys.*, 13:19918–19924, 2011.

[42] Anders Nilsson and Lars G. M. Pettersson. The structural origin of anomalous properties of liquid water. *Nat. Comm.*, 6:8988, 2016.

[43] Jared D. Smith, Christopher D. Cappa, Kevin R. Wilson, Ronald C. Cohen, Phillip L. Geissler, and Richard J. Saykally. Unified description of temperature-dependent hydrogen-bond rearrangements in liquid water. *Proc. Nat. Acad. Sci. of the United States of America*, 102(40): 14171–14174, 2005.

[44] Phillip L. Geissler. Temperature dependence of inhomogeneous broadening: on the meaning of isosbestic points. *J. Am. Chem. Soc.*, 127(42): 14930–14935, 2005.

[45] John David Jackson. *Classical Electrodynamics, 3rd Edition*. Wiley, London, 1998.

[46] A.H. Price Mansel Davies Nora E. Hill, Worth E. Vaughan. *Dielectric Properties and Molecular Behaviour*. Van Norstrand Reinhold Company, New York, 1963.

[47] David M. Bishop and Lap M. Cheung. Vibrational contributions to molecular dipole polarizabilities. *journal of Physical and Chemical Reference Data*, 11(1):119–133, 1982.

[48] I.R. Mcdonald. *Molecular Liquids: orientational order and dielectric properties.*, pages 341–371. 1986.

[49] B. J. Alder and T. E. Wainwright. Studies in molecular dynamics. i. general method. *J. Chem. Phys.*, 31(2):459–466, 1959.

[50] Martin Neumann. Computer simulation and the dielectric constant at finite wavelength. *Mol. Phys.*, 57(1):97–121, 1986.

[51] Martin Neumann and O Steinhauser. The influence of boundary conditions used in machine simulations on the structure of polar systems. *Mol. Phys.*, 39(2):437, 1980.

[52] Martin Neumann, Othmar Steinhauser, and G. Stuart Pawley. Consistent calculation of the static and frequency-dependent dielectric constant in computer simulations. *Mol. Phys.*, 52(1):97–113, 1984.

[53] O. Steinhauser. Computer simulation of polar liquids the influence of molecular shape. *Mol. Phys.*, 46(4):827–837, 1982.

[54] M. Neumann and O. Steinhauser. On the calculation of the dielectric constant using the ewald-kornfeld tensor. *Chem. Phys. Lett.*, 95(45):417 – 422, 1983.

[55] O. Steinhauser. On the dielectric theory and computer simulation of water. *Chemical Physics*, 79(3):465 – 482, 1983.

[56] M. Neumann and O. Steinhauser. Computer simulation and the dielectric constant of polarizable polar systems. *Chem. Phys. Lett.*, 106(6): 563.

[57] M. Neumann. Computer simulation and the dielectric constant at finite wavelength. *Mol. Phys.*, 57(1):97–121, 1986.

[58] Dann Frankel. *Understanding Molecular Simulation, 2nd Ed.* Academic Press, 2001.

[59] M.P. Allen and D.J. Tildesley. *Computer Simulation of Liquids*. Oxford University Press, 1989.

[60] S. W. de Leeuw, J. W. Perram, and E. R. Smith. Simulation of electrostatic systems in periodic boundary conditions. i. lattice sums and dielectric constants. 373(1752):27–56, 1980.

[61] Jirí Kolafa and Ivo Nezbeda. Effect of short and long range forces on the structure of water. ii. orientational ordering and the dielectric constant. *Mol. Phys.*, 98(19):1505–1520, 2000.

[62] David van der Spoel, Paul J. van Maaren, and Herman J. C. Berendsen. A systematic study of water models for molecular simulation: Derivation of water models optimized for use with a reaction field. *J. Chem. Phys.*, 108(24):10220–10230, 1998.

[63] Philip B. Allen. *Molecular Nanowires and Other Quantum Objects*, chapter Dipole Interactions in Nanosystems, pages 29–38. Springer Netherlands, Dordrecht, 2004. ISBN 978-1-4020-2093-3.

[64] Philip B. Allen. Dipole interactions and electrical polarity in nanosystems: The clausiusmossotti and related models. *J. Chem. Phys.*, 120(6): 2951–2962, 2004.

[65] B.T. Thole. Molecular polarizabilities calculated with a modified dipole interaction. *Chem. Phys.*, 59(3):341 – 350, 1981.

[66] C. J. Burnham, D. J. Anick, P. K. Mankoo, and G. F. Reiter. The vibrational proton potential in bulk liquid water and ice. *J. Chem. Phys.*, 128(15):154519, 2008.

[67] Sivert H. Glarum. Dielectric relaxation of polar liquids. *J. Chem. Phys.*, 33(5):1371–1375, 1960.

[68] Fröhlich. *Theory of Dielectrics*. Oxford University Press, London, 1949.

[69] B U Felderhof. Fluctuations of partial polarisations in dielectrics. *journal of Physics C: Solid State Physics*, 12(12):2423, 1979.

[70] B U Felderhof. Time-correlation functions of permanent dipole moments and induced polarisation in dielectrics. *journal of Physics C: Solid State Physics*, 12(15):3121, 1979.

[71] U. M. Titulaer and J. M. Deutch. Analysis of conflicting theories of dielectric relaxation. *J. Chem. Phys.*, 60(4):1502–1513, 1974.

[72] M.S. Wertheim. Theory of polar fluids. *Mol. Phys.*, 36(4):1217–1240, 1978.

[73] Paul Madden and Daniel Kivelson. *A Consistent Molecular Treatment of Dielectric Phenomena*, pages 467–566. John Wiley and Sons, Inc., 2007. ISBN 9780470142806.

[74] S. J. Suresh and V. M. Naik. Hydrogen bond thermodynamic properties of water from dielectric constant data. *J. Chem. Phys.*, 113(21): 9727–9732, 2000.

[75] Lars Onsager. Reciprocal relations in irreversible processes. i. *Phys. Rev.*, 37:405–426, Feb 1931.

[76] Lars Onsager. Reciprocal relations in irreversible processes. ii. *Phys. Rev.*, 38:2265–2279, 1931.

[77] Philippe A. Bopp, Alexei A. Kornyshev, and Godehard Sutmann. Static nonlocal dielectric function of liquid water. *Physical Review Letters*, 76: 1280, 1995.

[78] O. V. Dolgov, D. A. Kirzhnits, and E. G. Maksimov. On an admissible sign of the static dielectric function of matter. *Rev. Mod. Phys.*, 53: 81–93, Jan 1981.

[79] Charles Kittel. *Introduction to Solid State Physics*. John Wiley and Sons, Inc., New York, 8th edition, 2005.

[80] P Debye. *Polar Molecules*. Chemical Catalog Co., New York, 1929.

[81] Nora E. Hill. Interpretation of the dielectric properties of water. *Trans. Faraday Soc.*, 59:344–346, 1963.

[82] Abhishek Rastogi, Siddharth Yadav, and S. J. Suresh. Note: Extraction of hydrogen bond thermodynamic properties of water from dielectric constant and relaxation time data. *J. Chem. Phys.*, 135(8):086101, 2011.

[83] M. Tuckerman, B. J. Berne, and G. J. Martyna. Reversible multiple time scale molecular dynamics. *J. Chem. Phys.*, 97(3), 1992.

[84] M. Tuckerman. *Statistical Mechanics and Molecular Simulations*. Oxford Graduate Texts. Oxford University Press, UK, 2008. ISBN 9780191523465.

[85] Christian J. Burnham, Jichen Li, Sotiris S. Xantheas, and Maurice Leslie. The parametrization of a thole-type all-atom polarizable water model from first principles and its application to the study of water clusters (n=2-21) and the phonon spectrum of ice ih. *J. Chem. Phys.*, 110(9):4566–4581, 1999.

[86] Christian J. Burnham and Sotiris S. Xantheas. Development of transferable interaction models for water. iii. reparametrization of an all-atom polarizable rigid model (ttm2-r) from first principles. *J. Chem. Phys.*, 116(4):1500–1510, 2002.

[87] C. J. Burnham and S. S. Xantheas. Development of transferable interaction models for water. iv. a flexible, all-atom polarizable potential (ttm2-f) based on geometry dependent charges derived from an ab initio monomer dipole moment surface. *J. Chem. Phys.*, 116(12):5115–5124, 2002.

[88] George S. Fanourgakis and Sotiris S. Xantheas. The flexible, polarizable, thole-type interaction potential for water (ttm2-f) revisited. *J. Phys. Chem. A*, 110(11):4100–4106, 2006.

[89] Sho Imoto, Sotiris S. Xantheas, and Shinji Saito. Molecular origin of the difference in the hoh bend of the ir spectra between liquid water and ice. *J. Chem. Phys.*, 138(5):054506, 2013.

[90] Harry Partridge and David W. Schwenke. The determination of an accurate isotope dependent potential energy surface for water from extensive ab initio calculations and experimental data. *J. Chem. Phys.*, 106(11): 4618–4639, 1997.

[91] Orsolya Gereben and Lszl Pusztai. On the accurate calculation of the dielectric constant from molecular dynamics simulations: The case of spc/e and swm4-dp water. *Chem. Phys. Lett.*, 507(13):80 – 83, 2011.

[92] T.J. Morrow and E.R. Smith. Simulation calculation of dielectric constants: Comparison of methods on an exactly solvable model. *journal of Statistical Physics*, 61:187–201, 1990.

[93] Raymond D. Mountain. Shear viscosity and dielectric constant of liquid acetonitrile. *J. Chem. Phys.*, 107(10):3921–3923, 1997.

[94] Christopher J. Fennell, Libo Li, and Ken A. Dill. Simple liquid models with corrected dielectric constants. *J. Phys. Chem. B*, 116(23): 6936–6944, 2012.

[95] Howard E. Alper and Ronald M. Levy. Computer simulations of the dielectric properties of water: Studies of the simple point charge and transferrable intermolecular potential models. *J. Chem. Phys.*, 91(2), 1989.

[96] Manu Sharma, Raffaele Resta, and Roberto Car. Dipolar correlations and the dielectric permittivity of water. *Phys. Rev. Lett.*, 98:247401, Jun 2007.

[97] Chao Zhang and Michiel Sprik. Computing the dielectric constant of liquid water at constant dielectric displacement. *Phys. Rev. B*, 93:144201, 2016.

[98] Ilario G. Tironi, Roger M. Brunne, and Wilfred F. van Gunsteren. On the relative merits of flexible versus rigid models for use in computer simulations of molecular liquids. *Chem. Phys. Lett.*, 250(1):19 – 24, 1996.

[99] Olle Teleman, Bo Jnsson, and Sven Engstrm. A molecular dynamics simulation of a water model with intramolecular degrees of freedom. *Mol. Phys.*, 60(1):193–203, 1987.

[100] Yujie Wu, Harald L. Tepper, and Gregory A. Voth. Flexible simple point-charge water model with improved liquid-state properties. *J. Chem. Phys.*, 124(2):024503, 2006.

[101] Uri. Dinur. "flexible" water molecules in external electrostatic potentials. *J. Phys. Chem.*, 94(15):5669–5671, 1990.

[102] David M. Ferguson. Parameterization and evaluation of a flexible water model. *journal of Computational Chemistry*, 16(4):501–511, 1995.

[103] Michiel Sprik and Michael L. Klein. A polarizable model for water using distributed charge sites. *J. Chem. Phys.*, 89(12):7556–7560, 1988.

[104] S. B. Zhu, S. Yao, J. B. Zhu, Surjit Singh, and G. W. Robinson. A flexible/polarizable simple point charge water model. *J. Phys. Chem.*, 95(16):6211–6217, 1991.

[105] Guillaume Lamoureux, Jr. Alexander D. MacKerell, and Benoît Roux. A simple polarizable model of water based on classical drude oscillators. *J. Chem. Phys.*, 119(10):5185–5197, 2003.

[106] Haibo Yu, Tomas Hansson, and Wilfred F. van Gunsteren. Development of a simple, self-consistent polarizable model for liquid water. *J. Chem. Phys.*, 118(1):221–234, 2003.

[107] Revati Kumar, Fang-Fang Wang, Glen R. Jenness, and Kenneth D. Jordan. A second generation distributed point polarizable water model. *J. Chem. Phys.*, 132(1):014309, 2010.

[108] Pengyu Ren and Jay W. Ponder. Polarizable atomic multipole water model for molecular mechanics simulation. *J. Phys. Chem. B*, 107(24): 5933–5947, 2003.

[109] Paul J. van Maaren and David van der Spoel. Molecular dynamics simulations of water with novel shell-model potentials. *J. Phys. Chem. B*, 105(13):2618–2626, 2001.

[110] Jianhui Li, Zhongwu Zhou, and Richard J. Sadus. Role of nonadditive forces on the structure and properties of liquid water. *J. Chem. Phys.*, 127(15):154509, 2007.

[111] Lee-Ping Wang, Teresa Head-Gordon, Jay W. Ponder, Pengyu Ren, John D. Chodera, Peter K. Eastman, Todd J. Martinez, and Vijay S. Pande. Systematic improvement of a classical molecular model of water. *J. Phys. Chem. B*, 117(34):9956–9972, 2013.

[112] Philipp Tröster, Konstantin Lorenzen, Magnus Schwrer, and Paul Tavan. Polarizable water models from mixed computational and empirical optimization. *J. Phys. Chem. B*, 117(32):9486–9500, 2013.

[113] Harry A. Stern, F. Rittner, B. J. Berne, and Richard A. Friesner. Combined fluctuating charge and polarizable dipole models: Application to a five-site water potential function. *J. Chem. Phys.*, 115(5), 2001.

[114] Michael W. Mahoney and William L. Jorgensen. Quantum, intramolecular flexibility, and polarizability effects on the reproduction of the density anomaly of liquid water by simple potential functions. *J. Chem. Phys.*, 115(23):10758–10768, 2001.

[115] Taisuke Hasegawa and Yoshitaka Tanimura. A polarizable water model for intramolecular and intermolecular vibrational spectroscopies. *J. Phys. Chem. B*, 115(18):5545–5553, 2011.

[116] Haibo Yu and Wilfred F. van Gunsteren. Charge-on-spring polarizable water models revisited: From water clusters to liquid water to ice. *J. Chem. Phys.*, 121(19):9549–9564, 2004.

[117] Huafeng Xu, Harry A. Stern, and B. J. Berne. Can water polarizability be ignored in hydrogen bond kinetics? *J. Phys. Chem. B*, 106(8): 2054–2060, 2002.

[118] Jose Alejandre, Gustavo A. Chapela, Humberto Saint-Martin, and Noe Mendoza. A non-polarizable model of water that yields the dielectric constant and the density anomalies of the liquid: Tip4q. *Phys. Chem. Chem. Phys.*, 13:19728–19740, 2011.

[119] Rui Qi, Lee-Ping Wang, Qiantao Wang, Vijay S. Pande, and Pengyu Ren. United polarizable multipole water model for molecular mechanics simulation. *J. Chem. Phys.*, 143(1):014504, 2015.

[120] Yi Liu and Toshiko Ichiye. Soft sticky dipole potential for liquid water: a new model. *J. Phys. Chem.*, 100(7):2723–2730, 1996.

[121] Ming-Liang Tan, Justin T. Fischer, Amalendu Chandra, Bernard R. Brooks, and Toshiko Ichiye. A temperature of maximum density in soft sticky dipole water. *Chem. Phys. Lett.*, 376(56):646 – 652, 2003.

[122] Sanjib Senapati and Amalendu Chandra. Dielectric constant of water confined in a nanocavity. *J. Phys. Chem. B*, 105(22):5106–5109, 2001.

[123] Peter Höchtl, Stefan Boresch, Wolfgang Bitomsky, and Othmar Steinhauser. Rationalization of the dielectric properties of common three-site water models in terms of their force field parameters. *J. Chem. Phys.*, 109(12):4927–4937, 1998.

[124] Gabriele Raabe and Richard J. Sadus. Molecular dynamics simulation of the dielectric constant of water: The effect of bond flexibility. *J. Chem. Phys.*, 134(23):234501, 2011.

[125] Carlos Vega and Jose L. F. Abascal. Simulating water with rigid non-polarizable models: a general perspective. *Phys. Chem. Chem. Phys.*, 13:19663–19688, 2011.

[126] Thomas M. Nymand and Per Linse. Molecular dynamics simulations of polarizable water at different boundary conditions. *J. Chem. Phys.*, 112 (14):6386–6395, 2000.

[127] O. Steinhauser. Reaction field simulation of water. *Mol. Phys.*, 45(2): 335–348, 1982.

[128] N. Neumann. The dielectric constant of water. computer simulations with the mcy potential. *J. Chem. Phys.*, 82:5663, 1985.

[129] Martin Neumann. Dielectric relaxation in water. computer simulations with the tip4p potential. *J. Chem. Phys.*, 85(3):1567–1580, 1986.

[130] Hans W. Horn, William C. Swope, Jed W. Pitera, Jeffry D. Madura, Thomas J. Dick, Greg L. Hura, and Teresa Head-Gordon. Development of an improved four-site water model for biomolecular simulations: Tip4p-ew. *J. Chem. Phys.*, 120(20):9665–9678, 2004.

[131] J. L. F. Abascal and C. Vega. A general purpose model for the condensed phases of water: TIP4P/2005. *J. Chem. Phys.*, 123(23):234505, 2005.

[132] Miguel A. Gonzalez and Jose L. F. Abascal. A flexible model for water based on TIP4P/2005. *J. Chem. Phys.*, 135(22):224516, 2011.

[133] Michael W. Mahoney and William L. Jorgensen. A five-site model for liquid water and the reproduction of the density anomaly by rigid, nonpolarizable potential functions. *J. Chem. Phys.*, 112(20):8910–8922, 2000.

[134] Guo-Zhu Jia, Ka-Ma Huang, Li-Jun Yang, and Xiao-Qing Yang. Composition-dependent dielectric properties of dmf-water mixtures by molecular dynamics simulations. *International journal of Molecular Sciences*, 10(4):1590–1600, 2009.

[135] J. Verhoeven and A. Dymanus. Magnetic properties and molecular quadrupole tensor of the water molecule by beam-maser zeeman spectroscopy. *J. Chem. Phys.*, 52(6):3222–3233, 1970.

[136] S.L. Carnie and G.N. Patey. Fluids of polarizable hard spheres with dipoles and tetrahedral quadrupoles integral equation results with application to liquid water. *Mol. Phys.*, 47(5):1129–1151, 1982.

[137] Berk Hess, Carsten Kutzner, David van der Spoel, and Erik Lindahl. Gromacs 4: Algorithms for highly efficient, load-balanced, and scalable molecular simulation. *J. Chem. Theo. Comp.*, 4(3):435–447, 2008.

[138] D. van der Spoel, E. Lindahl, B. Hess, A. R. van Buuren, E. Apol, P. J. Meulenhoff, D. P. Tieleman, A. L. T. M. Sijbers, K. A. Feenstra, R. van Drunen, and H. J. C. Berendsen. *Gromacs User Manual version 4.6*, 2013.

[139] W.T. Parry and ASME. *ASME International Steam Tables for Industrial Use: Based on the IAPWS Industrial Formulation 1997 for the Thermodynamic Properties of Water and Steam (IAPWS-IF97).* ASME, 2006.

[140] J.N. Israelachvili. *Intermolecular and Surface Forces: Revised Third Edition.* Elsevier Science, 2011.

[141] Toshiko Fukasawa, Takaaki Sato, Junji Watanabe, Yoshimasa Hama, Werner Kunz, and Richard Buchner. Relation between dielectric and low-frequency raman spectra of hydrogen-bond liquids. *Phys. Rev. Lett.*, 95:197802, Nov 2005.

[142] O. Faurskov Nielsen. Chapter 2. low-frequency spetroscopic studies of interactions in liquids. *Annu. Rep. Prog. Chem. C: Phys. Chem.*, 90: 3–44, 1993.

[143] P. A. Madden and R. W. Impey. On the infrared and Raman spectra of water in the region 5250 cm^{-1}. *Chem. Phys. Lett.*, 123(6):502 – 506, 1986.

[144] J. B. Hasted, S. K. Husain, F. A. M. Frescura, and J. R. Birch. Far-infrared absorption in liquid water. *Chem. Phys. Lett.*, 118(6):622 – 625, 1985.

[145] B. Bagchi. *Molecular Relaxation in Liquids.* Oxford University Press, USA, 2012.

[146] A. K. Soper. Orientational correlation function for molecular liquids: The case of liquid water. *J. Chem. Phys.*, 101(8), 1994.

[147] M. S. Wertheim. Exact solution of the mean spherical model for fluids of hard spheres with permanent electric dipole moments. *J. Chem. Phys.*, 55(9):4291–4298, 1971.

[148] Yoshiteru Yonetani. A severe artifact in simulation of liquid water using a long cut-off length: Appearance of a strange layer structure. *Chem. Phys. Lett.*, 406(13):49 – 53, 2005.

[149] David van der Spoel and Paul J. van Maaren. The origin of layer structure artifacts in simulations of liquid water. *J. Chem. Theo. Comp.*, 2 (1):1–11, 2006.

[150] Gerald Mathias, Bernhard Egwolf, Marco Nonella, and Paul Tavan. A fast multipole method combined with a reaction field for long-range electrostatics in molecular dynamics simulations: The effects of truncation on the properties of water. *J. Chem. Phys.*, 118(24):10847–10860, 2003.

[151] Philippe Hunenberger and Maria Reif. *Single-Ion Solvation: Experimental and Theoretical Approaches to Elusive Thermodynamic Quantities*. 1 edition. ISBN 1847551874.

[152] Eric W. Weisstein. Primary parallelohedron, 2013. [Online; accessed 8-July-2013].

[153] M.P. Allen and D.J. Tildesley. Code from Computer Simulation of Liquids.

[154] journal H. Van Vleck and V. F. Weisskopf. On the shape of collision-broadened lines. *Rev. Mod. Phys.*, 17:227–236, Apr 1945.

[155] M. Toda, R. Kubo, N. Saitō, and N. Hashitsume. *Statistical Phys. II: Nonequilibrium Statistical Mechanics*. Series C. Springer Berlin Heidelberg, 1991. ISBN 9783540538332.

[156] R. Brendel and D. Bormann. An infrared dielectric function model for amorphous solids. *journal of Applied Physics*, 71(1):1–6, 1992.

[157] Yuri Feldman, Alexander Puzenko, and Yaroslav Ryabov. *Dielectric Relaxation Phenomena in Complex Materials*, pages 1–125. 2005. ISBN 9780471790266.

[158] A Y Zasetsky and R Buchner. Quasi-linear least squares and computer code for numerical evaluation of relaxation time distribution from broadband dielectric spectra. *journal of Physics: Condensed Matter*, 23(2): 025903, 2011.

[159] H. Schäfer, E. Sternin, R. Stannarius, M. Arndt, and F. Kremer. Novel approach to the analysis of broadband dielectric spectra. *Phys. Rev. Lett.*, 76:2177–2180, Mar 1996.

[160] C. J. Dias. Determination of a distribution of relaxation frequencies based on experimental relaxational data. *Phys. Rev. B*, 53:14212–14222, Jun 1996.

[161] Jrgen Weese. A reliable and fast method for the solution of fredhol integral equations of the first kind based on tikhonov regularization. *Computer Physics Communications*, 69(1):99 – 111, 1992.

[162] Enis Tuncer and J. Ross Macdonald. Comparison of methods for estimating continuous distributions of relaxation times. *journal of Applied Physics*, 99(7):074106, 2006.

[163] S.A. Ktitorov. Determination of the relaxation time distribution function from dielectric losses. *Technical Physics Letters*, 29(11):956–958, 2003.

[164] J Macutkevic, J Banys, and A Matulis. Determination of the distribution of the relaxation times from dielectric spectra. *Nonlinear Analysis*, 9(1): 75–88, 2004.

[165] J. Macutkevic, S. Kamba, J. Banys, A. Brilingas, A. Pashkin, J. Petzelt, K. Bormanis, and A. Sternberg. Infrared and broadband dielectric spectroscopy of pzn-pmn-psn relaxor ferroelectrics: Origin of two-component relaxation. *Phys. Rev. B*, 74:104106, Sep 2006.

[166] F. Alvarez, A. Alegra, and J. Colmenero. Relationship between the time-domain kohlrausch-williams-watts and frequency-domain havriliak-negami relaxation functions. *Phys. Rev. B*, 44:7306–7312, Oct 1991.

[167] R. Hilfer. H-function representations for stretched exponential relaxation and non-debye susceptibilities in glassy systems. *Phys. Rev. E*, 65: 061510, Jun 2002.

[168] A. K. Jonscher. The universal dielectric response. *Nature*, 267:673–679, 1977.

[169] Iwao Ohmine. Liquid water dynamics: Collective motions, fluctuation, and relaxation. *journal of Physical Chemistry*, 99(18):6767–6776, 1995.

[170] Alexander Puzenko, Yoshihito Hayashi, Yaroslav E. Ryabov, Igal Balin, Yuri Feldman, Udo Kaatze, and Ralph Behrends. Relaxation dynamics in glycerolwater mixtures: I. glycerol-rich mixtures. *J. Phys. Chem. B*, 109(12):6031–6035, 2005.

[171] Holger Nadolny, Andreas Volmari, and Hermann Weingrtner. Orientational dynamics of hydrogen-bonded liquids a comparative study of dielectric and nuclear magnetic relaxation in n-butanol-tetrachloromethane mixtures. *Berichte der Bunsengesellschaft für physikalische Chemie*, 102(6).

[172] J. T. Kindt and C. A. Schmuttenmaer. Far-infrared dielectric properties of polar liquids probed by femtosecond terahertz pulse spectroscopy. *J. Phys. Chem.*, 100(24):10373–10379, 1996.

[173] D. S. Venables and C. A. Schmuttenmaer. Far-infrared spectra and associated dynamics in acetonitrilewater mixtures measured with femtosecond thz pulse spectroscopy. *J. Chem. Phys.*, 108(12):4935–4944, 1998.

[174] Biman Bagchi. Water dynamics in the hydration layer around proteins and micelles. *Chem. Rev.*, 105(9):3197–3219, 2005.

[175] P.W. Rosenkranz. A model for the complex dielectric constant of supercooled liquid water at microwave frequencies. *Geoscience and Remote Sensing, IEEE Transactions on*, 53(3):1387–1393, March 2015.

[176] J.R. Wang and T.J. Schmugge. An empirical model for the complex dielectric permittivity of soils as a function of water content. *Geoscience and Remote Sensing, IEEE Transactions on*, GE-18(4):288–295, Oct 1980.

[177] S. Kneifel, S. Redl, E. Orlandi, U. Löhnert, M.P. Cadeddu, D.D. Turner, and M. Chen. Absorption properties of supercooled liquid water between 31 and 225 ghz: evaluation of absorption models using ground-based observations. *journal of Applied Meteorology and Climatology*, 53(4): 1028, 2014.

[178] Udo Kaatze. Dielectric spectroscopy of aqueous solutions. hydration phenomena and hydrogen-bonded networks. *J. Mol. Liq.*, 56:95 – 115, 1993.

[179] Far infrared spectroscopy of water at different temperatures: GHz to THz dielectric spectroscopy of water. *J. Mol. Liq.*, 112(3):125 – 135, 2004.

[180] T. Yamaguchi, S.-H. Chong, and F. Hirata. Dielectric relaxation spectrum of water studied by the sitesite generalized langevin modified modecoupling theory. *Mol. Phys.*, 101(8):1211–1220, 2003.

[181] Eli Shiratani and Masaki Sasai. Growth and collapse of structural patterns in the hydrogen bond network in liquid water. *J. Chem. Phys.*, 104(19), 1996.

[182] Shinji Saito and Iwao Ohmine. Dynamics and relaxation of an intermediate size water cluster $(H_2O)108$. *J. Chem. Phys.*, 101(7):6063–6075, 1994.

[183] Cecilie Ronne, Lars Thrane, Per-Olof strand, Anders Wallqvist, Kurt V. Mikkelsen, and So/ren R. Keiding. Investigation of the temperature dependence of dielectric relaxation in liquid water by thz reflection spectroscopy and molecular dynamics simulation. *J. Chem. Phys.*, 107(14), 1997.

[184] Noam Agmon. Tetrahedral displacement: the molecular mechanism behind the debye relaxation in water. *J. Phys. Chem.*, 100(3):1072–1080, 1996.

[185] V.I. Arkhipov. Hierarchy of dielectric relaxation times in water. *journal of Non-Crystalline Solids*, 305(13):127 – 135, 2002.

[186] J. G. Powles. Dielectric relaxation and the internal field. *J. Chem. Phys.*, 21(4):633–637, 1953.

[187] E Fatuzzo and P R Mason. A calculation of the complex dielectric constant of a polar liquid by the librating molecule method. *Proceedings of the Physical Society*, 90(3):729, 1967.

[188] TsuWei Nee and Robert Zwanzig. Theory of dielectric relaxation in polar liquids. *J. Chem. Phys.*, 52(12):6353–6363, 1970.

[189] B. Bagchi and A. Chandra. Dielectric relaxation in dipolar liquids: Route to debye behavior via translational diffusion. *Phys. Rev. Lett.*, 64:455–458, Jan 1990.

[190] Barthel, K. Bachhuber, R. Buchner, and H. Hetzenauer. Dielectric spectra of some common solvents in the microwave region. water and lower alcohols. *Chem. Phys. Lett.*, 165(4):369 – 373, 1990.

[191] J R Peacock. Millimetre wave permittivity of water near 25C. *J. Phys. D: Appl. Phys.*, 42(20):205501, 2009.

[192] Takaaki Sato and Richard Buchner. Dielectric relaxation processes in ethanol/water mixtures. *J. Phys. Chem. A*, 108(23):5007–5015, 2004.

[193] Uffe Moller, David G. Cooke, Koichiro Tanaka, and Peter Uhd Jepsen. Terahertz reflection spectroscopy of debye relaxation in polar liquids. *J. Opt. Soc. Am. B*, 26(9):A113–A125, 2009.

[194] Hiroyuki Yadaa, Masaya Nagaia, and Koichiro Tanaka. Origin of the fast relaxation component of water and heavy water revealed by terahertz time-domain attenuated total reflection spectroscopy. *Chem. Phys. Lett.*, 464(46):166 – 170, 2008.

[195] Toshiko Fukasawa, Takaaki Sato, Junji Watanabe, Yoshimasa Hama, Werner Kunz, and Richard Buchner. Relation between dielectric and low-frequency Raman spectra of hydrogen-bond liquids. *Phys. Rev. Lett.*, 95:197802, 2005.

[196] Hans J. Liebe, George A. Hufford, and Takeshi Manabe. A model for the complex permittivity of water at frequencies below 1 thz. *International journal of Infrared and Millimeter Waves*, 12(7):659–675, 1991.

[197] Amerigo Beneduci. Which is the effective time scale of the fast debye relaxation process in water? *J. Mol. Liq.*, 138(13):55 – 60, 2008.

[198] N. Q. Vinh, Mark S. Sherwin, S. James Allen, D. K. George, A. J. Rahmani, and Kevin W. Plaxco. High-precision gigahertz-to-terahertz spectroscopy of aqueous salt solutions as a probe of the femtosecond-to-picosecond dynamics of liquid water. *J. Chem. Phys.*, 142(16):164502.

[199] Matthias Heyden, Jian Sun, Stefan Funkner, Gerald Mathias, Harald Forbert, Martina Havenith, and Dominik Marx. Dissecting the THz spectrum of liquid water from first principles via correlations in time and space. *Proc. Natl. Acad. Sci. USA*, 107(27):12068–12073, 2010.

[200] Alenka Luzar and David Chandler. Hydrogen-bond kinetics in liquid water. *Nature*, 379(6560):55–57, 1996.

[201] Damien Laage and James T. Hynes. On the molecular mechanism of water reorientation. *J. Phys. Chem. B*, 112(45):14230–14242, 2008.

[202] D. C. Johnston. Stretched exponential relaxation arising from a continuous sum of exponential decays. *Phys. Rev. B*, 74:184430, Nov 2006.

[203] S. Woutersen, U. Emmerichs, and H. J. Bakker. Femtosecond mid-ir pump-probe spectroscopy of liquid water: Evidence for a two-component structure. *Science*, 278(5338):658–660, 1997.

[204] J. Poley. Microwave dispersion of some polar liquids. *App. Sci. Res. B*, 4(1):337–387, 1955.

[205] N E Hill. The influence of the poley absorption on the inertial fall-off of the dielectric absorption. *J. Phys. C.: Solid State Phys.*, 4(15):2322, 1971.

[206] B. Bagchi and A. Chandra. Molecular theory of underdamped dielectric relaxation: understanding collective effects in dipolar liquids. *Chem. Phys.*, 173(2):133 – 141, 1993.

[207] R. Ferraro and L. Basile. *Fourier Transform Infrared Spectra: Applications to Chem. Systems*, volume v. 1. Elsevier Science, 1978. ISBN 9780323140171.

[208] Minhaeng Cho, Graham R. Fleming, Shinji Saito, Iwao Ohmine, and Richard M. Stratt. Instantaneous normal mode analysis of liquid water. *J. Chem. Phys.*, 100(9):6672–6683, 1994.

[209] Akiko Saito, Osato Miyawaki, and Kozo Nakamura. Dielectric relaxation of aqueous solution with low-molecular-weight nonelectrolytes and its relationship with solution structure. *Bioscience, Biotechnology, and Biochemistry*, 61(11):1831–1835, 1997.

[210] Josef Barthel, Richard Buchner, K. Bachhuber, H. Hetzenauer, M. Kleebauer, and H. Ortmeier. Molecular processes in electrolyte solutions at microwave frequencies. *Pure and Applied Chemistry*, 62(12):2287–2296, 1990.

[211] A. S. Barker. Long-wavelength soft modes, central peaks, and the Lyddane-Sachs-Teller relation. *Phys. Rev. B*, 12:4071–4084, 1975.

[212] Daniel Kivelson and Harold Friedman. Longitudinal dielectric relaxation. *J. Phys. Chem.*, 93(19):7026–7031, 1989.

[213] A. Arbe, P. Malo de Molina, F. Alvarez, B. Frick, and J. Colmenero. Dielectric susceptibility of liquid water: Microscopic insights from coherent and incoherent neutron scattering. *Phys. Rev. Lett.*, 117:185501, 2016.

[214] A. Angulo-Sherman and H. Mercado-Uribe. Dielectric spectroscopy of water at low frequencies: The existence of an isopermitive point. *Chem. Phys. Lett.*, 503(46):327 – 330, 2011.

[215] H Jansson, R Bergman, and J Swenson. Hidden slow dynamics of water. *Phys. Rev. Lett.*, 104:017802, 2010.

[216] H Jansson, R Bergman, and J Swenson. Slow dielectric response of debye-type in water and other hydrogen bonded liquids. *J. Mol. Struct.*, 972:92–98, 2010.

[217] NiraliS. Shah, PoyaniS. Shah, and V.A. Rana. Dielectric and electrical properties of coconut water and distilled water in the frequency range 20 hz to 2 mhz at different temperatures. *Ionics*, pages 1–6, 2015.

[218] Ranko Richert, Alexander Agapov, and Alexei P. Sokolov. Appearance of a debye process at the conductivity relaxation frequency of a viscous liquid. *J. Chem. Phys.*, 134(10):104508, 2011.

[219] R. Casalini and C. M. Roland. On the low frequency loss peak in the dielectric spectrum of glycerol. *J. Chem. Phys.*, 135(9):094502, 2011.

[220] W. H. Hunter Woodward, Andrew J. Pasztor, Tirtha Chatterjee, and Alan I. Nakatani. On a different approach toward low-frequency dielectric spectroscopy measurements of conductive liquids. *Review of Scientific Instruments*, 84(8):085109, 2013.

[221] David P. Shelton. Slow polarization relaxation in water observed by hyper-rayleigh scattering. *Phys. Rev. B*, 72:020201, Jul 2005.

[222] David P. Shelton. Are dipolar liquids ferroelectric? *J. Chem. Phys.*, 123 (8):084502, 2005.

[223] David P. Shelton. Long-range orientation correlation in liquids. *J. Chem. Phys.*, 136(4):044503, 2012.

[224] David P. Shelton. Long-range orientation correlation in water. *J. Chem. Phys.*, 141(22):224506, 2014.

[225] David P. Shelton. Long-range orientation correlation in dipolar liquids probed by hyper-rayleigh scattering. *J. Chem. Phys.*, 143(13):134503, 2015.

[226] Lijuan Xie, Yang Yao, and Yibin Ying. The application of terahertz spectroscopy to protein detection: A review. *App. Spect. Rev.*, 49(6): 448, 2014.

[227] Valeria Conti Nibali and Martina Havenith. New insights into the role of water in biological function: Studying solvated biomolecules using terahertz absorption spectroscopy in conjunction with molecular dynamics simulations. *J. Am. Chem. Soc.*, 136(37):12800, 2014.

[228] Simon Ebbinghaus, Seung Joong Kim, Matthias Heyden, Xin Yu, Udo Heugen, Martin Gruebele, David M. Leitner, and Martina Havenith. An extended dynamical hydration shell around proteins. *Proc. Natl. Acad. Sci. USA*, 104(52):20749, 2007.

[229] Matthias Heyden and Martina Havenith. Combining THz spectroscopy and MD simulations to study protein-hydration coupling. *Methods*, 52 (1):74, 2010.

[230] SeungJoong Kim, Benjamin Born, Martina Havenith, and Martin Gruebele. Real-time detection of protein-water dynamics upon protein folding by terahertz absorption spectroscopy. *Angewandte Chemie International Edition*, 47(34):6486, 2008.

[231] Oleksandr Sushko, Rostyslav Dubrovka, and Robert S. Donnan. Terahertz spectral domain computational analysis of hydration shell of proteins with increasingly complex tertiary structure. *J. Phys. Chem. B*, 117(51):16486–16492, 2013.

[232] C. Brot, G. Bossis, and C. Hesse-Bezot. Molecular dynamics calculation of the dielectric constant. *Mol. Phys.*, 40(5):1053–1072, 1980.

[233] J. Higo, M. Sasai, H. Shirai, H. Nakamura, and T. Kugimiya. Large vortex-like structure of dipole field in computer models of liquid water and dipole-bridge between biomolecules. *Proc. Natl. Acad. Sci.*, 98(11): 5961, 2001.

[234] Rudolf Gut. The autoprotolysis constant of liquid anhydrous hydrogen fluoride. *journal of Fluorine Chemistry*, 15(2):163 – 167, 1980.

[235] Xingcai Su, L. Lianos, Y. Ron Shen, and Gabor A. Somorjai. Surface-induced ferroelectric ice on pt(111). *Phys. Rev. Lett.*, 80:1533–1536, Feb 1998.

[236] Yoshimichi Nakamura and Takahisa Ohno. Ferroelectric mobile water. *Phys. Chem. Chem. Phys.*, 13:1064–1069, 2011.

[237] Chuanfu Luo, Wei Fa, Jian Zhou, Jinming Dong, and Xiao Cheng Zeng. Ferroelectric ordering in ice nanotubes confined in carbon nanotubes. *Nano Letters*, 8(9):2607–2612, 2008.

[238] Jrgen Kfinger, Gerhard Hummer, and Christoph Dellago. Macroscopically ordered water in nanopores. *Proc. Nat. Acad. Sci.*, 105(36): 13218–13222, 2008.

[239] David N. LeBard and Dmitry V. Matyushov. Ferroelectric hydration shells around proteins: Electrostatics of the proteinwater interface. *J. Phys. Chem. B*, 114(28):9246–9258, 2010.

[240] Wolfgang Kleemann, George A. Samara, and Jan Dec. *Relaxor Ferroelectrics from Random Field Models to Glassy Relaxation and Domain States*, pages 275–301. Wiley-VCH Verlag GmbH and Co. KGaA, 2005. ISBN 9783527604654.

[241] George A Samara. The relaxational properties of compositionally disordered abo 3 perovskites. *journal of Physics: Condensed Matter*, 15(9): R367, 2003.

[242] B. P. Burton, E. Cockayne, S. Tinte, and U. V. Waghmare. First-principles-based simulations of relaxor ferroelectrics. *Phase Transitions*, 79(1-2):91–121, 2006.

[243] Hiroyuki Takenaka, Ilya Grinberg, and Andrew M. Rappe. Anisotropic local correlations and dynamics in a relaxor ferroelectric. *Phys. Rev. Lett.*, 110:147602, Apr 2013.

[244] Ilya Grinberg, Young-Han Shin, and Andrew M. Rappe. Molecular dynamics study of dielectric response in a relaxor ferroelectric. *Phys. Rev. Lett.*, 103:197601, Nov 2009.

[245] R. Pirc and R. Blinc. Vogel-fulcher freezing in relaxor ferroelectrics. *Phys. Rev. B*, 76:020101, 2007.

[246] A A Bokov, M A Leshchenko, M A Malitskaya, and I P Raevski. Dielectric spectra and vogel-fulcher scaling in pb(in 0.5 nb 0.5)o 3 relaxor ferroelectric. *J. Phys.: Cond. Mat.*, 11(25):4899, 1999.

[247] T A Vilgis. Random energies, random coordination numbers, the vogel-fulcher law, and non-exponential relaxation. *journal of Physics: Condensed Matter*, 2(15):3667, 1990.

[248] A. K. Tagantsev. Vogel-fulcher relationship for the dielectric permittivity of relaxor ferroelectrics. *Phys. Rev. Lett.*, 72:1100–1103, Feb 1994.

[249] Gerold Adam and Julian H. Gibbs. On the temperature dependence of cooperative relaxation properties in glass-forming liquids. *J. Chem. Phys.*, 43(1):139–146, 1965.

[250] Jeppe C. Dyre, Tina Hechsher, and Kristine Niss. A brief critique of the adamgibbs entropy model. *journal of Non-Crystalline Solids*, 355(1012): 624 – 627, 2009.

[251] Nicolas Giovambattista, Sergey V. Buldyrev, Francis W. Starr, and H. Eugene Stanley. Connection between adam-gibbs theory and spatially heterogeneous dynamics. *Phys. Rev. Lett.*, 90:085506, Feb 2003.

[252] Alexi A. Bokov and Zuo-Guang Ye. Dielectric relaxation in relaxor ferroelectrics. *journal of Advanced Dielectrics*, 02(02):1241010, 2012.

[253] M. D. Glinchuk and V. A. Stephanovich. Dynamic properties of relaxor ferroelectrics. *journal of Applied Physics*, 85(3), 1999.

[254] R. Kohlrausch. Theorie des elektrischen rckstandes in der leidener flasche. *Annalen der Physik*, 167(2):179–214, 1854.

[255] Graham Williams and David C. Watts. Non-symmetrical dielectric relaxation behaviour arising from a simple empirical decay function. *Trans. Faraday Soc.*, 66:80–85, 1970.

[256] Joseph Klafter and Michael F. Shlesinger. On the relationship among three theories of relaxation in disordered systems. *Proc. Nat. Acad. Sci.*, 83(4):848–851, 1986.

[257] Olle Edholm and Clas Blomberg. Stretched exponentials and barrier distributions. *Chemical Physics*, 252(12):221 – 225, 2000.

[258] Ismo Koponen. Random transition rate model of stretched exponential relaxation. *journal of Non-Crystalline Solids*, 189(12):154 – 160, 1995.

[259] Larry S. Liebovitch and Tibor I. Tóth. Distributions of activation energy barriers that produce stretched exponential probability distributions for the time spent in each state of the two state reaction a b. *Bulletin of Mathematical Biology*, 53:443–455, 1991.

[260] F. Sciortino, P. Gallo, P. Tartaglia, and S. H. Chen. Supercooled water and the kinetic glass transition. *Phys. Rev. E*, 54:6331–6343, Dec 1996.

[261] Ryogo Kubo. Statistical-mechanical theory of irreversible processes. i. general theory and simple applications to magnetic and conduction problems. *J. Phys. Soc. Jap.*, 12(6):570–586, 1957.

[262] Fernando O. Raineri and Harold L. Friedman. Static transverse dielectric function of model molecular fluids. *J. Chem. Phys.*, 98(11):8910–8918, 1993.

[263] Paul Madden and Daniel Kivelson. A consistent molecular treatment of dielectric phenomena. In *Adv. Chem. Phys.*, page 467. John Wiley & Sons, Inc., 2007.

[264] Jean-Pierre Hansen and Ian R. McDonald. Chapter 11 - molecular liquids. In Jean-Pierre Hansen and Ian R. McDonald, editors, *Theory of Simple Liquids*, page 341. Academic Press, 3rd edition, 2006.

[265] Davide Bertolini and Alessandro Tani. The frequency and wavelength dependent dielectric permittivity of water. *Mol. Phys.*, 75(5):1065–1088, 1992.

[266] Leonor Saiz, Elvira Guárdia, and Joan-Ángel Padró. Dielectric properties of liquid ethanol. a computer simulation study. *J. Chem. Phys.*, 113 (7):2814–2822, 2000.

[267] Philippe A. Bopp, Alexei A. Kornyshev, and Godehard Sutmann. Frequency and wave-vector dependent dielectric function of water: Collective modes and relaxation spectra. *J. Chem. Phys.*, 109(5):1939, 1998.

[268] Fernando O. Raineri, Haluk Resat, and Harold L. Friedman. Static longitudinal dielectric function of model molecular fluids. *J. Chem. Phys.*, 96(4):3068–3084, 1992.

[269] Philippe A. Bopp, Alexei A. Kornyshev, and Godehard Sutmann. Frequency and wave-vector dependent dielectric function of water: Collective modes and relaxation spectra. *J. Chem. Phys.*, 109(5):1939–1958, 1998.

[270] Jon M. Sorenson, Greg Hura, Robert M. Glaeser, and Teresa Head-Gordon. What can x-ray scattering tell us about the radial distribution functions of water? *J. Chem. Phys.*, 113(20), 2000.

[271] A.A. Kornyshev and G. Sutmann. Nonlocal dielectric function of water: How strong are the effects of intramolecular charge form factors? *J. Mol. Liq.*, 82(12):151 – 160, 1999. Contributions to the Seminar on the Structure of Liquids and Liquid Solutions of the Russian Academy of Sciences.

[272] M.P. Tosi, A.A. Kornyšev, and International Centre for Theoretical Phys. *Condensed Matter Phys. Aspects of ElectroChem.: Proceedings of the Conference 27 August-9 September 1990 Ictp, Trieste, Italy*. World Scientific Publishing Company, Incorporated, 1991. ISBN 9789810205607.

[273] Dmitry V. Matyushov. Dipole solvation in dielectrics. *J. Chem. Phys.*, 120(3):1375–1382, 2004.

[274] O. V. Dolgov, D. A. Kirzhnits, and E. G. Maksimov. On an admissible sign of the static dielectric function of matter. *Rev. Mod. Phys.*, 53: 81–93, Jan 1981.

[275] M. Rovere, R. Miniero, M. Parrinello, and M. P. Tosi. Gas-liquid transition in charged fluids. *Physics and Chemistry of Liquids*, 9(1):11–22, 1979.

[276] O. V. Dolgov, D. A. Kirzhnits, and E. G. Maksimov. On an admissible sign of the static dielectric function of matter. *Rev. Mod. Phys.*, 53: 81–93, 1981.

[277] M.S. Skaf. Nonlocal dielectric functions of molecular liquids from computer simulations. *Journal of Molecular Structure: THEOCHEM*, 505 (13):45 – 53, 2000.

[278] Alexei A. Kornyshev and Godehard Sutmann. The shape of the nonlocal dielectric function of polar liquids and the implications for thermodynamic properties of electrolytes: A comparative study. *J. Chem. Phys.*, 104(4), 1996.

[279] B. Mennucci and R. Cammi. *Continuum Solvation Models in Chemical Physics: From Theory to Applications*. Wiley, 2008. ISBN 9780470515228.

[280] Kossakowski D.A. Kornyshev, A.A. and M.A. Vorotyntsev. *Condensed Matter Phys. Aspects of ElectroChem.: Proceedings of the Conference 27 August-9 September 1990 Ictp, Trieste, Italy*, chapter On the Analytical Properties of the Static Dielectric Function of Water. In Tosi et al. [272], 1991. ISBN 9789810205607.

[281] I. P. Omelyan. Wavevector dependent dielectric constant of the mcy water model. *Phys. Lett. A*, 220(13):167–177, 1996.

[282] A. Hildebrandt, R. Blossey, S. Rjasanow, O. Kohlbacher, and H.-P. Lenhof. Novel formulation of nonlocal electrostatics. *Phys. Rev. Lett.*, 93:108104, Sep 2004.

[283] Christian Schaaf and Stephan Gekle. Dielectric response of the water hydration layer around spherical solutes. *Phys. Rev. E*, 92:032718, Sep 2015.

[284] Mikhail V. Basilevsky and Drew F. Parsons. Nonlocal continuum solvation model with oscillating susceptibility kernels: A nonrigid cavity model. *J. Chem. Phys.*, 108(21), 1998.

[285] M. A. Ricci, D. Rocca, G. Ruocco, and R. Vallauri. Theoretical and computer-simulation study of the density fluctuations in liquid water. *Phys. Rev. A*, 40:7226–7238, Dec 1989.

[286] Haluk Resat, Fernando O. Raineri, and Harold L. Friedman. A dielectric theory of the opticallike highfrequency mode in liquid water. *J. Chem. Phys.*, 97(4):2618, 1992.

[287] Song-Ho Chong and Fumio Hirata. Interaction-site-model description of collective excitations in liquid water. ii: Comparison with simulation results. *J. Chem. Phys.*, 111(7):3095–3104, 1999.

[288] Song-Ho Chong and Fumio Hirata. Interaction-site-model description of collective excitations in liquid water. i: Theoretical study. *J. Chem. Phys.*, 111(7):3083–3094, 1999.

[289] R. H. Lyddane, R. G. Sachs, and E. Teller. On the polar vibrations of alkali halides. *Phys. Rev.*, 59:673–676, Apr 1941.

[290] A. J. Sievers and J. B. Page. Generalized Lyddane-Sachs-Teller relation and disordered solids. *Phys. Rev. B*, 41:3455–3459, Feb 1990.

[291] E. Whalley. A detailed assignment of the oh stretching bands of ice i. *Canadian journal of Chemistry*, 55(19):3429–3441, 1977.

[292] M.C. Payne and J.C. Inkson. Longitudinal-optic-transverse-optic vibrational mode splittings in tetrahedral network glasses. *journal of Non-Crystalline Solids*, 68(23):351 – 360, 1984.

[293] Ken Sekimoto and Takeo Matsubara. TO-LO splittings of glassy dielectrics. *Phys. Rev. B*, 26:3411, 1982.

[294] J. C. Decius and R. M. Hexter. *Molecular Vibrations in Crystals*. McGraw-Hill, USA, 1977.

[295] J. C. Decius. Dipolar coupling and molecular vibration in crystals. i. general theory. *J. Chem. Phys.*, 49(3):1387–1392, 1968.

[296] Hans Mueller. Theory of the photoelastic effect of cubic crystals. *Phys. Rev.*, 47:947–957, 1935.

[297] Christopher M. Burba and Roger Frech. Existence of optical phonons in the room temperature ionic liquid 1-ethyl-3-methylimidazolium trifluoromethanesulfonate. *J. Chem. Phys.*, 134(13):134503, 2011.

[298] G. E. Walrafen. Raman spectral studies of water structure. *J. Phys. Chem.*, 40(11):3249, 1964.

[299] G. E. Walrafen. Raman spectrum of water: transverse and longitudinal acoustic modes below ≈ 300 cm^{-1} and optic modes above ≈ 300 cm^{-1}. *J. Phys. Chem.*, 94(6):2237–2239, 1990.

[300] G. E. Walrafen. Raman spectral studies of the effects of temperature on water structure. *J. Phys. Chem.*, 47(1):114–126, 1967.

[301] G. E. Walrafen, M. R. Fisher, M. S. Hokmabadi, and W.H. Yang. Temperature dependence of the low and highfrequency Raman scattering from liquid water. *J. Chem. Phys.*, 85(12):6970–6982, 1986.

[302] E. W. Castner, Y. J. Chang, Y. C. Chu, and G. E. Walrafen. The intermolecular dynamics of liquid water. *J. Chem. Phys.*, 102(2):653–659, 1995.

[303] H. R. Zelsmann. Temperature dependence of the optical constants for liquid H_2O and D_2O in the far IR region. *J. Mol. Str.*, 350(2):95–114, 1995.

[304] P.F. Aure and A. Chosson. The translational lattice-vibration Raman spectrum of single crystal ice 1h. *J. Glaciology*, 21(85):65–71, 1978.

[305] D. D. Klug, J. S. Tse, and E. Whalley. The longitudinaloptictranverseoptic mode splitting in ice Ih. *J. Chem. Phys.*, 95(9):7011–7012, 1991.

[306] D. D. Klug and E. Whalley. Origin of the high-frequency translational bands of ice i*. *J. Glaciology*, 21(85):55–63, 1978.

[307] F. L. Galeener and G. Lucovsky. Longitudinal optical vibrations in glasses: GeO_2 and SiO_2. *Phys. Rev. Lett.*, 37:1474–1478, 1976.

[308] G. Bolla. Su alcune nuove bande Raman dellacqua. *Il Nuovo Cimento*, 10(3):101–107, 1933.

[309] George E. Walrafen. Raman spectral studies of the effects of electrolytes on water. *J. Chem. Phys.*, 36(4):1035–1042, 1962.

[310] Ral Fuentes-Azcatl and José Alejandre. Non-polarizable force field of water based on the dielectric constant: TIP4P/ε. *J. Phys. Chem. B*, 118(5):1263–1272, 2014.

[311] Junmei Wang, Romain M. Wolf, James W. Caldwell, Peter A. Kollman, Tx V, Junmei Wang, and Key Words. Development and testing of a general AMBER force field. *J. Compt. Chem.*, 25:1157, 2004.

[312] Carl Caleman, Paul J. van Maaren, Minyan Hong, Jochen S. Hub, Luciano T. Costa, and David van der Spoel. Force field benchmark of organic liquids: Density, enthalpy of vaporization, heat capacities, surface tension, isothermal compressibility, volumetric expansion coefficient, and dielectric constant. *J. Chem. Theo. Comp.*, 8(1):61, 2012.

[313] Rafael Ramrez, Telesforo Lpez-Ciudad, Padma Kumar P, and Dominik Marx. Quantum corrections to classical time-correlation functions: Hydrogen bonding and anharmonic floppy modes. *J. Chem. Phys.*, 121(9): 3973–3983, 2004.

[314] Matthias Heyden, Jian Sun, Harald Forbert, Gerald Mathias, Martina Havenith, and Dominik Marx. Understanding the origins of dipolar couplings and correlated motion in the vibrational spectrum of water. *J. Phys. Chem. Lett.*, 3(16):2135–2140, 2012.

[315] B. Bagchi and A. Chandra. Ultrafast solvation dynamics: Molecular explanation of computer simulation results in a simple dipolar solvent. *J. Chem. Phys.*, 97(7), 1992.

[316] L.A. Woodward. *Introduction to the theory of molecular vibrations and vibrational spectroscopy*. Clarendon Press, 1972.

[317] D. C. Elton and M.-V. Fernández-Serra. Polar nanoregions in water: A study of the dielectric properties of TIP4P/2005, TIP4P/2005f and TTM3F. *J. Chem. Phys.*, 140(12):124504, 2014.

[318] Robert Wagner, Stefan Benz, Ottmar Mhler, Harald Saathoff, Martin Schnaiter, and Ulrich Schurath. Mid-infrared extinction spectra and optical constants of supercooled water droplets. *J. Phys. Chem. A*, 109 (32):7099–7112, 2005.

[319] W. J. Ellison. Permittivity of pure water, at standard atmospheric pressure, over the frequency range 0-25 THz and the temperature range 0100c. *J. Phys. Chem. Ref.D at.*, 36(1):1–18, 2007.

[320] Kaoru Iwano, Tetsuya Yokoo, Mitsugu Oguro, and Susumu Ikeda. Propagating librations in ice xi: Model analysis and coherent inelastic neutron scattering experiment. *journal of the Physical Society of Japan*, 79(6): 063601, 2010.

[321] Takeshi Shigenari and Kohji Abe. Vibrational modes of hydrogens in the proton ordered phase XI of ice: Raman spectra above 400 cm^1. *J. Chem. Phys.*, 136(17):174504, 2012.

[322] Quan Wan, Leonardo Spanu, Giulia A. Galli, and Franois Gygi. Raman spectra of liquid water from ab initio molecular dynamics: Vibrational signatures of charge fluctuations in the hydrogen bond network. *J. Chem. Theo. Comp.*, 9(9):4124–4130, 2013.

[323] Michael. Haughney, Mauro. Ferrario, and Ian R. McDonald. Molecular-dynamics simulation of liquid methanol. *J. Phys. Chem.*, 91(19): 4934–4940, 1987.

[324] Toshio Yamaguchi, C. J. Benmore, and A. K. Soper. The structure of subcritical and supercritical methanol by neutron diffraction, empirical potential structure refinement, and spherical harmonic analysis. *J. Chem. Phys.*, 112(20):8976–8987, 2000.

[325] M. Matsumoto and K. E. Gubbins. Hydrogen bonding in liquid methanol. *J. Chem. Phys.*, 93(3):1981–1994, 1990.

[326] M. Maroncelli, P. V. Kumar, A. Papazyan, M. L. Horng, S. journal Rosenthal, and G. R. Fleming. Studies of the inertial component of polar solvation dynamics. *AIP Conference Proceedings*, 298(1):310, 1994.

[327] Gene A. Crowder and Bobby R. Cook. Acetonitrile: far-infrared spectra and chemical thermodynamic properties. discussion of an entropy discrepancy. *J. Phys. Chem.*, 71(4):914–916, 1967.

[328] Dean S. Venables, Allan Chiu, and Charles A. Schmuttenmaer. Structure and dynamics of nonaqueous mixtures of dipolar liquids. i. infrared and far-infrared spectroscopy. *J. Chem. Phys.*, 113(8):3243, 2000.

[329] Roberto Lobo, John E. Robinson, and Sergio Rodriguez. High frequency dielectric response of dipolar liquids. *J. Chem. Phys.*, 59(11):5992–6008, 1973.

[330] Roberto Lobo, Sergio Rodriguez, and John E. Robinson. Collective excitations of dipolar systems. *Phys. Rev.*, 161:513–525, Sep 1967.

[331] E. L. Pollock and B. journal Alder. Frequency-dependent dielectric response in polar liquids. *Phys. Rev. Lett.*, 46:950–953, Apr 1981.

[332] Igor P. Omelyan. Wavevector- and frequency-dependent dielectric constant of the stockmayer fluid. *Mol. Phys.*, 87(6):1273–1283, 1996.

[333] E Fatuzzo and P R Mason. A calculation of the complex dielectric constant of a polar liquid by the librating molecule method. *Proc. Phys. Soc.*, 90(3):729, 1967.

[334] R. Buchner, Barthel, and journal Stauber. Collective modes in dipolar liquids - detection of dipolar plasmons. *Chem. Phys. Lett.*, 39(1):23, 1976.

[335] A. Gerschel, T. Grochulski, Z. Kisiel, L. Pszczolkowski, and K. Leibler. High frequency rotational mode in liquid methyl chloride. *Mol. Phys.*, 54(1):97–117, 1985.

[336] M.N. Afsar, G.W. Chantry, J.R. Birch, and H. Kilp. Far-infrared reflection measurements on nitromethane and the relevance of the plasmon model. *Infr. Phys.*, 18(56):843 – 848, 1978.

[337] A. Chandra and B. Bagchi. Collective excitations in a dense dipolar liquid: How important are dipolarons in the polarization relaxation of common dipolar liquids? *J. Chem. Phys.*, 92(11):6833, 1990.

[338] B. Bagchi and A. Chandra. *Collective Orientational Relaxation in Dense Dipolar Liquids*. Number 80 in Adv. Chem. Phys. Wiley, 2009. ISBN 9780470141908.

[339] Felix Sedlmeier, Shahriar Shadkhoo, Robijn Bruinsma, and Roland R. Netz. Charge/mass dynamic structure factors of water and applications to dielectric friction and electroacoustic conversion. *J. Chem. Phys.*, 140 (5):054512, 2014.

[340] S. C. Santucci, D. Fioretto, L. Comez, A. Gessini, and C. Masciovecchio. Is there any fast sound in water? *Phys. Rev. Lett.*, 97:225701, Nov 2006.

[341] M. Sampoli, G. Ruocco, and F. Sette. Mixing of longitudinal and transverse dynamics in liquid water. *Phys. Rev. Lett.*, 79:1678–1681, Sep 1997.

[342] G. Garberoglio, R. Vallauri, and G. Sutmann. Instantaneous normal mode analysis of correlated cluster motions in hydrogen bonded liquids. *J. Chem. Phys.*, 117(7):3278–3288, 2002.

[343] Wayne B. Bosma, Laurence E. Fried, and Shaul Mukamel. Simulation of the intermolecular vibrational spectra of liquid water and water clusters. *J. Chem. Phys.*, 98(6):4413–4421, 1993.

[344] D. Bolmatov, V. V. Brazhkin, and K. Trachenko. The phonon theory of liquid thermodynamics. *Sci. Rep.*, 2:421, 2012.

[345] R. P. Feynman. Space-time approach to non-relativistic quantum mechanics. *Rev. Mod. Phys.*, 20:367–387, Apr 1948.

[346] R. P. Feynman. Atomic theory of the λ transition in helium. *Phys. Rev.*, 91:1291–1301, Sep 1953.

[347] David Chandler and Peter G. Wolynes. Exploiting the isomorphism between quantum theory and classical statistical mechanics of polyatomic fluids. *J. Chem. Phys.*, 74(7), 1981.

[348] M. Parrinello and A. Rahman. Study of an f center in molten kcl. *J. Chem. Phys.*, 80(2):860–867, 1984.

[349] Ian R. Craig and David E. Manolopoulos. Quantum statistics and classical mechanics: Real time correlation functions from ring polymer molecular dynamics. *J. Chem. Phys.*, 121(8), 2004.

[350] Alexander Witt, Sergei D. Ivanov, Motoyuki Shiga, Harald Forbert, and Dominik Marx. On the applicability of centroid and ring polymer path integral molecular dynamics for vibrational spectroscopy. *J. Chem. Phys.*, 130(19):194510, 2009.

[351] Randall W. Hall and B. J. Berne. Nonergodicity in path integral molecular dynamics. *J. Chem. Phys.*, 81(8), 1984.

[352] Tyler D. Hone, Peter J. Rossky, and Gregory A. Voth. A comparative study of imaginary time path integral based methods for quantum dynamics. *J. Chem. Phys.*, 124(15):154103, 2006.

[353] Scott Habershon, George S. Fanourgakis, and David E. Manolopoulos. Comparison of path integral molecular dynamics methods for the infrared absorption spectrum of liquid water. *J. Chem. Phys.*, 129(7): 074501, 2008.

[354] Jianshu Cao and Gregory A. Voth. A unified framework for quantum activated rate processes. i. general theory. *J. Chem. Phys.*, 105(16), 1996.

[355] Seogjoo Jang and Gregory A. Voth. Path integral centroid variables and the formulation of their exact real time dynamics. *J. Chem. Phys.*, 111 (6), 1999.

[356] Bastiaan J. Braams and David E. Manolopoulos. On the short-time limit of ring polymer molecular dynamics. *J. Chem. Phys.*, 125(12):124105, 2006.

[357] Francesco Paesani and Gregory A. Voth. Nonlinear quantum time correlation functions from centroid molecular dynamics and the maximum entropy method. *J. Chem. Phys.*, 129(19):194113, 2008.

[358] Gabriela S. Del Buono, Peter J. Rossky, and Jrgen Schnitker. Model dependence of quantum isotope effects in liquid water. *J. Chem. Phys.*, 95(5):3728–3737, 1991.

[359] J. Lobaugh and Gregory A. Voth. A quantum model for water: Equilibrium and dynamical properties. *J. Chem. Phys.*, 106(6), 1997.

[360] Dominik Marx and Martin H Mser. Path integral simulations of rotors: theory and applications. *journal of Physics: Condensed Matter*, 11(11): R117, 1999.

[361] Francesco Paesani and Gregory A. Voth. A quantitative assessment of the accuracy of centroid molecular dynamics for the calculation of the infrared spectrum of liquid water. *J. Chem. Phys.*, 132(1):014105, 2010.

[362] Matt Glover. *PhD Thesis : "Path Integral Computer Simulations of Liquid Water"*. PhD thesis, University of York, 2004.

[363] Jianshu Cao and Bruce J. Berne. On energy estimators in path integral monte carlo simulations:dependence of accuracy on algorithm. *J. Chem. Phys.*, 91(10), 1989.

[364] Motoyuki Shiga and Wataru Shinoda. Calculation of heat capacities of light and heavy water by path-integral molecular dynamics. *J. Chem. Phys.*, 123(13):134502, 2005.

[365] Michael Alexander Witt. *PhD Thesis*. PhD thesis, Ruhr University, 2012.

[366] C P Herrero and R Ramrez. Path-integral simulation of solids. *J. Phys. Cond. Matt.*, 26(23):233201, 2014.

[367] Robert A. Kuharski and Peter J. Rossky. A quantum mechanical study of structure in liquid H2O and D2O. *J. Chem. Phys.*, 82(11), 1985.

[368] A. Wallqvist and B.J. Berne. Path-integral simulation of pure water. *Chem. Phys. Lett.*, 117(3):214 – 219, 1985.

[369] Lisandro Hernndez de la Pea and Peter G. Kusalik. Quantum effects in liquid water and ice: Model dependence. *J. Chem. Phys.*, 125(5):054512, 2006.

[370] Nicholas Blinov and Pierre-Nicholas Roy. Connection between the observable and centroid structural properties of a quantum fluid:application to liquid para-hydrogen. *J. Chem. Phys.*, 120(8), 2004.

[371] Kahled Toukan and Aneesur Rahman. Molecular-dynamics study of atomic motions in water. *Phys. Rev. B*, 31:2643–2648, Mar 1985.

[372] Francesco Paesani, Soohaeng Yoo, Huib J. Bakker, and Sotiris S. Xantheas. Nuclear quantum effects in the reorientation of water. *J. Phys. Chem. Lett.*, 1(15):2316–2321, 2010.

[373] Thomas F. Miller and David E. Manolopoulos. Quantum diffusion in liquid water from ring polymer molecular dynamics. *J. Chem. Phys.*, 123(15):154504, 2005.

[374] Bertrand Guillot and Yves Guissani. Quantum effects in simulated water by the feynmanhibbs approach. *J. Chem. Phys.*, 108(24), 1998.

[375] Jens Aage Poulsen, Gunnar Nyman, and Peter J. Rossky. Static and dynamic quantum effects in molecular liquids: A linearized path integral description of water. *Proceedings of the National Academy of Sciences of the United States of America*, 102(19):6709–6714, 2005.

[376] Jian Liu, William H. Miller, Francesco Paesani, Wei Zhang, and David A. Case. Quantum dynamical effects in liquid water: A semiclassical study on the diffusion and the infrared absorption spectrum. *J. Chem. Phys.*, 131(16):164509, 2009.

[377] Lisandro Hernandez de la Pena and Peter G. Kusalik. Temperature dependence of quantum effects in liquid water. *journal of the American Chemical Society*, 127(14):5246–5251, 2005.

[378] Shuji Kawada. Dielectric dispersion and phase transition of koh doped ice. *journal of the Physical Society of Japan*, 32(5):1442–1442, 1972.

[379] Syuji Kawada. Dielectric properties of koh-doped D2O ice. *journal of the Physical Society of Japan*, 58(1):295–300, 1989.

[380] Syuji Kawada and Kazuki Shimura. Dielectric studies of rboh-doped ice and its phase transition. *journal of the Physical Society of Japan*, 55 (12):4485–4491, 1986.

[381] W.M. Haynes. *CRC Handbook of Chemistry and Physics, 93rd Edition*. CRC Handbook of Chemistry and Physics. Taylor & Francis, 2012. ISBN 9781439880494.

[382] R. Ramrez and C. P. Herrero. Quantum path integral simulation of isotope effects in the melting temperature of ice ih. *J. Chem. Phys.*, 133 (14):144511, 2010.

[383] Carl McBride, Juan L. Aragones, Eva G. Noya, and Carlos Vega. A study of the influence of isotopic substitution on the melting point and temperature of maximum density of water by means of path integral simulations of rigid models. *Phys. Chem. Chem. Phys.*, 14:15199–15205, 2012.

[384] B. Pamuk, J. M. Soler, R. Ramírez, C. P. Herrero, P. W. Stephens, P. B. Allen, and M.-V. Fernández-Serra. Anomalous nuclear quantum effects in ice. *Phys. Rev. Lett.*, 108:193003, May 2012.

[385] Francesco Paesani, Satoru Iuchi, and Gregory A. Voth. Quantum effects in liquid water from an ab initio-based polarizable force field. *J. Chem. Phys.*, 127(7), 2007.

[386] Robert P. Auty and Robert H. Cole. Dielectric properties of ice and solid D2O. *J. Chem. Phys.*, 20(8), 1952.

[387] G. P. Johari. The dielectric properties of H2O and D2O ice ih at mhz frequencies. *J. Chem. Phys.*, 64(10), 1976.

[388] Shuji Kawada. Dielectric properties of heavy ice ih (D2O ice). *J. Phys. Soc. Jap.*, 47(6):1850–1856, 1979.

[389] P.V. Hobbs. *Ice Physics*. Oxford Classic Texts in the Physical Sciences. 2010. ISBN 9780199587711.

[390] G. P. Johari and S. J. Jones. Dielectric properties of polycrystalline d_2o ice ih (hexagonal). *Proceedings of the Royal Society of London. A. Mathematical and Physical Sciences*, 349(1659):467–495, 1976.

[391] G. P. Johari and E. Whalley. The dielectric properties of ice ih in the range 272133 k. *J. Chem. Phys.*, 75(3), 1981.

[392] T. Matsuo. Calorimetric study of a phase transition in D2O ice ih doped with kod: Ice XI. *J. Phys. Chem. Sol.*, 47(2):165 – 173, 1986.

[393] George A. Vidulich, Douglas Fennell Evans, and Robert L. Kay. The dielectric constant of water and heavy water between 0 and 40.degree. *J. Phys. Chem.*, 71(3):656–662, 1967.

[394] Thomas R. Dyke and J. S. Muenter. Electric dipole moments of low j states of H2O and D2O. *J. Chem. Phys.*, 59(6), 1973.

[395] Shepard A. Clough, Yardley Beers, Gerald P. Klein, and Laurence S. Rothman. Dipole moment of water from stark measurements of H2O, hdo, and D2O. *J. Chem. Phys.*, 59(5):2254–2259, 1973.

[396] Shelley L. Shostak, William L. Ebenstein, and J. S. Muenter. The dipole moment of water. i. dipole moments and hyperfine properties of H2O and hdo in the ground and excited vibrational states. *J. Chem. Phys.*, 94(9): 5875–5882, 1991.

[397] L. G. Groves and S. Sugden. 221. the dipole moments of vapours. part ii. *J. Chem. Soc.*, pages 971–974, 1935.

[398] Robert L. Cook, Frank C. De Lucia, and Paul Helminger. Molecular force field and structure of water: Recent microwave results. *journal of Molecular Spectroscopy*, 53(1):62 – 76, 1974.

[399] J. Lobaugh and Gregory A. Voth. A quantum model for water: Equilibrium and dynamical properties. *J. Chem. Phys.*, 106(6), 1997.

[400] Francesco Paesani, Wei Zhang, David A. Case, Thomas E. Cheatham, and Gregory A. Voth. An accurate and simple quantum model for liquid water. *J. Chem. Phys.*, 125(18):184507, 2006.

[401] Harry A. Stern and B. J. Berne. Quantum effects in liquid water: Path-integral simulations of a flexible and polarizable ab initio model. *J. Chem. Phys.*, 115(16), 2001.

[402] Bin Chen, Ivaylo Ivanov, Michael L. Klein, and Michele Parrinello. Hydrogen bonding in water. *Phys. Rev. Lett.*, 91:215503, 2003.

[403] Joseph A. Morrone and Roberto Car. Nuclear quantum effects in water. *Phys. Rev. Lett.*, 101:017801, Jul 2008.

[404] Pedro Augusto Franco Pinheiro Moreira and Maurice de Koning. Nuclear quantum fluctuations in ice Ih. *Phys. Chem. Chem. Phys.*, pages 24716–21, 2015.

[405] R. P. Bell and I. E. Coop. The dipole moments of hydrogen and deuterium chlorides. *Trans. Faraday Soc.*, 34:1209–1214, 1938.

[406] C. W. Kern and R. L. Matcha. Nuclear corrections to electronic expectation values: Zeropoint vibrational effects in the water molecule. *J. Chem. Phys.*, 49(5):2081–2091, 1968.

[407] Jean-Joseph Max and Camille Chapados. Isotope effects in liquid water by infrared spectroscopy. iii. H2O and D2O spectra from 6000 to 0 cm^{-1}. *J. Chem. Phys.*, 131(18):184505, 2009.

[408] Ross H. McKenzie, Christiaan Bekker, Bijyalaxmi Athokpam, and Sai G. Ramesh. Effect of quantum nuclear motion on hydrogen bonding. *J. Chem. Phys.*, 140(17):174508, 2014.

[409] W. Kohn and L. J. Sham. Self-consistent equations including exchange and correlation effects. *Phys. Rev.*, 140:A1133–A1138, Nov 1965.

[410] Jue Wang, G. Romn-Pérez, Jose M. Soler, Emilio Artacho, and M.-V. Fernndez-Serra. Density, structure, and dynamics of water: The effect of van der waals interactions. *J. Chem. Phys.*, 134(2):024516, 2011.

[411] Fabiano Corsetti, Emilio Artacho, José M. Soler, S. S. Alexandre, and M.-V. Fernández-Serra. Room temperature compressibility and diffusivity of liquid water from first principles. *J. Chem. Phys.*, 139(19), 2013.

[412] Romain Jonchiere, Ari P. Seitsonen, Guillaume Ferlat, A. Marco Saitta, and Rodolphe Vuilleumier. Van der waals effects in ab initio water at ambient and supercritical conditions. *J. Chem. Phys.*, 135(15):154503, 2011.

[413] Jochen Schmidt, Joost Vande-Vondele, I.-F. William Kuo, Daniel Sebastiani, J. Ilja Siepmann, Jürg Hutter, and Christopher J. Mundy. Isobaricisothermal molecular dynamics simulations utilizing density functional theory: An assessment of the structure and density of water at near-ambient conditions. *J. Phys. Chem. B*, 113(35):11959–11964, 2009.

[414] Robert A. DiStasio, Biswajit Santra, Zhaofeng Li, Xifan Wu, and Roberto Car. The individual and collective effects of exact exchange and dispersion interactions on the ab initio structure of liquid water. *J. Chem. Phys.*, 141(8):084502, 2014.

[415] Alex P. Gaiduk, Franois Gygi, and Giulia Galli. Density and compressibility of liquid water and ice from first-principles simulations with hybrid functionals. *J. Phys. Chem. Lett.*, 6(15):2902–2908, 2015. PMID: 26267178.

[416] I-Chun Lin, Ari P. Seitsonen, Maurcio D. Coutinho-Neto, Ivano Tavernelli, and Ursula Rothlisberger. Importance of van der waals interactions in liquid water. *J. Phys. Chem. B*, 113(4):1127–1131, 2009.

[417] Elvira Guardia, Ioannis Skarmoutsos, and Marco Masia. Hydrogen bonding and related properties in liquid water: A carparrinello molecular dynamics simulation study. *J. Phys. Chem. B*, 119(29):8926–8938, 2015.

[418] Giacomo Miceli, Stefano de Gironcoli, and Alfredo Pasquarello. Isobaric first-principles molecular dynamics of liquid water with nonlocal van der waals interactions. *J. Chem. Phys.*, 142(3):034501, 2015.

[419] Cui Zhang, Jun Wu, Giulia Galli, and Franois Gygi. Structural and vibrational properties of liquid water from van der waals density functionals. *J. Chem. Theo. Comp.*, 7(10):3054–3061, 2011.

[420] Andreas Mogelhoj, André K. Kelkkanen, K. Thor Wikfeldt, Jakob Schiotz, Jens Jorgen Mortensen, Lars G. M. Pettersson, Bengt I. Lundqvist, Karsten W. Jacobsen, Anders Nilsson, and Jens K. Norskov. Ab initio van der waals interactions in simulations of water alter structure from mainly tetrahedral to high-density-like. *J. Phys. Chem. B*, 115 (48):14149–14160, 2011.

[421] Michael J. Gillan, Dario Alfé, and Angelos Michaelides. Perspective: How good is DFT for water? *J. Chem. Phys.*, 144(13), 2016.

[422] Michele Ceriotti, Wei Fang, Peter G. Kusalik, Ross H. McKenzie, Angelos Michaelides, Miguel A. Morales, and Thomas E. Markland. Nuclear quantum effects in water and aqueous systems: Experiment, theory, and current challenges. *Chem. Rev.*, 116(13):7529–7550, 2016.

[423] Scott Habershon, Thomas E. Markland, and David E. Manolopoulos. Competing quantum effects in the dynamics of a flexible water model. *J. Chem. Phys.*, 131(2):024501, 2009.

[424] Xin-Zheng Li, Brent Walker, and Angelos Michaelides. Quantum nature of the hydrogen bond. *Proceedings of the National Academy of Sciences*, 108(16):6369–6373, 2011.

[425] Anita Zeidler, Philip S. Salmon, Henry E. Fischer, Jörg C. Neuefeind, J. Mike Simonson, Hartmut Lemmel, Helmut Rauch, and Thomas E. Markland. Oxygen as a site specific probe of the structure of water and oxide materials. *Phys. Rev. Lett.*, 107:145501, Sep 2011.

[426] Thomas E. Markland and B. J. Berne. Unraveling quantum mechanical effects in water using isotopic fractionation. *Proceedings of the National Academy of Sciences*, 109(21):7988–7991, 2012.

[427] Giovanni Romanelli, Michele Ceriotti, David E. Manolopoulos, Claudia Pantalei, Roberto Senesi, and Carla Andreani. Direct measurement of competing quantum effects on the kinetic energy of heavy water upon melting. *J. Phys. Chem. Lett.*, 4(19):3251–3256, 2013.

[428] W. F. Kuhs and M. S. Lehmann. Bond-lengths, bond angles and transition barrier in ice Ih by neutron scattering. *Nature*, 294(5840):432–434, 1981.

[429] Mariana Rossi, Wei Fang, and Angelos Michaelides. Stability of complex biomolecular structures: van der waals, hydrogen bond cooperativity, and nuclear quantum effects. *J. Phys. Chem. Lett.*, 6(21):4233–4238, 2015.

[430] L.D. Landau and E.M. Lifshitz. *Statistical Physics*. Number v. 5. Pergamon Press, 1969.

[431] Sriram Ganeshan, R. Ramírez, and M. V. Fernández-Serra. Simulation of quantum zero-point effects in water using a frequency-dependent thermostat. *Phys. Rev. B*, 87:134207, Apr 2013.

[432] David Chandler and Peter G. Wolynes. Exploiting the isomorphism between quantum theory and classical statistical mechanics of polyatomic fluids. *J. Chem. Phys.*, 74(7):4078–4095, 1981.

[433] Lukasz Walewski, Harald Forbert, and Dominik Marx. Quantum induced bond centering in microsolvated HCl: Solvent separated versus contact ion pairs. *J. Phys. Chem. Lett.*, 2(24):3069–3074, 2011.

[434] Nicholas Guggemos, Petr Slavíček, and Vitaly V. Kresin. Electric dipole moments of nanosolvated acid molecules in water clusters. *Phys. Rev. Lett.*, 114:043401, Jan 2015.

[435] Federico Giberti, Ali A. Hassanali, Michele Ceriotti, and Michele Parrinello. The role of quantum effects on structural and electronic fluctuations in neat and charged water. *J. Phys. Chem. B*, 118(46):13226–13235, 2014.

[436] Ji Chen, Xin-Zheng Li, Qianfan Zhang, Angelos Michaelides, and Enge Wang. Nature of proton transport in a water-filled carbon nanotube and in liquid water. *Phys. Chem. Chem. Phys.*, 15:6344–6349, 2013.

[437] Thomas E. Markland, Scott Habershon, and David E. Manolopoulos. Quantum diffusion of hydrogen and muonium atoms in liquid water and hexagonal ice. *J. Chem. Phys.*, 128(19):194506, 2008.

[438] Sergei D. Ivanov, Ian M. Grant, and Dominik Marx. Quantum free energy landscapes from ab initio path integral metadynamics: Double proton transfer in the formic acid dimer is concerted but not correlated. *J. Chem. Phys.*, 143(12):124304, 2015.

[439] Lu Wang, Stephen D. Fried, Steven G. Boxer, and Thomas E. Markland. Quantum delocalization of protons in the hydrogen-bond network of an enzyme active site. *Proceedings of the National Academy of Sciences*, 111(52):18454–18459, 2014.

[440] Jingzhi Pu, Jiali Gao, and Donald G. Truhlar. Multidimensional tunneling, recrossing, and the transmission coefficient for enzymatic reactions. *Chem. Rev.*, 106(8):3140–3169, 2006.

[441] Christof Drechsel-Grau and Dominik Marx. Quantum simulation of collective proton tunneling in hexagonal ice crystals. *Phys. Rev. Lett.*, 112: 148302, Apr 2014.

[442] Alejandro Pérez, Mark E. Tuckerman, Harold P. Hjalmarson, and O. Anatole von Lilienfeld. Enol tautomers of watsoncrick base pair models are metastable because of nuclear quantum effects. *journal of the American Chemical Society*, 132(33):11510–11515, 2010.

[443] Jeremy O. Richardson, Cristóbal Pérez, Simon Lobsiger, Adam A. Reid, Berhane Temelso, George C. Shields, Zbigniew Kisiel, David J. Wales, Brooks H. Pate, and Stuart C. Althorpe. Concerted hydrogen-bond breaking by quantum tunneling in the water hexamer prism. *Science*, 351(6279):1310–1313, 2016.

[444] Pablo E. Videla, Peter J. Rossky, and D. Laria. Communication: Isotopic effects on tunneling motions in the water trimer. *J. Chem. Phys.*, 144 (6):061101, 2016.

[445] Jeremy O. Richardson, David J. Wales, Stuart C. Althorpe, Ryan P. McLaughlin, Mark R. Viant, Orion Shih, and Richard J. Saykally. Investigation of terahertz vibrationrotation tunneling spectra for the water octamer. *J. Phys. Chem. A*, 117(32):6960–6966, 2013.

[446] Jeremy O. Richardson, Stuart C. Althorpe, and David J. Wales. Instanton calculations of tunneling splittings for water dimer and trimer. *J. Chem. Phys.*, 135(12):124109, 2011.

[447] Thomas Spura, Hossam Elgabarty, and Thomas D. Kuhne. On-the-fly coupled cluster path-integral molecular dynamics: impact of nuclear

quantum effects on the protonated water dimer. *Phys. Chem. Chem. Phys.*, 17:14355–14359, 2015.

[448] Alexander Witt, Sergei D. Ivanov, and Dominik Marx. *High Performance Computing in Science and Engineering, Garching/Munich 2009: Transactions of the Fourth Joint HLRB and KONWIHR Review and Results Workshop, Dec. 8-9, 2009, Leibniz Supercomputing Centre, Garching/Munich, Germany*, chapter Ab Initio Path Integral Simulations of Floppy Molecular Systems, pages 675–686. Springer Berlin Heidelberg, Berlin, Heidelberg, 2010. ISBN 978-3-642-13872-0.

[449] Yu Kay Law and Ali A. Hassanali. Role of quantum vibrations on the structural, electronic, and optical properties of 9-methylguanine. *J. Phys. Chem. A*, 119(44):10816–10827, 2015.

[450] Rafael Ramírez, Carlos P. Herrero, and Eduardo R. Hernández. Path-integral molecular dynamics simulation of diamond. *Phys. Rev. B*, 73: 245202, Jun 2006.

[451] Changming Fang, Wun-Fan Li, Rik S. Koster, Jiri Klimes, Alfons van Blaaderen, and Marijn A. van Huis. The accurate calculation of the band gap of liquid water by means of gw corrections applied to plane-wave density functional theory molecular dynamics simulations. *Phys. Chem. Chem. Phys.*, 17:365–375, 2015.

[452] C. Vega, M. M. Conde, C. McBride, J. L. F. Abascal, E. G. Noya, R. Ramirez, and L. M. Sesé. Heat capacity of water: A signature of nuclear quantum effects. *J. Chem. Phys.*, 132(4):046101, 2010.

[453] Jan Kessler, Hossam Elgabarty, Thomas Spura, Kristof Karhan, Pouya Partovi-Azar, Ali A. Hassanali, and Thomas D. Khne. Structure and dynamics of the instantaneous water/vapor interface revisited by path-integral and ab initio molecular dynamics simulations. *J. Phys. Chem. B*, 119(31):10079–10086, 2015.

[454] Yuki Nagata, Ruben E. Pool, Ellen H. G. Backus, and Mischa Bonn. Nuclear quantum effects affect bond orientation of water at the water-vapor interface. *Phys. Rev. Lett.*, 109:226101, Nov 2012.

[455] Animesh Agarwal and Luigi Delle Site. Path integral molecular dynamics within the grand canonical-like adaptive resolution technique: Simulation of liquid water. *J. Chem. Phys.*, 143(9):094102, 2015.

[456] Sebastian Fritsch, Raffaello Potestio, Davide Donadio, and Kurt Kremer. Nuclear quantum effects in water: A multiscale study. *J. Chem. Theo. Comp.*, 10(2):816–824, 2014.

[457] Chris John, Thomas Spura, Scott Habershon, and Thomas D Kühne. Quantum ring-polymer contraction method: Including nuclear quantum effects at no additional computational cost in comparison to ab-initio molecular dynamics. 2015.

[458] Thomas Spura, Christopher John, Scott Habershon, and Thomas D. Khne. Nuclear quantum effects in liquid water from path-integral simulations using an ab initio force-matching approach. *Molecular Physics*, 113(8):808–822, 2015.

[459] Mariana Rossi, Michele Ceriotti, and David E. Manolopoulos. How to remove the spurious resonances from ring polymer molecular dynamics. *J. Chem. Phys.*, 140(23):234116, 2014.

[460] Harry Partridge and David W. Schwenke. The determination of an accurate isotope dependent potential energy surface for water from extensive ab initio calculations and experimental data. *J. Chem. Phys.*, 106(11): 4618–4639, 1997.

[461] M. Tuckerman, B. J. Berne, and G. J. Martyna. Reversible multiple time scale molecular dynamics. *J. Chem. Phys.*, 97(3):1990–2001, 1992.

[462] Joseph A. Morrone, Thomas E. Markland, Michele Ceriotti, and B. J. Berne. Efficient multiple time scale molecular dynamics: Using colored noise thermostats to stabilize resonances. *J. Chem. Phys.*, 134(1):014103, 2011.

[463] Michele Ceriotti, Michele Parrinello, Thomas E. Markland, and David E. Manolopoulos. Efficient stochastic thermostatting of path integral molecular dynamics. *J. Chem. Phys.*, 133(12):124104, 2010.

[464] Thomas E. Markland and David E. Manolopoulos. An efficient ring polymer contraction scheme for imaginary time path integral simulations. *J. Chem. Phys.*, 129(2):024105, 2008.

[465] George S. Fanourgakis, Thomas E. Markland, and David E. Manolopoulos. A fast path integral method for polarizable force fields. *J. Chem. Phys.*, 131(9):094102, 2009.

[466] Ryan P. Steele. Multiple-timestep ab initio molecular dynamics using an atomic basis set partitioning. *J. Phys. Chem. A*, 119(50):12119–12130, 2015.

[467] Nathan Luehr, Thomas E. Markland, and Todd J. Martínez. Multiple time step integrators in *ab initio* molecular dynamics. *J. Chem. Phys.*, 140(8), 2014.

[468] Eduardo Anglada, Javier Junquera, and José M. Soler. Efficient mixed-force first-principles molecular dynamics. *Phys. Rev. E*, 68:055701, 2003.

[469] Ondrej Marsalek and Thomas E. Markland. Ab initio molecular dynamics with nuclear quantum effects at classical cost: Ring polymer contraction for density functional theory. *J. Chem. Phys.*, 144(5):054112, 2016.

[470] Xiaolu Cheng, Jonathan D. Herr, and Ryan P. Steele. Accelerating ab initio path integral simulations via imaginary multiple-timestepping. *J. Chem. Theo. Comp.*, 2016. PMID: 26966920.

[471] V. Kapil, J. VandeVondele, and M. Ceriotti. Accurate molecular dynamics and nuclear quantum effects at low cost by multiple steps in real and imaginary time: Using density functional theory to accelerate wavefunction methods. *J. Chem. Phys.*, 144(5):054111, 2016.

[472] Hua Y. Geng. Accelerating ab initio path integral molecular dynamics with multilevel sampling of potential surface. *journal of Computational Physics*, 283:299 – 311, 2015.

[473] Rafael Ramírez, Telesforo López-Ciudad, Padma Kumar P, and Dominik Marx. Quantum corrections to classical time-correlation functions: Hydrogen bonding and anharmonic floppy modes. *J. Chem. Phys.*, 121(9): 3973–3983, 2004.

[474] B. Pamuk, J. M. Soler, R. Ramírez, C. P. Herrero, P. W. Stephens, P. B. Allen, and M.-V. Fernández-Serra. Anomalous nuclear quantum effects in ice. *Phys. Rev. Lett.*, 108:193003, May 2012.

[475] John P. Perdew, Kieron Burke, and Matthias Ernzerhof. Generalized gradient approximation made simple. *Phys. Rev. Lett.*, 77:3865–3868, 1996.

[476] Kristian Berland and Per Hyldgaard. Exchange functional that tests the robustness of the plasmon description of the van der waals density functional. *Phys. Rev. B*, 89:035412, Jan 2014.

[477] M. Dion, H. Rydberg, E. Schröder, D. C. Langreth, and B. I. Lundqvist. Van der waals density functional for general geometries. *Phys. Rev. Lett.*, 92:246401, Jun 2004.

[478] M. Mandel and P. Mazur. *Physica*, 22:116, 1958.

[479] David Fox and Robert M. Hexter. Crystal shape dependence of exciton states in molecular crystals. *J. Chem. Phys.*, 41(4):1125–1139, 1964.

[480] F. W. de Wette and G. E. Schacher. Internal field in general dipole lattices. *Phys. Rev.*, 137:A78–A91, Jan 1965.

Appendix A

Relation of crystal shape & structure to LO-TO splitting

The following sections contain a pedagogical derivation of eqn 10.6, which relates LO-TO splitting to crystal geometry. The treatment is completely classical. We assume our system is a system of point dipoles on a lattice. Each dipole has a permanent dipole moment $\boldsymbol{m}$ and a polarizability $\boldsymbol{\alpha}$. The relation between LO-TO splitting and crystal structure is complicated and unfortunately not 1-to-1 – many different crystal structures may be consistent with any level of LO-TO splitting.

A.0.1 Energy of the dipolar crystal

An expression for the energy of a system of polarizable dipoles in an applied field was derived by Mandel and Mazur in 1958.[478] Although we are interested in the case when the applied field is zero, we perform the derivation with the applied field because the results are interesting. For our case we assume the polarizability tensor $\boldsymbol{\alpha}$ is isotropic. We assume we have an applied field $\boldsymbol{\mathcal{E}}_0$. In what follows we drop the bold notation on all of the vectors and matrices. We introduce the following vectors: $p \equiv (\boldsymbol{p}_1, \boldsymbol{p}_2, \cdots, \boldsymbol{p}_N)$, a vector of length $3N$, and $E_0 \equiv (\boldsymbol{\mathcal{E}}_1, \boldsymbol{\mathcal{E}}_2, \cdots \boldsymbol{\mathcal{E}}_N)$, a vector of the applied electric field, also of length $3N$. When a vector appears to the right of a matrix it is understood to be a column vector, and when on the left, a row vector. We also introduce

the following matrices:

$$T \equiv \begin{bmatrix} 0 & \boldsymbol{T}_{12} & \boldsymbol{T}_{13} & \cdots \\ \boldsymbol{T}_{21} & 0 & \boldsymbol{T}_{23} & \cdots \\ \boldsymbol{T}_{31} & \boldsymbol{T}_{32} & 0 & \cdots \\ \vdots & \vdots & \vdots & 0 \end{bmatrix} \alpha \equiv \begin{bmatrix} \boldsymbol{\alpha} & 0 & 0 & \cdots \\ 0 & \boldsymbol{\alpha} & 0 & \cdots \\ 0 & 0 & \boldsymbol{\alpha} & \cdots \\ \vdots & \vdots & \vdots & \boldsymbol{\alpha} \end{bmatrix} \quad I \equiv \begin{bmatrix} 1 & 0 & 0 & \cdots \\ 0 & 1 & 0 & \cdots \\ 0 & 0 & 1 & \cdots \\ \vdots & \vdots & \vdots & 1 \end{bmatrix} \tag{A.1}$$

Then the equation for the dipole moments is:

$$p = m + \alpha(E_0 - Tp) \tag{A.2}$$

This leads to

$$\begin{aligned} p + \alpha T p &= m + \alpha E_0 \\ p &= (I + \alpha T)^{-1}(m + \alpha E_0) \\ p &= (I + \alpha T)^{-1} m + (I + \alpha T)^{-1} \alpha E_0 \\ p &= p_0 + A E_0 \end{aligned} \tag{A.3}$$

Where we define

$$p_0 \equiv (I + \alpha T)^{-1} m \tag{A.4}$$

$$A \equiv \alpha (I + \alpha T)^{-1} \tag{A.5}$$

Mandel & Mazur employ a very non-obvious identity:

$$(I + \alpha T)^{-1} = I - AT = I - TA \tag{A.6}$$

They then compute the local field, F:

$$\begin{aligned} F &= E_0 - Tp \\ &= E_0 - T(p_0 + AE_0) \quad \text{using eqn. A.3} \\ &= (I - TA)E_0 - Tp_0 \quad \text{using eqns. A.6 \& A.5} \end{aligned} \tag{A.7}$$

leading to:

$$F = \alpha^{-1} A E_0 - T p_0 \tag{A.8}$$

We are now in a position to compute the electrostatic part of the energy of the system. The electrostatic energy is broken into three parts:

$$V_{\text{el}} = V_{\text{in}} + V_{\text{dip}} + V_{\text{E}_0} \tag{A.9}$$

here V_{in} is the "internal" energy of the polarization dipoles, V_{dip} is the the dipole-dipole interaction energy, and V_{E_0} is the interaction energy of the system

with the electric field.

The internal energy is:

$$\begin{aligned} V_{\text{int}} &= \sum_j \int_{m_j}^{p_j} F_j \cdot dp_j = \sum_j \alpha \int_0^{F_j} F_j \cdot dF_j \\ &= \frac{1}{2}\alpha(E_0 - Tp)^2 \\ &= \frac{1}{2}\alpha^{-1}(AE_0 - Tp_0)^2 \quad \text{Using A.8} \\ &= \frac{1}{2}\alpha p_0 T^2 p_0 - E_0 A T p_0 + \frac{1}{2}\alpha^{-1} E_0 A^2 E_0 \end{aligned} \tag{A.10}$$

The dipole-dipole energy, $V_{\text{dip}} = \frac{1}{2}pTp$ is found to be:

$$V_{\text{dip}} = \frac{1}{2}p_0 T p_0 + p_0 T A E_0 + \frac{1}{2}ATAE_0 \tag{A.11}$$

When one sums the internal energy and the dipole energy there is a cancellation of terms, leading to:

$$V_{\text{int}} + V_{\text{dip}} = \frac{1}{2}mTp_0 + \frac{1}{2}E_0 A E_0 \tag{A.12}$$

The energy due to interaction with the applied field is

$$V_{\text{E}_0} = -pE_0 \tag{A.13}$$

When we sum up all three energy terms and do some simplification we get:

$$V_{\text{el}} = \frac{1}{2}mTp_0 - p_0 E_0 - \frac{1}{2}E_0 A E_0 \tag{A.14}$$

When the applied field E_0 is zero, the energy of the system is:

$$V_{\text{el}}^0 = \frac{1}{2}mTp_0 = \frac{1}{2}mT(I + \alpha T)^{-1}m \tag{A.15}$$

A.0.2 The frequency shift

We now can compute the *frequency shift* of a dipolar molecule, that is, the shift when the molecule is moved from the gas phase to the solid phase.[295] We are interested in the $k = 0$ case. In this case *all of the dipole moments are equal in magnitude and direction.* As we will see, in general the shift will

be different depending whether the dipolar wave travels in the longitudinal or transverse direction.

Single molecule per unit cell

As before, we store all of the dipole moments in a vector of length 3N $\mu = (\boldsymbol{\mu}_1, \boldsymbol{\mu}_2, \cdots \boldsymbol{\mu}_N,)$ We expand the dipole moment vector in terms of the unit cell normal coordinates:

$$\mu = \mu_0 + \sum_k Q_k \frac{\partial \mu}{\partial Q_k} \tag{A.16}$$

We now look for the term in the expansion of the potential energy $\frac{1}{2} m T p_0$ (eqn. A.15) which is quadratic with respect to the normal coordinates. This term is :

$$V = \frac{1}{2} \sum_k \frac{\partial \mu}{\partial Q_k} T (I + \alpha T)^{-1} \frac{\partial \mu}{\partial Q_k} Q_k^2 \tag{A.17}$$

The entire problem reduces to finding the energy given in eqn. A.15. We use the index t to label the lattice sites - in otherwords, it labels 3x3 blocks in the matrix T. The problem reduces to calculating the sum:

$$\sum_{t't''} T_{tt'} (I + \alpha T)^{-1}_{t't''} \tag{A.18}$$

Since all of the sites are identical, we only need to consider the sum over t'' for fixed t'. Note that we can perform a Taylor expansion:

$$(I + \alpha T)^{-1} = I - \alpha T + \alpha^2 T^2 - \alpha^3 T^3 \cdots \tag{A.19}$$

Thus we can write:

$$\sum_{t''} (I + \alpha T)^{-1}_{t't''} = I_3 - \alpha S + \alpha^2 S^2 - \alpha^3 S^3 \cdots \tag{A.20}$$

Where we have defined the 3x3 matrix $\boldsymbol{S}$:

$$\boldsymbol{S} \equiv \sum_{t''} T_{t't''} \tag{A.21}$$

Simple cubic lattice, shape dependence

In the case of a simple cubic lattice, it is well known that the the summation $\sum_{t''}$ vanishes and *only depends on the shape of the boundary.* One possible

choice is to consider an infinite slab, with the boundary consisting of two planes parallel to the x and y axes. This geometry allows us to distinguish two types of phonons in the $k = 0$ limit: "longitudinal phonons" travel along x and y and transverse phonons travel along z. Then one finds:[479]

$$\boldsymbol{S} \equiv \frac{4\pi n}{3} \begin{bmatrix} -1 & 0 & 0 \\ 0 & -1 & 0 \\ 0 & 0 & 2 \end{bmatrix} \tag{A.22}$$

Where n is the "number density" $n = N/V = 1/v$. For transverse phonons, the shift in the energy is:

$$\frac{1}{2}\boldsymbol{S}_z(1+\alpha\boldsymbol{S}_z)^{-1}\left(\frac{\partial\boldsymbol{\mu}}{\partial Q_k}\right)Q_k^2 = (4\pi n/3)(1-4\pi n\alpha/3)^{-1}\left(\frac{\partial\boldsymbol{\mu}}{\partial Q_k}\right)^2 Q_k^2 \tag{A.23}$$

For longitudinal phonons it is

$$\frac{1}{2}\boldsymbol{S}_x(1+\alpha\boldsymbol{S}_x)^{-1}\left(\frac{\partial\boldsymbol{\mu}}{\partial Q_k}\right)Q_k^2 = (8\pi n/3)(1+8\pi n\alpha/3)^{-1}\left(\frac{\partial\boldsymbol{\mu}}{\partial Q_k}\right)^2 Q_k^2 \tag{A.24}$$

The frequency shifts are:

$$\begin{aligned} \omega_T^2 &= \omega_0^2 - (4\pi n/3)(1-4\pi n\alpha/3)^{-1}\left(\frac{\partial\boldsymbol{\mu}}{\partial Q_k}\right)^2 \\ \omega_L^2 &= \omega_0^2 + (8\pi n/3)(1+8\pi n\alpha/3)^{-1}\left(\frac{\partial\boldsymbol{\mu}}{\partial Q_k}\right)^2 \end{aligned} \tag{A.25}$$

The frequency splitting is:

$$\omega_L^2 - \omega_T^2 = \frac{4\pi n}{3}\left(2(1-4\pi n\alpha/3)^{-1} - (1+8\pi n\alpha/3)^{-1}\right)\left(\frac{\partial\boldsymbol{\mu}}{\partial Q_k}\right)^2 \tag{A.26}$$

In the case where the molecules have zero polarizability this formula simplifies to :

$$\boxed{\omega_L^2 - \omega_T^2 = \frac{4\pi n}{3}\left(\frac{\partial\boldsymbol{\mu}}{\partial Q_k}\right)^2} \tag{A.27}$$

This equation assumed the crystal has the shape of a plane (finite in the z direction and infinite in the x and y directions). More generally, one can

consider crystals that are ellipsoids. In that case $\boldsymbol{S}$ takes the form:[294][479]

$$\boldsymbol{S} \equiv \frac{4\pi g}{3v} \begin{bmatrix} -1 & 0 & 0 \\ 0 & -1 & 0 \\ 0 & 0 & 2 \end{bmatrix} \tag{A.28}$$

the formula is modified to:

$$\omega_L^2 - \omega_T^2 = \frac{4\pi g}{3v} \left(\frac{\partial \boldsymbol{\mu}}{\partial Q_k} \right)^2 \tag{A.29}$$

Here g is a factor that depends on the ratio c/a. *In the case of a spherical crystal ($c/a = 1$), $g = 0$ and the splitting disappears.*[479, 294] Ignoring the effects of polarizability simplifies the analysis by removing the term $(1 + \alpha \boldsymbol{S})^{-1} \equiv \boldsymbol{B}$. The equation for the splitting becomes:

$$\omega_L^2 - \omega_T^2 = \frac{4\pi n}{3}(S_{zz} - S_{xx}) \left(\frac{\partial \boldsymbol{\mu}}{\partial Q_k} \right)^2 \tag{A.30}$$

Non cubic simple lattices

We now consider non-cubic lattices, again with one dipole per unit cell. We assume the crystals have a spherical shape, that is , we perform our sum in a spherical region and let $L \to 0$. In general the sum in this sphere will not be equal to zero as it would be in the case of a simple cubic lattice. However, for certain symmetry groups, the matrix $\boldsymbol{S}$ will be diagonal. According to Decius, these are the groups C_n with $n > 3$, D_n, C_{nv}, C_{nh} with $n > 3$ D_{nh}, D_{nd} and Sn. For primitive tetragonal or hexagonal lattices, the appropriate sums have been evaluated by Mueller (1935),[296] who reports the "Lorentz factors" L_x, L_y and L_z for simple tetragonal lattices. Lorentz factors are defined by the equation:

$$F_i = E_{0i} + 4\pi L_i P_i \qquad i = x, y, z \tag{A.31}$$

Where $\boldsymbol{F}$ is the local field and $\boldsymbol{E}_0$ is the applied field. This relation assumes that the dipole moments are parallel to the applied field. Decius gives the relations between L_x, L_y and L_z and S_{xx}, S_{yy} and S_{zz}. If k is parallel to z, then

$$\begin{aligned} S_{xx} &= S_{yy} = -4\pi n L_x \\ S_{zz} &= -4\pi n (L_z - 1) \end{aligned} \tag{A.32}$$

If k is perpendicular to z then

$$\begin{aligned} S_{xx} &= -4\pi n(L_x - 1) \\ S_{yy} &= -4\pi n L_y \\ S_{zz} &= -4\pi n L_z \end{aligned} \tag{A.33}$$

A method of efficiently calculating Lorentz factors (internal fields) using rapidly converging sums for lattices of arbitrary symmetry is explained by de Wette and Schacher (1965).[480]

Extension to lattices with a basis

The above theory can be generalized to lattices with a basis - ie. with more than one dipole per unit cell. To accommodate this we use the indices t, t' and t'' to label unit cells. Let us assume m molecules per unit cell. Then A and T become $3mN$x$3mN$, where N is now the number of unit cells. The 3x3 polarizability matrix $\boldsymbol{\alpha}$ becomes a $3m$x$3m$ polarizability matrix for the entire cell. The 3x3 dipole interaction tensors $\boldsymbol{T}$ are replaced with $3m$x$3m$ tensors of the form:

$$\boldsymbol{T}_{t't'} = \begin{bmatrix} \boldsymbol{T}_{11} & \boldsymbol{T}_{12} & \boldsymbol{T}_{13} & \cdots \\ \boldsymbol{T}_{21} & \boldsymbol{T}_{22} & \boldsymbol{T}_{23} & \cdots \\ \boldsymbol{T}_{31} & \boldsymbol{T}_{32} & \boldsymbol{T}_{33} & \cdots \\ \vdots & \vdots & \vdots & \boldsymbol{T}_{mm} \end{bmatrix}_{t,t'} \tag{A.34}$$

where $(\boldsymbol{T}_{ij})_{t't''}$ gives the interaction between a molecule of type i in unit cell t' with a molecule of type j in unit cell t''. The $\boldsymbol{S}$ matrix likewise becomes $3m$x$3m$ and takes the form:

$$\boldsymbol{S}_{t't'} = \begin{bmatrix} \boldsymbol{S}_{11} & \boldsymbol{S}_{12} & \boldsymbol{S}_{13} & \cdots \\ \boldsymbol{S}_{21} & \boldsymbol{S}_{22} & \boldsymbol{S}_{23} & \cdots \\ \boldsymbol{S}_{31} & \boldsymbol{S}_{32} & \boldsymbol{S}_{33} & \cdots \\ \vdots & \vdots & \vdots & \boldsymbol{S}_{mm} \end{bmatrix}_{t,t'} \tag{A.35}$$

If the symmetry class of the crystal falls into one of the classes mentioned in section A.0.2, then each of the submatrices $\boldsymbol{S}_{ij}$ will be diagonal.

Appendix B

RDFs

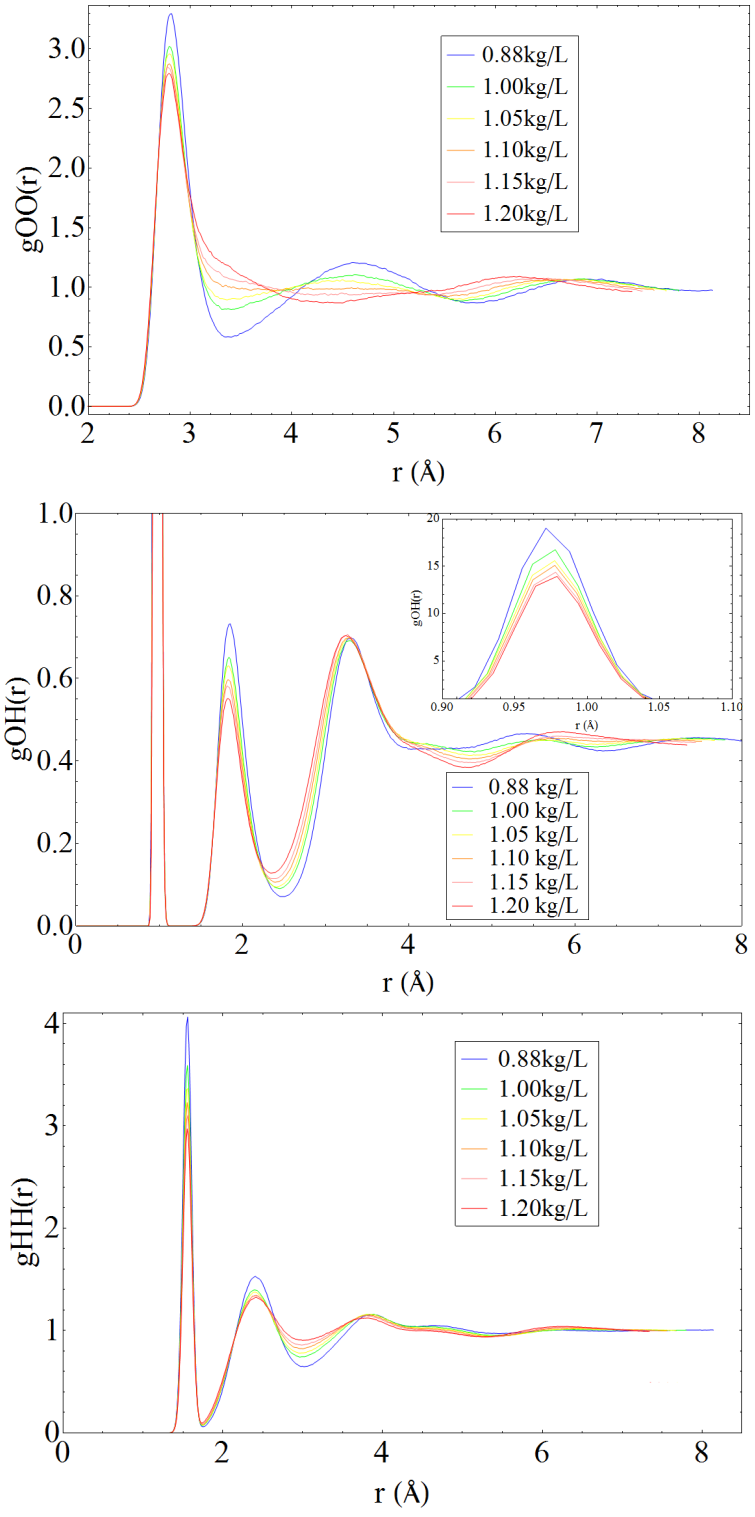

Figure B.1: RDFs at different densities for 128 TTM3F.

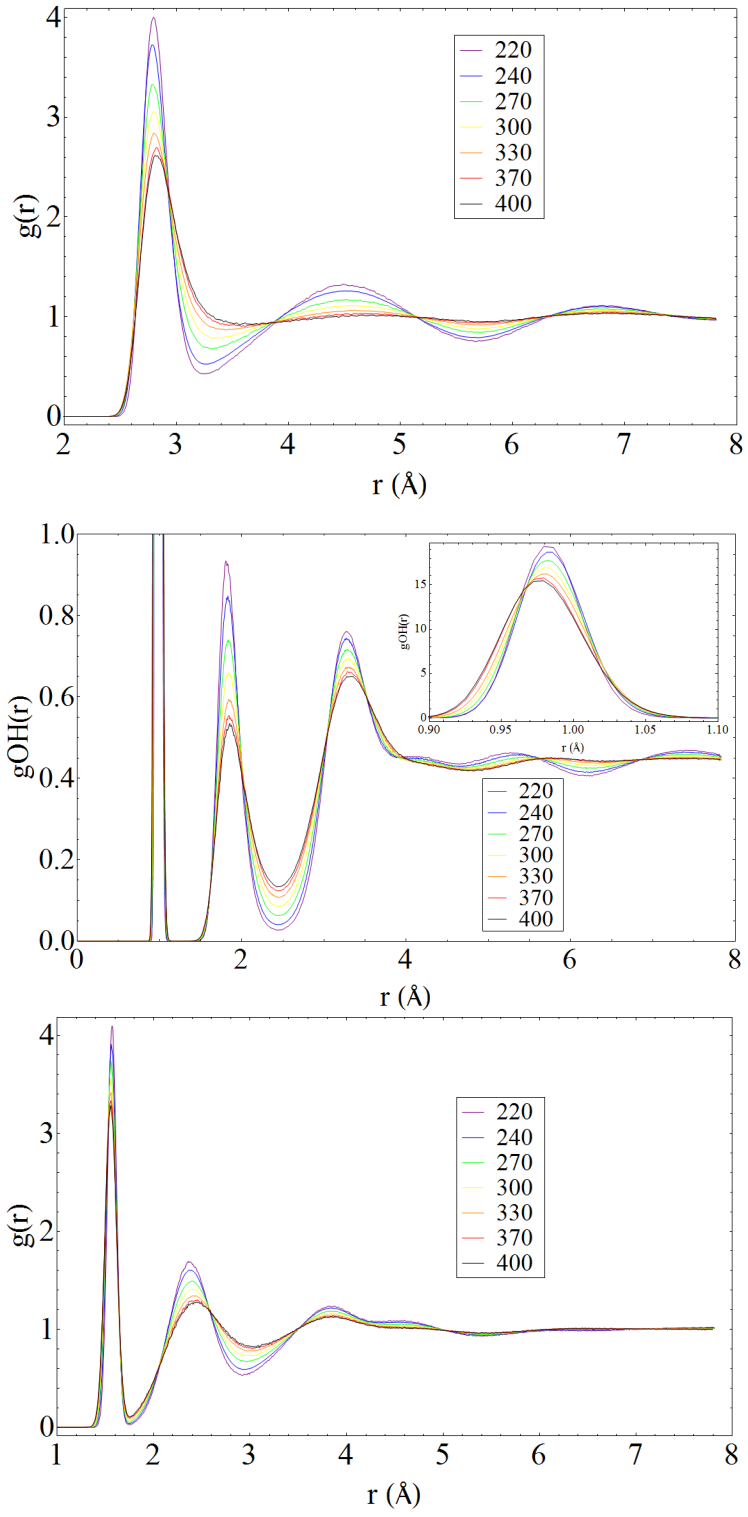

Figure B.2: RDFs at different temperatures for 128 TTM3F.

Appendix C

PIMDF90 program options

The code is available at https://github.com/delton137/PIMD. The input file is variable format and contains lines of the form *key value*, where 'key' is a case-sensitive name of a variable in the program, and *value* is a value. Boolean keys are specified as ".t." (true) or ".f" (false). The characters "!" or "#" may be used to comment lines, and blank lines are ignored.

C.0.3 Required options

fconfig	(string)	input filename - either a .xyz or .img (full bead simulation img)
fsave	(string)	label to be appended to all the output files
eq_timesteps	(int)	number of timesteps to equilibrate
run_timesteps	(int)	number of timesteps to run
delt	(real)	timestep in fs
pot_model	(int)	Model to be used: 2=ttm21f 3=ttm3f 4=qspcfw 5=spcf 6=SIESTA

C.0.4 Optional options

Output options

name	(type, default)	description
coord_out	(Bool, .f.)	centroid coordinates output
momenta_out	(Bool, .f.)	centroid velocities output
dip_out	(Bool, .f.)	all dipoles output
Edip_out	(Bool, .f.)	electronic (polarization) dipoles output
TD_out	(Bool, .f.)	total dipole output
images_out	(Bool, .f.)	coordinates for all images output
IMAGEDIPOLESOUT	(Bool, .f.)	dipoles for all images output
TP_out	(Bool, .f.)	Temp/Press (.t. to file, .f. to terminal)
ENERGYOUT	(Bool, .f.)	total energy output (separate file)
HISTOUT	(Bool, .t.)	OH histograms output (separate file)
BOXSIZEOUT	(Bool, .f.)	box size running average output
CALCGEOMETRY	(Bool, .t.)	compute average geometry of H2O molecules & output at end
CALCDIFFUSION	(Bool, .t.)	computes diffusion constant of oxygen & output at end
read_method	(Bool, 1)	.xyz file format (0 for OO....HHH and 1 for OHHOHH...)
CALCIRSPECTRA	(Bool, .f.)	store dipole moments and calculate IR spectra at end of run
CALCDOS	(Bool, .t.)	store H velocities and calculate DOS spectra at end of run
CALC_RADIUS_GYRATION	(Bool, .t.)	output avg. radius of gyration (column in TempPress file)
DIELECTRICOUT	(Bool, .t.)	output $\varepsilon(0)$, running avg. of eqn. 4.22 (column in TempPress file)
CHARGESOUT	(Bool, .f.)	charges on atoms output (to separate file)
WRITECHECKPOINTS	(Bool, .t.)	configurations of all beads output (to separate file)
td_freq	(int, 1)	Total dipole output frequency
tp_freq	(int, 10)	Temp/Press output frequency
ti_freq	(int, 2000)	all images output frequency
t_freq	(int, 10)	Output frequency for everything else
checkpoint_freq	(int, 2000)	checkpoint output frequency
RESTART	(Bool, .f.)	restart? (this will append to previous output files)

MD options

name	(type, default)	description
Nbeads	(int, 1)	Number of beads
setNMfreq	(real, 0)	frequency (cm^{-1}) to scale normal modes to (0 for none/RPMD)
PIMD_type	(string, 'full')	type of PIMD run ("full", "contracted", or "monomerPIMD")
intra_timesteps	(int, 10)	ratio of slow timestep / fast timestep for contraction scheme
Rc	(real, $L_{\min}/2$)	realspace cutoff (Å)
rc1	(real, .8 *Rc*)	start of switched VdW cutoff (Å)
eps_ewald	(real, 1.d-6)	eps for aewald
massO	(real, 15.994)	mass of Oxygen (au)
massH	(real, 1.008)	mass of Hyrdrogen (au)

Optional thermostat options

name	(type, default)	description
GENVEL	(Bool, .t.)	generate velocities
THERMOSTAT	(Bool, .f.)	Global Nose-Hoover thermostat?
BEADTHERMOSTAT	(Bool, .f.)	Bead thermostat?
CENTROIDTHERMOSTAT	(Bool, .f.)	thermostat bead centroid?
bead_thermostat_type	(string, 'none')	bead thermostat - "Nose-Hoover", "Langevin"(PILE) or "none"
temp	(real, 300)	Temperature (Kelvin)
tau	(real, .1)	τ for global thermostat (ps)
tau_centroid	(real, .1)	τ for centroid thermostat (ps)
global_chain_length	(int, 4)	global Nose-Hoover chain length
bead_chain_length	(int, 4)	bead Nose-Hoover chain length
BAROSTAT	(Bool, .f.)	Berendson barostat (untested! probably not working)?
tau_P	(real, 0.2)	τ for barostat (ps)
press	(real, 1.0	reference pressure (bar)
PEQUIL	(Bool, .f.)	pressure coupling during equilibration only?

TTM options

name	(type, default)	description
polar_maxiter	(int, 15)	max polarization dipole iterations
polar_sor	(real, 0.7)	TTM pol factor
polar_eps	(real, 1.d-3)	accuracy to converge dipoles to (tweaked for speed)
guess_initdip	(Bool, .t.)	guess initial, use predictor-corrector for dip iterations (increases speed)
print_dipiters	(Bool, .f.)	print info about pol. dipole convergence

SIESTA related options

name	(type, default)	description
sys_label	(str. ,required)	system label of .fdf file
siesta_name	(string, "siesta")	name of siesta executable
num_SIESTA_nodes	(int, 1)	# processors available for SIESTA calculations
SIESTA_MON_CALC	(Boolean, .f.)	option to enable SIESTA monomer calculation
mon_siesta_name	(str., required)	name of SIESTA executable for monomer calculation

For backwards compatibility with the older type of input file, the keyword *old* may be placed at the top of an old-style input and it will be read accordingly.

C.0.5 Note on periodic boundary conditions

The program only works for a cubic box, but it could be modified for arbitrary box. The box is automatically centered so that molecules span $[-L/2, L/2]$. The periodic boundary conditions follow the bead centroid - if the bead centroid crosses the edge of the box, then all the beads move with it. This means that at any time, some beads may lie outside the box. The potential() subroutine must be able to handle situations where beads are outside the box. All places in the code where PBCs are used are marked with *!PBC* in the code.